

---

Electronic Theses and Dissertations, 2004-2019

---

2013

## Theoretical Studies Of Nanostructure Formation And Transport On Surfaces

Maral Aminpour  
*University of Central Florida*



Part of the [Physics Commons](#)

Find similar works at: <https://stars.library.ucf.edu/etd>

University of Central Florida Libraries <http://library.ucf.edu>

This Doctoral Dissertation (Open Access) is brought to you for free and open access by STARS. It has been accepted for inclusion in Electronic Theses and Dissertations, 2004-2019 by an authorized administrator of STARS. For more information, please contact [STARS@ucf.edu](mailto:STARS@ucf.edu).

---

### STARS Citation

Aminpour, Maral, "Theoretical Studies Of Nanostructure Formation And Transport On Surfaces" (2013).  
*Electronic Theses and Dissertations, 2004-2019*. 2826.

<https://stars.library.ucf.edu/etd/2826>



THEORETICAL STUDIES OF NANOSTRUCTURE FORMATION AND  
TRANSPORT ON SURFACES

by

MARAL AMINPOUR  
B.Sc. University of Tehran, 2003  
M.Sc. University of Kashan, 2006

A dissertation submitted in partial fulfillment of the requirements  
for the degree of Doctor of Philosophy  
in the Department of Physics  
in the College of Science  
at the University of Central Florida  
Orlando, Florida

Fall Term  
2013

Major Professor: Talat S. Rahman

© 2013 Maral Aminpour

## ABSTRACT

This dissertation undertakes theoretical and computational research to characterize and understand in detail atomic configurations and electronic structural properties of surfaces and interfaces at the nano-scale, with particular emphasis on identifying the factors that control atomic-scale diffusion and transport properties. The overarching goal is to outline, with examples, a predictive modeling procedure of stable structures of novel materials that, on the one hand, facilitates a better understanding of experimental results, and on the other hand, provide guidelines for future experimental work. The results of this dissertation are useful in future miniaturization of electronic devices, predicting and engineering functional novel nanostructures. A variety of theoretical and computational tools with different degrees of accuracy is used to study problems in different time and length scales. Interactions between the atoms are derived using both *ab-initio* methods based on Density Functional Theory (DFT), as well as semi-empirical approaches such as those embodied in the Embedded Atom Method (EAM), depending on the scale of the problem at hand. The energetics for a variety of surface phenomena (adsorption, desorption, diffusion, and reactions) are calculated using either DFT or EAM, as feasible. For simulating dynamic processes such as diffusion of ad-atoms on surfaces with dislocations the Molecular Dynamics (MD) method is applied. To calculate vibrational mode frequencies, the infinitesimal displacement method is employed. The combination of non-equilibrium Green's function (NEGF) and DFT is used to calculate electronic transport properties of molecular devices as well as interfaces and junctions.



*This dissertation is dedicated to  
my father, Parviz Aminpour, who raised me to be like Farzan*

## ACKNOWLEDGMENTS

Foremost, I would like to express my sincere gratitude to my advisor Prof. Talat S. Rahman for her continuous guidance, support, immense knowledge, and her critical approaches to the problems that always helped me to explore for better and learn more. Her patience and understanding helped me through many occasions.

I am most grateful to the members of my committee, Dr. Sergei Stolbov, Dr. Beatriz Roldán Cuenya and Dr. Richard G. Blair for their time, and expertise throughout this study.

I am grateful to Dr. Duy Le for his generosity, his helpful scientific discussions and his efforts to make things simple and transparent for me to understand in several projects during my PhD study. Thanks to the friendship and support of my student and post-doc colleagues, G. Shafai Erfani, Z. Hooshmand, N. Neyyar, A. Kabir, T. Rawal and S. Acharya, F. Khalilzadeh Rezaei, L. Memarzadeh, Dr. M. A. Ortigoza, Dr. V. Turkowski, Dr. S. Hong, Dr. G. Nandipati, Dr. A. Ramirez, Dr. V. Chis and Dr. H. Yildirim.

I was involved in a number of collaborations during my PhD studies; I would like to acknowledge for their contributions which helped me to take steps forward in the learning curve. Dr. Oleg Trushin (Russian Academy of Sciences, Jaroslavl), Dr. Zdenek Chvoj (Institute of Physics of the Academy of Sciences of the Czech Republic), Dr. Michael Tringides (Iowa State University), Dr. Zdenka Chromcová (Institute of Physics of the Academy of Sciences of the Czech Republic), Dr. Tony F. Heinz (Columbia University), Dr. Adam Kiejna (Institute of Experimental Physics, University of Wroclaw), Dr. Ludwig Bartels and his research group (University of California,

Riverside), Dr. Richard G. Blair (NanoScience Technology Center, UCF), Dr. Pavel Jelínek and Prokop Hapala (Institute of Physics of the Academy of Sciences of the Czech Republic). I want to thank also to Dr. Richard Klemm for his willingness to teach and discuss whenever I seek for advice. I thank Mr. Lyman Baker for many conversations and invaluable comments which made the writing of this dissertation possible.

Lastly, I would like to thank my family for all their love and encouragement. My deepest thanks go to my parents, both of whom, especially my mother (my lovely Noonish), made many sacrifices to provide opportunities for me to be independent and to have a better life. Without their encouragement, the pursuit of this advanced degree would have never been started.

And most of all for my loving, supportive, encouraging, and patient husband Dr. Mustafa Gül whose faithful support during different stages of this PhD study is so appreciated. Also, thanks to Mastan and Ayicik for their unlimited love and support.

## TABLE OF CONTENTS

LIST OF FIGURES .....	xii
LIST OF TABLES .....	xxiv
CHAPTER 1. INTRODUCTION .....	1
CHAPTER 2. THEORETICAL METHODS.....	12
2.1 The Embedded Atom Model.....	12
2.2 Density Functional Theory .....	15
2.2.1 The Born-Oppenheimer Approximation.....	16
2.2.2 The Hartree-Fock Approximation.....	17
2.2.3 The Thomas-Fermi Model .....	19
2.2.4 Hohenberg and Kohn (H-K) Theorems .....	20
2.2.4.1 The First Hohenberg and Kohn Theorem .....	21
2.2.4.2 The second Hohenberg-Kohn Theorem.....	23
2.3 Kohn-Sham (K-S) Method:.....	24
2.4 The Exchange Correlation Functional .....	27
2.4.1 The Local Density Approximation (LDA) .....	29
2.4.2 The Generalized Gradient Approximation (GGA) .....	30
2.5 Solving the Kohn-Sham Equations.....	32
2.6 Pseudo-Potential Approximation .....	32

2.7	Bloch's Theorem.....	34
2.8	Calculation of the Kohn-Sham States.....	36
2.9	K-point Sampling.....	39
2.10	Molecular Dynamics (MD) Simulations.....	40
2.11	Molecular Statics Simulations .....	42
2.12	Nudged Elastic Band (NEB) Method .....	43
2.13	The Small Displacement Method for Phonon Calculations.....	43
2.14	Setting up the Transport Problem .....	45
2.15	Landauer-Buttiker Method.....	49
2.16	Non-equilibrium Green's Function (NEGF) for an Open System.....	53
CHAPTER 3. EFFECT OF INTERFACES ON ELECTRON TRANSPORT PROPERTIES OF MoS <sub>2</sub> -Au CONTACTS .....		57
3.1	Introduction.....	57
3.2	Methodology and Computational Details.....	57
3.3	Construction of Model Sample Au-MoS <sub>2</sub> -Au.....	60
3.4	Charge Density Analysis.....	63
3.4.1	Projected Redistribution of Average Charge Density in the Z Direction .....	63
3.4.2	Direction and Size of Charge Transfer .....	66
3.4.2.1	Barder Analysis.....	66
3.4.2.2	Charge-Neutrality Level (CNL).....	67

3.5	Electron Transport Properties .....	68
3.5.1	Zero Bias Transmission .....	68
3.5.2	I-V Curves.....	71
3.5.3	Schottky Barriers .....	72
3.6	Conclusions.....	79
CHAPTER 4. PREDICTIVE MODELING OF FUNCTIONAL MATERIALS .....		80
4.1	Part I: MoS <sub>x</sub> Square-like Novel Material .....	80
4.1.1	Introduction.....	80
4.1.2	Computational Details .....	83
4.1.3	An MoS <sub>x</sub> Structure with High Affinity for Adsorbate Interaction.....	84
4.1.4	Geometrical and Vibrational Properties of S-Cu/Cu(111) Models.....	86
4.1.5	Geometrical and Vibrational Properties of the Mo <sub>2</sub> S <sub>3</sub> /Cu(111) and Mo <sub>2</sub> S <sub>5</sub> /Cu(111) Models .....	89
4.1.6	Discussions and Conclusions.....	91
4.2	Part II: Mo <sub>6</sub> S <sub>6</sub> Nanowire .....	92
4.2.1	Introduction.....	92
4.2.2	Methods.....	93
4.2.3	Results and Discussions .....	94
4.2.4	Conclusions.....	101

CHAPTER 5. ELECTRONIC STRUCTURE AND GROWTH OF Mg(0001) FILM  
MORPHOLOGIES 102

5.1 Part I: Electronic Structure Features Controlling the Limit of and Reactivity in  
the Thin-Film Regime, Stacking Fault of Mg Adislands and Adatom Self-Diffusion 102

5.1.1	Introduction.....	102
5.1.2	General Computational Details.....	104
5.1.3	Results and Discussion .....	106
5.1.3.1	Bulk.....	106
5.1.3.2	Binding and Stacking Fault of an Mg Adatom and of Adislands on Mg(0001).....	131
5.1.3.3	Self-Diffusion of Mg Adatom on Terraces.....	146
5.1.4	Conclusions.....	148

5.2 Part II: Mg film Morphologies: A multi-scale Study of Mg(0001) Growth... 149

5.2.1	Introduction.....	149
5.2.2	Results and Discussion .....	151
5.2.3	Conclusions.....	153

CHAPTER 6. ANISOTROPY IN SURFACE DIFFUSION DUE TO PROXIMITY  
TO MISFIT DISLOCATION ..... 154

6.1 Part I: Cu/Ni(111)..... 156

6.1.1	Introduction.....	156
-------	-------------------	-----

6.1.2	Construction of the Cu/Ni(111) Model Sample.....	157
6.1.3	Computational Details .....	158
6.1.4	Mapping the Potential Energy Surface of Cu Adatom on Ni(111).....	159
6.1.5	MD Simulations of Adatom Diffusion on the Cu Film on Ni(111).....	160
6.1.6	Energy Barriers for Adatom Diffusion .....	161
6.1.7	Conclusions.....	163
6.2	Part II: Ni/Cu(111).....	164
6.2.1	Introduction.....	164
6.2.2	Computational Details .....	165
6.2.3	Construction of the Model Systems.....	165
6.2.4	MD Simulation of Adatom Diffusion in the Presence of Tensile and Compressive Dislocations .....	167
6.2.5	Conclusions.....	171
CHAPTER 7.	CONCLUSIONS.....	173
	LIST OF REFERENCES .....	176
	APPENDIX A: COPYRIGHTS AND PERMISSIONS .....	189
	APPENDIX B: LIST OF PUBLICATIONS.....	206



## LIST OF FIGURES

Figure 1-1. Interplay between theory, experiment and simulation. ....	2
Figure 1-2. (a) Structure of monolayer MoS <sub>2</sub> (b) MoS <sub>2</sub> crystal (c) Three-dimensional schematic view of single-monolayer MoS <sub>2</sub> transistors. [Reprinted Figure with permission from “B. Radisavljevic, A. Radenovic, J. Brivio, V. Giacometti and A. Kis, Nature Nanotechnology, 6(3), 147 (2011). Copyright (2011) by the American Physical Society.”].....	5
Figure 1-3. Chapter 3: Effect of interfaces on electron transport properties of MoS <sub>2</sub> -Au contacts. ....	8
Figure 1-4. Chapter 4: Predictive modeling of functional materials. [Reprinted Figure with permission from “D. Sun, W. Lu, D. Le, Q. Ma, M. Aminpour, M. Alcantara-Ortigoza, S. Bobek, J. Mann, J. Wyrick, T. S. Rahman, and L. Bartels, Angew. Chem. Int. Ed. 51, 10284 (2012). Copy right (2012) by the Angewandte Chemie.”] 9	9
Figure 1-5. Chapter 5: Mg(0001): (a) Diffusion on step and terraces of Mg(0001) step. (b) The thin-film limit and stacking fault of small Mg adislands.....	10
Figure 1-6. Chapter 6: Anisotropy in surface diffusion due to proximity to misfit dislocation. ....	11
Figure 2-1. Schematic representation of the Embedded Atom Method.....	14
Figure 2-2. Adiabatic or Born-Oppenheimer approximation decouples the electronic and nuclear degrees of freedom. (a) A real system consists of electrons and nuclei, both in motion. (b) Electronic equations can be solved assuming fixed positions for nuclei. (c) Each nucleus is then treated as moving as a classical particles affected by the potential generated by the electrons.....	17

Figure 2-3. (a) Electrons moving about fixed nuclei. (b) The single- electron or independent-particle model: each electron moves independently in a potential created by the nuclei and the rest of the electrons. ....	18
Figure 2-4. The Kohn-Sham approach to DFT.....	25
Figure 2-5. Self-consistent Kohn-Sham (K-S) algorithm.....	27
Figure 2-6. A simplified algorithm of how a MD simulation is performed. ....	41
Figure 2-7. The small displacement method for phonon calculations.....	45
Figure 2-8. Three different perspectives on the transport problem in a nano device: (a) Thermodynamics (b) Quantum mechanics (c) Electro-statistical points of view.....	46
Figure 2-9. Schematic representation of scattered wave functions by a potential barrier $V(r)$ .....	50
Figure 2-10. Self-energies of the leads as the effect of electrodes in terms of an effective interaction. ....	54
Figure 2-11. Flow-chart of the Sméagol program, highlighting the interconnection between SMÉAGOL and FIREBALL. Adapted from [38].....	56
Figure 3-1. Ball–stick model of armchair and zigzag edges of MoS <sub>2</sub> . Dark (blue) and light (yellow) balls represent Mo and S atoms, respectively. ....	61
Figure 3-2. Different samples with different interfaces of MoS <sub>2</sub> -Au used for approximation of Schottky barriers. ....	62
Figure 3-3. Atomic representation of the relaxed arrangement of single layer MoS <sub>2</sub> with different edges coupled with Au contacts: (a) Mo00S00 (b) Mo00S100 (c) Mo100S00 and (d) Mo100S100. ....	63

Figure 3-4. Electronic structure at the interfaces of MoS<sub>2</sub> and the Au contacts: (a) Sample models (b) planner (110) averaged charge density difference. The dashed lines represent the position of the Au-slab and MoS<sub>2</sub> layers. Positive values indicate an accumulation of charge; negative values indicate a depletion of charge with respect to the separated fragments. (c) 3D charge density redistribution [ $\Delta \rho(\mathbf{r}) = \rho(\text{MoS}_2 + \text{Au}) - \rho(\text{MoS}_2) - \rho(\text{Au})$ ]. Isosurfaces are drawn with isovalue of 0.01 unit. The blue and red surfaces represent, respectively, the charge accumulation and deficit regions. (i.e. charge flows from red to blue regions) (d) Charge density redistribution plotted along the vertical plane passing through two Mo atoms of MoS<sub>2</sub> molecule (y-z plane). Contours are drawn in scale from 0.003 to 1 unit at interval of 0.05. .... 64

Figure 3-5. Averaged charge density difference along Z direction for fcc, hcp and top sites. .... 66

Figure 3-6. Partial density of states of total system, MoS<sub>2</sub> molecules and the Au electrodes for 4 different Au-MoS<sub>2</sub>-Au samples. The red line and green lines depict the Fermi level and the charge neutrality level (CNL), respectively. .... 68

Figure 3-7. The equilibrium transmission in zero bias versus energy curve of the various sorts of Au-Mo-Au junctions. Right-hand side graphs show the logarithmic form of the Transmission versus Bias = 0. Because of the exclusion principle, it is apparent that the electron will pass from filled states to empty states. .... 69

Figure 3-8. Transmission peaks of the sample when (a) bias voltage increases (positive bias) or (b) bias voltage decreases (negative bias). .... 70

Figure 3-9. Transmission curves in various biases versus energy curve of the various types of Au-Mo-Au junctions. .... 71

Figure 3-10. I-V curves for various sorts of Au-Mo-Au junctions with different interfaces of Au-MoS <sub>2</sub> .....	72
Figure 3-11. Average Hartree potential of (a) MoS <sub>2</sub> , (b) Au (1x1x16) along Z direction (c) Band structure of single-layer MoS <sub>2</sub> . ....	74
Figure 3-12. P-type Mo00 –Au contact Schottky barrier. ....	75
Figure 3-13. P-type Mo00 –Au contact Schottky barrier. ....	76
Figure 3-14. P-type S00–Au contact Schottky barrier.....	77
Figure 3-15. N-type Mo100–Au contact Schottky barrier.....	78
Figure 4-1. STM (Scanning Tunneling Microscope) image of MoS <sub>x</sub> structures (Imaging parameters: bias: 0.93 V, current: 0.21 nA, scale bar: 5 nm).[Reprinted Figure with permission from “D. Sun, W. Lu, D. Le, Q. Ma, M. Aminpour, M. Alcantara-Ortigoza, S. Bobek, J. Mann, J. Wyrick, T. S. Rahman, and L. Bartels, <i>Angew. Chem. Int. Ed.</i> 51, 10284 (2012). Copy right (2012) by the Angewandte Chemie.”]	80
Figure 4-2. Single layer MoS <sub>2</sub> /Cu(111) (a) geometrical structure and (b) simulated STM image corresponding to it. [Reprinted Figure with permission from “D. Le, D. Sun, W. Lu, L. Bartels, and T. S. Rahman, <i>Phys. Rev. B</i> 85, 075429 (2012). Copy right (2012) by the American Physical Society .”].....	81
Figure 4-3. DFT-optimized adsorption geometry of AQ on (a) Mo <sub>2</sub> S <sub>3</sub> horizontal (BE= 3.36 eV), (b) Mo <sub>2</sub> S <sub>3</sub> vertical (BE= 1.92 eV), (c) Prince Model (BE= 1.47) and (d) MoS <sub>2</sub> (BE= 1.32 eV) adsorption configurations, respectively. ....	86
Figure 4-4. (a) Cu–S overlayer models of Domange and Oudar, Foss and Saïdy. yellow: sulfur, light brown: Cu atoms, dark brown: surface Cu atoms (b) STM images of	

Prince, Foss and Saidy models. (Occupied states, LDOS: -1 to 0.0 eV, Isovalue: 10-5 e/A.) .....	87
Figure 4-5. Phonon density of state curves of the Foss and Prince models (a) all range (0 to 35 meV), (b) low frequencies (1to 10 meV) and (c) high frequencies (27 to 32 meV). .....	89
Figure 4-6. Top and side view of (a) Mo <sub>2</sub> S <sub>5</sub> and (b) Mo <sub>2</sub> S <sub>3</sub> models.....	90
Figure 4-7. Phonon density of states (meV) of Mo <sub>2</sub> S <sub>5</sub> and Mo <sub>2</sub> S <sub>3</sub> samples (a) full frequencies (b) high frequencies (c) low frequencies .....	91
Figure 4-8. Atomic model of Mo <sub>6</sub> S <sub>6</sub> nanowires (a,b) and the Cu(111) surface (c). Panels (d) and (e) show models of two potential configurations of Mo <sub>6</sub> S <sub>6</sub> nanowires on Cu(111), a symmetric one (d) and an asymmetric one (e). We superimpose simulated STM images, in which we mark the maxima with black circles. While in (d) both maxima have the same height, in (e) the ones on the right are more prominent than those on the left.....	95
Figure 4-9. STM images (current: 0.13 nA, bias: -0.82 V) of a) isolated Mo <sub>6</sub> S <sub>6</sub> nanorod on Cu(111) in good agreement with the simulated STM image Figure 4-8(d); b) overview of our sample preparation showing the nanorods, the sulfur termination of Cu(111) as hexagonal pattern of apparent protrusions, and MoS <sub>2</sub> islands with characteristic brim state (grey, smooth areas); c) cluster of aligned and equally spaced Mo <sub>6</sub> S <sub>6</sub> nanorods at 4D separation. .[Reprinted Figure with permission from “D. Le, D. Sun, W. Lu, M. Aminpour, C. Wang, Q. Ma, T. S. Rahman, and L. Bartels, Surface Science, 611, 1-4 (2013).Copyright (2013) by the American Physical Society. ”].....	97

Figure 4-10. Interaction energy between two isolated  $\text{Mo}_6\text{S}_6$  nanowires per  $\text{Mo}_6\text{S}_6$  repeat unit (left ordinate) as functions of their separation measured in Cu-Cu bond length  $D$ . Binding energy of two  $\text{Mo}_6\text{S}_6$  nanowires to the Cu(111) substrate per  $\text{Mo}_6\text{S}_6$  repeat unit (right ordinate) as a function of their separation. The values are taken for the adsorption configuration (symmetric/asymmetric) that yields optimal binding energy at the indicated separations. .... 99

Figure 5-1. Calculated energetic and structural properties of Mg(0001) as a function of the number of layers forming the slab,  $N$ : (a) Formation energy per atom,  $E(N)/N$ ; the dashed line indicates the cohesive energy of bulk Mg, (b) surface energy and (c) the change (%) in the first interlayer distance with respect to the bulk value,  $\Delta d_{12}$ . In (b) and (c), the dashed line is a guide for the reader indicating the convergent value of surface energy  $\sigma$  and  $\Delta d_{12}$ , respectively. Grey (red) circles and black squares are data from Ref. [105] and this work, respectively. [Reprinted black squares in Figure with permission from “Li, X. G.; Zhang, P.; Chan, C. K., PHYSICA B; 390, 1-2; 225 (2007) . Copy right (2013) Elsevier”] [106]..... 110

Figure 5-2. Calculated changes in the first ( $\Delta d_{12}$ ), second ( $\Delta d_{23}$ ), and third ( $\Delta d_{34}$ ) interlayer distances of Mg(0001) with respect to the bulk value. The (orange) bar represents the experimental value as measured by LEED [20]. The number inside the round parenthesis corresponds to the number of layers in the slab used in previous calculation and, in the case of the present PW91 calculation, the convergent value obtained from analyzing slabs formed by 2 to 30 layers. The numbers inside the squared parenthesis correspond to the references of previous works [106]. .... 112

Figure 5-3. Calculated slab thickness dependence of the first, second and third interlayer relaxations,  $\Delta d_{12}$ ,  $\Delta d_{23}$  and  $\Delta d_{34}$  [106]. ..... 114

Figure 5-4. Normalized nearly free-electron like LDOS of the  $3s^{2-x} 3p^x$  valence electrons of Mg(0001) surface atoms for a 30-layer slab [106]. ..... 116

Figure 5-5. Calculated LDOS around the Fermi level for the surface atom of Mg(0001) as a function of the number of layers of the slab, which are indicated by the numbers labeling the curves. The LDOS is normalized and the scale in each inset is the same. .... 117

Figure 5-6. Comparison between experiment and electronic density of states calculations to explain the oxidation rate of Mg films (a) The relative weight of the intensity of the oxygen-induced peak in the Mg 2p spectrum (indicative of the oxidation rate) as a function of the number of layers, N, taken from [135]; (b) Calculated total  $DOS_{EF}(N)$  of a Mg(0001) slab (taken from [136]); (c) Calculated  $LDOS_{EF}(N)$  of the surface atoms of Mg(0001). The dashed line is a guide for the eye to compare the maxima/minima of the oxidation rate as a function of N with those of the calculation [106]. ..... 119

Figure 5-7. (Calculated in-plane ( $p_x+p_y+d_{xy}+d_{x^2-y^2}$ ) PLDOS of the first- and second-layer atoms of Mg(0001) for varying N (a) from 4 to 6; (b) from 6 to 8; (c) from 8 to 10; (d) from 10 to 13; (e) from 13 to 16; and (f) from 17 to 19. The PLDOS scale in each inset is the same. The arrows are a guide for the eye to identify the centroids of the PLDOS peaks around  $E_F$  and recognize how they shift as a function of number of layers [106]. ..... 124

Figure 5-8. Comparison between experiment and theories to explain the oxidation rate of Mg films (a) The relative weight of the intensity of the oxygen-induced peak in the Mg 2p spectrum (indicative of the oxidation rate) as a function of the number of layers, N, taken from [135]; (b) Calculated in-plane ( $p_x+p_y+d_{xy}+d_{x^2-y^2}$ ) PLDOS<sub>EF</sub>(N) of the first- and second-layer atoms of Mg(0001); (c) Mg electronic charge density decay length into vacuum (calculated in analogy with the penetration depth of a wave-function into the classically forbidden region of the three dimensional finite square well) as a function of N, taken from [137]. The dashed line is a guide for the eye to compare the maxima/minima of the oxidation rate as a function of N with those of the calculation [106]..... 125

Figure 5-9. Fig. 4 from [130] 2D Electron-density-difference distributions near the relaxed Mg(0001) surface relative to the average electron density in the bulk expressed as a percentage of the latter and cut along the (10-10) plane. The atomic configuration commensurates with the optimized positions calculated in the LDA is also shown. Darker grey is used to indicate regions with smaller charge density while lighter shades represent regions with charge density above average. [Copyright included in Appendix A] ..... 127

Figure 5-10. Change in the charge density profiles perpendicular to the surface for the bulk-truncated surfaces of Mg(0001). The electron densities are normalized by the average bulk value The figures are adopted from (a) Fig. 4 (Cho *et al.*), (b) Fig. 1 (Staikov *et al.*) and (c) Fig.1 (Wachowicz *et al.*) of references [129, 134, 141]. [Reprinted Figure with permission from “J. Cho, Ismail, Z. Zhang and E.W. Plummer, Phys. Rev. B 59, 1677–1680 (1999). Copy right (1999) by the American



Physical Society ” and “Reprinted Figure with permission from “P. Staikov, Talat. S. Rahman, Phys. Rev. B 60, 15613–15616 (1999). Copy right (1999) by the American Physical Society.” and see Appendix A]..... 129

Figure 5-11. (higher insets) Difference between the charge density of bulk Mg and that of a non-relaxed bulk-terminated Mg(0001) surface (a) Isosurfaces. The z-axis is perpendicular to the surface. The blue balls represent the first four layers of the slab. The red color indicates the region of Mg(0001) that displays more charge density than the corresponding one in bulk Mg. (b) [0001] Cross section of the isosurface in (a). (Lower insets) [0001] Cross sectional planes of the total charge density around (c) the fully relaxed Mg(0001) and (d) bulk Mg. Darker (brown) regions in (c) and (d) indicate less charge. In (b)-(d), the plane is located at the height of the surface or bulk atoms under consideration in order to highlight the charge accumulation around the fcc hollow site of Mg(0001) [106]..... 130

Figure 5-12. [0001] Cross section of the total charge density of (a) non-relaxed bulk-terminated Mg(0001) and (b) fully relaxed Mg(0001). Darker (brown) regions indicate less charge. The plane is located at  $\sim 1.2 \text{ \AA}$  above the position of the surface atoms [106]. ..... 138

Figure 5-13. Three dimensional charge-density difference isosurfaces showing the Friedel oscillations in (a) Mg(0001) and (b) Be(0001). The charge density isovalue is the same for both surfaces. The difference is taken between the charge density of bulk Mg and that of a non-relaxed bulk-terminated Mg(0001) surface. The z-axis is perpendicular to the surface. The light blue and green balls represent the three layers

of the slab. The red surfaces indicate the regions in the surface displaying more charge density than the corresponding one in bulk [106]. ..... 145

Figure 5-14. (a) Model system with thickness of 7 atomic layers as substrate and one atomic layer as step (b) Side view of 3 top layers of the model system. The darkest gray is the (3x4) step layer. The gray color get lighter as it goes toward the inner layers. (c) Top view of the model system The white and the light gray triangles represent the fcc and hcp sites of the Mg(0001) step Model. The arrows point to the actual sites where it initializes (fcc) and ends up (hcp). The number corresponding to each arrow shows the energy barrier of the i diffusion path illustrated by arrows. The Ehrlich-Schwoebel barrier energy of steps A and B are depicted as ESA and ESB correspondingly..... 152

Figure 6-1. Summary (2D) of the procedure for preparing of a sample illustrated here with a 5-layer film to study the diffusion: (a) Relaxation of the sample using standard MD cooling energy minimization; (b) Formation of an extended Cu island, resulting from application of RBP, followed by a second phase of MD cooling; (c) Removal of the island; (d) Addition of a single Cu adatom atop the film. (In this study, we vary the position of this adatom with respect to the defect). ..... 158

Figure 6-2. A Cu adatom on the dislocated surface of a 5-layer Cu film on a Ni(111) substrate. .... 159

Figure 6-3. Potential Energy Surface for (a) the defect-free surface and (b) for the dislocated surface..... 159

Figure 6-4. (a) A typical isotropic trajectory of the adatom on a defect-free surface. The arrow shows the starting point of the simulation. (b) A typical anisotropic trajectory

of the adatom on a defective surface when its initial position is one row distant from the dislocation line, which runs parallel to the edge of the slab  $26 \text{ \AA}$  from it. The arrow shows the starting point of the simulation. .... 160

Figure 6-5. Trajectory from MD simulations of attachment and detachment of adatom along the dislocation line (starting point is  $21 \text{ \AA}$  away from the edge of the slab). The white dot is the starting point of the simulation. .... 161

Figure 6-6. Locations of the adatom on the dislocated surface ..... 162

Figure 6-7. Energy barriers (a) on a defect-free and (b) on a defective surface for any diffusion path from an fcc to an fcc site (by way of an hcp site). The highest barrier corresponds to the motion in the direction perpendicular to dislocation line. .... 163

Figure 6-8. Schematic cross-section of slab containing a dislocation: (a) in a tensilely strained system (b) in a compressively strained system. The numbers of atoms in the Z and X directions is the same for both samples, as are the numbers of atoms in the Y direction of the two substrates:  $N_Z = 7$ ;  $N_X = 10$ ;  $N_Y (\text{Cu-substrate}) = 40 = N_Y (\text{Ni-substrate})$ . But in the tensilely strained system (a), the number of atoms in the Y dimension of the (Ni) film is one more (41) than in the substrate, while in the compressively strained system the number of atoms in the Y direction of the (Cu) film is one less (39). The closed line in Fig 2a and Fig.2b are the Burgers circuits around the dislocation misfits ( $f = (a_{\text{film}} - a_{\text{substrate}})/a_{\text{film}} \times 100$ ) – negative when the dislocation results from tensile strain, positive when it results from compressive strain. Note that the X direction is in to the sheet. .... 167

Figure 6-9. (a), (c) Typical isotropic trajectories of an adatom on defect-free surfaces (b), (d) Typical anisotropic trajectories of an adatom on dislocated surfaces generated by different types of strain. .... 169

Figure 6-10. Energy barriers for diffusion of (a) Ni on non-defective and (tensilely generated) defective Ni/Cu(111) and of (b) Cu on non-defective and compressively generated defective Cu/Ni(111) – in each case from an fcc to an fcc site by way of an hcp site, as schematized in (d). The contrast between the relative strengths of barriers to diffusion along paths parallel and perpendicular to the dislocation line is schematized in the juxtaposition of (d) and (f), for tensilely and compressively generated dislocations, respectively..... 171

## LIST OF TABLES

Table 3-1. Charge transfer results with different methods .....	67
Table 5-1. Calculated (at 0 K) and measured lattice parameters (a and c/a), cohesive energy, and bulk modulus of Mg [106]. .....	107
Table 5-2. Calculated changes (%) in the interlayer distances between the surface layers of Mg(0001) with respect to the bulk value (2.582 Å), $\Delta d_{i,j+1}$ , for a 23-layer slab using both the ultra-soft PW91 within the Quantum espresso code (QE) and the PAW PBE pseudopotentials within the VASP code [106]. .....	109
Table 5-3. Changes in the first ( $\Delta d_{12}$ ), second ( $\Delta d_{23}$ ), and third ( $\Delta d_{34}$ ) interlayer distances of 23 layers of Mg(0001) with respect to the bulk value as rendered by our PAW-PBE-VASP calculations, our US-PW91-QE calculations, previous calculations and experiment [106]. .....	113
Table 5-4. Slab thickness dependence of the adatom binding energy at the fcc and hcp sites, $E_B(\text{fcc})$ and $E_B(\text{hcp})$ , respectively, and of the stacking fault energy, $\Delta E_B = E_B(\text{fcc}) - E_B(\text{hcp})$ [106]. .....	133
Table 5-5. Binding energy, $E_B$ , and stacking fault, $\Delta E_B$ , per atom of Mg adislands on Mg(0001) – from a monomer to an octamer – and of a full overlayer placed at both the fcc and the hcp sites for a structure in which (a) the whole system is totally relaxed (b) only the Mg adisland atoms are allowed to relax but the Mg(0001) substrate is kept frozen [106]. .....	134
Table 5-6. Structural characterization of the Mg adislands -- dimer, trimer and tetramer – on the Mg(0001) surface. These values correspond to the case in which all atoms are allowed to relax. The distance among atoms forming the adislands are denoted by	

$d_{IA}$ ;  $Z_{AS}$  stands for the height (vertical distance) of the atoms forming the adisland with respect to their non-equivalent substrate neighbors,  $d_{NN-S}$  stands for distance between the atoms forming the island and their substrate non-equivalent nearest neighbors [106]..... 136

Table 5-7. Structural characterization of the Mg adislands -- dimer, trimer and tetramer -- on the Mg(0001) surface. These values correspond to the case in which only the atoms of the adisland are allowed to relax while the atoms of the substrate are kept frozen. The distance among atoms forming the adislands are denoted by  $d_{IA}$ ;  $Z_{AS}$  stands for the height (vertical distance) of the atoms forming the adisland with respect to their non-equivalent substrate neighbors,  $d_{NN-S}$  stands for distance between the atoms forming the island and their non-equivalent substrate nearest neighbors [106]..... 137

Table 5-8. Two-dimensional plots of the total charge density of the n-mers ( $n=1, \dots, 4$ ) at the fcc and hcp sites of a bulk-like Mg(0001) substrate. The plots correspond to a plane parallel to the substrate at  $\sim 1.2 \text{ \AA}$  above it (see Sec.3d). The scale is such that dark regions denote less charge. The left-most column displays the stacking-fault energy per atom,  $\Delta E_B$ . [106]..... 141

Table 5-9. Two-dimensional plots of the total charge density of the totally relaxed n-mers ( $n=1, \dots, 4$ ) at the fcc and hcp sites of Mg(0001). The plots correspond to a plane parallel to the substrate at  $\sim 1.2 \text{ \AA}$  above it (see Sec.3d). The scale is such that dark regions denote less charge. The left-most column displays the stacking-fault energy per atom,  $\Delta E_B$ . (\*) Note that, strictly speaking, the dimer does not sit at hcp sites but rather at the bridge [106]..... 142

Table 5-10. Slab thickness dependence of the adatom diffusion energy barrier from fcc to hcp,  $\Delta E_D(\text{fcc} \rightarrow \text{hcp})$ , and from hcp to fcc,  $\Delta E_D(\text{hcp} \rightarrow \text{fcc})$  [106]. ..... 146

## CHAPTER 1. INTRODUCTION

Construction and application of nanostructured surface and interface is an active multi-interdisciplinary research area involving physics, chemistry, materials science, and biology. Methods used for fabrication of nanostructured surfaces and interfaces are commonly catalogued as “top-down” or “bottom-up”, or a combination of these. Examples are lithography (top-down), soft-lithography (combination), self-assembly (bottom-up), and chemical synthesis (combination: synthesis of nano-entities with controlled surface and interface).

Understanding phenomena on surfaces has been one of the long-term goals of material science for the sake of technological applications. For example, understanding of the underlying electronic factors governing chemical activity can be the key to the engineering of surfaces with such features. To understand the physical and chemical phenomena at nanometer scale on structured surfaces and interfaces, we need to understand the interaction of functional small molecules and of nano-entities with nanostructured surfaces and interfaces. Of particular interest is the role of nanostructured surfaces and interfaces in unconventional chemical reactions. Such roles be further associated with the local physical properties of these surfaces and interfaces, thanks to scanning probe microscopy and other surface-sensitive methods for characterization.

The use of structured surfaces and interfaces as platforms offers the prospect of realizing new types of functional materials and devices. High performances are expected, e.g. increased conductivity with reduced size and structural ordering of sensing materials, and unconventional physical properties of chemicals prepared by on-surface chemistry.

As noted when the U.S. national nanotechnology research agenda was first conceived, “fundamental understanding and highly accurate predictive methods are critical to successful



manufacturing of nanostructured materials, devices and systems” (Roco Williams, and P. Alivisatos 1999, 25). Over the past ten years, the main focus in theory, modeling and simulation research has been on explaining the properties of materials and devices in terms of the geometric and electronic structures of matter at the nanoscale. Consequently, theory, modeling, and simulation have played an essential role in developing a fundamental understanding of nano-scale building blocks [1].

Computer experiments play a very significant role in science today. In the past, physical sciences were distinguished by interplay between experiment and theory. In experiment, results (in numeric form) are obtained from a set of systematic measurements. In theory, a model of the system is constructed as a set of mathematical concepts and equations. The theoretical based model is then validated by its capability to describe the system’s behavior in a few simple cases in special circumstances that make it easy to solve [2].

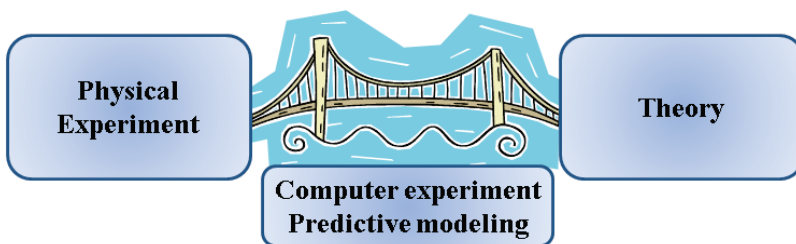


Figure 1-1. Interplay between theory, experiment and simulation.

Unfortunately, many real physical problems of extreme interest is beyond the realm of these special circumstances. Among different special circumstances, one could mention the physics and chemistry of surfaces, defects, organic molecules and clusters of atoms – all of which involves a large number of degrees of freedom. Nowadays, the advent of high speed

computers changed the picture by inserting a new element right in between experiment and theory: the computer experiment. In this way, complexity can be introduced to investigate more realistic systems, opening a road towards a better understanding of real experiments [2].

On one side, computer simulations raised the demand for accuracy of the models. Therefore, simulation brings to life the theoretical models, disclosing critical areas and providing suggestions to improve them. On the other side, simulation can often mimic experimental conditions, to the extent that computer results can sometimes be compared directly with experimental results. Therefore, simulation becomes an exceedingly powerful tool not only for understanding and interpreting the experiments at the microscopic level, but also for studying regions which are not accessible experimentally, or which would need very expensive experiments. Simulation can even explore a set of possible possibilities in advance of experiment with an eye to distinguishing more promising from less promising avenues for eventual experimental and engineering investigation.

Design of novel nano-electronic devices is challenging because it requires one to take into account not only the device-level quantum effects due to miniaturization, but also the changes in properties of the material itself, which can once again be explained by quantum mechanics. As an example consider the case of single-layer molybdenum disulfide, which is considered a transistor material. While owing to challenges in fabrication and manufacture, such a transistor is as yet far from production, the calculational demonstration of its properties is a clear indicator of two characteristics of the future semiconductor devices in general: (a) because the nature and properties of the material used for these devices will play an important role in the behavior of the devices themselves, there will be a constant push to find new materials with

desired properties, and (b) the atomistic dimensions of the novel nano-devices will prompt an atomistic analysis of their behavior unavoidable.

Molybdenum disulfide is an intriguing material. It is a prototypical semiconducting material consists of stacked hexagonal S-Mo-S layers. These layers, conventionally referred to as monolayers, are weakly bound by van der Waals forces. In a manner similar to that common in the production of graphene, MoS<sub>2</sub> samples consisting of a single or a few monolayers can be produced by micromechanical exfoliation. Owing to their atomic-scale thickness, two-dimensional materials such as graphene and MoS<sub>2</sub> have significant potential for application in the next generation of nano-electronics. Graphene [3, 4] is a famous 2D material with its high mobility [5]. Yet pristine graphene does not have a bandgap, which is a very important property for many applications, as in transistors. There are different ways to engineer a graphene with bandgap, such as applying a high voltage [6, 7], but unfortunately increasing in the band gap reduces the mobility or requires high voltages [8-10]. On the other hand, MoS<sub>2</sub> monolayers have an intrinsic direct bandgap of 1.8 eV [11] (bulk band gap= 1.2 eV [12]). Mobility in single-layer MoS<sub>2</sub> is comparable with that of silicon films. On/off ratio as well as ability to amplify signals have been recently demonstrated. Because monolayer MoS<sub>2</sub> has a direct bandgap [11], it can be used to construct inter-band tunnel FETs, which provide lower power consumption than classical transistors [13]. Monolayer MoS<sub>2</sub> could also complement graphene in applications that require thin transparent semiconductors, as do optoelectronics and energy harvesting.

One of the fundamental challenges in MoS<sub>2</sub> technology is the growth process, in as much as any practical application requires the development of techniques that can produce large quantities of single-layer MoS<sub>2</sub> in a controlled manner. Predictive modeling (in which theory and

computation work hand-in-hand with experiments) can play a helpful role in bringing to light the fundamental processes that facilitate layer-by-layer growth of MoS<sub>2</sub>.

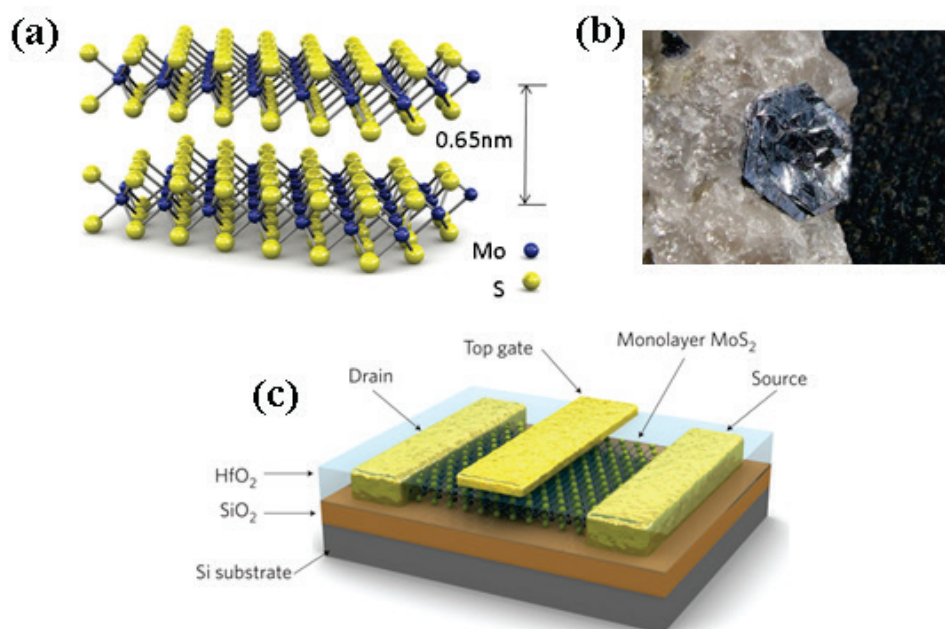


Figure 1-2. (a) Structure of monolayer MoS<sub>2</sub> (b) MoS<sub>2</sub> crystal (c) Three-dimensional schematic view of single-monolayer MoS<sub>2</sub> transistors. [Reprinted Figure with permission from “B. Radisavljevic, A. Radenovic, J. Brivio, V. Giacometti and A. Kis, Nature Nanotechnology, 6(3), 147 (2011). Copyright (2011) by the American Physical Society.”]

To study growth process one requires a multi-scale approach owing to the fact that growth proceeds in seconds and minutes in real observations, while the relevant atomistic processes transpire in the time scale of nanoseconds. There has been great effort for the last two decades towards a better understanding of the underlying principles governing the growth of thin metal films because of their potential relevance in technological applications [23]. The Nobel Prize in Chemistry 2013 awarded to Martin Karplus, Michel Levitt and Arieh Warshel for “Development of Multiscale models for Complex Chemical Systems” is recognition of how the

multiscale modeling has transformed modern research in Physics, chemistry, materials science and the life sciences.

To study the growth and formation of nanostructures on surfaces, electronic structure calculations play an important role on determining the height of diffusion energetics by evaluating the binding energies of the adsorbates on surfaces [30, 31]. It is also shown that for some surfaces mass transport at step edges is the crucial criterion for the resulting growth morphology [24]. It was demonstrated that the height of the Ehrlich-Schoewebel (E-S) barrier -- the additional diffusion barrier encountered by a surface atom, when crossing a step -- can be correlated to the observed growth morphology [25, 26]. Systems with large E-S barrier are expected to grow rough 3D films (Volmer–Weber and Stransky-Krastanov growth) as mass transport is prohibitive. Contrarily, small E-S barrier allows growth of smooth films, and growth mechanism is layer-by-layer (Frank–van der Merwe growth). It is also established that diffusion of single atoms on surfaces can occur via two different diffusion mechanisms, namely hopping and exchange [27].

Recently attention has also been directed toward understanding the growth on heterostructure systems in which the atoms are deposited on a substrate of another element. Note that hetero diffusion is dissimilar to homo because of the presence of the strain induced by the misfit between the film and substrate elements. In general, growth of a thin-film on a dissimilar substrate results in lattice-mismatch strain in the interface of the two different materials that at a certain critical point is relieved through the formation of network of dislocations [6]. Each dislocation line in the film generates a long-range inhomogeneous strain field, which alters

atoms' potential energy surface, resulting in anisotropy in atomic transportation on the thin film and consequently formation of patterned nano-structures and self-assembly process.

In Chapter 1, I describe the problems undertaken in this dissertation towards the ultimate goal of understanding the factors that control thin-film growth and lead to an understanding of the physical properties of functional materials. I explain the importance of the prototypical system chosen to extract the controlling parameters for building functionalized materials. I set forth the relevant background for each problem, and summarize the current status of each. Finally, I introduce the theoretical methods used in this study, and explain the reason(s) for their selection.

In Chapter 2, I describe in detail each theoretical method employed in the studies that comprise this dissertation. The first sections discuss the energy models by which the interactions between the atoms in the systems are described. It then provides details of the calculation in the molecular dynamics (MD) and molecular statics (MS) simulations and the finite displacement method, adopted for calculating phonon density of states. The last section discusses the non-equilibrium Green's function (NEGF) method, employed to calculate electrons transport properties.

In Chapter 3, in the light of recent experimental findings, I discuss my *ab-initio* density functional theory (DFT) calculations in combination with the non-equilibrium Green's function method to examine the effect of Au contacts on the electronic transport properties of single layer MoS<sub>2</sub>. Our results indicate that Au, the most common contact metal in this system [5], forms a tunnel barrier at the interface, which causes electron injection into MoS<sub>2</sub>. The ultimate of this systematic study is to calculate the Schottky barriers for different interfaces of MoS<sub>2</sub> and Au

contact, a fundamental understanding of which is critical to successful manufacturing of MoS<sub>2</sub> transistors. Charge density analysis, transmission spectra, and I-V curves will be reported and discussed as a function of MoS<sub>2</sub> and Au interfaces of varying geometry.

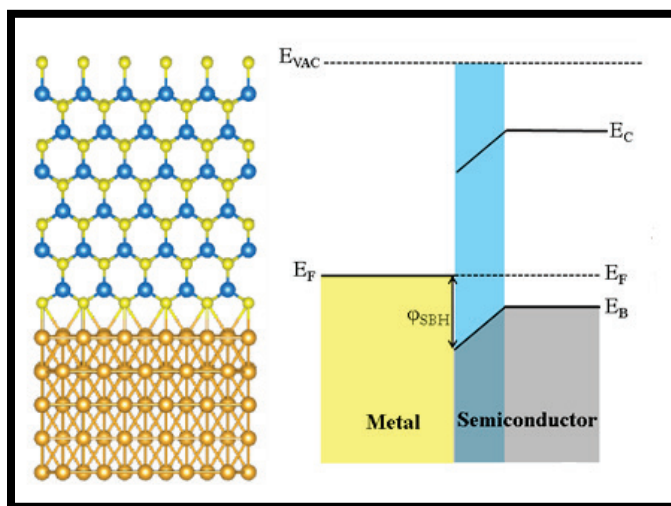


Figure 1-3. Chapter 3: Effect of interfaces on electron transport properties of MoS<sub>2</sub>-Au contacts.

In Chapter 4, I undertake to predict and reveal the novel MoS<sub>x</sub> structure on Cu(111) surfaces using the predictive modeling procedure that is explained in detail in Chapter 4. Examination of the structural, dynamical and thermodynamical properties is crucial in understanding growth, catalysis and many other phenomena. We found a novel MoS<sub>x</sub> surface structure on copper, which we propose to have the composition (Mo<sub>2</sub>S<sub>3</sub> or Mo<sub>2</sub>S<sub>5</sub>), whose ability to interact and activate adsorbates far exceeds that of MoS<sub>2</sub> while proving to be of similar thermal stability and recoverable after adsorption through annealing. We also predict the possibility of growing of Mo<sub>6</sub>S<sub>6</sub> nanowires grown on Cu(111) surfaces.

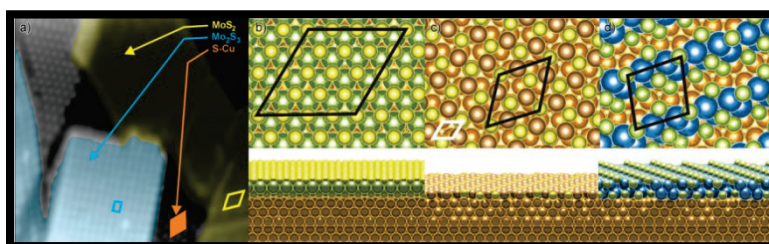


Figure 1-4. Chapter 4: Predictive modeling of functional materials. [Reprinted Figure with permission from “D. Sun, W. Lu, D. Le, Q. Ma, M. Aminpour, M. Alcantara-Ortigoza, S. Bobek, J. Mann, J. Wyrick, T. S. Rahman, and L. Bartels, *Angew. Chem. Int. Ed.* 51, 10284 (2012). Copy right (2012) by the Angewandte Chemie.”]

In Chapter 5, I discuss the diffusion of single metal Mg atoms on flat and stepped metal surfaces of Mg(0001). The ultimate goal of the study is to derive insights into possible growth mechanisms for Mg surface by means of calculating the diffusion barriers both at terraces and near step edges, and hence determine the so-called E-S barriers. E-S [25, 26], which are the key parameter for atomic mass transport at step-edges. I also report the stacking fault of Mg(0001) that originates from the famous Fridel oscillations on Mg(0001) surface. The results contribute towards an understanding of the role of these mechanisms in controlling the growth on these surfaces.



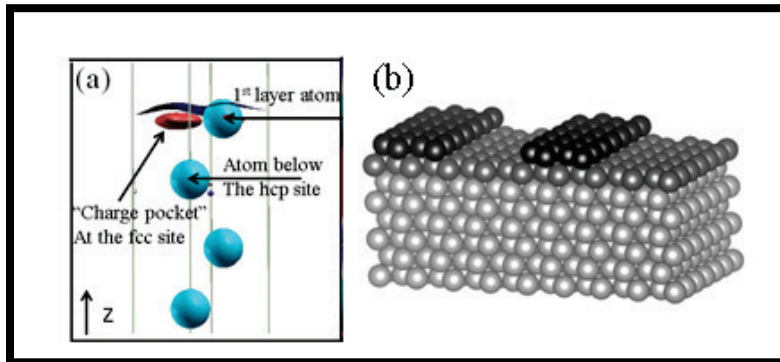


Figure 1-5. Chapter 5: Mg(0001): (a) Diffusion on step and terraces of Mg(0001) step. (b) The thin-film limit and stacking fault of small Mg adislands.

In Chapter 6, I carry out a systematic study of the adatom diffusion on tensilely strained dislocation (Ni/Cu) and compressively strained dislocation (Cu/Ni) surfaces with dislocations. The results demonstrate that the dislocation network is as a promising template for steering growth of adislands toward predetermined nucleation sites an efficient way for self-assembly. Engineering of ordered self-assembled nano-patterns plays an increasingly important role in design and development of functional nanometer-scale materials and devices, as an alternative to conventional costly and time-consuming top-down approaches and to artificially drawing nanostructures by atomic manipulation with a scanning tunneling microscopy tip or through electron-beam lithography.

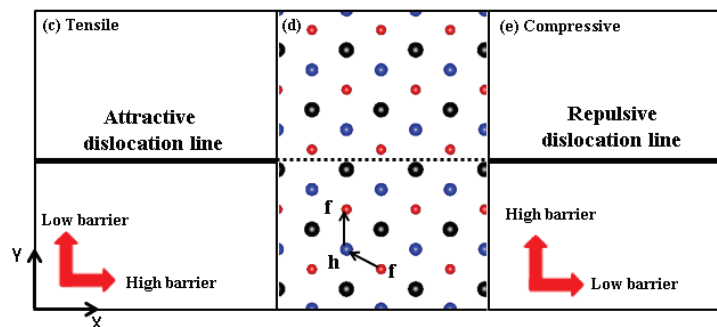


Figure 1-6. Chapter 6: Anisotropy in surface diffusion due to proximity to misfit dislocation.

In Chapter 7, I present the main conclusions of this dissertation and outline some prospects for future studies.

## CHAPTER 2. THEORETICAL METHODS

This chapter introduces the theoretical methods that are employed to study different problems addressed in the course of this dissertation. In the next two sections, two energy models for describing the interactions among the atom are presented. The first model belongs to the class of models based upon semi-empirical interaction potentials, which are built by fitting the potential parameters to a set of well-known material properties derived from experimental observations. The Embedded Atom Method (EAM) is one of the semi-empirical methods which will be described in Section (2.1). The second model belongs to the class of *ab-initio* models. *Ab-initio* is a Latin term meaning "from the beginning." *Ab-initio* methods do not rely on any experimental input. While they are considered to be the most accurate available ones to date, they have significant limitations in realistically modeling of large systems (several hundred or thousands of atoms). Yet realistic simulation of large systems is essential for properties that are time- and temperature-dependent, like growth phenomena. Hence, in order to describe the total energy of such systems, we need to introduce simplifications into certain parameterized expressions, instead of resorting to the kinds of approximations typically used in *ab-initio* methods for solving the Schrödinger equations. A realistic simulation of different properties of low-symmetric metallic surfaces such as those with defects requires methods that can simulate large numbers of atoms. Semi-empirical potentials are good alternatives to *ab-initio* methods owing to their lower computational cost.

### 2.1 *The Embedded Atom Model*

A realistic simulation of different Semi-empirical properties of low-symmetric metallic surfaces such as those with defects requires methods that can simulate large numbers of atoms.

Semi-empirical potentials are good alternatives to ab-initio methods owing to their lower computational cost. One of the early simple potentials is the two-body Lennard-Jones (LJ) potential, which was successfully used in studying the properties of rare gases. However, the LJ potential cannot provide sufficiently accurate description of such properties of metals as the bond length. LJ potential is not a good candidate for transition metals like Cu and Ni since in the relaxation process it predicts outward expansion of the surface atoms instead of inward contraction, which is experimentally known to be the case for most of the transition metals. It also fails to describe the Cauchy relation (equality of  $C_{12}$  and  $C_{44}$  elastic constants) for most of the metals. The shortcoming of LJ potential originates from the absence of a volume-dependent term. The inclusion, however, of many-body interactions as well as pair-wise interactions ensures the realistic description of such metal surface properties as relaxations and reconstructions. The first embedded-atom method (EAM) potential was proposed by Baskes and Daw [2, 3] in 1984 on the basis of the concept of local density, which is considered as the key variable in inter-atomic potentials. The idea behind the EAM potential model is based on the Quasi-atom [4] and Effective-medium theories (EMT) [5]. In EAM, it is assumed that each atom in the system is embedded in a host consisting of all the other atoms (See Figure 2-1). The energy to embed an atom within the host (embedding energy) is described as being dependent on the electron density. The density dependence of the embedding energy guarantees the volume dependence of the potential. The main advantage of the volume dependence that it enables one to describe the variation of the bond strength with coordination, for example, increase of the coordination decreases the strength of each of the individual bonds and consequently increases the bond length.

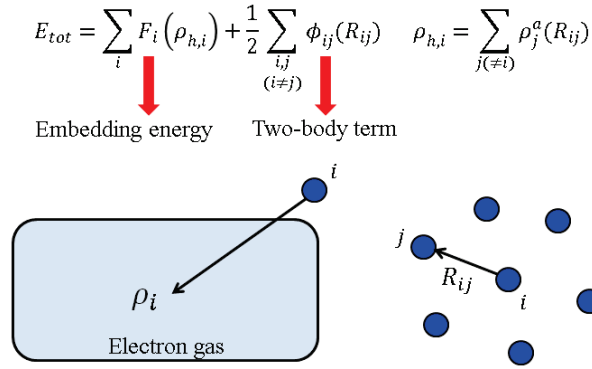


Figure 2-1. Schematic representation of the Embedded Atom Method.

In EAM, the total energy of the system is written as the addition of the embedding energy and that of the two-body terms, as in Eqn. (2.1),

$$E_{tot} = \sum_i F_i(\rho_{h,i}) + \frac{1}{2} \sum_{\substack{ij \\ (i \neq j)}} \phi_{ij}(R_{ij}) \quad (2.1)$$

In the former term of Eqn. (2.1),  $\rho_{h,i}$  is the sum of the individual atomic densities ( $\rho_j^a$ ) as given by Eqn. (2.2),

$$\rho_{h,i} = \sum_{j(\neq i)} \rho_j^a(R_{ij}) \quad (2.2)$$

where  $\rho_j^a$  is the contribution of the atom  $j$  of type  $a$  to the electron charge density at the location of the atom  $I$ , and  $F_i$  is an embedding functional that represents the energy required to place atom  $i$  into the electron cloud when  $R_{ij}$  is the distance between atoms  $i$  and  $j$ . Therefore, the total energy of the system is a function of the atomic positions.

In the latter term of Eqn. (2.1),  $\phi_{ij}$  is the short-range pair potential, where  $Z$  is the atomic number of the atoms.

$$\phi_{ij}(r) = Z_i(r)Z_j(r)/r \quad (2.3)$$

The total energy of the system given in Eqn. (2.1) has an attractive and a repulsive part. The attractive part (first term) describes the embedding of a positively charged core in to the electron density formed by the surrounding atoms, while the repulsive part (second term) describes the interactions between the ion cores. In Chapter 6, the EAM potential of Cu and Ni is used in Molecular dynamics simulations.

## 2.2 Density Functional Theory

In the 20<sup>th</sup> century, development of quantum mechanics along with numerous experimental observations is one of the most significant scientific advances. Amazingly, this theory of matter describes the universe we live in with a very high accuracy. In this section we review the important key ideas (most basic equations) of quantum mechanics that underline density functional theory. The key task in most approaches in solid-state physics and quantum chemistry aimed at elucidating the electronic structure of matter is to discover solutions to the time-independent, non-relativistic Schrödinger equation:

$$\hat{H}\Psi = E\Psi \quad (2.4)$$

“This equation is a nice form for putting on a t-shirt or a coffee mug, but to understand it better we need to define the equations that appear in it [14].”

$$\hat{H}\Psi_i(\vec{x}_1, \vec{x}_1, \dots, \vec{x}_N, \vec{R}_1, \vec{R}_1, \dots, \vec{R}_M) = E_i\Psi_i(\vec{x}_1, \vec{x}_1, \dots, \vec{x}_N, \vec{R}_1, \vec{R}_1, \dots, \vec{R}_M) \quad (2.5)$$

where  $\hat{H}$  is the Hamiltonian for a system consisting of  $M$  nuclei and  $N$  electrons.

$$\hat{H} = -\frac{\hbar^2}{2m_e} \sum_{i=1}^N \nabla_i^2 - \frac{\hbar^2}{2m} \sum_{I=1}^M \frac{1}{M_I} \nabla_A^2 - \sum_{i=1}^N \sum_{A=1}^M \frac{Z_I}{r_{iA}} + \sum_{i=1}^N \sum_{j>i}^N \frac{1}{r_{ij}} + \sum_{I=1}^M \sum_{J>A}^M \frac{Z_I Z_J}{R_{IJ}} \quad (2.6)$$

Here  $I$  and  $J$  run over the  $M$  nuclei while  $i$  and  $j$  denote the  $N$  electrons in the system.  $m$  and  $M$  are the mass of nucleus and electron. The first two terms in Eqn. (2.6) describe the kinetic energy of the electrons and nuclei. The next three terms define the attractive electrostatic interaction between the nuclei and the electrons, and the repulsive potential due to the electron-electron and nucleus-nucleus interactions, respectively. Solving this many-body problem is an impossible task, since the motion of  $N$  electrons and  $M$  ions are coupled ( $3N + 3M$  degrees of freedom) -- unless a series of simplifications is employed.

### 2.2.1 The Born-Oppenheimer Approximation

In atoms, each proton or neutron in a nucleus has more than 1800 times the mass of an individual electron. Roughly speaking, owing to this huge disproportion between their masses, the nuclei move so much more slowly than the electrons that we can consider the electrons as moving in the field of fixed nuclei. Consequently, nuclear kinetic energy is considered to be zero and the potential energy of a given species of nucleus is merely a constant.

.Decoupling the degrees of freedom of electron and nuclei leads to decoupling of the wave functions are the electronic and nuclear wave functions --  $\phi(\vec{V}, \vec{R})$  and  $\Theta(\vec{R})$ , respectively.

The electronic Hamiltonian thus reduces to:

$$\hat{H}_{elec} = -\frac{\hbar^2}{2m} \sum_{i=1}^N \nabla_i^2 - \sum_{i=1}^N \sum_{A=1}^M \frac{Z_A}{r_{iA}} + \sum_{i=1}^N \sum_{j>i}^N \frac{1}{r_{ij}} = \hat{T} + \hat{V}_{Ne} + \hat{V}_{ee} \quad (2.7)$$

$$\hat{H}_{elec} \Psi_{elec} = E_{elec} \Psi_{elec} \quad (2.8)$$

The total energy  $E_{tot}$  is then the sum of  $E_{elec}$  and the constant nuclear repulsion term  $E_{nuc}$ .

$$E_{tot} = E_{elec} + E_{nuc} \quad \text{where} \quad E_{nuc} = \sum_{I=1}^M \sum_{J>A}^M \frac{Z_I Z_J}{R_{IJ}} \quad (2.9)$$

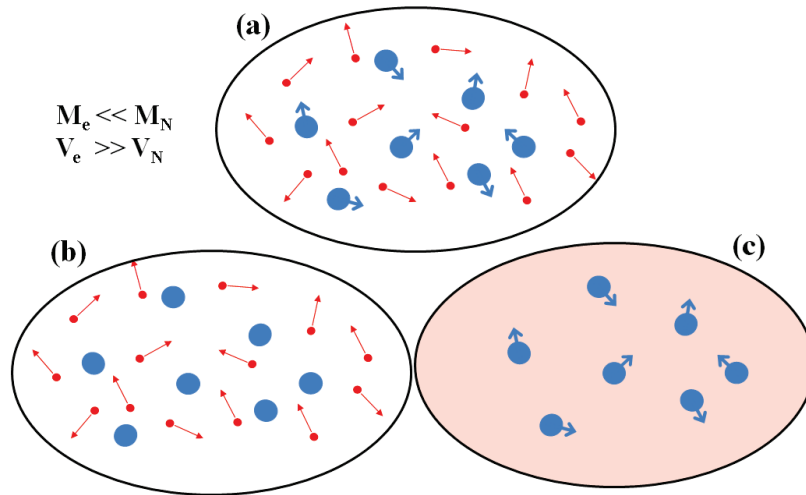


Figure 2-2. Adiabatic or Born-Oppenheimer approximation decouples the electronic and nuclear degrees of freedom. (a) A real system consists of electrons and nuclei, both in motion. (b) Electronic equations can be solved assuming fixed positions for nuclei. (c) Each nucleus is then treated as moving as a classical particles affected by the potential generated by the electrons.

This approach is known as the Born-Oppenheimer (BO) or adiabatic approximation [7]. In BO approximation, ions move on the potential of energy surface of electrons in the ground state. After employing the BO approximation, the problem of solving the Schrödinger equation is reduced to solving the electronic Eqn. (2.9). An exact solution of this problem is numerically possible only single-electron systems (such as  $H$ , hydrogenoid atoms and  $H_2^+$ ). At this point in time, finding a suitable approximation for describing many electron-electron interactions is the main difficulty to deal with.

### 2.2.2 The Hartree-Fock Approximation

In 1927, Hartree introduced a procedure that belongs to the class of wave function methods to approximate wave functions and energies of different atoms. The expansion for the wave function is approximated by the product of single-electron wave function ( $\Psi$ ) as:



$$\Psi(\vec{r}_1, \vec{r}_2, \vec{r}_3, \dots, \vec{r}_N) = \Psi_1(\vec{r}_1) \Psi_2(\vec{r}_2) \dots \Psi_N(\vec{r}_N) \quad (2.10)$$

This expansion is known as the Hartree product. In this method, electrons are supposed to interact with each other through an effective potential, which is a function of the total density of electrons.

$$\hat{V}_{eff}(r, R) = V(r, R) + e^2 \sum_{j \neq i}^N \frac{\rho_j(\vec{r})}{|\vec{r} - \vec{r}_j|} \quad , \quad \rho_i(\vec{r}) = |\varphi(\vec{r}_i)|^2 \quad (2.11)$$

The first term in Eqn. (2.11) describes the contribution of the effective potential from the ions, while the second term represents the electronic potential corresponding to the interaction of the electron with the other electrons.

The Hartree method reduces the many-body problem to the problem of one-particle equation in an effective potential (see Figure 2-3) as follows:

$$\left( -\frac{\hbar^2}{2m} \nabla^2 + \hat{V}_{eff}^{(i)}(\vec{R}, \vec{r}) \right) \varphi_i(\vec{r}) = \varepsilon_i \varphi_i(\vec{r}) \quad (2.12)$$

where  $\varepsilon_i$  is the eigen energy of the  $i^{th}$  electron and  $\varphi_i(\vec{r})$  is the one-electron wave function (orbital).

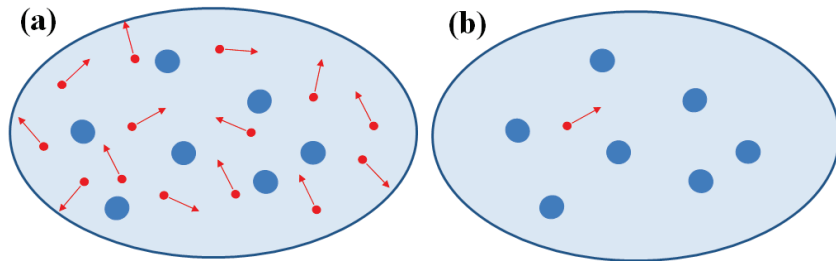


Figure 2-3. (a) Electrons moving about fixed nuclei. (b) The single-electron or independent-particle model: each electron moves independently in a potential created by the nuclei and the rest of the electrons.

The drawback of this method is lies in ignoring the fact that the system does not consider electrons as fermions (indistinguishable particles). According to the Pauli Exclusion Principle, the wave function of the electron should change the sign under the label interchange. Some years later Hartree's students Fock and Slater individually proposed a method that treats the electrons as Fermions with anti-symmetric wave functions. In this method, the total multi- electron wave function can be represented by the Slater determinant of one-particle orbitals. In this way, if two orbitals are equal ( $i = j$ ), the Slater determinant will be zero, so that the Pauli Exclusion Principle will be satisfied.

$$\Phi(\vec{r}, \sigma) = \frac{1}{\sqrt{N!}} \begin{vmatrix} \phi_1(\vec{r}_1, \sigma_1) & \phi_1(\vec{r}_2, \sigma_2) & \cdots & \phi_1(\vec{r}_N, \sigma_N) \\ \phi_1(\vec{r}_1, \sigma_1) & \phi_1(\vec{r}_2, \sigma_2) & \cdots & \phi_1(\vec{r}_N, \sigma_N) \\ \vdots & \vdots & \ddots & \vdots \\ \vdots & \vdots & \ddots & \vdots \\ \phi_N(\vec{r}_1, \sigma_1) & \phi_N(\vec{r}_2, \sigma_2) & \cdots & \phi_N(\vec{r}_N, \sigma_N) \end{vmatrix} \quad (2.13)$$

The calculation of Hartree-Fock methods is computationally very costly since the wave function is a very complicated quantity that cannot be measured experimentally, and depends on  $4N$  variables, where  $N$  is the number of electrons.

### 2.2.3 The Thomas-Fermi Model

In the same year (1927) as the Hartree product was proposed, Thomas and Fermi [15, 16] proposed the first approximation based on a statistical model (eventually named the “uniform electron gas model”) to solve the many-body problem with its large number of degrees of freedom. In this model, the energy of atoms is computed by approximating the distribution of electrons in an atom. They proposed the density function for kinetic energy is:

$$T_{TF}[\rho(\vec{r})] = \frac{3}{10} (3\pi^2)^{\frac{2}{3}} \int \rho^{\frac{5}{3}}(\vec{r}) d\vec{r} \quad (2.14)$$

The energy of the atom is finally obtained by adding two classic terms of nuclear-nuclear and electron-electron interactions to kinetic energy, both of which can be given in terms of the electron density.

$$E_{TF}[\rho(\vec{r})] = \frac{3}{10} (3\pi^2)^{2/3} \int \rho^{5/3}(\vec{r}) d\vec{r} - Z \int \frac{\rho(\vec{r})}{r} d\vec{r} + \frac{1}{2} \int \int \frac{\rho(\vec{r}_1)\rho(\vec{r}_2)}{r_{12}} d\vec{r}_1 d\vec{r}_2 \quad (2.15)$$

Initially, the Thomas-Fermi approximation did not contain the exchange energy of atom which is a result of exclusion according to the Pauli Principle and is incorporated in the Hartree-Fock theory. Within a year however, Dirac added an exchange energy functional term to Thomas-Fermi Model. In order to determine the correct density in Eqn. (2.15), they assumed that the ground state of system is related to the  $\rho(\vec{r})$  for which the energy is minimized under the condition of  $\int \rho(\vec{r})d\vec{r} = N$ , where  $N$  is the number of the atoms. The drawback of the doing so was a crude approximation of kinetic energy and complete neglect of the electron-correlation effect.

#### 2.2.4 Hohenberg and Kohn (H-K) Theorems

In 1964, Hohenberg and Kohn published a paper entitled “Inhomogeneous Electron Gas,” which established the foundations of the basics of the modern density functional theory. Two notable theorems were proved showing that the electron density is the key quantity for describing electronic interactions. The first H-K theorem points out that the ground-state energy uniquely depends on the electron density, since  $E_0 = E[\rho(r)]$ , where  $E_0$  is the ground-state energy of the system and  $\rho(r)$  is the particle’s density. The second H-K theorem states that the ground-state energy can be obtained by minimizing the energy of the system.

### 2.2.4.1 The First Hohenberg and Kohn Theorem

Let us consider the Hamiltonian of a system of  $N$  interacting electrons under the effect of an external potential with ground state energy ( $E_0$ ) as

$$\hat{H}_{e1} = \hat{T}_e + \hat{V}_{ee} + \hat{V}_{ext} \quad (2.16)$$

where  $\hat{T}_e$  is the kinetic energy of the electrons, and  $\hat{V}_{ee}$  and  $\hat{V}_{ext}$  are the electron-electron interaction potential and external potential, respectively. If  $\hat{V}_{ext}$  is known, the electron density can be evaluated. In the first H-K theorem, the approach is the opposite. In this case, the ground-state electron density is used to evaluate  $\hat{V}_{ext}$ . To be precise, the external potential is a unique functional of the electron density; since the external potential in turn fixes the Hamiltonian, we can say that the electron density uniquely determines all properties of the system. To prove that the full many-body ground state is a unique functional of electron density we employ the ‘‘proof by contradiction’’ method as follows.

Proof: suppose that there are two different external potentials as  $V_{ext}(\vec{r})$  and  $V'_{ext}(\vec{r})$ , each giving the same electron density of the system.  $\hat{H}'$  and  $\hat{H}$  are two different Hamiltonians whose ground state ( $E_0$ ) is same although the wave functions ( $\Psi, \Psi'$ ) are different. The variational principle for two systems as  $(\hat{H}, E_0, \Psi)$  and  $(\hat{H}', E'_0, \Psi')$  with the same ground state charge density is as follows:

$$\begin{aligned} E_0 < \langle \Psi' | \hat{H} | \Psi' \rangle &= \langle \Psi' | \hat{H}' | \Psi' \rangle + \langle \Psi' | \hat{H} - \hat{H}' | \Psi' \rangle \\ &= E'_0 + \int \rho(\vec{r}) [V_{ext}(\vec{r}) - V'_{ext}(\vec{r})] d\vec{r} \end{aligned} \quad (2.17)$$

$$\begin{aligned}
E'_0 < \langle \Psi | \hat{H}' | \Psi \rangle &= \langle \Psi | \hat{H} | \Psi \rangle + \langle \Psi | \hat{H}' - \hat{H} | \Psi \rangle \\
&= E_0 + \int \rho(\vec{r}) [V_{ext}(\vec{r}) - V'_{ext}(\vec{r})] d\vec{r} \quad (2.18)
\end{aligned}$$

Combining these two in equalities, we will get a contradiction:

$$E_0 + E'_0 < E'_0 + E_0 \quad (2.19)$$

This indicates that the assumption of the existence of the second  $V_{ext}$  that gives the same  $\rho(\vec{r})$  for its ground state is invalid. An immediate result of the Hohenberg-Kohn theorem is that the ground-state electron density uniquely determines all the properties, including the energy and wave function of the ground state. This result gives us a new avenue for solving the Schrödinger equation by finding electron density with 3 degrees of freedom, rather than the wave function of  $3N$  variables. For example, for a nanoparticle of 100 Pt atoms, this theorem reduces the problem to a problem with just 3 dimensions from approximately more than 23,000 dimensions.

Since  $\rho(\vec{r})$  is sufficient to determine all the properties of the ground state like the kinetic energy, the potential energy and the total energy, which all are functionals of the charge density, the total energy can be written as:

$$\begin{aligned}
E[\rho] &= E_{Ne}[\rho] + T[\rho] + E_{ee}[\rho] \\
&= \int \rho(\vec{r}) V_{Ne}(\vec{r}) d\vec{r} + F_{HK}[\rho], \quad F_{HK}[\rho] = T[\rho] + E_{ee} \quad (2.20)
\end{aligned}$$

“The functional  $F_{HK}[\rho]$  is the holy grail of density functional theory. If it were known we would have solved the Schrödinger equation exactly! [17].”  $F_{HK}[\rho]$  is a universal functional totally independent of the system under study. For example, it can be applied equally well to single atoms as to gigantic molecules such as DNA [17]. Although, the first theorem rigorously proves that there exists a unique functional of the electron density that can be used to solve

Schrödinger equation, the theorem proposes nothing about what the functional actually is. The explicit form of  $T[\rho]$  and  $E_{ee}$  functionals in Eqn. (2.20) are completely in dark and we can rewrite the equation Eqn. (2.20) as classical (*cl*) and non-classical (*ncl*) parts.

$$E_{ee}[\rho] = \frac{1}{2} \int \int \frac{\rho(\vec{r}_1)\rho(\vec{r}_2)}{r_{12}} d\vec{r}_1 d\vec{r}_2 + E_{ncl}[\rho] \quad (2.21)$$

where  $E_{ncl}$  is the contribution to the e-e interaction as self-interaction correction, exchange and coulomb correlation. To put it in a nutshell, the explicit form of the  $T[\rho]$  and  $E_{ncl}[\rho]$  is the major challenge of DFT.

#### 2.2.4.2 The second Hohenberg-Kohn Theorem

The second H-K theorem states that  $F_{HK}[\rho]$ , the functional that provides the ground state energy of system, also provides the lowest energy, if and only if the input charge density is the true ground-state density. Again, we will use “proof by contradiction” to show that ground state energy results in the lowest total energy if and only if the exact ground density is inserted in equation (2.23).

Proof: Let assume that  $\rho_0(\vec{r})$  and  $\tilde{\rho}(\vec{r})$  can be the electron density at the ground state (with  $E_0[\rho]$  and  $E_0[\tilde{\rho}]$  energies) and at a trial state ( $\tilde{\Psi}$  and  $\tilde{\Psi}_0$  wave functions), respectively. Since the variational method is valid for ground state energy, we cannot use this strategy for the problem of excited states energies.

$$\langle \tilde{\Psi} | \hat{H} | \tilde{\Psi} \rangle > \langle \tilde{\Psi}_0 | \hat{H} | \tilde{\Psi}_0 \rangle \quad (2.22)$$

$$T[\tilde{\rho}] + E_{ee}[\tilde{\rho}] + \int \tilde{\rho}(\vec{r}) V_{ext} d\vec{r} \geq \langle \tilde{\Psi}_0 | \hat{H} | \tilde{\Psi}_0 \rangle \quad (2.23)$$

$$E[\tilde{\rho}] \geq E_0[\tilde{\rho}] \quad (2.24)$$

The inequality above proves that the electron density at ground state  $E_0[\rho]$  gives the lowest total energy of the system of interacting electrons.

### 2.3 Kohn-Sham (K-S) Method:

H-K theorems simplified the many-body problem by demonstrating that there exists a one-to-one mapping relation between the universal electron density functional and properties of the system, but they do not show what exactly these equations are. In 1965, Kohn and Sham published a paper entitled “Self-consistent equations including exchange and correlation effects” [18]. Only one year after the publication of the significant H-K paper, Kohn and Sham suggested an alternative way to implement it in the DFT. In this paper, they have replaced the interaction of the multi-electron problem with the problem of non-interacting electrons as an effective potential. In order to find the true electron density described by the H-K theorem, Kohn and Sham propose a single-electron set of equations superficially similar to Schrödinger equations, with the difference that K-S equations omit the summations over different electrons that appears inside the full Schrödinger equation. To go beyond earlier methods that suppose a system of non-interacting particles, further ansatz proposed in the K-S approach. The ground state electron charge density of the virtual non-interacting system is the same as that of the non-interacting (reference) system (see Figure 2-4). In the resulting independent particle equations, the energy functional can be written as:

$$E[\{\psi_i\}] = E_{known}[\{\psi_i\}] + E_{XC}[\{\psi_i\}] \quad (2.25)$$

where we split the energy functional in to two terms. The first term in Eqn. (2.25) is the known part, which contains the terms that can be written in a simple analytical form. The known terms include four contributions:

$$E_{known}[\{\psi_i\}] = \frac{\hbar^2}{2m} \sum_i \int \psi_i^* \nabla^2 \psi_i d^3r + \int V(r) \rho(r) d^3r + \frac{e^2}{2} \iint \frac{\rho(r)\rho(r')}{|r-r'|} d^3r d^3r' + E_{ion} \quad (2.26)$$

The four terms in Eqn. (2.26), in order, are the kinetic energy of electron, the coulomb interactions between the electrons and the nuclei, the coulomb interactions between pairs of electrons and the coulomb interactions between pairs of the nuclei.

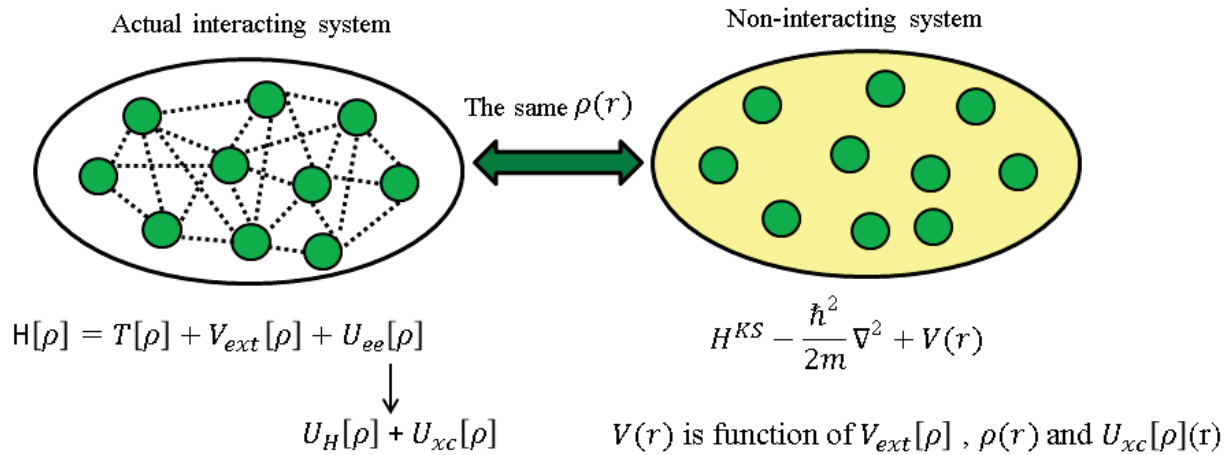


Figure 2-4. The Kohn-Sham approach to DFT.

The second term in Eqn. (2.25) is the unknown part which contains everything else related to many-body effects that are not included in “known” part. They are all the unknown terms swept under a carpet named “the exchange correlation” ( $E_{xc}$ ) functional. The exchange correlation functional accounts for: I) The exchange effects correction known as Pauli repulsion as the Fock term appearing in the Hartree-Fock theory; II) the self-interaction correction and III) the correlation effect correction, that is the tendency for two electrons of unequal spin to choose different orbitals to avoid each other while moving in the space.



The Kohn-Sham equations have the form:

$$\left[ -\frac{\hbar^2}{2m} \nabla^2 + V(r) + V_H(r) + V_{XC}(r) \right] \psi_i(r) = \varepsilon_i \psi_i(r) \quad (2.27)$$

The solution of these equations are the single-electron wave functions (orbitals),  $\Psi_i(r)$ , that depend on only 3 spatial variables. The first term in Eqn. (2.27) is a “known” kind of potential that defines the interaction between an electron and the collection of atomic nuclei. The second term is called Hartree potential and is defined as:

$$V_H(r) = e^2 \int \frac{n(r')}{|r - r'|} d^3r' \quad (2.28)$$

The Hartree potential describes the coulomb repulsion between the single electron of one of the K-S equations and the total electron density defined by all electrons in the case under consideration. The Hartree potential includes a “self-interaction” contribution, because the electron we are describing in the Eqn. 2.28) is also a part of the total electron density. Therefore, a part of Hartree potential involves a coulomb interaction between the electron and itself. The self-interaction part is an unphysical term, and is a part of corrections incorporated in the exchange and correlation potential exchange correlation potential is defined as a functional derivative of the exchange correlation energy.

$$V_{XC}(r) = \frac{\delta E_{XC}(r)}{\delta \rho(r)} \quad (2.29)$$

A more detailed description of  $E_{XC}[\rho]$  and the approximations related to it will be described in Section 2.11.

There is something circular about the discussion of the K-S equations. To solve K-S equations, the Hartree potential needs to be defined, and to define the Hartree potential, the

electron density needs to be known. To find the electron density, we must know the single-electron wave function, and to know these wave functions we must solve the K-S equations. The prescription for breaking this circle takes an iterative form as outlined in the algorithm summarized in Figure 2-5. The main issue in this approach is the knowledge of the explicit form of exchange-correlation functional. For the moment, we assume that the exchange-correlation is available in some approximated way.

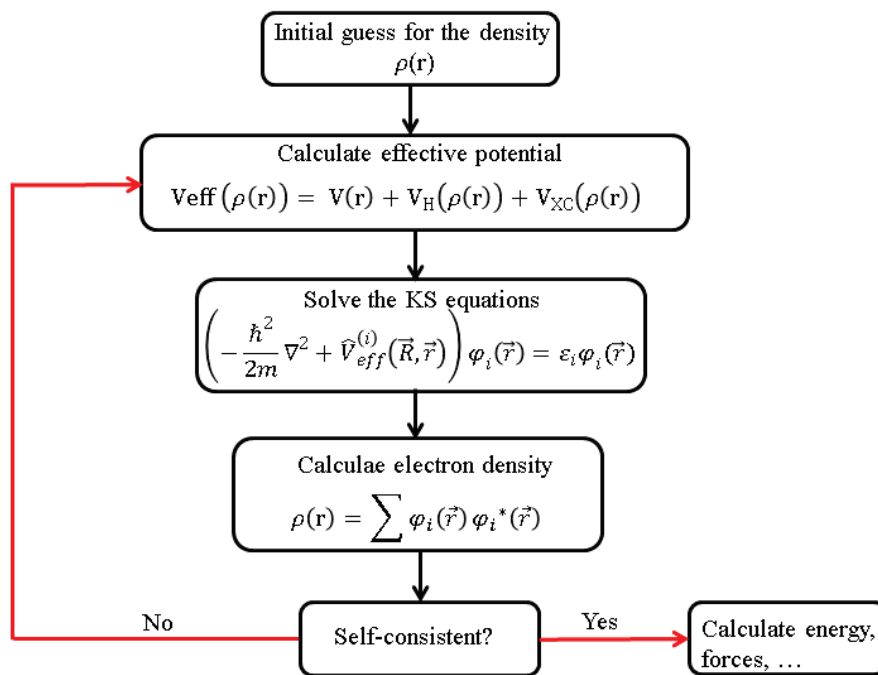


Figure 2-5. Self-consistent Kohn-Sham (K-S) algorithm.

#### 2.4 The Exchange Correlation Functional

The beautiful solution provided by Kohn, Hohenberg, and Sham for the many-body problem showed us that the ground-state energy that can be found by minimizing the energy of an energy functional can be achieved by using a self-consistent method to solve a set of single-

particle equations. The only intricacy remaining is to specify the exchange-correlation functional. We can write the  $E_{xc}[\rho]$  as a sum of pure exchange and correlation:

$$E_{xc}[\rho] = E_x[\rho] + E_c[\rho] \quad (2.30)$$

The exchange part can be written explicitly in terms of one-particle orbitals from the Fock determinant:

$$E_x[\{\phi_i\}] = \frac{e^2}{2} \sum_{i,j} \int d^3r \int d^3r' \frac{\phi_i^*(\vec{r})\phi_j^*(\vec{r}')\phi_i(\vec{r}')\phi_j(\vec{r})}{|\vec{r}-\vec{r}'|} \quad (2.31)$$

However the expression of the exchange energy as a functional of the electron density known exactly in only a simple case: the homogeneous electron gas (HEG), for which the electron density is constant in all points in space. ( $\rho(r) = \text{constant}$ ):

$$\bar{\rho}(r) = \frac{N}{V} \quad (2.32)$$

In view of the fact that the exact form of exchange correlation functional is not known, the problem of finding efficient and effective approximations for  $E_{xc}$  is critical, as is indicated by the number of publications that have discussed this issue. Strictly speaking since, it is the remainder between the exact value of the total energy and the sum of the repulsive Hartree energy and the kinetic energy of the non-interacting system.  $E_{xc}$ , whose existence is guaranteed by the H-K theorem, is a functional of electron density. As such it is universal – i.e., should work for all materials.

There are many ways to approximate  $E_{xc}$ . In these theorems, we discuss merely the two most widely used approximations: 1) the local density approximation and 2) the generalized-gradient approximation functional.

### 2.4.1 The Local Density Approximation (LDA)

The local density approximation (LDA) was introduced by Kohn and Sham in 1965[18]. In this approximation, the  $E_{xc}$  per electron at a point  $\vec{r}$  of the interacting-electron system consisting of N electrons is the same as that of a homogeneous electron gas with the same electron density. In this approximation the exchange energy ( $E_x$ ) and the exchange potential can be calculated as:

$$E_x(\bar{\rho}) = \int \rho(\vec{r}) V_x(\vec{r}) d\vec{r} \quad (2.33)$$

and

$$E_x^{HEG}(\bar{\rho}) = -\frac{3e^2}{4} \left(\frac{3}{\pi}\right)^{1/3} V \bar{\rho}^{4/3} = -C_x V \frac{N}{V} \bar{\rho}^{1/3} \quad (2.34)$$

Another explicit expression in terms of  $\bar{\rho}$  can be derived for the correlation part in several ways as the extrapolation to the usual physical densities in the high density limit of HEG. In other words, at high electron densities, where the kinetic contribution dominates, an expression for the correlation energy can be derived from perturbation theory. The parameterized form of  $E_c$  can be obtained from quantum Monte-Carlo simulations of the HEG at selected densities. All the expressions for the correlation energy of HEG can be written as:

$$E_c(\bar{\rho}) = \int \rho(\vec{r}) V_c(\vec{r}) d\vec{r} \quad (2.35)$$

where  $E_c(\bar{\rho})$  is the expression for the correlation energy per electron and can be evaluated.

The next step is to generalize the case for electron densities that are not uniform in space. In order to obtain the

$$E_{xc}^{LDA}[\rho] = \int d^3r \rho(\vec{r}) e_{xc}^{HEG}(\rho(\vec{r})) \quad (2.36)$$

where the  $\bar{\rho}$  is replaced by the local density at the point  $\vec{r}$  and volume  $V$ , Volume is treated as a summation of small cells in which the system is supposed to be homogenous. As a result, LDA is a good approximation for systems in which the electron density varies little and slowly.

The drawbacks of LDA approximation can be summarized as follows:

- 1) The LDA tends to over-bind yielding computed cohesive energy that is too large by about 30%.
- 2) The long range Van der Waals effects are left out of account, owing to highly local nature of the LDA. As a consequence it fails in calculating the adsorption energy of weakly bound molecules on solid surfaces.
- 3) Lattice constants are reported to be under-estimated in comparison with experimental values.
- 4) The hydrogen bond is poorly accounted for (leading to, for example, a misleading characterization of the structure of liquid water).

#### 2.4.2 The Generalized Gradient Approximation (GGA)

LDA is widely criticized because any real electron system is non-homogenous. A first attempt to improve LDA consisted in including the gradient/or higher derivatives of the density with respect to spatial coordinates. However, the approximations that contained the lowest-order gradients such as the gradient expansion approximation (GEA) turned out to be unsuccessful. Numerous alternative prescriptions for choosing the  $E_X^{GGA}[\rho(\vec{r}), \nabla\rho(\vec{r})]$  exist, each of which leads to distinct GEA's. Typically, the exchange correlation functional in these kinds of approximations can be written as following:

$$E_{xc}^{GGA}[\rho, \sigma] = E_{xc}^{LDA}[\rho, \sigma] + \int d^3r e_{xc}^{GGA}(\rho(\vec{r}), \nabla\rho(\vec{r})) \quad (2.37)$$

There are two different approaches for obtaining GGA functional: the *ab-initio* approach and the empirical approach. In the former, one starts with the derivation of a theoretical expression of the exchange-correlation functional that satisfies some or all known properties of exchange and correlation energy. In the latter the value for the functional is fitted to the large set of known experimental values for which accurate many-body calculations of the exchange-correlation energy are available. There are many versions of the exchange correlation functional derived from via the *ab-initio* method but the most important and widely used ones are PW86 [19], LYP [20], PW91 [21] and PBE [22].

In the present study, mostly PW91 and PBE have been employed. Some of the general properties of solutions obtained by employing a GGA functional in comparison with those produced by LDA are summarized as below:

- 1) GGA sometimes overcorrects LDA: Lattice constants are over-estimated, LDA results are closer to those of experiments than those of GGA. Binding energies are 0-2% larger than experiments (better compared to LDA), cohesive energy is 10-20% smaller.
- 2) GGA often predicts surface energies that are lower than those of experiments (and LDA).
- 3) GGA cannot describe long range effects properly.
- 4) GGA usually performs well in describing Hydrogen.
- 5) GGA is not suited for strongly correlated electron systems.

## 2.5 *Solving the Kohn-Sham Equations*

So far, in the preceding sections, we have settled on the BO approximation to separate the degrees of freedom of electrons from that of the nuclei [23] and then reduced the many-body problem to  $N$  one-orbital K-S equations.[24], where  $N$  is the number of electrons. Additional methods still need to be considered in order to make possible calculations that are computationally efficient. Using Bloch's theorem (considering a periodic system), employing simple, efficient and complete basis sets, and wisely choosing among available pseudo potentials for treating core and outer-shell valance electrons are among the ways that allow theorists to get around the problem. Still since there are infinite number of electrons and nuclei in a realistic system and the problem is still unsolvable in a fully realistic way.

## 2.6 *Pseudo-Potential Approximation*

With all the approximations discussed in previous section, the problem of solving Kohn-Sham equations for systems with a huge number of atoms and electrons is still very expensive. Nevertheless, in addressing many problems in chemistry and physics, a distinction between core electrons (spectator electrons) and valance electrons (active electrons) can be made.

The core electrons are more atomic-like, with a strong bonding to the nuclei. Since they do not participate in chemical interactions; they do not play a crucial role in chemical behavior of the materials. In contrast, it is the valance electrons are the outermost electrons loosely bonded to nuclei that are indeed responsible for chemical interactions between atoms. In the pseudo-potential plane-wave approach, the action of core electrons and the potential within a cutoff radius around the core is replaced by an effective smoother and weaker potential known as a pseudo-potential.

A pseudo-potential does not operate on a true electronic wave function but on a node less pseudo-wave function. Since true wave functions are often oscillating in the space close to the nuclei, a large number of plane waves need to be expanded. Consideration of soft pseudo potentials, which need plane-wave basis sets with fewer members, is clearly advantageous from computational point of view. The pseudo-potential and pseudo-wavefunctions constructed for a given atom must match the real potential and wave functions at the boundary identified by the cut-off radius. One of the important classes of pseudo potentials is that of norm-conserving pseudo-potentials [25]. The condition for norm conservation is that the total charge generated by the pseudo potential in the core area of the atom be equivalent to that generated by real wave functions.

In 1990, Vanderbilt proposed ultra-soft pseudo potentials (USPP) [26] produced by relaxing so-called norm-conserving pseudo potentials, the result is that there is some charge loss in the core region owing to the fact that a USPP does not satisfy the norm conserving condition. This loss of charge, however, is compensated for by an augmentation charge calculated from the difference between pseudo wave functions and the true wave functions of the atom. The USPP works accurately for most of the systems except for magnetic systems. In 1994, Blöchl proposed the projector-augmented wave (PAW) method that is equivalent to an all-electron method [27]. But though, the PAW method is thus a good choice for high accuracy DFT simulations. It was not widely used until 1999, when Cresse and Joubert introduced a modified version of PAW [28]. They used transformation operator that can act on the true wave functions and map them onto pseudo wave functions.



Since pseudo-wave functions are computationally more favorable, they are used in K-S equations. Once pseudo-wave functions are obtained, the transformation operator builds the real wave functions. Since the evaluation of observables is based on true wave functions, the PAW method can be as accurate and powerful as all-electron methods.

## 2.7 Bloch's Theorem

Bloch's theorem is based on the translational invariance of a periodic system [29]. In a perfect crystal, nuclei are regularly placed on a periodic array defined by a set of Bravais lattice vectors ( $R_i$ ). For such an ideal crystal, the electron density and the unperturbed external potential keep the same periodicity of the crystal, as expressed in the following:

$$A(\vec{r}) = A(\vec{r} + \vec{R}_i) \quad (A = n, V_{cxt}) \quad (2.38)$$

Let us write the K-S equation in the following form.

$$\left(-\frac{\hbar^2}{2m}\nabla_i^2 + V_{eff}(\vec{r})\right)\phi(\vec{r}) = \varepsilon\phi(\vec{r}) \quad (2.39)$$

where the effective K-S potential ( $V_{eff}$ ) is a periodic function.

$$V_{eff}(\vec{r} + \vec{R}_i) = V_{eff}(\vec{r}) \quad (2.40)$$

Let us assume that the translation operator of vector  $\vec{R}_i$  as  $\hat{T}(\vec{R}_i)$  operates on any position-dependent function, such as  $f(\vec{r})$ :

$$\hat{T}(\vec{R}_i)f(\vec{r}) = f(\vec{r} + \vec{R}_i) \quad (2.41)$$

This equation implies that the function  $f(\vec{r})$  is periodic. Since  $V_{eff}$  is periodic, the K-S Hamiltonian is also periodic. Therefore the translation operator and K-S Hamiltonian commute.

Moreover, the translation operators commute with each other. Consequently, the eigenfunctions of translation also serve as eigenfunctions of the Hamiltonian as in the following equation:

$$\hat{T}(\vec{R}_i)\Phi(\vec{r}) = \Phi(\vec{r} + \vec{R}_i) = \lambda(\vec{R}_i)\Phi(\vec{r}) \quad (2.42)$$

where  $\lambda(\vec{R}_i)$  is the eigenfunction of the translation operator  $\hat{T}(\vec{R}_i)$ . By multiplying equation Eqn. 2.41) by the translation operator acting on  $R_j$  given the commutation property of translation operators ( $\hat{T}(\vec{R}_i)\hat{T}(\vec{R}_j) = \hat{T}(\vec{R}_i + \vec{R}_j)$ ), one obtains the following equation:

$$\hat{T}(\vec{R}_i)\hat{T}(\vec{R}_j)\Phi(\vec{r}) = \hat{T}(\vec{R}_i + \vec{R}_j)\Phi(\vec{r}) = \lambda(\vec{R}_i)\lambda(\vec{R}_j)\Phi(\vec{r}) = \lambda(\vec{R}_i + \vec{R}_j)\Phi(\vec{r}) \quad (2.43)$$

$$|\lambda(\vec{R}_i)|^2 = 1 \quad (2.44)$$

Where the eigenfunction  $\lambda(\vec{R}_i)$  is normal ( $|\lambda(\vec{R}_i)|^2 = 1$ ). Eqn. (2.43) can be satisfied if:

$$\hat{T}(\vec{R}_i)\Phi(\vec{r}) = e^{i\vec{k}\vec{R}_i}\Phi(\vec{r}) \quad (2.45)$$

Finally:

$$\hat{T}(\vec{R}_i)\Phi(\vec{r}) = \Phi(\vec{r} + \vec{R}_i) = e^{i\vec{k}\vec{R}_i}\Phi(\vec{r}) \quad (2.46)$$

Eqn. (2.46) indicates that  $e^{i\vec{k}\vec{r}}$  are the eigenvalues of the  $\hat{T}(\vec{R}_i)$ .

To put it in a nutshell, Bloch's theorem states that in a periodic potential, the wave function of an electron can be expanded by

$$\Phi_{n,\vec{k}}(\vec{r}) = e^{i\vec{k}\vec{r}}u_{\vec{k}}(\vec{r}) \quad (2.47)$$

where  $\Phi_{n,\vec{k}}(\vec{r})$  is a product of a wave-like part ( $e^{i\vec{k}\vec{r}}$ ) and a part defining the periodicity of the lattice:

$$u_{\vec{k}}(\vec{r}) = u_{\vec{k}}(\vec{r} + \vec{R}_i) \quad (2.48)$$

## 2.8 Calculation of the Kohn-Sham States

So far, we have not discussed a method for calculating the Kohn-Sham wavefunctions. There are different approaches to this task. One of the potential lines of attack adopts a real-space perspective [30]. In this approach, the wave function and Hamiltonian can be written over some numerical grid. Another tactic is to expand Kohn-Sham wave functions (orbitals) as a linear combination of a given basis set, reducing the problem to that of finding the expansion coefficients that minimize Eqn. (2.39). One of the widely used choice of basis sets is the combination of plane waves [31], in which one usually sums over as many as  $k$  wave vectors as required for appropriately describing the wavefunction  $\Psi_i(r)$ .

According to the Bloch's theorem, the electronic wave function in a periodic system is as follows:

$$e^{-i\vec{k}\cdot(\vec{r})}\Phi_{n,\vec{k}}(\vec{r}) = u_{\vec{k}}(\vec{r}) \quad (2.49)$$

where the function  $u$  has the periodicity of the Bravais lattice and  $e^{-i\vec{k}\cdot(\vec{r})}$  represents a plane wave function.  $u_{n,\vec{k}}(\vec{r})$  can be expanded using a basis set that includes plane waves whose wave vectors are the reciprocals of the lattice vectors.

$$u_{\vec{k}}(\vec{r}) = \sum_{\vec{G}_j} C_{(\vec{k},\vec{G}_j)} e^{i\vec{G}_j\cdot\vec{r}} \quad (2.50)$$

Consequently, Eqn. (2.49) can be written as follows:

$$\Phi_{n,\vec{k}}(\vec{r}) = \sum_{\vec{G}_j} C_{(\vec{k},\vec{G}_j)} e^{i(\vec{k}+\vec{G}_j)\cdot\vec{r}} \quad (2.51)$$

Since  $u_{n,\vec{k}}(\vec{r})$  has the periodicity of the lattice vector,  $u_{n,\vec{k}}(\vec{r} + \vec{R}) = u_{n,\vec{k}}(\vec{r})$ , one can rewrite Eqn. (2.48) as follows:

$$\psi_{n,\vec{k}}(\vec{r} + \vec{R}) = e^{i\vec{k}\cdot\vec{R}}\psi_{n,\vec{k}}(\vec{r}) \quad (2.52)$$

In principle, one needs to consider an infinite number of plane waves in order accurately to expand a wave function, but as is shown in Eqn. (2.53), the coefficient  $C_{n,k+\vec{G}}$  decreases as  $|\vec{k} + \vec{G}|$  increases, so that the expansion of plane waves can be truncated at a finite value of  $|\vec{k} + \vec{G}|$  that associates with a kinetic energy cutoff ( $E_{cut}$ ) defined as in Eqn. (2.53).

$$\frac{1}{2}|\vec{k} + \vec{G}|^2 \leq E_{cut}, \quad E_{cut} = \frac{\hbar^2}{2m} |\vec{G}_{max}|^2 \quad (2.53)$$

For each system under study, the value of the cutoff energy needs to repeatedly tested until it yields converged results. Substituting wave functions expanded by using a plane-wave basis set in the K-S equation, one can get the following equation after integrating over the vector  $\vec{r}$ :

$$\frac{1}{2}|\vec{k} + \vec{G}|^2 C_{(\vec{k}+\vec{G})} + \sum_{\vec{G}_i} V_{\vec{G}_j,\vec{G}_i} C_{(\vec{k}+\vec{G}_j)} = E(\vec{k})C_{(\vec{k}+\vec{G}_j)} \quad (2.54)$$

where

$$V_{\vec{G}_j,\vec{G}_i} = \int_v V_{eff}(\vec{r}) e^{i(\vec{G}_j - \vec{G}_i)\cdot\vec{r}} dr. \quad (2.55)$$

By representing the integral as a sum over a finite number of  $k$  points, one performs the integration numerically over the Brillouin zone (BZ), given by:

$$\int_{BZ} \frac{1}{V_{BZ}} dk \rightarrow \sum_j \omega_j. \quad (2.56)$$

Then the integral over the over the BZ can be expressed as:

$$\frac{V}{(2\pi)^3} \int_{BZ} F(\vec{k}) dk = \sum_j \omega_j F(\vec{k}_j) . \quad (2.57)$$

where  $F(\vec{k})$  is a function of momentum,  $V$  is the unit cell volume and  $\omega_j$ 's are the weight factors. Eqn. (2.57) can be solved by diagonalizing the corresponding matrix, whose number of elements is determined by  $E_{cut}$ . The solutions will provide the necessary coefficients ( $C_{i,\vec{k}+\vec{g}}$ ) of Kohn-Sham eigenstates and their corresponding eigenvalues. Plane wave choice seems a natural one since it is equivalent to the complex Fourier expansion of the real-space wave function. Given this property, the problem of finding  $\Psi_i$  can be treated in the reciprocal space, taking advantage of fast Fourier algorithms to make the calculations more efficient [32]. Furthermore, the only parameter controlling the accuracy of  $\Psi_i$  is the maximum number of  $k$  wave-vectors that are used. Obviously, the choice of maximum number depends on the system under study. The larger the number of the wave-vectors, the more accurate the calculation is. The choice of wave-vectors can also result in calculations that are computationally more expensive (more memory and numerically intensive) calculations for large-scale systems.

A drawback of the plane-wave choice is the necessity of including a large number of wave vectors ( $k$ ) in order to describe localized states. In addition, plane wave expansion codes treat the vacuum on the same footing as the molecules or the surface under study. A possible way around this problem is to use localized basis sets instead of plane waves. The localized basis sets can be considered as Gaussian or Slater type orbitals or they can even be made to look more like atomic orbitals. Under this strategy, the Kohn-Sham orbitals can be expanded as:

$$\psi_i(\vec{r}) = \sum_l C_l^i \phi_l(\vec{r}) \quad (2.58)$$

where  $\phi_l(\vec{r})$  is a set of functions with an atomic-like character.

There are a number of advantages in using a localized basis set. First of all, because the range of interaction is finite, Hamiltonian matrix elements vanish for orbitals that are far apart. As a result, the Hamiltonian and overlap matrices ( $S_{ij} = \langle \varphi_i | \varphi_j \rangle$ ) become relatively sparse, saving computational cost. Another important virtue is that the Hamiltonian and other matrices are represented in a tight-binding-like form, is a form similar to that needed in the non-equilibrium Green's function method (NEGF) that will be discussed in next chapter. In this dissertation, both forms of the basis sets have been used.

## 2.9 *K-point Sampling*

In principle, solving the K-S equations requires calculations for an infinite number of K-points. But considering the fact that the wave-functions do not change much over a small distance in K-space will help reduce the number of K-point and simplify the problem. Since many quantities (like charge density and total energy) require integration over the BZ, the assumption of similarity of physical properties for two close values of K-point makes it possible to perform such integrations as summations over a finite number of K-point lying within the first BZ. The set of these certain k-points is known as K-point sampling. Sampling of K-point is crucial for the accuracy of the integration. The most famous methods to sample K-point in the BZ are tetrahedron [33] and the special-point method [34].

In 1976, Monkhorst and Pack proposed a simple method to sample BZ by imposing upon it an equally-spaced mesh as a grid. In this method, one can determine those special K-points that reflect the properties of the whole BZ by employing symmetry arguments. The integration is then performed as the weighted summation over a grid of these special K-points. For metals, since the bands cross the Fermi energy, there will be a discontinuity in the occupation, which

leads to complication of the integration over the Fermi surface. Therefore, in the metal's case it is important to choose a sufficient number of K-points. In different studies comprised in this thesis, a large number of calculations are performed by testing different number of K-points to reach the convergence.

### 2.10 Molecular Dynamics (MD) Simulations

Molecular dynamics is one of the principal tools in the computer simulation, results of which provide insights in to the physical movements of a set of interacting atoms through an interacting potential (such as EAM) for a given time and temperature. The MD technique was first introduced in 1950's [35] , but the first paper reporting the application of a working implementation of the process weren't published until 1957 by Alder and Wainwright in 1957 [36].

The simple idea behind the MD method is illustrated in Figure 2-6. In MD simulation, the classical mechanics (Newton's second law) is employed to calculate the forces on each atom in an iterative way. Thereby, the time and space evolution of the system is obtained. The force acting on atom  $i$  ( $F_i$ ) is derived from the interatomic potential energy  $V(q_N t)$  as in Eqn. (2.59),

$$F_i = m_i \ddot{q}_i = -\nabla_{q_i} V(q_1(t), \dots, q_N(t)) \quad i = 1, N \quad (2.59)$$

where  $m_i$  is the mass of the atom  $i$  and  $q_N(t) = q_1(t), \dots, q_N(t)$  represents the complete set of  $3N$  atomic coordinates. Accordingly  $\ddot{q}_i = d^2 q_i / dt^2$  is the acceleration of the  $i^{th}$  atom.

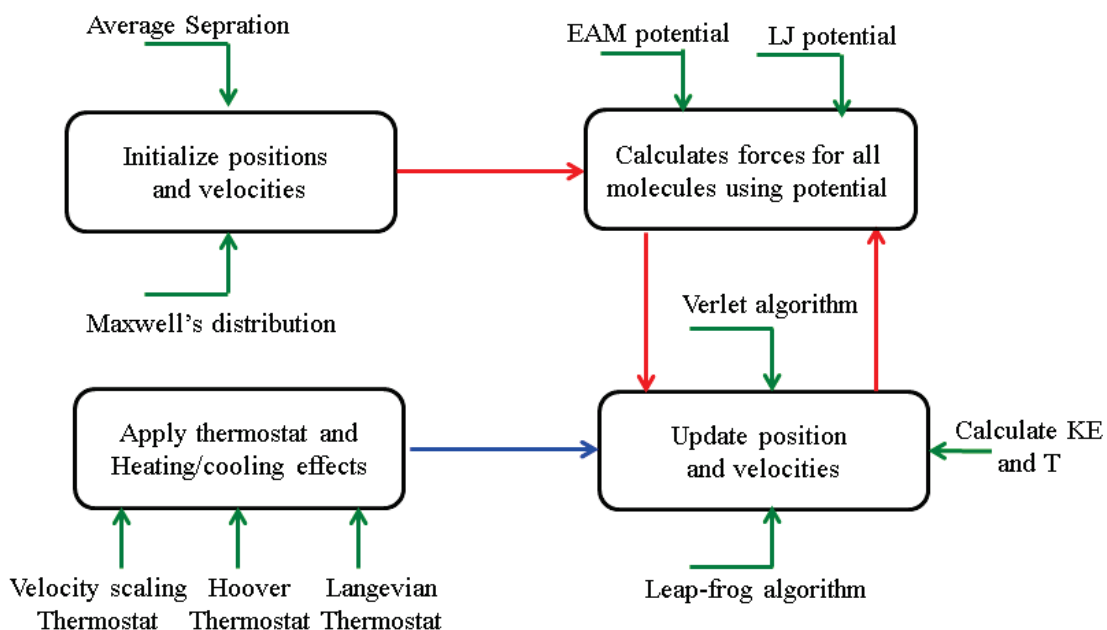


Figure 2-6. A simplified algorithm of how a MD simulation is performed.

In the first step, the initial atomic positions (for example, a crystal or nano-cluster structure) and velocities (obtained from a random number generator) is provided. In Step 2, the forces acting on atoms are calculated explicitly from the interatomic potential by obtaining the equation of motion. In Step 3, the new positions and velocities are generated employing time integration algorithms like leap-frog or velocity-verlet. This cycle is repeated several times until the time termination condition is met.

In order to collect enough statistics to reveal the true thermodynamical properties, an ensemble average -- averaging over consecutive configurations of the system (or replicas) -- over the time is required.

MD simulations start with a thermalization step (i.e., a cooling method) that usually terminates in a few thousands of time steps, until the system reaches a desired thermodynamic state using a temperature-scaling method. Thermostat methods are employed to control the



temperature of the system during the simulation. The Nose-Hoover thermostat and Langevin dynamics are the two most widely used thermostats to add or remove energy from the system.

Potentials that are used in MD calculations (i.e. EAM), have an infinite range. Therefore, in practical applications it is common to define a cutoff radius  $R_C$  and discard the interactions between atoms separated by more than  $R_C$ .

For realistic simulation of systems of  $N$  atoms, avoiding spurious surface at the edges (of 2D system) or surfaces (of 3D system) effects is necessary because atoms at the boundaries of the system would have fewer neighbors than atoms inside. A periodic boundary condition (PBC) helps to eliminate these effects of surface. Under a PBC, the atoms of the system are enclosed in a box and this box is replicated to infinity in all 3 Cartesian directions. This permits each atom to interact with its neighbor and its image, the result is that the number of atoms in the representative system remains computationally manageable without introducing spurious edge or surface effects. In order to reduce the number of interacting pairs, which increases enormously as an effect of PBC, the minimum image criterion is used. Among all the possible images of a particle in box, the closest one is chosen to for inclusion of interaction, and the remoter ones left out of account. This operating criterion greatly simplifies the setup of a MD program. Of course, to satisfy this criterion, the box size must be at least  $2R_c$  ( $R_c$  = cut off radius) along all the PBC directions.

### *2.11 Molecular Statics Simulations*

Understanding transition processes like chemical reactions and diffusion of atoms on surfaces of materials is a significant problem in condensed matter physics and chemistry. since at a finite temperature, atoms move around equilibrium positions, and the system moves to the set

of energy paths that corresponds to the lowest free-energy maximum. Although there are many possible reaction paths from a local minimum (initial-state configuration) to another local minimum (final-state configuration), the path that costs the lowest activation energy is statistically the most probably the minimum energy path (MEP). The highest energy configuration along the transition path is called the transition state or saddle point.

### 2.12 *Nudged Elastic Band (NEB) Method*

This is an efficient method for finding the MEP for a given transition path when both initial and final states are known *a priori*. The MEP is found by constructing a set of arbitrary images with equal distance from each other between the initial and final states. In this method [37], between adjacent images a spring like interaction potential is added to mimic an elastic band. The total force acting on an image is the summation of the spring force along the local tangent and the true force perpendicular to the local tangent. Linearly interpolating a set of images between the known initial and final states, minimizes the energy of the each of the images. Once each of the images is minimized, the MEP can be determined. At any point along the transition path, the force acting on the images points along the path while the energy is constant for any degree of freedom in the direction perpendicular to the transition path. Consequently, the NEB method can provide both the transition state configuration of images and insight in to the characteristics of the energy landscape.

### 2.13 *The Small Displacement Method for Phonon Calculations*

There are basically two types of methods in use in the first principle calculations of phonon frequencies: One is based on linear response theory, the other one is one or another direct approach. In the linear response approach, the dynamical matrix is evaluated through

DFPT as linearly response of the ground-state electron charge density. The information required for making this evaluation is obtained from comparison of a perturbed with the unperturbed system. There are two avenues for a direct approach: frozen phonon and direct force-constant method. In the frozen-phonon strategy, the changes in total energy are calculated by displacing the atoms (within a Cartesian coordinate system) from their equilibrium positions. And from the energy as a function of displacement amplitude the phonon frequency is obtained. This method is restricted to wave-vectors for which the phonon displacement pattern is commensurable with the supercell used in the calculations. Wave-lengths should fit to the supercell size (i.e., only for short wave-length phonon for reasonable supercell size). Another point is that the frozen-phonon method works for the models for which we already know the displacements or wave-vectors. In the second type of direct supercell approach, the forces related to the displacements of atoms in the supercell are considered instead of energies in the frozen phonon approach. After every atom in the finite crystal is displaced, the resulting forces are obtained by use of the Hellmann-Feynman theorem. From these in turn, the elements of force constant matrix are calculated, from which the dynamical matrix is determined by a Fourier transformation, and the phonon frequencies and wave-vectors evaluated by a diagonalization of this matrix. The small displacement algorithm for phonon calculations is depicted in Figure 2-7.

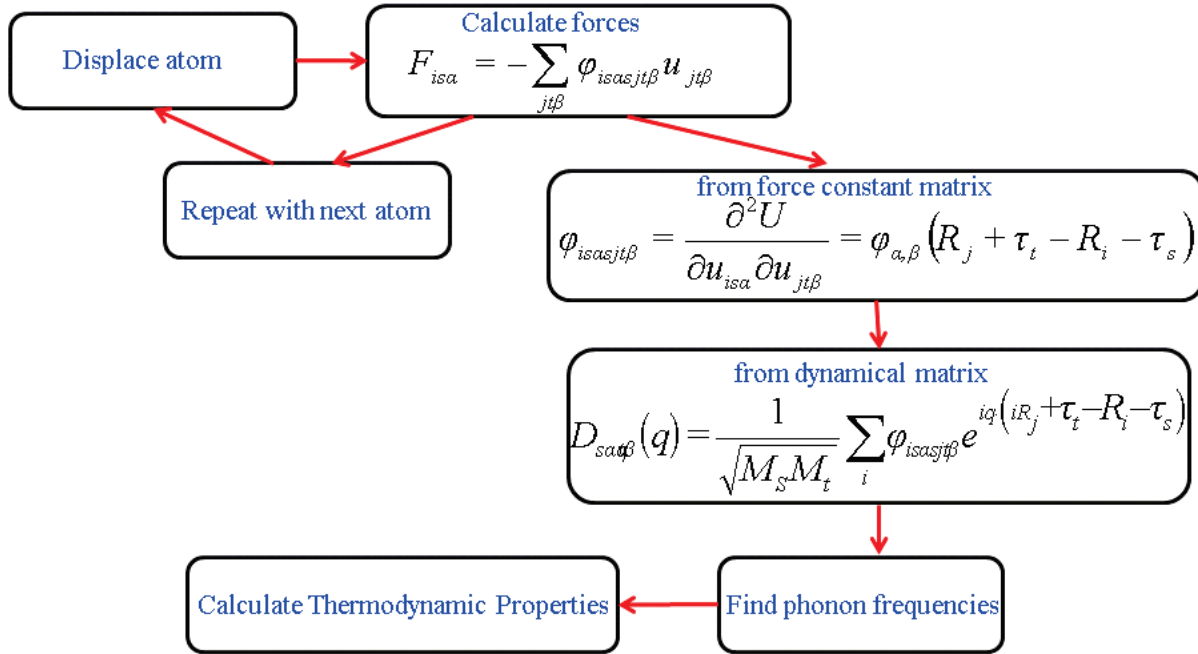


Figure 2-7. The small displacement method for phonon calculations.

### 2.14 Setting up the Transport Problem

There are three different perspectives on the transport problem in a nano device: thermodynamics, quantum mechanics, electro-statistics. Figure 2-8 depicts these schematically. From a thermo-dynamical point of view, the nanoscale system comprises of two bulk leads and a central region. In other words, it consists of two charge reservoirs bridged by a nanoscale molecule or a surface. The central region including some parts of the leads is called the external molecule (EM). If a voltage is applied on two leads at both sides of the charge reservoirs, current flows within the EM according to two different chemical potentials ( $\mu_R \neq \mu_L$ ). When the bias is zero, however, the system is in thermodynamic equilibrium ( $\mu_R = \mu_L$ ) and can be regarded as canonical ensemble [38].

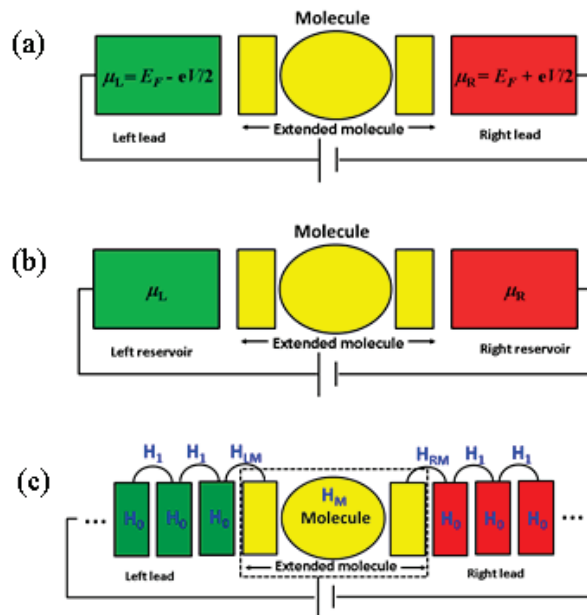


Figure 2-8. Three different perspectives on the transport problem in a nano device: (a) Thermodynamics (b) Quantum mechanics (c) Electro-statistical points of view.

From an electrostatic point of view, the first assumption is that the current/voltage probes have a regular periodic structure, so that a unit cell can be defined along the direction of transport. For this perspective to apply, the problems must be made from high quality metals in order to preserve local charge neutrality of the system. In this case, the effect of an external bias voltage on leads at both sides will bring about a rigid shift of the whole energy spectrum. In contrast, if a nontrivial potential profile develops over the extended molecule sandwiched between two leads, it needs to be calculated self-consistently. The resulting self-consistent electrostatic potential needs to be matched that of the leads at the boundaries between the extended molecule and the leads. To avoid any discontinuity of the electrostatic potential at the boundaries of the extended molecule, several layers of leads are usually embedded in the extended molecule. The choice of the number of layers depends on the screening length of the metal leads, but for most problems, a small numbers of atomic layers (between two and four) are

adequate. Another reason to add a few layers of leads to the EM is to prevent the molecules from attaching to reconstructed metallic surfaces through corrosive chemical groups.

In the studies reported in this dissertation, we formulate on the basis a linear combination of atomic orbitals (LCAO). It is obvious that the choice of (LCAO) will lead to sparsity of the Hamiltonian. Taking to account the sparsity of the Hamiltonian, it is convenient to introduce the concept of principle layer (PL). A principle layer is the smallest all in the direction of the transport ( $Z$  direction) that repeats periodically. It is constructed in such a way to interact only with nearest neighbor PL's. This implies that all the matrix elements between atoms belonging to two non-adjacent PL's go to zero.

At the Hamiltonian level, the system under study is described by an infinite Hermitian matrix ( $H$ ).

$$H = \begin{pmatrix} H_L & H_{LM} & 0 \\ H_{ML} & H_M [n_M] & H_{MR} \\ 0 & H_{RM} & H_R \end{pmatrix} \quad (2.60)$$

Different elements of the matrix ( $H_o$ ,  $H$ ,  $H_M$ ,  $H_{LM}$ ,  $H_{ML}$ ) can be defined in detail as following.

1.  $H(N \times N)$  matrix: describes all the interactions within a principle layer as a  $N \times N$  dimension matrix, where  $N$  is the total number of degrees of freedom (total number of basis functions) in the PL:
2.  $H_L(N \times N)$ : describes interactions between two PL's.
3.  $H_M(M \times M)$ : describes the extended molecule.

4.  $H_{LM}(N \times M)$ : contains the interactions between the last PL of the left hand lead and the extended molecule.
5.  $H_{ML}(M \times N)$ : describes the interactions between the first PL of the right hand side of the lead and the extended molecule.

For a non-orthogonal basis set, the overlap matrix ( $S$ ) has the same structure as the Hamiltonian matrix ( $H$ ). The relations of the various blocks of  $S$  are as  $S_0, S_1, S_{LM}, S_{RM}$  and  $S_M$  – similarly, respectively to their counterparts in Hamiltonian. In principle, in order to find the electron wave function and consequently determine all quantum mechanical properties of the system under investigation, one needs to diagonalize  $H$ . However, the Hamiltonian is neither finite nor translationally invariant because  $H_{ML}, H_{MR}, H_{RM}$  and  $H_M$  matrices break the translational symmetry of the system. In this case, Bloch's theorem cannot be applied to the entire system. Since, the diagonalization of an infinite matrix is a formidable task, this issue must be treated with a different way. A possible approach is to assume that the states deep inside the leads (electrodes) are associated to Bloch states of a finite system. These states are scattered by the potential created by the central EM. Hence, one can employ an approach based on a Green's function [39, 40] or a wave function [41, 42] to calculate the electronic properties of the ground state (including the wave function) of an open system. The resulting wave function can be regarded as a combination of Bloch states for the region deep inside the electrodes and localized atomic-like state for the central region of EM. Even if, one is able to calculate the Hamiltonian and the corresponding wave function, the problem of transport still needs to be addressed separately. We proceed now to explain how this is done.

### 2.15 Landauer-Buttiker Method

Heralding a new era in electrical conduction formalism, in 1957, Rolf Landauer proposed a simple ballistic 1D channel formula relating the conductance of a device (an elastic scatterer) with the quantum mechanical transmission ( $T = 1 - R$ ) properties of the one electron wave function as it approaches a scattering potential. In many ways, the Landauer-Buttiker formula is the Ohm's Law for low-dimensional systems [43, 44]. It should be noted that Landauer considered both the resistance of a quantum system (as) between the equilibrium contacts and the local resistance of a system itself. In fact, the latter one is the zero temperature residual resistance. As a result, the one-channel conductance can be calculated from what has come to be called the "first Landauer formula" as follows

$$G = \frac{e^2}{h} \frac{T}{1-T} = \frac{e^2 T}{h R}. \quad (2.61)$$

Let's consider two limiting cases. At low transmission ( $T \rightarrow 0$ ), the conductance is also small ( $G \rightarrow 0$ ). On the other hand, according to Eqn. (2.61), since when  $T \rightarrow 1$  there is no scattering, the conductance will go to infinity ( $G \rightarrow \infty$ ). If we want to consider the spin degeneracy in these formulas, one has to multiply the conductance by a factor of 2.

However, the conductance through a quantum system (QS) between two equilibrium contacts, calculated by the linear response method [45, 46] behaves in accordance with a quite different equation.

$$G = \frac{e^2}{h} \quad (2.62)$$

According to Eqn. (2.62), the conductance is finite in the case of perfect transmission through the junction ( $T = 1$ ). The inconsistency between the two formulas caused much



confusion and controversy – until, eventually, it was shown that both are reasonable and yield the same current, but correspond to the voltage differences between pairs of points. The key difference between Eqn. 2.61) and Eqn. (2.62) is that the first is for the conductance between either the leads or at the reservoirs, while the latter gives the conductance inside the scattering region.

In Landauer-Buttiker method, the voltage probes are treated on an equal footing, as the contacts and reservoirs, having well defined equal chemical potentials. The puzzle with the finite resistance at  $(T = 1)$  Eqn. (2.61) is also understood. Since there is a finite number of conductance channels, the corresponding conductance is also finite in the case of zero temperature without scattering. In other words, the number of electrons going through the system is limited, as well as the current related to one-electron state, consequently the average current depends on the number of channels, their transmission and the level population.

We can consider the Landauer-Buttiker method as a scattering problem. In this formulation free electrons with energy  $E$  are injected from the left side and are scattered by the step potential formula.

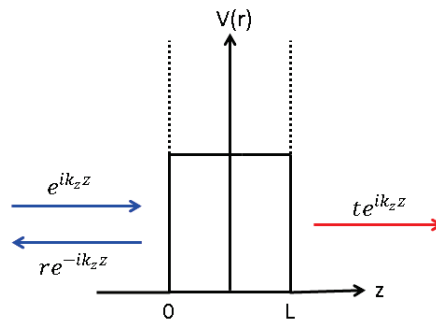


Figure 2-9. Schematic representation of scattered wave functions by a potential barrier  $V(r)$ .

The total wave function of this problem is

$$|\Phi_{Total}\rangle = |\Phi_{in}\rangle + |\Phi_{0L}\rangle + |\Phi_{out}\rangle. \quad (2.63)$$

with

$$\langle z|\Phi_{Total}\rangle = \begin{cases} \langle z|\Phi_{in}\rangle = e^{ik_z z} + r e^{-ik_z z} & 0 \leq z \\ \langle z|\Phi_{0L}\rangle = A e^{\kappa_z z} + B e^{-\kappa_z z} & 0 \leq z \leq L \\ \langle z|\Phi_{out}\rangle = t e^{ik_z z} & z > L \end{cases} \quad (2.64)$$

$K_z$  ( $-K_z$ ) is the wave vector of partially back scattered (transmitted) of an incoming electron.

$$k_z = \frac{\sqrt{2mE}}{\hbar} \quad (2.65)$$

$$\kappa_z = \frac{\sqrt{2m(V-E)}}{\hbar} \quad (2.66)$$

Wave-vectors can be imaginary or real depending on whether  $V < E$  or  $V > E$ . The coefficients  $A$ ,  $B$ ,  $r$  and  $t$  can be evaluated by imposing the continuity condition of the total wave function and their derivatives at the boundaries of the potential.

Alternatively, the scattering problem can be explained in terms of the scattering matrix ( $S$ ):

$$S = \begin{pmatrix} r & t' \\ t & r' \end{pmatrix} \quad (2.67)$$

where  $|\Phi_{in}\rangle$  and  $|\Phi_{out}\rangle$  are entering or leaving wave functions through the channel as,

$$|\Phi_{in}\rangle = S|\Phi_{out}\rangle \quad (2.68)$$

And  $t$  and  $r$  ( $t'$  and  $r'$ ) in the  $S$  matrix are the transmission and reflection coefficients for incoming waves from the left (or outgoing waves to the right). Following the second Landauer formula, Fisher-Lee defined the multi-channel conductance as

$$\Gamma = \frac{e^2}{h} \sum_{\sigma} \sum_{ij} 'T_{ij}^{\sigma} = \frac{e^2}{h} \sum_{\sigma} Tr[t_{\sigma} t_{\sigma}^{\dagger}] = \frac{G_0}{2} \sum_{\sigma} Tr[t_{\sigma} t_{\sigma}^{\dagger}] \quad (2.69)$$

where  $\sum_{ij}$  summation is performed over all channels at the Fermi energy (the open channels) and  $\sum_{\sigma}$  summation introduces the spin index  $\sigma$  ( $\sigma = up$  and down).

We can clearly see that the conductance in Eqn. (2.69) is written in the terms of conductance quantum ( $G_0 = \frac{2e^2}{h}$ ). Moreover, the conductance is associated with the transmission coefficients (coefficients of out scattered wave-functions) of our problem. Here, the energy dependent transmission probability is

$$T^{\sigma}(E) = Tr[t_{\sigma}(E)t_{\sigma}^{\dagger}(E)] \quad (2.70)$$

In multi-channel formalism the following general Landauer formula is called for.

$$I(V) = \frac{e}{h} \int_{-\infty}^{\infty} \bar{T}(E, V) [f_L(E + eV) - f_R(E)] dE \quad (2.71)$$

where  $\bar{T}(E, V) = T_r(\hat{t}\hat{t}^{\dagger})$  is the effective transmission function for the particles with the energy  $E$ . The most important advantage of this formula is that the transmission function can be calculated from the quantum scattering theory. Thus, the kinetic problem is reduced to the pure quantum mechanical problem of a single particle in a static potential. The formula Eqn. (2.71) is the most general two-terminal formula.

An important contribution was made by Buttiker, who extended the Landauer formula to a multi-terminal case [47, 48]. In particular, the four-terminal case is of great importance for experiments. The current from the  $i^{th}$  contact to the system is

$$I_i = \frac{e}{h} \int_{-\infty}^{\infty} \sum_{j \neq i} \bar{T}_{ij}(E, V) [f_i(E + eV_{ij}) - f_j(E)] dE \quad (2.72)$$

where  $V_{ij}$  is the voltage between contacts  $i$  and  $j$ .

### 2.16 Non-equilibrium Green's Function (NEGF) for an Open System

As was pointed out in the previous preceding section (Section 2.15), we are dealing with an infinite-dimensional non-periodic Hermitian problem. This problem can be treated by solving the Green's function equation.

$$[e^+S - H]G^R(E) = I \quad (2.73)$$

$$e^+ = \lim_{\delta \rightarrow 0^+} E + i\delta \quad (2.74)$$

where  $I$  is an infinite-dimensional identity matrix,  $\varepsilon^+$  is equal to  $\lim_{\delta \rightarrow 0} E + i\delta$  and  $E$  is the energy of the system. From now on, we will drop the symbol “ $R$ ” indicating the retarded quantities. Eqn. (2.73) can be written in terms of the block-diagonal matrices of Hamiltonian ( $H$ ) and overlap matrix ( $S$ ).

$$\begin{pmatrix} e^+S_L - H_L & e^+S_{LM} - H_{LM} & 0 \\ e^+S_{ML} - H_{ML} & e^+S_M - H_M & e^+S_{MR} - H_{MR} \\ 0 & e^+S_{RM} - H_{RM} & e^+S_R - H_R \end{pmatrix} \begin{pmatrix} \mathcal{G}_L & \mathcal{G}_{LM} & \mathcal{G}_{LR} \\ \mathcal{G}_{ML} & \mathcal{G}_M & \mathcal{G}_{MR} \\ \mathcal{G}_{RL} & \mathcal{G}_{RM} & \mathcal{G}_R \end{pmatrix} = \begin{pmatrix} J & 0 & 0 \\ 0 & I_M & 0 \\ 0 & 0 & J \end{pmatrix} \quad (2.75)$$

where  $G_R(G_L)$  are the left (right)-hand side leads,  $G_{LM}(G_{RM})$  are the direct scattering between the leads  $G_{LR}$  and the block matrix of the extended molecule (GM), and  $H_L, H_R, H_{LM}, H_{RM}$  and their corresponding overlap matrices, are respectively the Hamiltonian of the left (right) hand side leads and the coupling matrix indicating the leads and the EM.

To solve Eqn. (2.75), one needs to write down the Green's function equation for EM and the surface of the left and right hand side of the principle layer. Since there is no alternation in the electronic structure of the left and right hand side reservoirs arising from neither the coupling of molecule nor through appliance of external bias, one can merely focus on the EM and eliminate the degrees of freedom of the electrodes one by one from deep inside the leads all the way toward the interface with the EM.

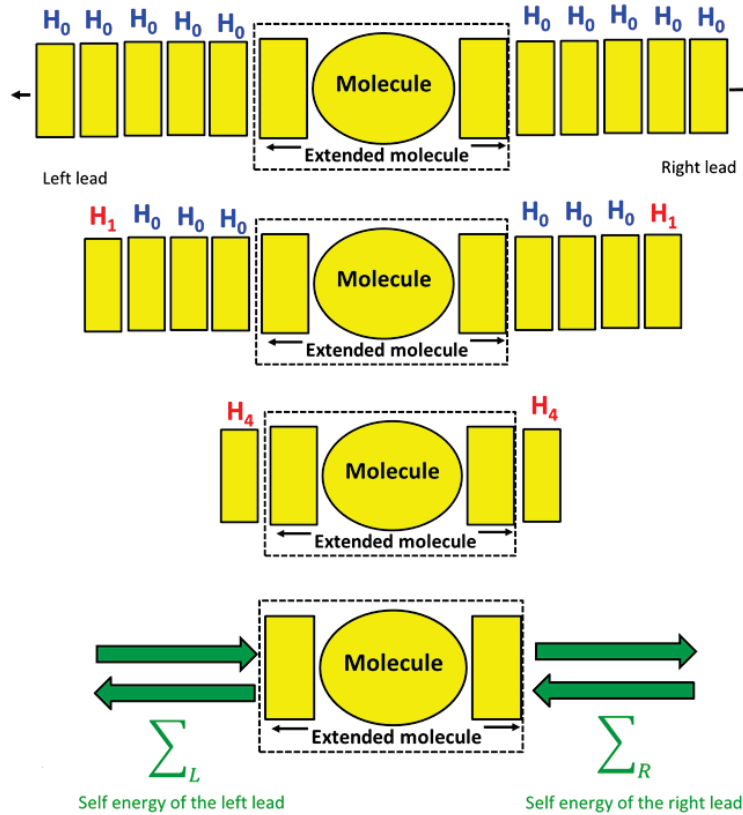


Figure 2-10. Self-energies of the leads as the effect of electrodes in terms of an effective interaction.

In this way the effect of electrodes will be replaced by an effective interaction potential.

The final expression for the retarded Green's function for the EM ( $G_M^R$ ) is as follows:

$$G_M^R(E) = [e^+ S_M - H_M - \Sigma_L^R(E) - \Sigma_R^R(E)]^{-1} \quad (2.76)$$

where  $\Sigma_L^R(E)$  and  $\Sigma_R^R(E)$  are the retarded self-energies of the left-and right hand-side.

$$\Sigma_L^R(E) = (e^+ S_{ML} - H_{ML}) G_L^{OR}(E) (e^+ S_{LM} - H_{LM}) \quad (2.77)$$

$$\Sigma_R^R(E) = (e^+ S_{RM} - H_{MR}) G_R^{OR}(E) (e^+ S_{RM} - H_{RM}) \quad (2.78)$$

$G_L^{OR}$  and  $G_R^{OR}$  in the Equations (2.77) and (2.78) are the retarded surface Green's function of the leads, corresponding to the right lower (left higher) block of the retarded Green's function of the whole left (right) hand side semi-infinite lead.

$$G_L^{OR}(E) = [e^+ S_L - H_L]^{-1} \quad (2.79)$$

$$G_R^{OR}(E) = [e^+ S_R - H_R]^{-1} \quad (2.80)$$

It is worth to mention that  $G_L^{OR}(G_R^{OR})$  are the Green's functions of the isolated semi-infinite leads, while  $G_L^R(G_R^R)$  are the Green's function of the scattering region. The good news is that there is no need to solve Eqn. (2.79) and Eqn. (2.80) in order to calculate the Green's function of the leads. Moreover,  $G_M^R$  is the retarded Green's function associated with the effective Hamiltonian as,

$$H_{eff} = H_M + \Sigma_L^R(E) + \Sigma_R^R(E) \quad (2.81)$$

where  $G_M^R$  contains all the electronic structure information of the extended molecule, and can be used to construct the zero-bias conductance of the system through the Fisher-Lee [39, 45] equation.

$$G = \frac{2e^2}{h} \sum_{Tr} [\Gamma_L G^{RtM} \Gamma_R G_M^R] \quad (2.82)$$

where

$$\Gamma_{\alpha}(E) = i[\Sigma_{\alpha}^R(E) - \Sigma_{\alpha}^R(E)^{\dagger}] \quad (2.83)$$

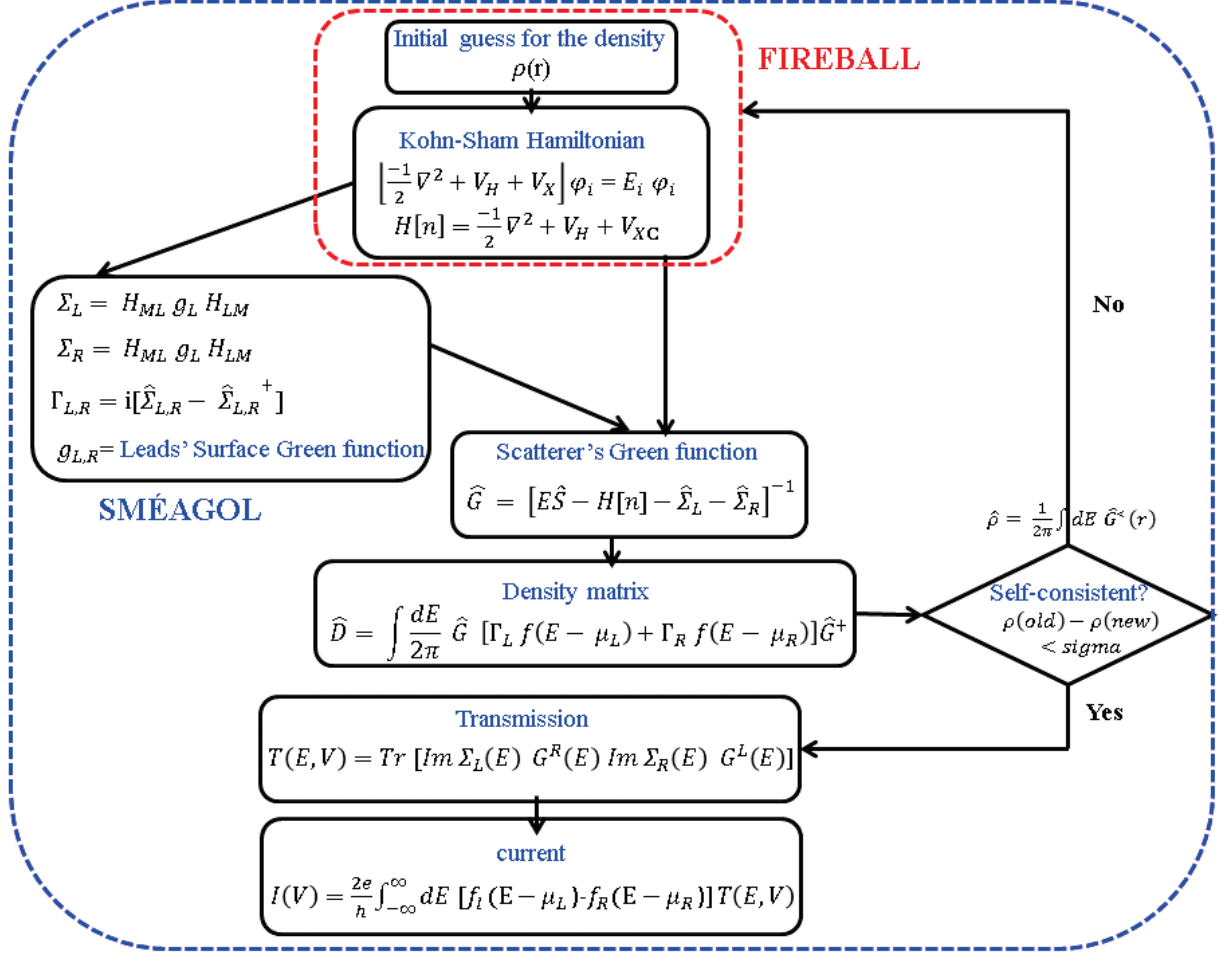


Figure 2-11. Flow-chart of the Sméagol program, highlighting the interconnection between SMÉAGOL and FIREBALL. Adapted from [38].

In Figure 2-11, a general flow chart of Sméagol and how it interfaces with FIREBALL. It can be seen that FIREBALL provides the KS Hamiltonian and Sméagol introduces the self-energies turning the system from periodic to central scattering region attached to semi-infinite electrodes. The codes exchange Hamiltonians and density matrices iteratively until self-consistency is achieved. Then Sméagol is used to calculate the transport properties such as transmission coefficients and the I-V characteristics.

## CHAPTER 3. EFFECT OF INTERFACES ON ELECTRON TRANSPORT PROPERTIES OF MoS<sub>2</sub>-Au CONTACTS

### 3.1 Introduction

In nanoscopic conductors every atom counts and the transport properties are strongly dependent on the detailed atomic arrangement. Hence, in order to make theoretical predictions that can be compared with experimental results, it is important, to have a reliable description of, the atomic structure of the conductor and of the electronic structure that accompanies it. This can be achieved most conveniently with the aid of *ab-initio* electronic structure methods.

A related question partially addressed in this chapter is to what extent the interface of the MoS<sub>2</sub> and the electrodes introduces variations in the conductance and how these depend on the chemical nature of the atoms involved.

### 3.2 Methodology and Computational Details

We used the first principle code of the SMÉAGOL package [49, 50] to calculate transport properties. SMEAGOL is based on the combination of DFT with a local-orbital basis (as implemented in the FIREBALL code [51]) with the non-equilibrium Green's function (NEGF) technique [52, 53].

Nanoscale devices consist of an atomic-scale system coupled with two semi-infinite electrodes. The NEGF method splits up a two-terminal nano-device under investigation into three distinct regions, a left (L) and a right electrodes (R) and a central scattering region, consisting of an extended molecule (M). The scattering region actually includes a portion of the semi-infinite electrodes. The Hamiltonian of the total system in the localized atomic basis is



given by the sum of the Hamiltonians of each of the isolated parts plus the Hamiltonian of the contact-molecule interactions for the left and right electrodes ( $H_{LM}$  and  $H_{RM}$ ), respectively.

$$H = H_L + H_R + H_M + H_{LM} + H_{RM} \quad (3.1)$$

The orbitals are assumed to make up a complete set but are permitted to be non-orthogonal. In order to deal with the problem posed by an infinite system without translation invariance, it is convenient to use one-body Green's functions as we describe in the following.

It worth mentioning that aside from its numerical efficiency [51], the great advantage of using a local-orbital basis in DFT calculations is that beyond some distance the Hamiltonian interactions are strictly zero beyond some distance. This circumstance allows us to partition the system unambiguously, and thus to define regions where we will do different parts of the calculation as described above. Moreover, because the Hamiltonian takes the same form as in empirical tight-binding calculations, the techniques developed in this context (i. e., the NEGF method) can be straightforwardly applied.

The main quantity of the NEGF method in our transport calculation is the retarded Green's function of the central scattering region.

$$\hat{G} = \lim_{\delta \rightarrow 0} [(E + i\delta)\hat{S} - \hat{H}_{\hat{S}[\rho]} - \hat{\Sigma}_L - \hat{\Sigma}_R]^{-1} \quad (3.2)$$

where  $E$  is the energy,  $\hat{H}_{\hat{S}[\rho]}$  is the DFT Hamiltonian — which depends on the charge density  $\rho(\mathbf{r})$  and  $\hat{\Sigma}_L$  and  $\hat{\Sigma}_R$  — are the self-energies for the left and right lead respectively. The self-energy contains information about the electronic structure of both the semi-infinite electrode and its coupling to the scattering region. A self-consistent procedure for the two-probe systems is designed as follows. First the self-energies associated to the leads are calculated from the

retarded Green's function of the isolated semi-infinite leads. Then the scattering Hamiltonian  $\hat{H}_{S[\rho]}$  is constructed for an initial  $\rho_0(r)$  and the Green's function using Eqn. (3.2) is calculated.

This allows us to evaluate the density matrix in the following manner

$$\rho = \int \frac{dE}{2\pi} \hat{G} [\Gamma_L f(E - \mu_L) + \Gamma_R f(E - \mu_R)] \hat{G}^+, \quad (3.3)$$

where  $\Gamma_\alpha = i[\hat{\Sigma}_\alpha - \hat{\Sigma}_\alpha^+]$ . Since the DFT Hamiltonian  $H_S$  depends solely on the density matrix, Eqn. (3.1) and Eqn. (3.2) can be iterated until self-consistency is achieved.

The current through the nanoscale system can be calculated from the corresponding Green's function and self-energies using the Landauer-Buttiker formula as follows [54]

$$I(V) = \frac{2e}{h} \int_{-\infty}^{+\infty} dE [f_L(E - \mu_L) - f_R(E - \mu_R)] T(E, V) \quad (3.4)$$

where  $\mu_L$  and  $\mu_R$  are the electrochemical electron distribution of the two electrodes.  $T(E, V)$  is the transmission coefficient at energy  $E$ , and  $V$  is the bias voltage, which can be calculated from the converged Green's function thus:

$$T(E, V) = Tr [Im \Sigma_L(E) G^R(E) Im \Sigma_R(E) G^L(E)] \quad (3.5)$$

Finally, conductance is simply proportional to  $T(E)$  evaluated at the Fermi level ( $E_F$ ) at zero bias ( $V=0$ ):

$$G = \frac{e^2}{h} T(E_F) \quad (3.6)$$

In the calculations for the studies discussed in this chapter, FIREBALL-SMEAGOL code is used within the local density approximation (LDA) for the exchange–correlation functional. In FIREBALL, the wave functions of valence electrons are expanded in the basis of the so-called FIREBALL orbitals, i.e. a set of strictly localized pseudo-atomic orbitals, which are exactly zero

for distances larger than the cutoff radius  $R_C$ . Several tests have been performed to optimize the local-orbital basis set, yielding a good description of the structural and electronic properties of the studied system. Pseudopotentials are used to treat the core electrons in the calculations. We have used the following optimized basis set of numerical atomic orbitals: s,p,d for Mo atoms, s,p,d for S atoms and s,p,d for Au atoms. The cutoff radii (in a.u.) of those orbitals are: (6.2, 6.2, 5.8), (4.5, 5.0, 5.0) and (5, 5.6, 4.7) for orbitals of Mo, S and Au, respectively. The set of k-points used in our calculations consists of 16 k-points in the first 2D Brillouin zone of the Au electrodes. The total-energy convergence with respect to the choice of k-points was checked by repeating the calculation with a different set of k-points and comparing the results.

### 3.3 Construction of Model Sample Au-MoS<sub>2</sub>-Au

The geometry of the edges of MoS<sub>2</sub> is well understood [55-57] It is either the armchair or the zigzag, as seen in Figure 3-1. As a result of the symmetry inherent in a layer of MoS<sub>2</sub>, there are two types of zigzag edges: S zigzag edge ( $\underline{1}010$ ) and Mo zigzag edge ( $10\underline{1}0$ ). Note that either Mo or S atoms could terminate the zigzag edge. Thus, there are in total four types of zigzag edges: S edge-S, Mo edge -Mo, S edge-Mo, and Mo edge-S, where Mo and in the second part indicate the edge termination. The geometry of the first two zigzag edges is shown in Figure 3-1. By removing the outermost atom-row of these edges, the geometry of the S edge-Mo and Mo edge-S type of edges can be obtained [58].

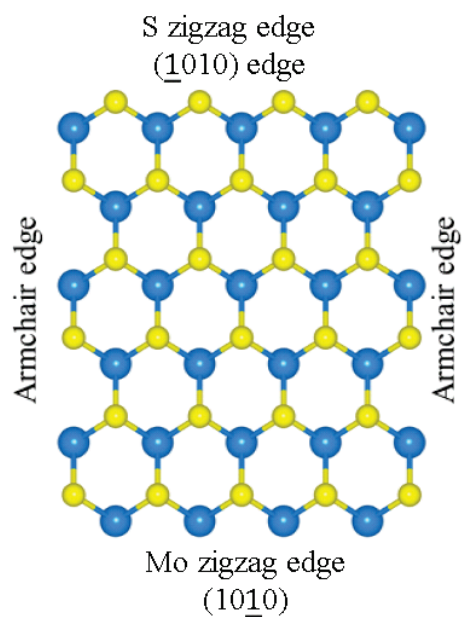
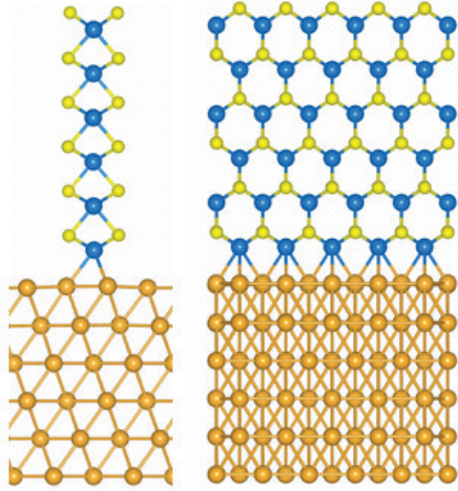


Figure 3-1. Ball-stick model of armchair and zigzag edges of MoS<sub>2</sub>. Dark (blue) and light (yellow) balls represent Mo and S atoms, respectively.

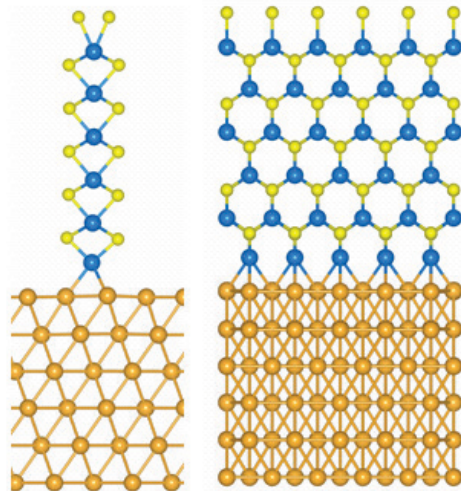
To simplify indices of the edges in what follows, we replace [Mo edge – 00%S], [S edge – 00%Mo], [Mo edge – 1 00%S] and [S edge – 100%Mo] with Mo00, S00, Mo100 and S00, respectively. (See Figure 3-2)

In our two probe model system, the extended molecule includes MoS<sub>2</sub> molecule coupled with two layers of the Au. The Au electrodes have been modeled by 3 layers (111) oriented-Au slabs with a 2×4 surface unit cell. The structural model for our theoretical analysis is illustrated in Figure 3-3.

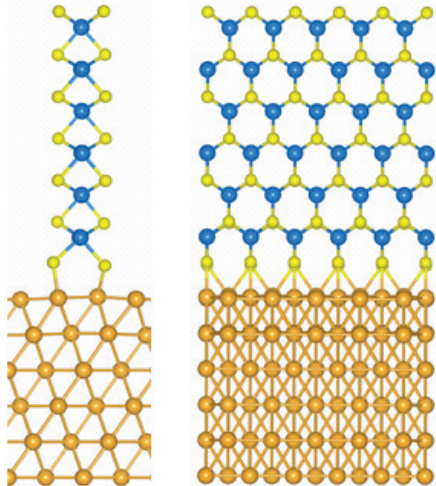
(a) [Mo edge - 00% S] (Mo00)



(b) [S edge - 00% S] (S00)



(c) [Mo edge - 100% S] (Mo100)



(d) [S edge - 100% S] (S100)

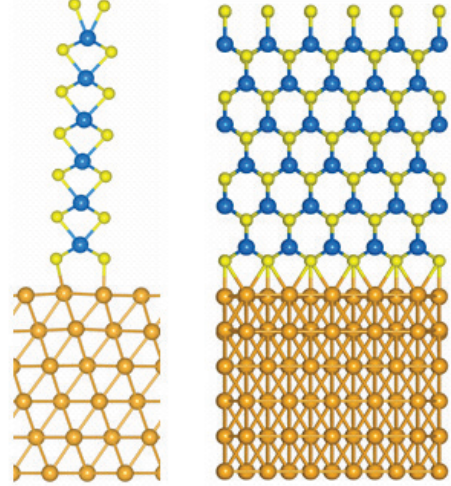


Figure 3-2. Different samples with different interfaces of MoS<sub>2</sub>-Au used for approximation of Schottky barriers.

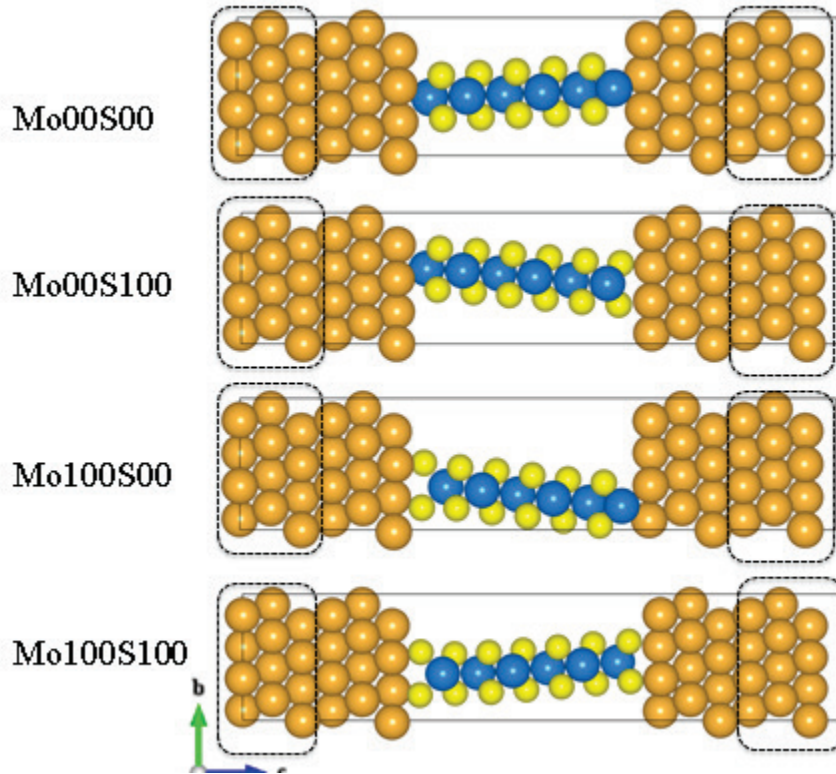


Figure 3-3. Atomic representation of the relaxed arrangement of single layer MoS<sub>2</sub> with different edges coupled with Au contacts: (a) Mo00S00 (b) Mo00S100 (c) Mo100S00 and (d) Mo100S100.

### 3.4 Charge Density Analysis

#### 3.4.1 Projected Redistribution of Average Charge Density in the Z Direction

A measure of charge rearrangement at the interface of the Molecule and contacts can be obtained by subtracting the density of the two isolated fragments (MoS<sub>2</sub> and Au, each with atoms at final relaxed positions in the total molecule-slab system) from the density of the total system. The result is the deformation or difference of the charge density due to the molecule-contact interaction:

$$\Delta \rho(\mathbf{r}) = \rho(\text{MoS}_2 + \text{Au}) - \rho(\text{MoS}_2) - \rho(\text{Au}) \quad (3.7)$$



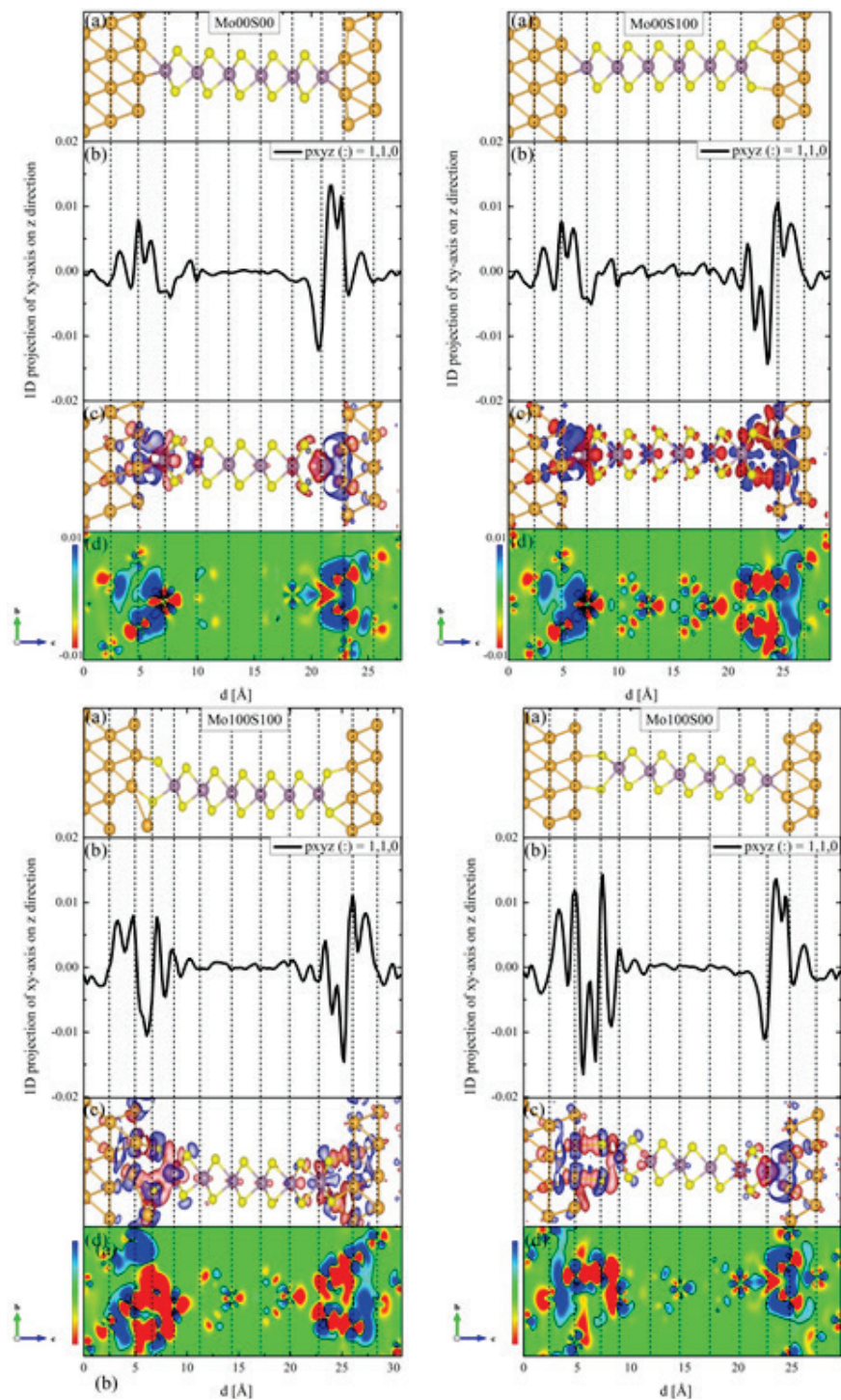


Figure 3-4. Electronic structure at the interfaces of MoS<sub>2</sub> and the Au contacts: (a) Sample models (b) planner (110) averaged charge density difference. The dashed lines represent the position of the Au-slab and MoS<sub>2</sub> layers. Positive values indicate an accumulation of charge; negative values indicate a depletion of charge with respect to the separated fragments. (c) 3D charge density redistribution [ $\Delta \rho(\mathbf{r}) = \rho(\text{MoS}_2 + \text{Au}) - \rho(\text{MoS}_2) - \rho(\text{Au})$ ]. Isosurfaces are drawn

with isovalue of 0.01 unit. The blue and red surfaces represent, respectively, the charge accumulation and deficit regions. (i.e. charge flows from red to blue regions) (d) Charge density redistribution plotted along the vertical plane passing through two Mo atoms of MoS<sub>2</sub> molecule (y-z plane). Contours are drawn in scale from 0.003 to 1 unit at interval of 0.05.

To enable a more quantitative analysis, it is useful to average the charge density redistribution  $[\Delta\rho(r)]$  on planes parallel to the slab, at various positions in the direction perpendicular to the surface (z) resulting in a profile

$$\rho_{\text{ave}}(z) = \int_A \Delta\rho(r) dx dy \quad (3.8)$$

where  $A$  represents the surface of the cell perpendicular to the z direction. As may be expected,  $\rho_{\text{ave}}(z)$  exhibits oscillations in the interface, but the broad features are as an accumulation of electronic charge in the interface area, and a depletion in the region occupied by the MoS<sub>2</sub>. To visualize the charge transfer between the MoS<sub>2</sub> and Au, we used both the code FIREBALL (with local-orbital basis set) and the plane-wave *ab-initio* code VASP [59]. Since the trend of the results with VASP did not differ from those obtained with FIREBALL; we regard the accuracy of the local basis-set calculations with FIREBALL to be sufficient for our purposes.



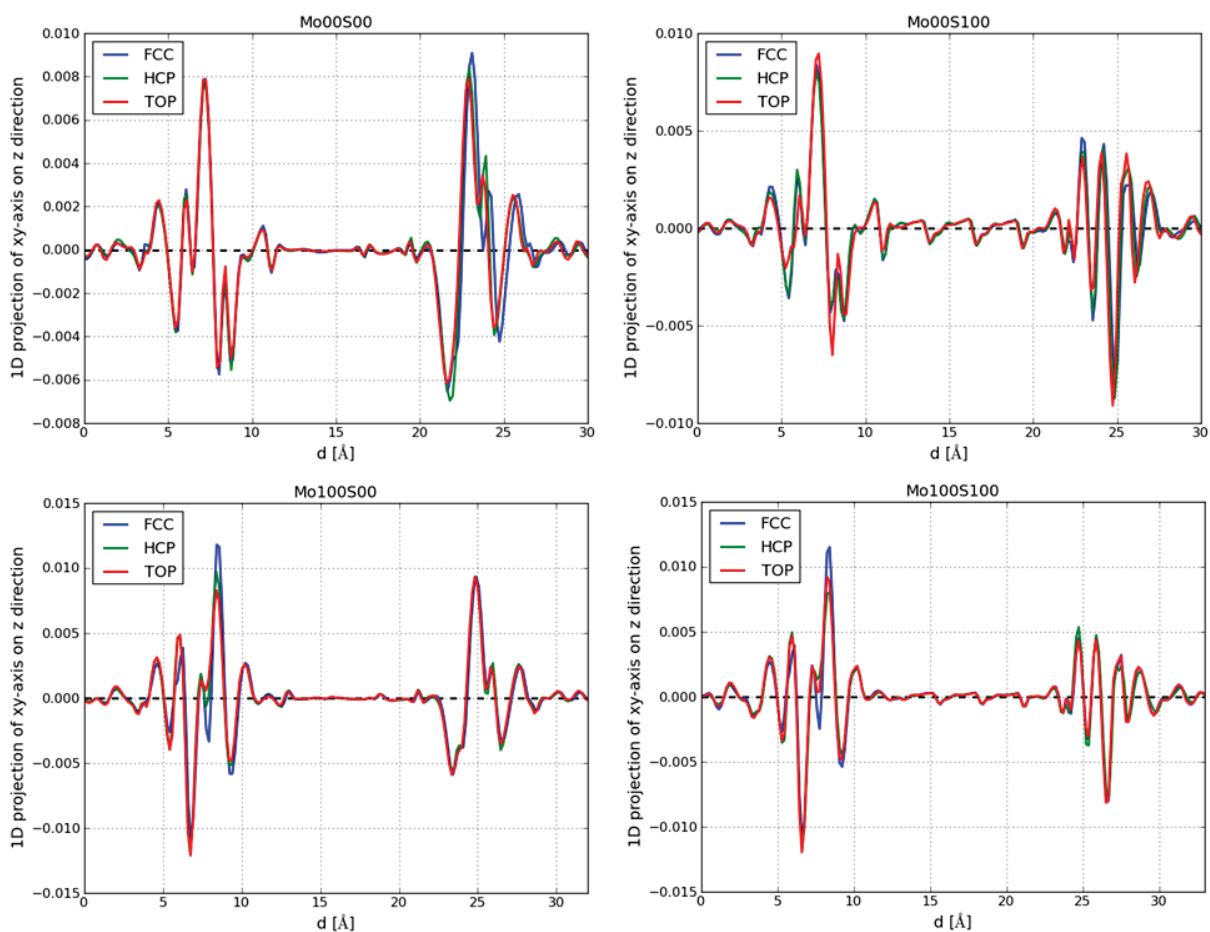


Figure 3-5. Averaged charge density difference along Z direction for fcc, hcp and top sites.

### 3.4.2 Direction and Size of Charge Transfer

We used two different methods to find the direction and value of the charge transfer.

#### 3.4.2.1 Bader Analysis

First, we performed Bader analysis to approximate total electronic charge of the separate atoms MoS<sub>2</sub> and Au atoms in the total system.

Bader developed an intuitive way of dividing molecules into atoms. His definition of an atom is based purely on the electronic charge density. He uses what are called zero-flux surfaces

to divide atoms. A zero flux surface is a 2-D surface on which the charge density is a minimum perpendicular to the surface. Since in molecular systems, the charge density typically reaches a minimum between atoms, this is a natural place to separate atoms from each other (see Table 3-1).

Table 3-1. Charge transfer results with different methods

Sample	n_atom (Mo+S)	Charge transfer (e)	Charge flow Direction	Charge transfer	Charge flow Direction
		Fireball-CNL	Fireball-CNL	VASP-Bader	VASP-Bader
Mo00S00	6+10	0.445 e	MoS <sub>2</sub> → Au	0.839	MoS <sub>2</sub> → Au
Mo00S100	6+12	0.277e	MoS <sub>2</sub> → Au	0.144	MoS <sub>2</sub> → Au
Mo100S00	6+12	0.347e	MoS <sub>2</sub> → Au	0.336	MoS <sub>2</sub> → Au
Mo100S100	6+14	0.270e	MoS <sub>2</sub> → Au	-0.483	Au → MoS <sub>2</sub>

### 3.4.2.2 Charge-Neutrality Level (CNL)

Another way to calculate the value and direction of the charge transfer is using the concept of the charge-neutrality level (CNL) located at a given position within the PDOS. As an illustration, the CNL location is given in Figure 3-6. The charge transfer at the interface is controlled by the difference between the Fermi level of the electrode and the MoS<sub>2</sub> charge-neutrality level. The offset between the CNL of the MoS<sub>2</sub> molecule and the metal Fermi level determines whether and in which direction charge is transferred between the metal and the MoS<sub>2</sub> molecule. If  $E_F$  is below the CNL (i.e. CNL is greater than  $E_F$ ), the negative charge is transferred from the molecule to the metal, if  $E_F$  is above the CNL (i.e. CNL is smaller than  $E_F$ ), the negative charge is transferred from the metal to molecule.

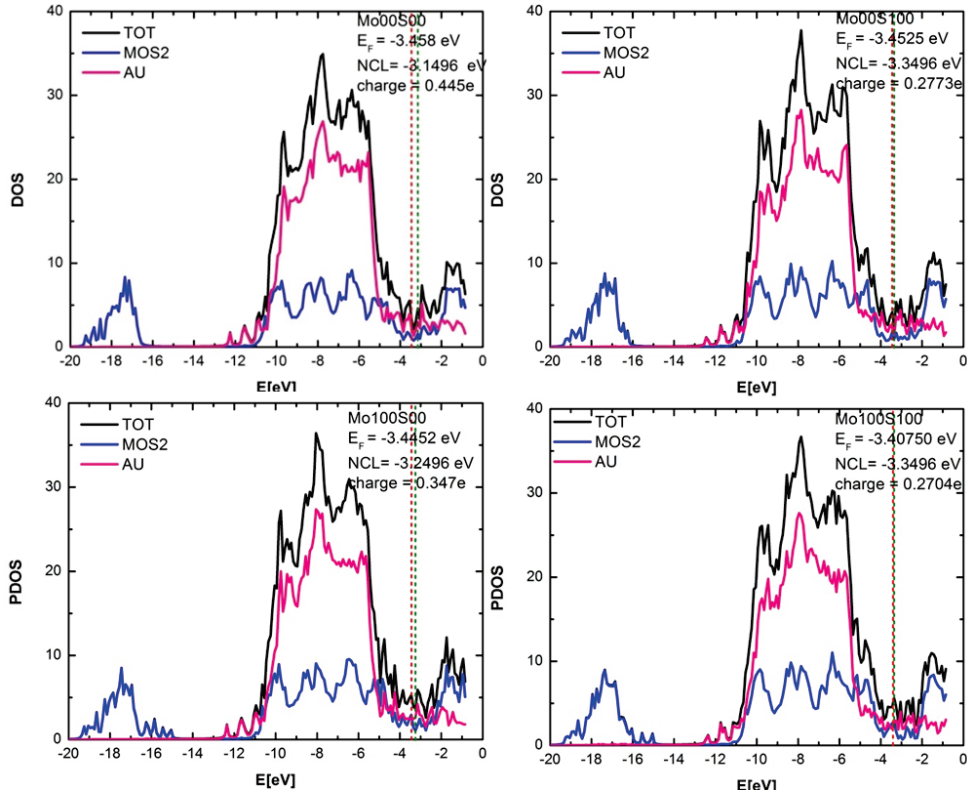


Figure 3-6. Partial density of states of total system, MoS<sub>2</sub> molecules and the Au electrodes for 4 different Au-MoS<sub>2</sub>-Au samples. The red line and green lines depict the Fermi level and the charge neutrality level (CNL), respectively.

### 3.5 Electron Transport Properties

In this section, we study three different electron transport properties of four different Au-MoS<sub>2</sub>-Au samples

#### 3.5.1 Zero Bias Transmission

$T(E)$  is the probability of an electron of a given energy to pass through the system (from filled initial states of one electrode to empty final states of the other). It is elastic scattering, so it is adiabatic - electron energy is conserved, so it must pass from initial states of one electrode to final states of the other electrode, where both states has the same energy.

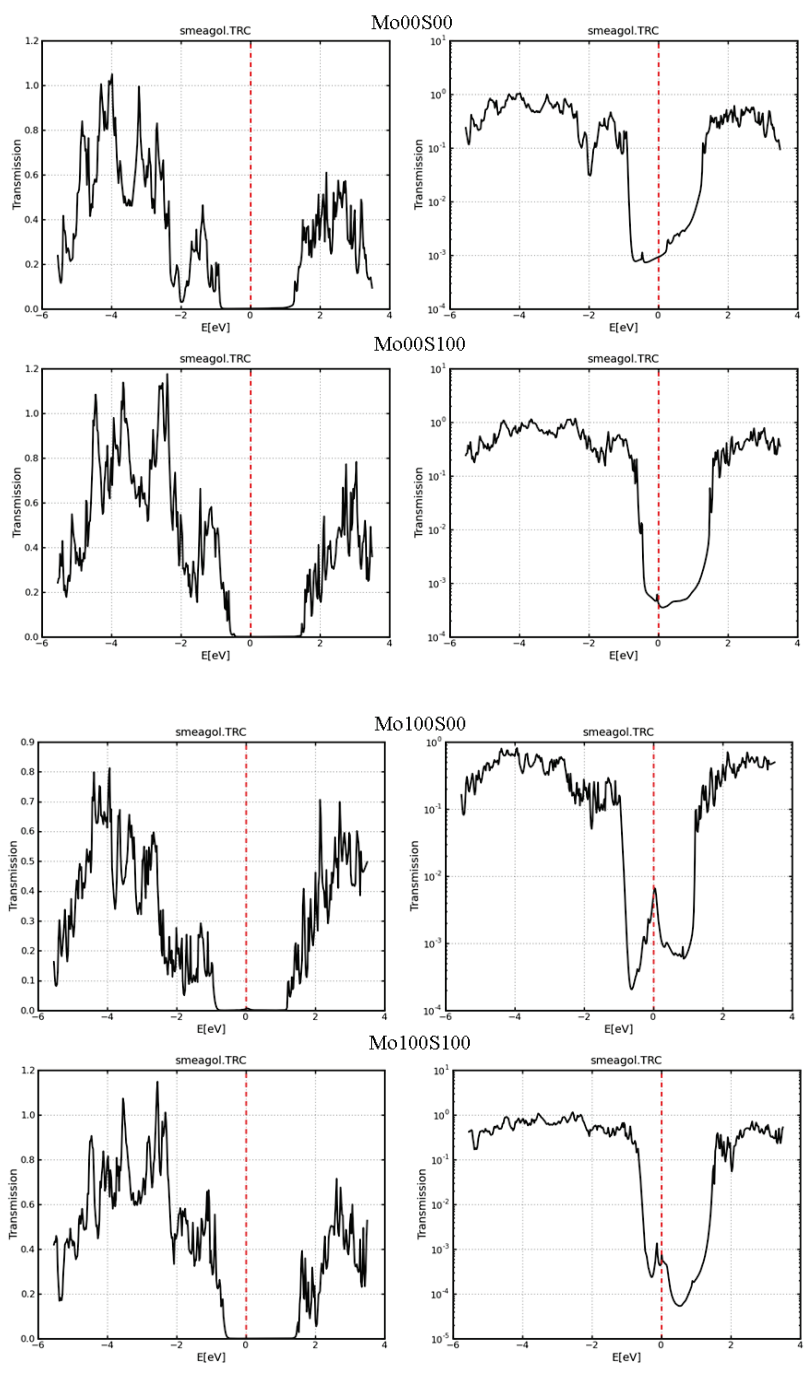


Figure 3-7. The equilibrium transmission in zero bias versus energy curve of the various sorts of Au-Mo-Au junctions. Right-hand side graphs show the logarithmic form of the Transmission versus Bias = 0. Because of the exclusion principle, it is apparent that the electron will pass from filled states to empty states.

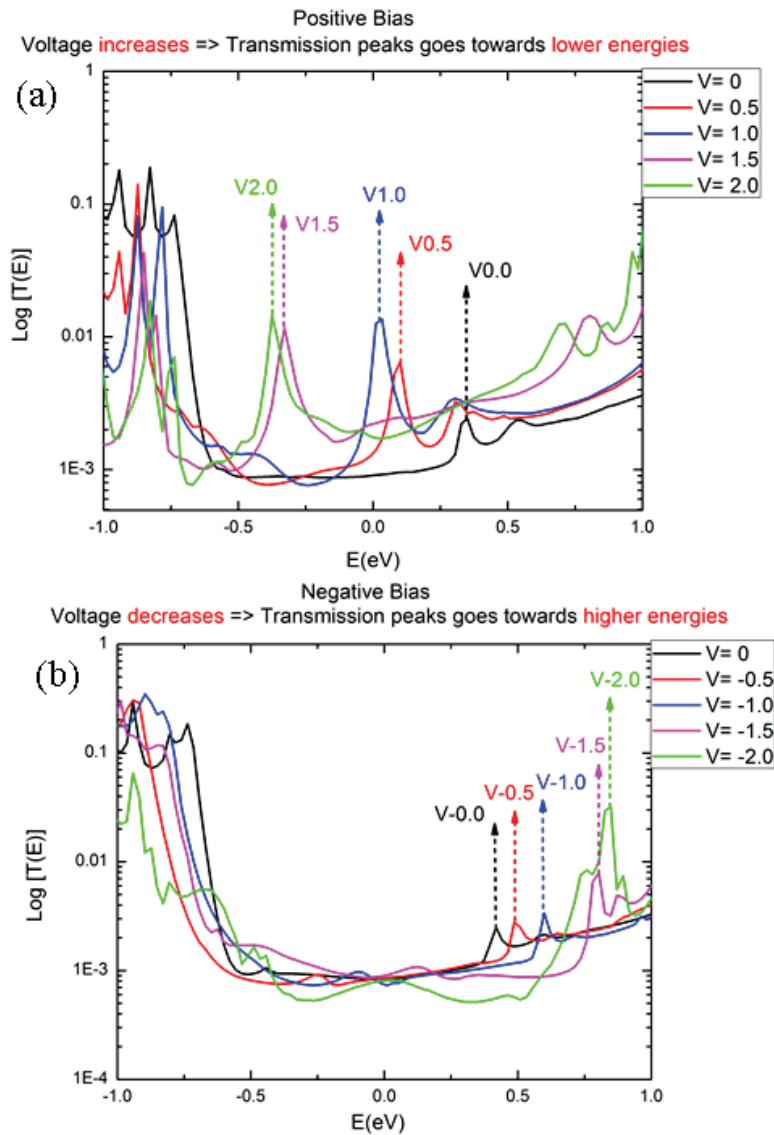


Figure 3-8. Transmission peaks of the sample when (a) bias voltage increases (positive bias) or (b) bias voltage decreases (negative bias).

Looking carefully at the peaks in the gap of the transmission curves, we observe two complementary patterns. When bias is positive, transmission peaks go toward lower energies as the voltage increases. Whereas for negative biases, they go toward higher energies as voltage decreases.

### 3.5.2 I-V Curves

The current that passes through the single-layer MoS<sub>2</sub> sandwiched between two gold electrodes can be found from integration of the transmission curves for different ranges of energy.

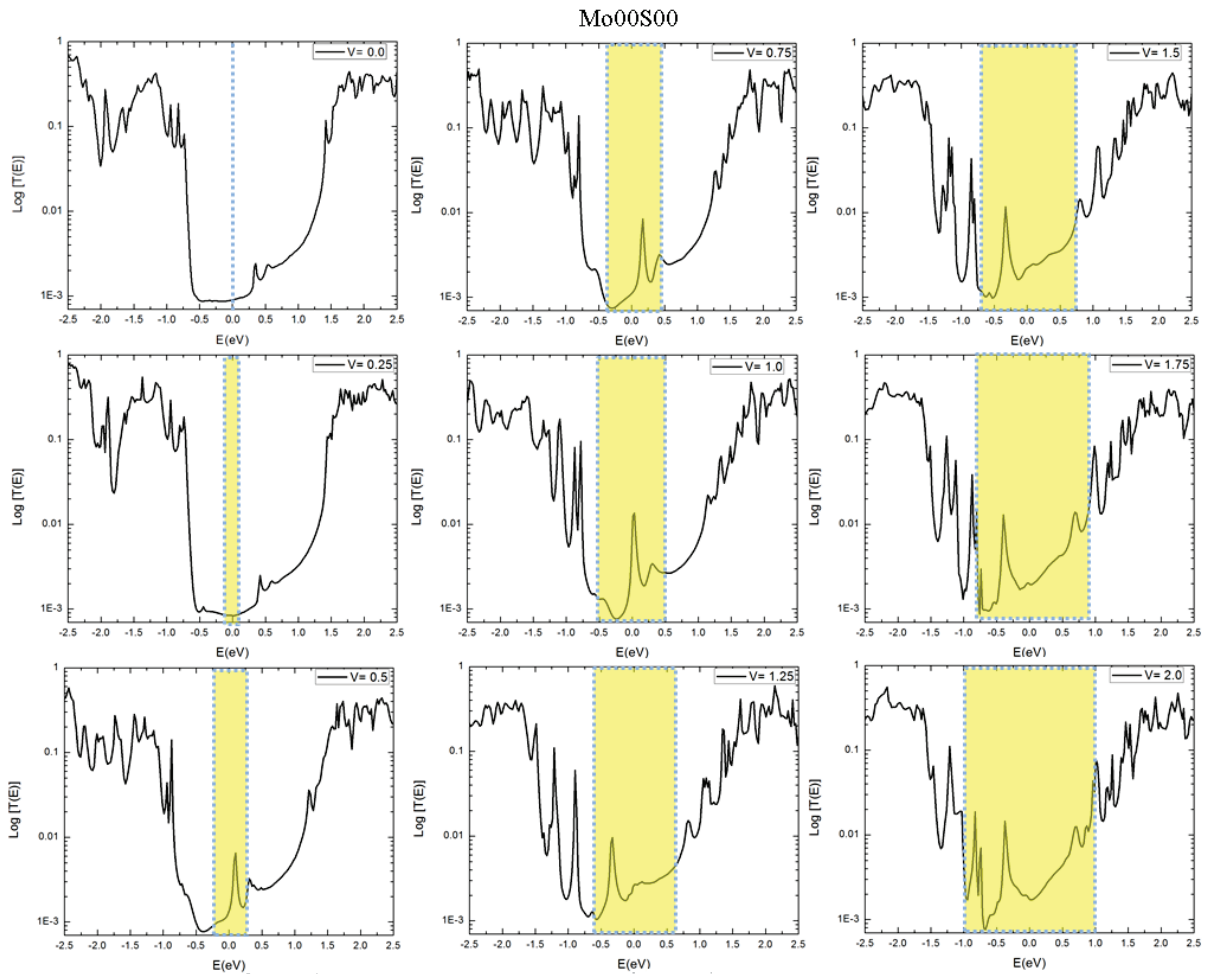


Figure 3-9. Transmission curves in various biases versus energy curve of the various types of Au-Mo-Au junctions.

Given current for each bias, we can summarize the I-V curves related to each sample as shown in Figure 3-10.

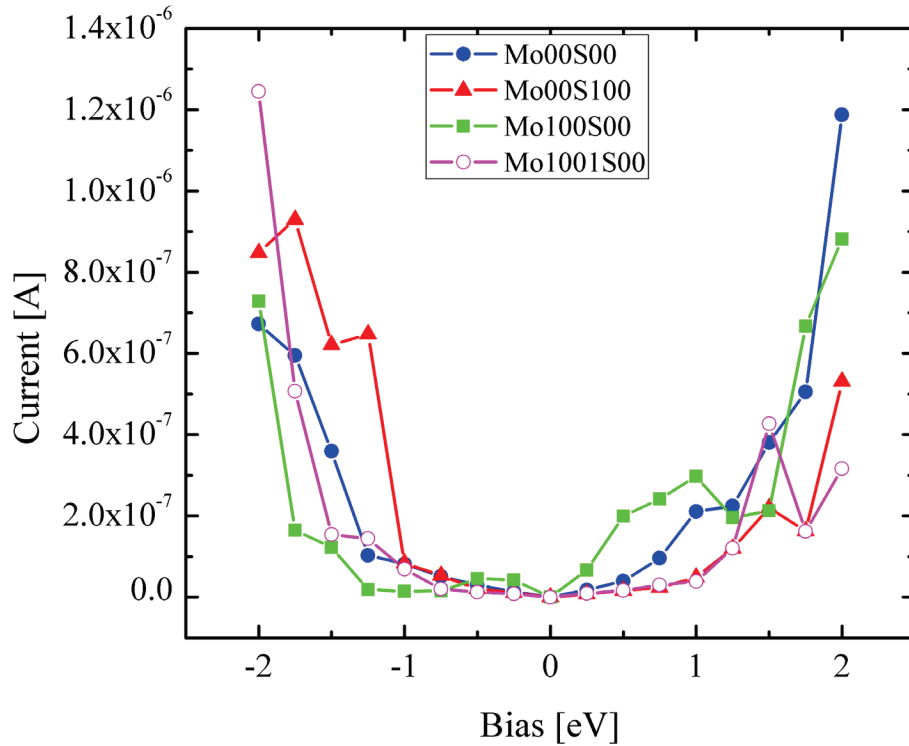


Figure 3-10. I-V curves for various sorts of Au-Mo-Au junctions with different interfaces of Au-MoS<sub>2</sub>.

### 3.5.3 Schottky Barriers

Many modern electronic devices (most notably transistors) rely on a metal/semiconductor contact. The electronic structure at the interface of semiconductor and metal plays a fundamental role in the performance of atomic sized devices. One of the crucial parameters at the interfaces is the height of the Schottky barrier (SBH). SBH is a measure of the voltage barrier to transport the majority carriers at metal-semiconductor junctions.. The principle that leads to SBH is the mismatch in equilibrium of energy between Fermi levels of the metal and the semiconductor leads to bending of the majority carrier band.

When a semiconductor comes into contact with a metal, the wave functions of the two sides interact and new wanefunctions are formed in the immediate neighborhood of the interface.

For convenience, an interface specific region (ISR) can be imagined that serves as a transition region between the metal and the semiconductor. There are two types of SBH, n type and p-type, distinguished by whether the majority carrier is electrons or holes.

An n-type Schottky barrier occurs when the work function of the metal is larger than the work function of the semiconductor ( $\Phi_m > \Phi_S$ ). In this case the Schottky barrier is The difference between the work function of the metal and the conduction band-edge of the semiconductor which is also referred as electron affinity ( $\chi$ ).

In p-type Schottky barrier, the work function of the metal is smaller than that of the semiconductor ( $\Phi_m < \Phi_S$ ). The SBH of a p-type semiconductor is the minimum energy required to sufficiently excite an electron from the semiconductor valance band and to place it across the metal-semiconductor interface at the Fermi level of the metal. In other words, the barrier is the offset of the work function of the metal and valance band edge of the semiconductor. In both cases the extent of the band bending and formation of interface specific region depend on the extent of the charge transfer across the interface.

To calculate the Schottky barriers we used the potential line up method [60] as discussed in the previous section. The electron affinity for MoS<sub>2</sub> and work function of Au are calculated from average Hartree potential of MoS<sub>2</sub> and Au (1x1x16) along Z direction. Band gap of the MoS<sub>2</sub> is calculated from band structure MoS<sub>2</sub>. (see Figure 3-11)

Since the single layer MoS<sub>2</sub> is not transnationally invariant, there are four different edges of MoS<sub>2</sub> with gold. In samples with different sorts of interfaces of MoS<sub>2</sub>-Au used to model and approximate the Schottky barriers S00, Mo00, S100 and Mo100 are respectively presenting.



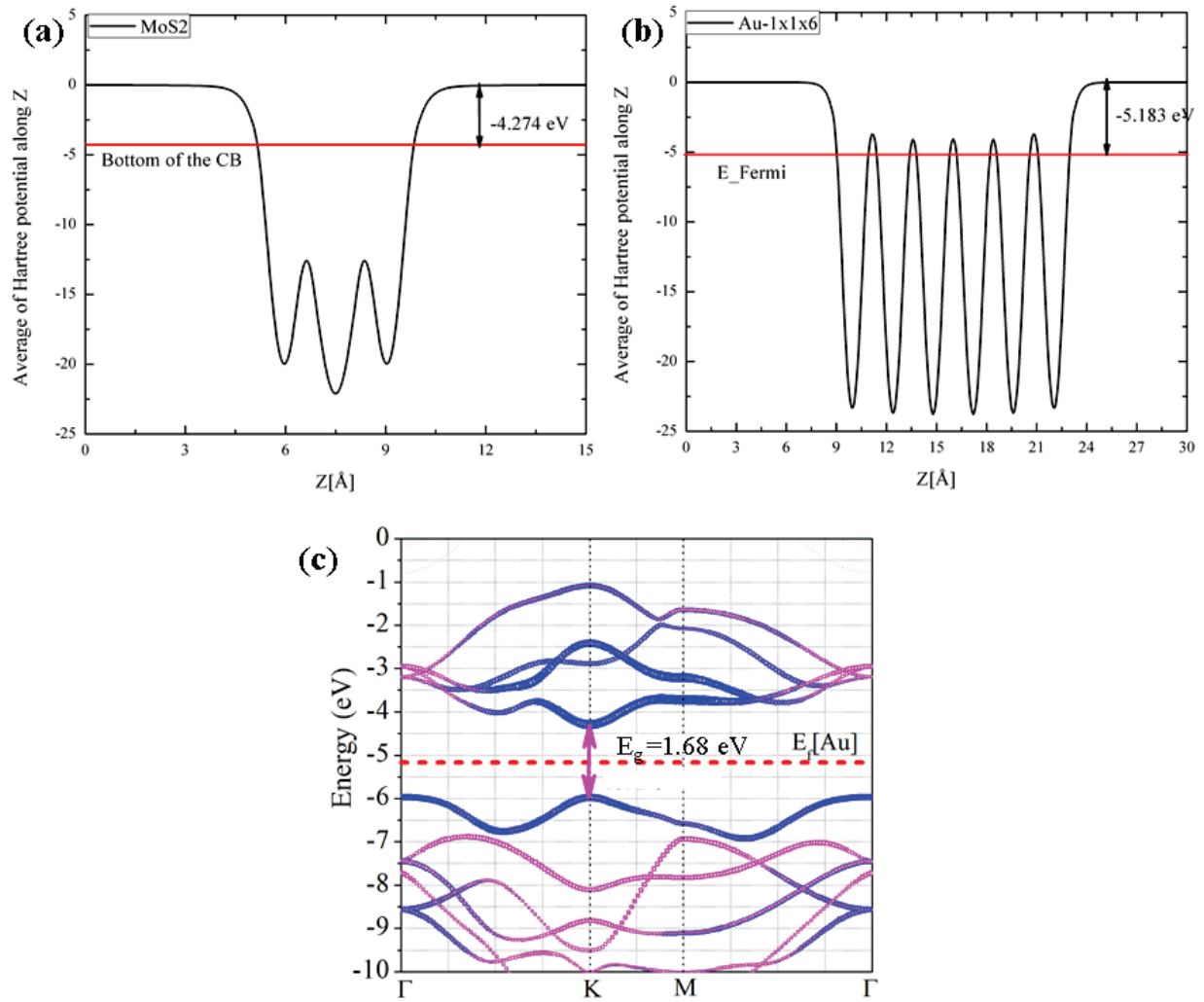


Figure 3-11. Average Hartree potential of (a) MoS<sub>2</sub>, (b) Au (1x1x6) along Z direction (c) Band structure of single-layer MoS<sub>2</sub>.

Schematic illustration of p-type and n-type Schottky barriers of Mo00–Au, Mo100–Au, S00–Au and S100–Au contacts are shown in the.  $\Phi_m$ ,  $E_{FM}$ ,  $\chi_s$ ,  $E_g$ ,  $E_{VAC}$ ,  $\Phi_{SBH}$ ,  $E_C$  and  $E_V$  are metal work function, Fermi level energy of Au, electron affinity, bandgap energy, vacuum level energy, conduction band energy and valance band energies, respectively.

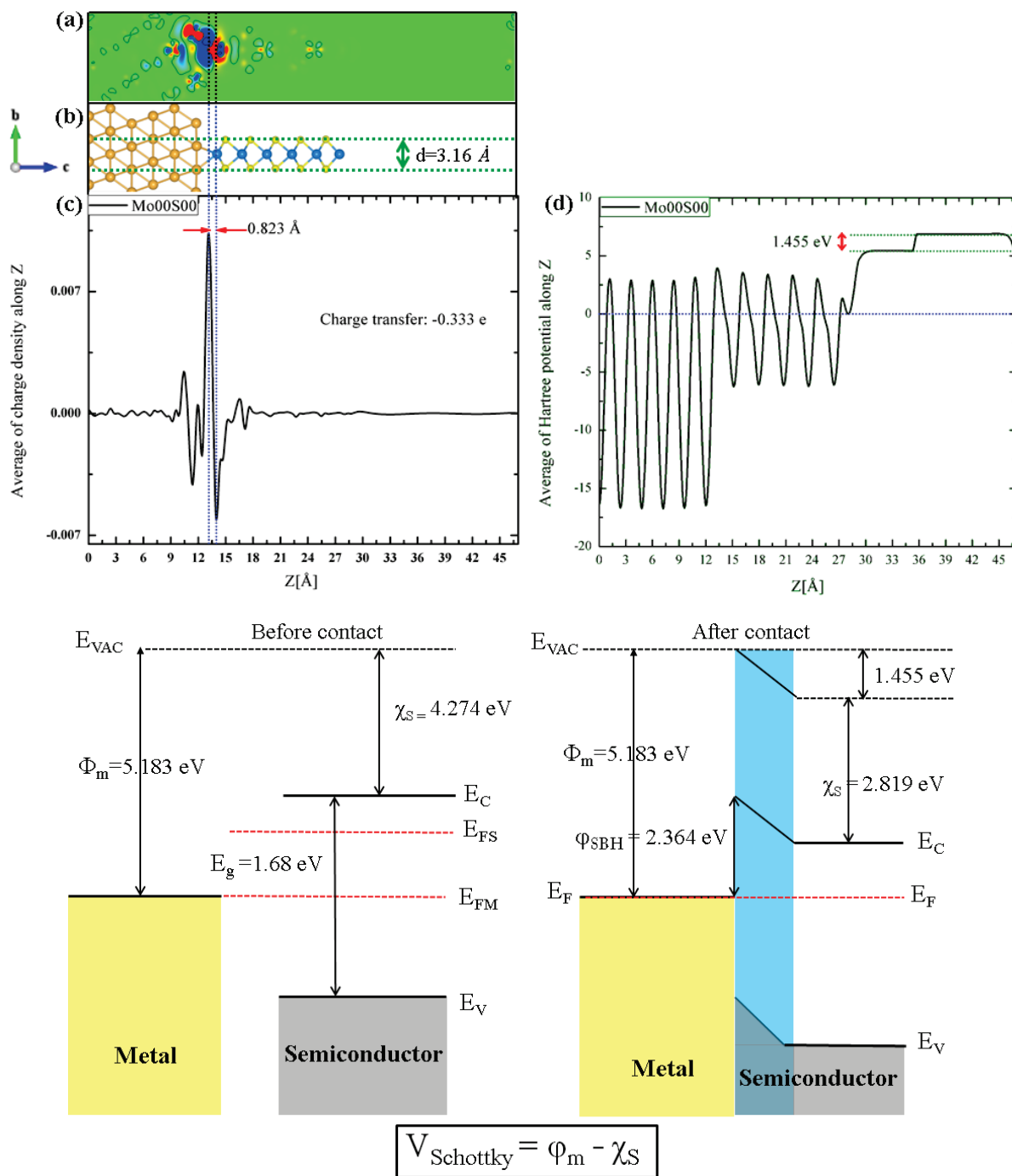


Figure 3-12. P-type Mo00 –Au contact Schottky barrier.

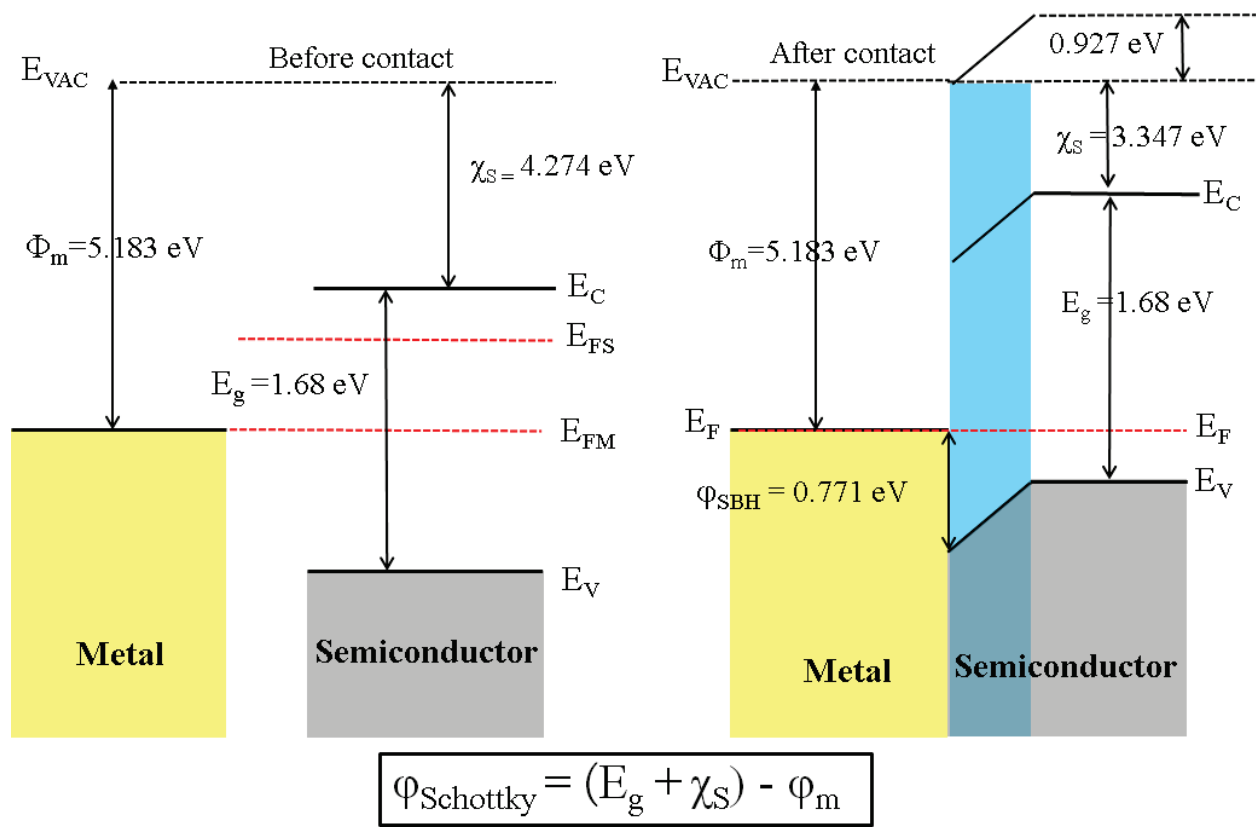
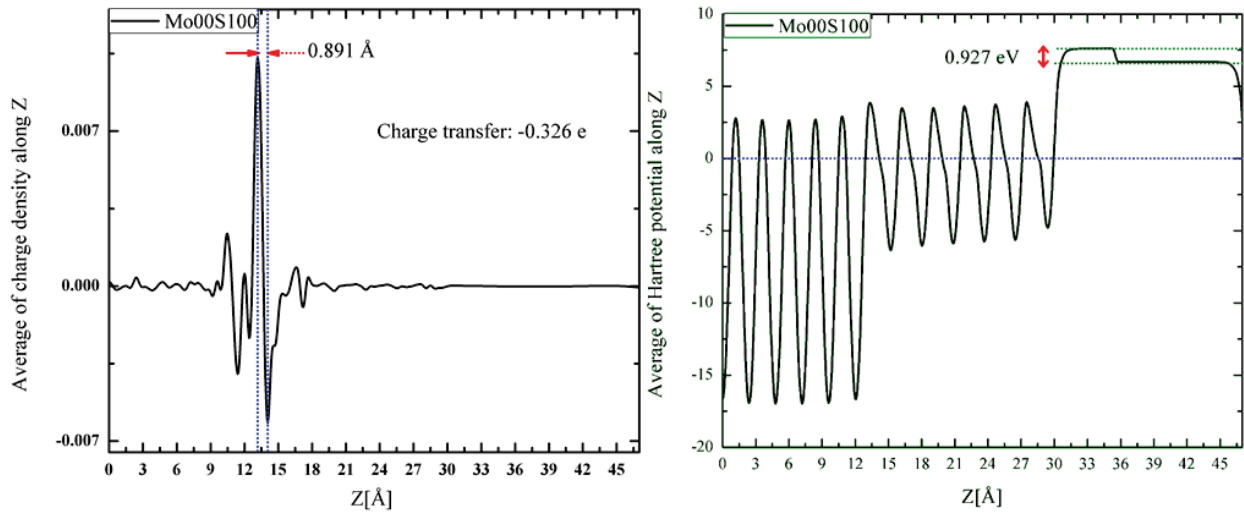


Figure 3-13. P-type Mo00 –Au contact Schottky barrier.

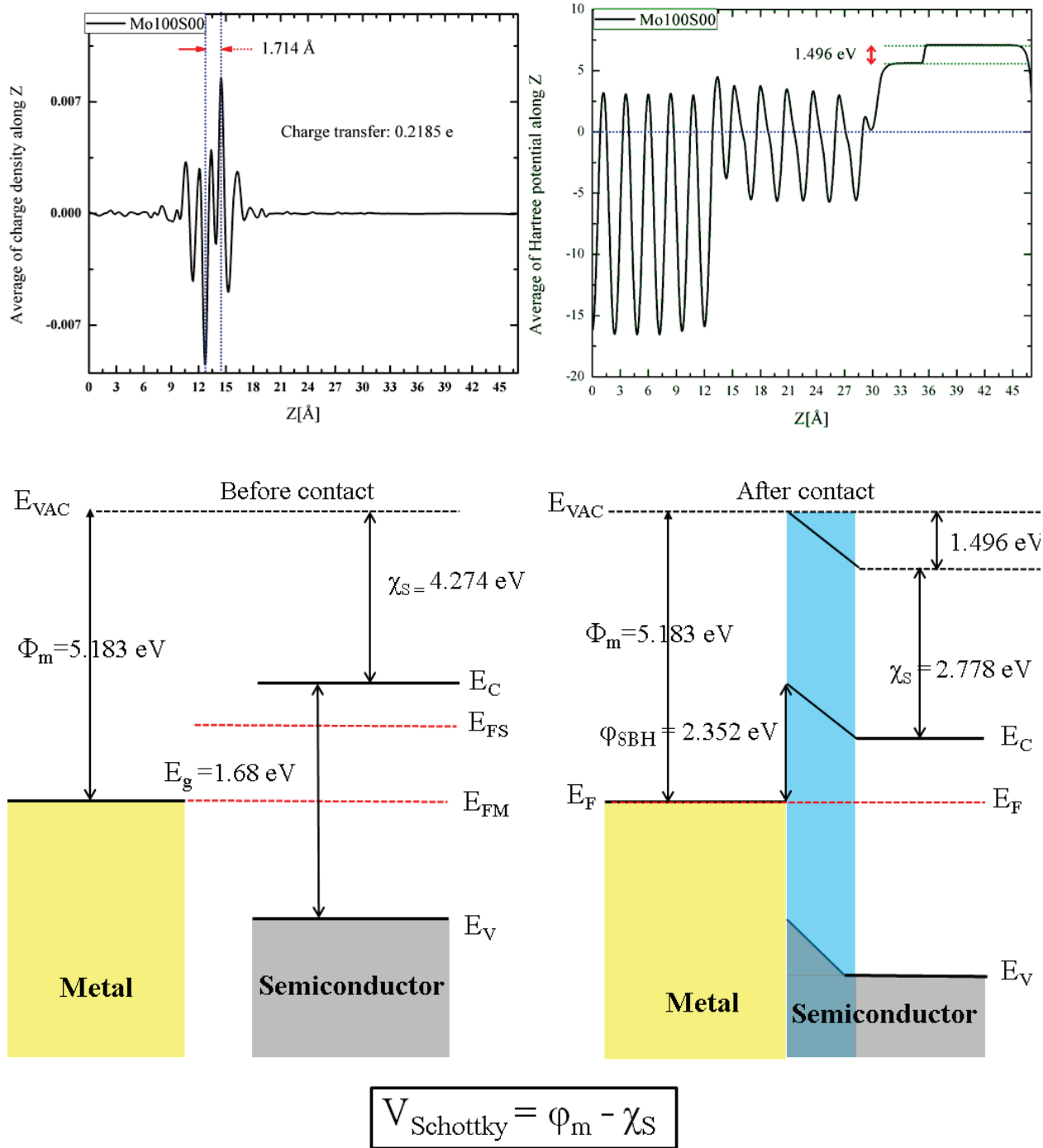
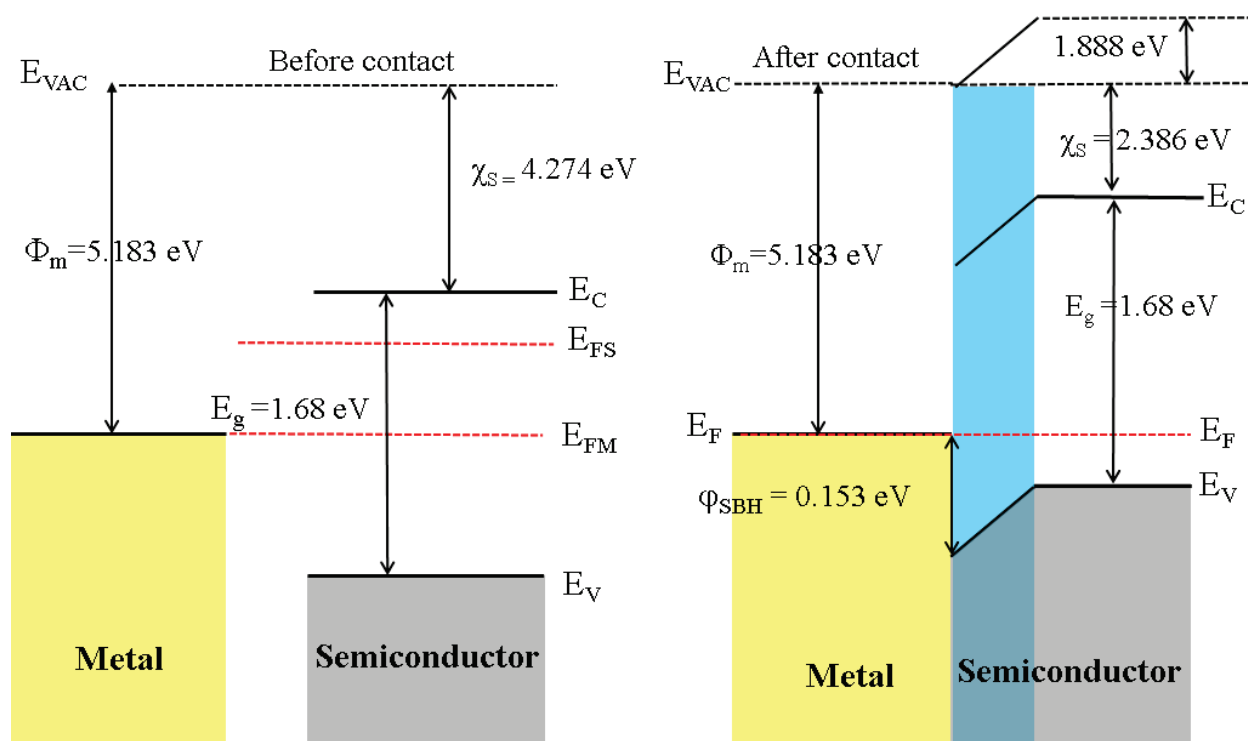
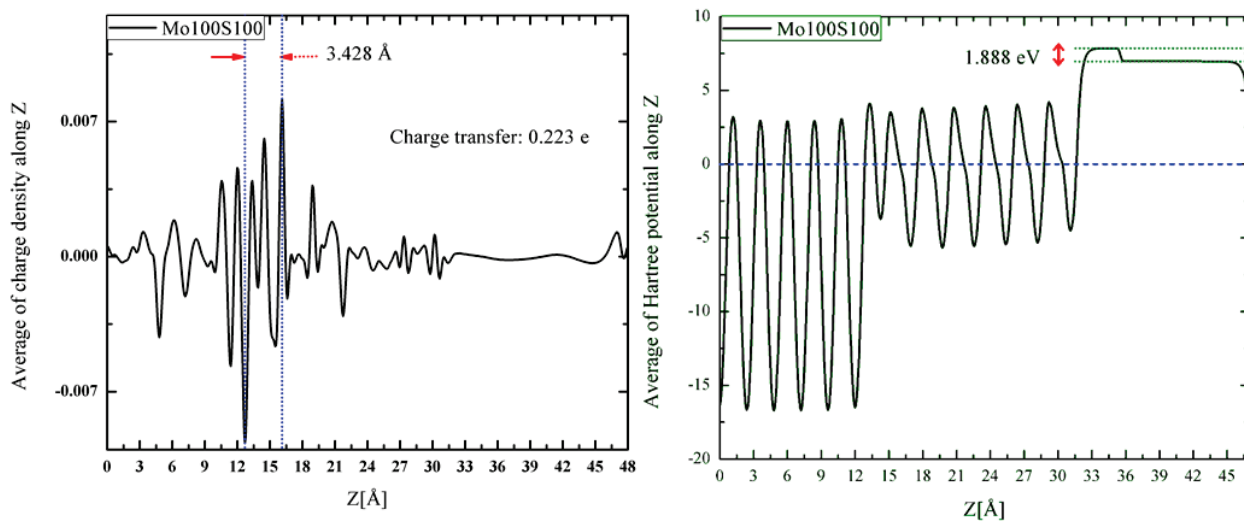


Figure 3-14. P-type S00–Au contact Schottky barrier.



$$\varphi_{\text{Schottky}} = (E_g + \chi_s) - \varphi_m$$

Figure 3-15. N-type Mo100–Au contact Schottky barrier.

### 3.6 *Conclusions*

In summary, we studied the electronic structure of the four types of interface possible between single-layer MoS<sub>2</sub> and Au leads. Electrostatic potentials and the charge redistributions at the interface between the metal and the MoS<sub>2</sub>, differ significantly among the four types, as do the type (n or p) and strength of the calculated Schottky barriers. One type (Mo00S100) exhibits the greatest current. The Schottky barriers related to p-type Mo00, p-type S100, P-type S00 and n-type-Mo100 are equal to 2.364, 0.771, 2.352 and 0.153, respectively. The lowest Schottky barrier belongs to n-type Mo100-Au contact.

## CHAPTER 4. PREDICTIVE MODELING OF FUNCTIONAL MATERIALS

### 4.1 Part I: $\text{MoS}_x$ Square-like Novel Material

#### 4.1.1 Introduction

Recent experiments have successfully synthesized  $\text{MoS}_x$  nanostructures in a controlled manner by depositing Mo adatoms on the S-Cu monolayer that forms on Cu(111) upon sulfur preloading [61]. STM observations have suggested three possible structures for  $\text{MoS}_x$  on Cu(111). All the experiments in this study have been done by our experimentalist collaborators from UC-Riverside [62].

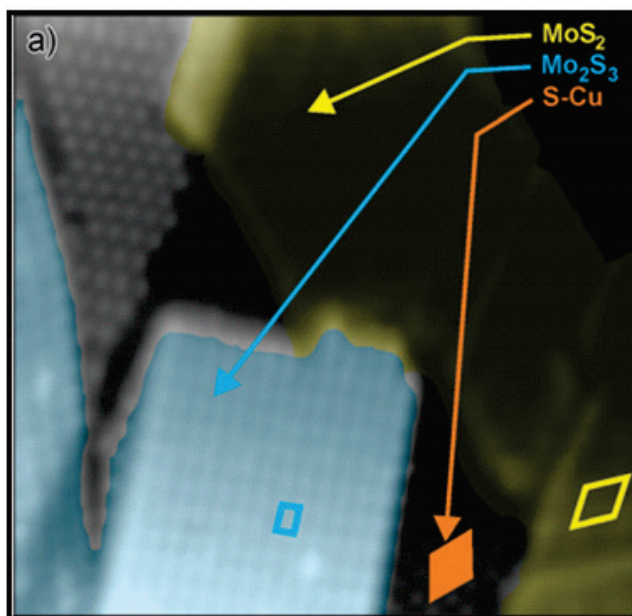


Figure 4-1. STM (Scanning Tunneling Microscope) image of  $\text{MoS}_x$  structures (Imaging parameters: bias: 0.93 V, current: 0.21 nA, scale bar: 5 nm).[Reprinted Figure with permission from “D. Sun, W. Lu, D. Le, Q. Ma, M. Aminpour, M. Alcantara-Ortigoza, S. Bobek, J. Mann, J. Wyrick, T. S. Rahman, and L. Bartels, *Angew. Chem. Int. Ed.* 51, 10284 (2012). Copy right (2012) by the Angewandte Chemie.”]

One of these three possible structures has been identified as MoS<sub>2</sub>. All MoS<sub>2</sub> films and islands were found to align with the crystallographic axes of the substrate, and appear in STM with a characteristic Moiré pattern formed by the epitaxial growth of (4×4) unit cells of MoS<sub>2</sub> on (5×5) atoms of the Cu(111) substrate [61].

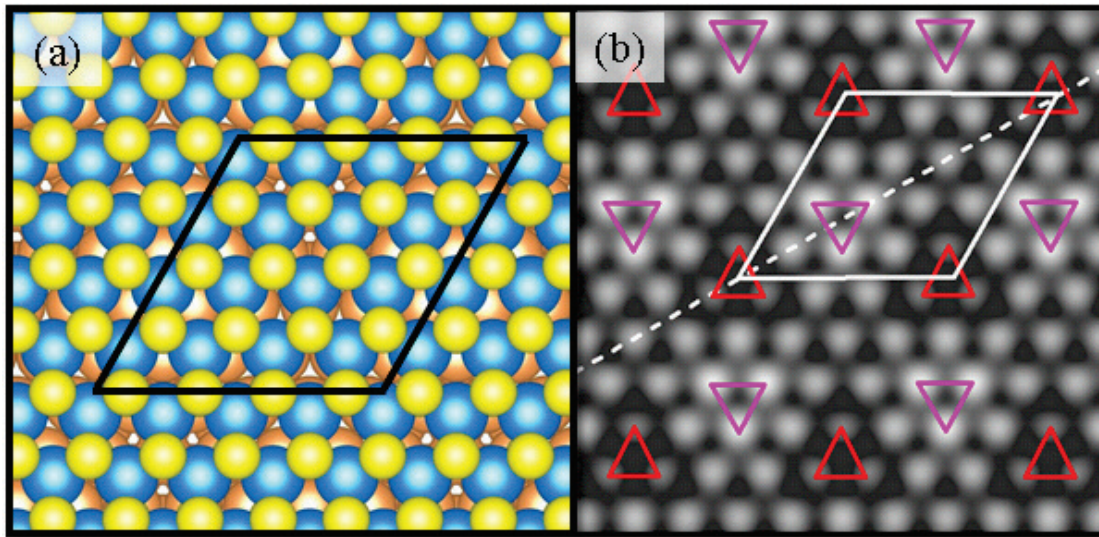


Figure 4-2. Single layer MoS<sub>2</sub>/Cu(111) (a) geometrical structure and (b) simulated STM image corresponding to it. [Reprinted Figure with permission from “D. Le, D. Sun, W. Lu, L. Bartels, and T. S. Rahman, Phys. Rev. B 85, 075429 (2012). Copy right (2012) by the American Physical Society .”]

A different pattern is a novel one that corresponds to well-ordered islands with unit cell with  $\sqrt{7}$  long sides, but at angles of 82° and 98° - or  $\begin{bmatrix} 2 & 1 \\ -2 & 3 \end{bmatrix}$  in vector notation. It provides the closest approximation to a square unit cell achievable with short unit vectors on an fcc(111) surface. It is found that up to 20% of the sample surface is covered by this structure. Scanning Tunneling Spectroscopy (STS) performed on the MoS<sub>2</sub> and MoS<sub>x</sub> novel patterns resulted in fundamentally different (I/V) spectra. MoS<sub>2</sub> has little variation of the tunneling current at negative bias but large variation at positive bias, indicating the MoS<sub>2</sub> conduction band. MoS<sub>x</sub>,



shows little variation of the current at either positive or negative biases, attesting, in agreement to DFT simulations to the absence of band edges near the Fermi level [62].

In our first report [62], after a thorough computational screening of about 50 possible  $\text{MoS}_x$  structures on Cu(111), targeted to find the lowest-energy structure and the one whose calculated STM image most resembled the observed one, we originally found good correspondence of these nearly square patches with the properties of an  $\text{Mo}_2\text{S}_3$  layer [62].

Comparison of DFT-minimized structures cannot directly lead to identification of the observed one, since the structures may have different numbers of atoms in the unit cell. Instead, very precise comparisons need to be made of the subtle features in the calculated and measured STM images. Yet even this latter comparison failed to eliminate all ambiguity: in our search for the lowest-energy structure with the best resemblance to experimental STM observations, we turned up not only  $\text{Mo}_4\text{S}_6$  (=  $\text{Mo}_2\text{S}_3$ ) but also  $\text{Mo}_2\text{S}_5$ , both of which yielded calculated STM images in good agreement with the observed one. Hence in the present study we turn to calculation of the vibrational frequencies of these two candidate geometries. Observation of vibrational modes is a powerful tool in material characterization. Vibrational spectroscopy is a sensitive probe of the atomic structure and of the chemical bonding and thus of the electronic structure.

Such calculations depend on what is taken to be the structure of the S-Cu monolayer on which the Mo atoms are deposited. The effect of S poisoning of transition metal surfaces has long been of special interest in studies of catalysis.

The earliest demonstration that deposition of S on Cu results is a compound  $\sqrt{7} \times \sqrt{7}$  R19° S-Cu monolayer emerged (1986) from Domange and Oudar's [63] LEED (Low-Energy

Electron Diffraction) experiments. Subsequently, a number of experimental techniques have been brought to bear in an attempt to pin down precisely the exact number and location of the two species of atoms in this monolayer: These range from surface extended X-ray absorption fine structure (SEXAFS) and normal incidence X-ray standing waves (NIXSW) [64], registered through STM [65, 66], to XPS (X-ray Photoelectron Spectroscopy) and AES (Auger Electron Spectroscopy) [67]. The most quantitatively precise proposal resulting from these studies was that of Prince in 1990 [64]. Another model is proposed by Foss *et al.* (1997) [68]. In (1999), Saidy *et al.* [69] rejected the Foss Model in favor of a modified version of Prince's.

For reasons explained in section 4.1.3, we base our investigations of the vibrational frequencies of the two models for of the novel MoS<sub>x</sub> pattern on the assumption that the S-Cu film on which it forms accords with Prince's model.

#### 4.1.2 Computational Details

We use Density-functional-theory (DFT) in VASP (Vienna *Ab-initio* Simulation Package) code to relax the structures [59]. We use the Projector-Augmented-Wave (PAW) method [70-72] pseudo-potentials with the opB88-vdW version of the exchange functional and the non-local correlation functional developed by Dion *et al.* [73, 74]. We use the Román-Pérez and Soler algorithm [75] to speed up the calculation of the non-local correlation energy. We expand the electronic wave functions in a plane-wave basis set with the kinetic energy cut-off at 680 eV and the kinetic energy for augmentation of charges at 10000 eV. For the integrations inside the BZ, we sample the space according to the Monkhorst-Pack scheme [76], with a uniform grid of k-points of dimensions 6x6x1 for our 4x4 surface. The integrations over the zone use the Gaussian broadening technique for the level occupation with a smearing parameter of

0.15 eV. We converge the total energy of any ionic configuration to  $3 \times 10^{-6}$  eV, and relax the systems by minimizing the forces on the atoms to 0.003 eV/Å. In all calculations, we model the Cu(111) substrate with a 6-layer slab separated from its periodic images by  $\sim 20$  Å. We perform phonon calculations using the small displacement method [77] with a finite atomic displacement of  $\pm 0.01$  Å as implemented in the PHONOPY code [78]. In turn, these displacements induce Hellmann-Feynman forces. From the forces as a function of displacement, we construct the dynamical matrix. Eigenvectors and eigenvalues (frequencies of the modes) are evaluated by diagonalization of this matrix. Our results provide the vibronic fingerprints that will enable experiment to identify the structure. We deposit DFT-derived simulated topography as an isosurface of energy-integrated (from  $-1.0$  to  $0$  eV) local density of states of  $10^{-4}$  eÅ<sup>-3</sup> convoluted with a tip radius of 2.4 Å.

#### 4.1.3 An MoS<sub>x</sub> Structure with High Affinity for Adsorbate Interaction

To get insight into the interaction of the surface of the novel MoS<sub>x</sub> patterns with the adsorbates, Anthraquinone (AQ) is exposed as a test adsorbate on the samples [62]. AQ is a large and rigid molecule so the adsorption geometry of which can be imaged easily. We were expecting that the AQ would adsorb on MoS<sub>2</sub> patterns because of the existence of their brim edges but ended up observing that it adsorbs exclusively at the MoS<sub>x</sub> new patterns. Initially AQ forms molecular rows at intermolecular distances of  $\sqrt{7}$ , quite similar to AQ rows on Cu(111), for which the presence of non-negligible intermolecular hydrogen bonds is found. Further increasing the dosage of AQ molecules, first an exclusive increase in the coverage of MoS<sub>x</sub> is observed until a dense layer of AQ molecules adsorbed parallel to the substrate (see Figure 4-3(a)). As coverage further increases, the AQ molecules continue to avoid the sulfur-terminated substrate as well as

MoS<sub>2</sub> structures. As a result, a denser packing of AQ layer on MoS<sub>x</sub> forms in the upright configuration (see Figure 4-3 (b)). Using DFT calculation, we find the binding energy to be 3.36 eV and 1.92 eV in the planner and upright configurations, respectively. It is observed that AQ molecules populate the MoS<sub>2</sub> structures (see Figure 4-3(d)) and their brim areas after they attach to the sulfur-terminated copper surfaces (Figure 4-3(c)) [62]. Our calculations also show that the binding energy of AQ on sulfur-terminated Cu (1.47 eV) is lower than that of the Mo<sub>2</sub>S<sub>3</sub> structure even in the upright configuration. AQ preferentially forms an array of molecular rows, which are almost always in anti-phase with adjacent rows, though occasionally in-phase lateral stacking of rows is also observed. The spacing of AQ molecules (at 6.75 Å center to center) is very tight, thus enabling intermolecular hydrogen bonding. Since the periodicity of the AQ layer on MoS<sub>2</sub> is incommensurate with the Moiré pattern of the (4x4) MoS<sub>2</sub> layer on (5x5) Cu(111) layers, we calculated the adsorption energy (1.32 eV) by modeling an isolated molecule on MoS<sub>2</sub>/Cu slab (1.20 eV) and adding to that the lateral AQ-AQ interactions calculated on a MoS<sub>2</sub> monolayer (0.12 eV). The sequence of the DFT adsorption energies is in agreement with the relative preference for AQ adsorption on the three different surface structures that we report here.

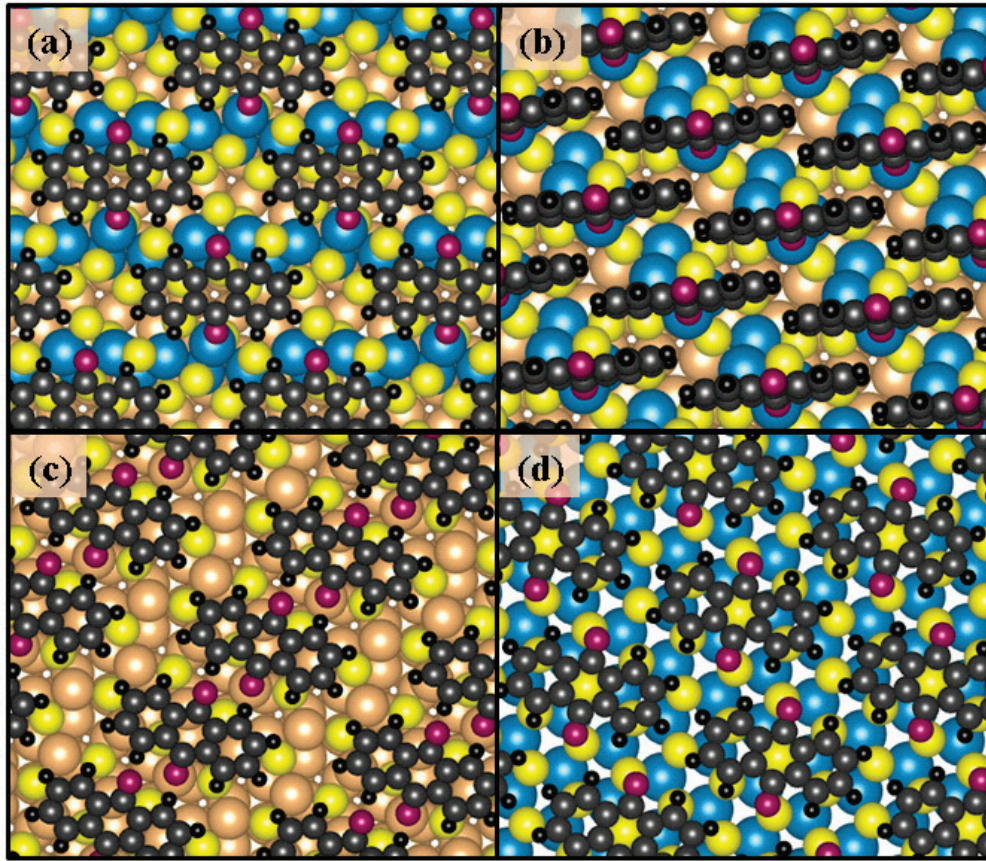


Figure 4-3. DFT-optimized adsorption geometry of AQ on (a)  $\text{Mo}_2\text{S}_3$  horizontal (BE= 3.36 eV), (b)  $\text{Mo}_2\text{S}_3$  vertical (BE= 1.92 eV), (c) Prince Model (BE= 1.47) and (d)  $\text{MoS}_2$  (BE= 1.32 eV) adsorption configurations, respectively.

#### 4.1.4 Geometrical and Vibrational Properties of S-Cu/Cu(111) Models

Deposition of S on Cu(111) results in a compound of  $\sqrt{7} \times \sqrt{7}$  R19° S-Cu monolayer on Cu(111) substrate. As discussed in 4.1.1 section, three different Models have been proposed as Prince (1990), Foss (1997) and Saidy (1999) (See Figure 4-4(a)). In Prince Model [64], in each unit cell, three S atoms bind directly to the substrate (one on an fcc, one on an hcp, and one on a top site) and the three Cu atoms lie above the top-S atom in the three hollow sites surrounding it. According to the Prince Model, the nearest neighbor S-Cu DFT calculated distances after

relaxation shows that S-fcc, S-hcp and S-top atoms remains on their positions while the three Cu atoms move slightly away from hollow sites around S-atom toward the bridge sites [79].

In the Foss Model [68] each unit cell contains 3 S and 4 Cu atoms: The first two S atoms are located on fcc and hcp sites. The other S atom is on a square-like  $\text{Cu}_4$  fragment centered in turn on the top site of the substrate. In the original paper the exact locations of the four Cu atoms in the  $\text{Cu}_4\text{S}$  fragment were not specified. In 2012, Alfonso [79] used DFT calculations to demonstrate that an energetically minimum  $\text{Cu}_4\text{S}$  in the Foss model comprises a pair of Cu atoms on two opposite sites, and the other pair on the two second-nearest-neighbor sites, forming a square-like  $\text{Cu}_4$  fragment, atop of which the S atom sits.

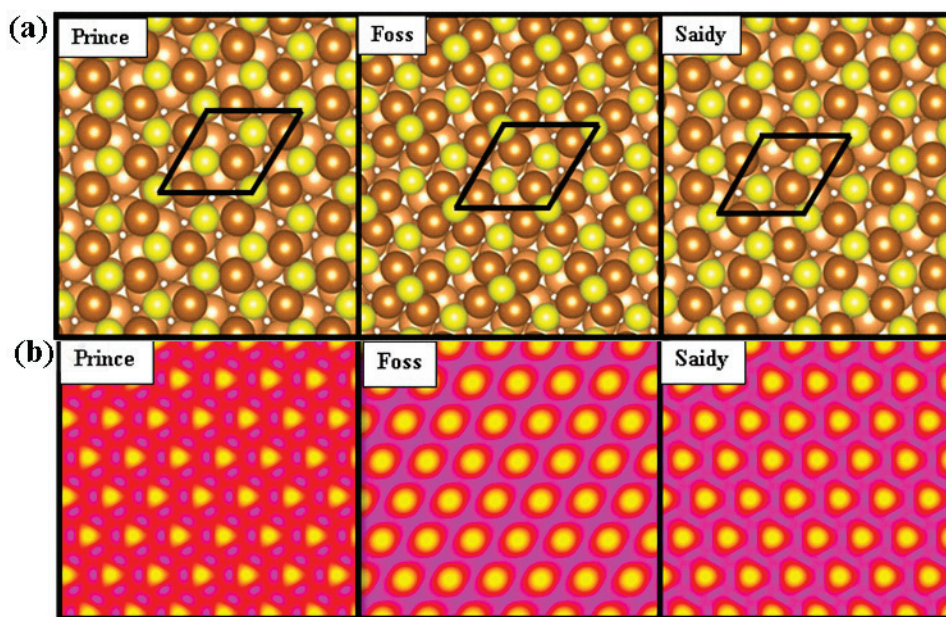


Figure 4-4. (a) Cu-S overlayer models of Domange and Oudar, Foss and Saily. yellow: sulfur, light brown: Cu atoms, dark brown: surface Cu atoms (b) STM images of Prince, Foss and Saily models. (Occupied states, LDOS: -1 to 0.0 eV, Isovalue:  $10^{-5}$  e/A.)

The DFT-based simulated STM (See (b)) of all three models are in good agreement with experiment. Saidy Model [69] posits the same number of S and Cu adsorbate atoms in the unit cell as Prince Model. Both models contain 3 Cu and 3 S atoms, with two of the S atoms upon an fcc and an hcp site, respectively. But Saidy places the remaining S atom not upon a Cu top atom but upon a vacancy generated by removing that Cu-top atom from the substrate (which ends up with fewer Cu atoms than the substrate in the Prince model).

Using DFT calculations, we relaxed three candidates for S-Cu/Cu(111) Models. Among the three, Saidy turned out not to be stable. As a result, we leave it aside in our predictive modeling process. Here, relying on the calculated phonon-frequencies and eigenvectors of the remaining two models (Foss and Prince), we use the finite-displacement method to expose the vibronic fingerprints that will enable experiment to decide between them. The phonon density-of-states curve will provide the instability energy associated with a particular phonon mode. The instabilities are manifested as phonons with negative  $\omega^2$ . Since we do not have any negative frequencies in our phonon density of states, we can infer that both the models are stable.

Our DFT calculations of the vibrational spectra at the surface Brillouin zone center (G) for some of the proposed hexagonal sulfur terminations of Cu(111) confirm that both the structure reported by Prince [63] and the Cu<sub>4</sub>-based structure studied by Foss *et al.* [68] are dynamically stable. Although the phonon densities of states at G show structure-distinctive frequencies, the differences between the two spectra are too subtle to determine an energetic difference.



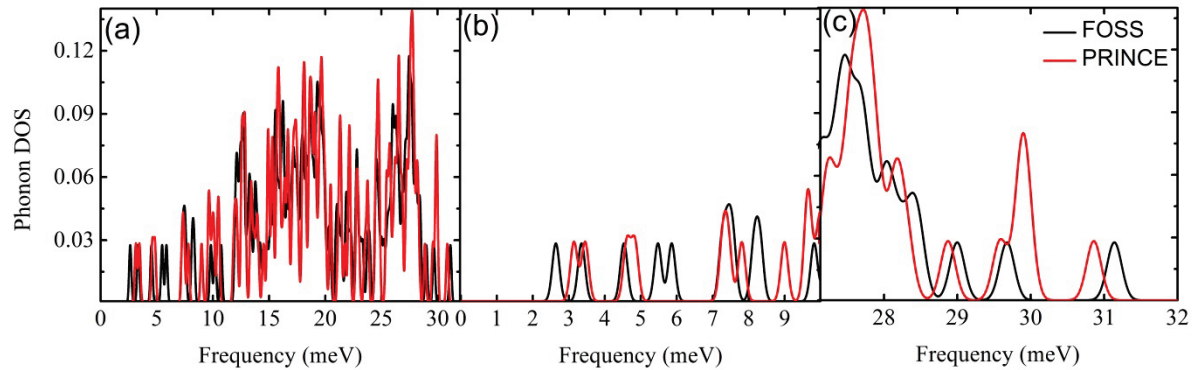


Figure 4-5. Phonon density of state curves of the Foss and Prince models (a) all range (0 to 35 meV), (b) low frequencies (1 to 10 meV) and (c) high frequencies (27 to 32 meV).

In the following, since both all experimental and theoretical work so far supports so far Prince's model, we take the structure proposed by Prince as our initial base for depositing Mo and S atoms.

#### 4.1.5 Geometrical and Vibrational Properties of the $\text{Mo}_2\text{S}_3/\text{Cu}(111)$ and $\text{Mo}_2\text{S}_5/\text{Cu}(111)$ Models

After a thorough and careful computational screening of many possible  $\text{MoS}_x$  structures by adding Mo and S on the surface of the Prince structure, targeting to find the lowest-energy structure and the one whose calculated STM image most resembles the observed one, we end up with two candidate models as  $\text{Mo}_2\text{S}_3$  and  $\text{Mo}_2\text{S}_5$ . The geometrical properties for  $\text{Mo}_2\text{S}_3$  and  $\text{Mo}_2\text{S}_5$  can be summarized as follows:  $\sqrt{7}$  long sides, at angles of  $82^\circ$  and  $98^\circ$  - or  $\begin{bmatrix} 2 & 1 \\ -2 & 3 \end{bmatrix}$  in vector notation. The unit-cell for  $\text{Mo}_2\text{S}_3$  contains four molybdenum atoms and six sulfur atoms and the unit cell for  $\text{Mo}_2\text{S}_5$  contains two Molybdenum atoms and five sulfur atoms.



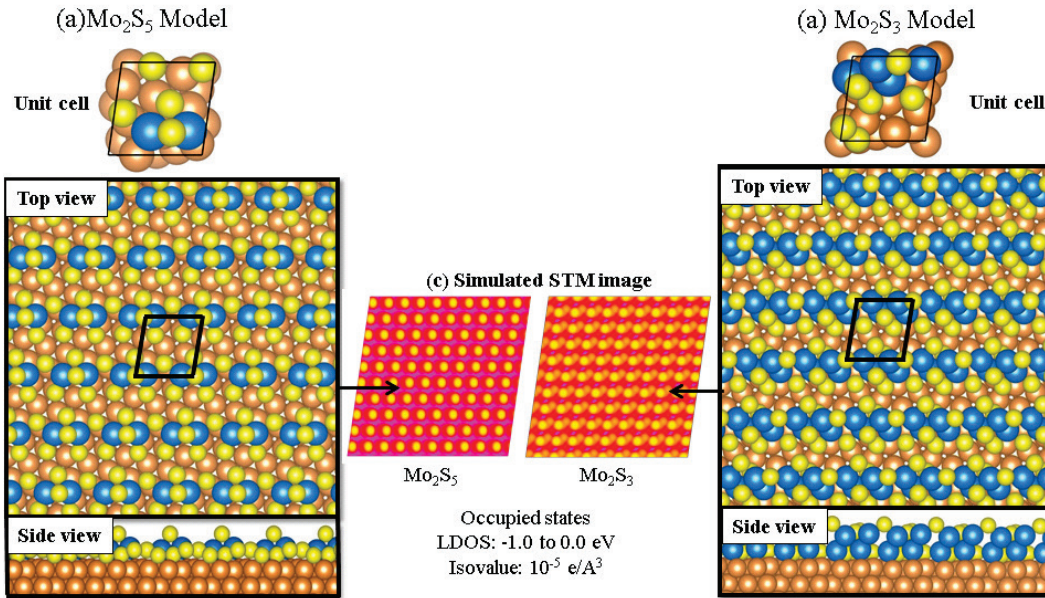


Figure 4-6. Top and side view of (a) Mo<sub>2</sub>S<sub>5</sub> and (b) Mo<sub>2</sub>S<sub>3</sub> models.

Theoretical calculation of vibrational mode frequencies and intensities from first principles is very helpful in finding the stable structure and the fingerprint frequencies required for identification by experiment. Since both of the model structures (Mo<sub>2</sub>S<sub>3</sub> and Mo<sub>2</sub>S<sub>5</sub>) are dynamically stable, each passes the first condition to be chosen as the model candidate for MoS<sub>x</sub> Structure. Most frequently used experimental techniques to calculate phonon density of states are: (1) neutron scattering, which though technically is difficult, can display the entire dispersion is observable, (2) infrared (IR) spectroscopy which though in comparison to the first method, makes only some modes observable. (3) Raman spectroscopy, though likewise comparatively simple method, can reveal only a different subset of modes. Raman spectroscopy is often considered to be complementary to IR spectroscopy. For symmetrical molecules with a center of inversion, Raman and IR are mutually exclusive. In other words, bonds that are IR-active will not be Raman-active and vice versa. Other molecules may have bonds that are either Raman-active or IR-active, or neither or both. Raman scattering occurs in two ways. If the emitted

radiation is of lower frequency than the incident radiation, then it is called Stokes scattering. If it is of higher frequency, then it is called anti-Stokes scattering. In IR scattering, most often the emitted radiation is of the same frequency as the incident light. Two features ( $\nu=45.460$  meV,  $\nu=56.821$  meV) of  $\text{Mo}_2\text{S}_5$  structure distinguishable with either Raman or IR spectroscopy to decide which structure is the real one.

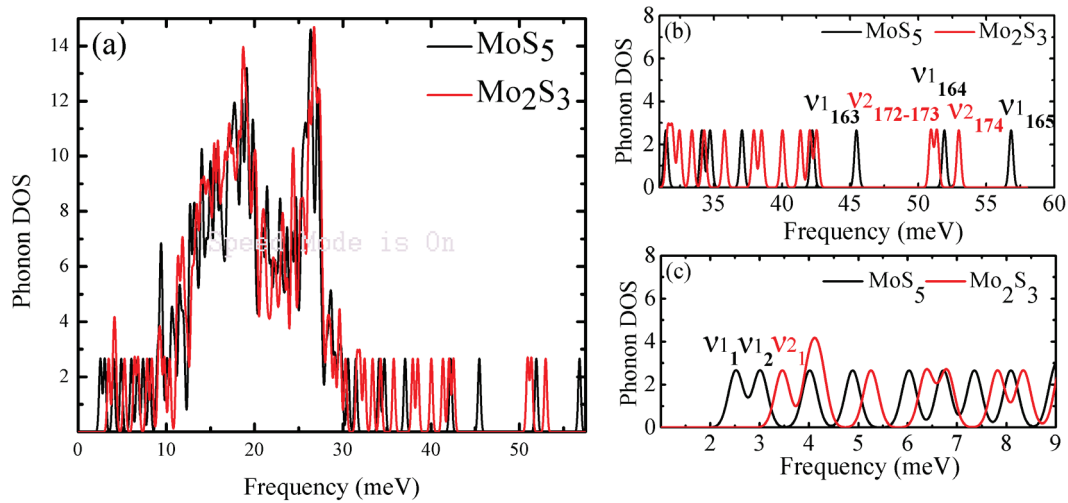


Figure 4-7. Phonon density of states (meV) of  $\text{Mo}_2\text{S}_5$  and  $\text{Mo}_2\text{S}_3$  samples (a) full frequencies (b) high frequencies (c) low frequencies

#### 4.1.6 Discussions and Conclusions

Recent experiments have successfully synthesized  $\text{MoS}_x$  nanostructures in a controlled manner by evaporating Mo adatoms on the copper sulfide monolayer that forms on Cu(111) upon sulfur preloading. Based on STM observations and DFT total-energy calculations, including *ab-initio* van-der-Waals interactions, several structures for  $\text{MoS}_x/\text{Cu}(111)$  have been proposed. In this study, we investigate the plausibility of those structures and provide elements for further experimental substantiation or refutation. In particular, we perform density-

functional-theory calculations of the total energy and the vibrational spectrum of the proposed structure to (1) test their dynamical stability, (2) compare their thermodynamic stability as obtained from their total free energy, and (3) provide the vibrational frequencies that uniquely fingerprint the proposed structures. Since both of the model structures ( $\text{Mo}_2\text{S}_3$  and  $\text{Mo}_2\text{S}_5$ ) are dynamically stable, at least at Gamma, the calculated dynamical stability cannot discern or favor one structure or the other.  $\text{Mo}_2\text{S}_3$  has several high-frequency features while  $\text{Mo}_2\text{S}_5$  quite clearly distinguishable frequencies, well separated. The feature of  $\text{Mo}_2\text{S}_3$  structure could suffice to clarify which is the real structure.

## 4.2 Part II: $\text{Mo}_6\text{S}_6$ Nanowire

### 4.2.1 Introduction

Molybdenum-sulfide compounds have recently attracted considerable attention for a broad range of applications as we discussed in Chapter 1. As is the case with carbon, compounds of molybdenum and sulfur may assume a number of nanoscale forms such as nanotubes [80], nanorods [81] and nanoparticles [82, 83]. Here we describe the formation of one-dimensional (1D)  $\text{Mo}_6\text{S}_6$  nanowires, which may serve as a building block for nanoelectronic devices [84, 85]. The  $\text{Mo}_6\text{S}_6$  nanowires assembled by  $60^\circ$ -rotated AB stacking of  $\text{Mo}_3\text{S}_3$  building blocks that consist of a triangle of Mo atoms decorated with three sulfur atoms at the outside sides (Figure 4-8a, b).

Recently, Kibsgaard and coworkers [86] have grown molybdenum-sulfur nanowire bundles on highly ordered pyrolytic graphite (HOPG); they suggest that their bundles consist of several  $\text{Mo}_6\text{S}_6$  units side by side. The wires were found to grow in a disordered fashion: substrate interactions appear to be insufficiently strong to align them with the HOPG crystallographic

directions. Here we show theoretically, with the support from our experimentalist collaborators, that the use of a more interactive substrate, Cu(111), permits the growth of molybdenum sulfide nanowires that consist of a single stack of Mo<sub>6</sub>S<sub>6</sub> units only and that are aligned with the substrate directions. Moreover, we find a preferred spacing between adjacent Mo<sub>6</sub>S<sub>6</sub> wires, slightly larger than their van-der-Waals (vdW) separation in the gas phase, highlighting the importance of substrate interactions and suggesting the latter's ability to both align and space the wires evenly.

#### 4.2.2 Methods

Density functional theory (DFT) simulations are carried out using the projector-augmented (PAW) method [87] and a plane-wave basis set which are implemented in the VASP [59]. In order to take into account vdW interactions, which are expected to play an important role in the attraction between Mo<sub>6</sub>S<sub>6</sub> nanowires, we use the optB88-vdW version [74] of the van der Waals density functional (vdW-DF) [88, 89] to describe the exchange-correlation interaction of the electrons, as implemented in the code of Ref. [90]. The Román-Pérez and Soler algorithm [75] is used for speeding up the evaluation of the non-local energy. The pseudo-potentials are generated using the Perdew-Burke-Ernzerhof (PBE) functional [22] for which 11, 6, and 6 valence electrons are treated explicitly for Cu, Mo, and S, respectively. Tests show that extending the pseudo-potentials to include semicore electrons does not affect the results significantly. We set the cutoff energy for the plane-wave expansion at 500 eV.

For simulating Mo<sub>6</sub>S<sub>6</sub> on Cu(111), we use supercells consisting of a 5-layer Cu(111) slab in a  $\begin{pmatrix} n & n \\ -1 & 1 \end{pmatrix}$  geometry based on the vectors  $\vec{a}_1$  and  $\vec{a}_2$ , as shown in Figure 4-8(c): the 1<sup>st</sup> and 2<sup>nd</sup>

translational vectors are  $n\bar{a}_1 + n\bar{a}_2$  and  $-\bar{a}_1 + \bar{a}_2$ , respectively. Depending on the nanowire property in question, the supercells contain one or two adjacent  $\text{Mo}_6\text{S}_6$  wires and a vacuum of 20 Å. The Brillouin zone is sampled with a  $k \times 13 \times 1$  mesh, where  $k$  is 7, 5, and 1 for  $n$  equal to 3, 4, and greater than 6, respectively. During structural relaxations the bottom two Cu layers are held fixed and the calculation terminates when all force-components acting on each free ion are smaller than 0.01 eV/Å. The binding energy of a  $\text{Mo}_6\text{S}_6$  unit on Cu(111) is calculated as the difference between the total energy of the  $\text{Mo}_6\text{S}_6/\text{Cu}(111)$  system and the sum of the total energies of a Cu(111) slab and of a  $\text{Mo}_6\text{S}_6$  wire which is separated from its periodical images by a distance of 15 Å. We simulate STM topologies as the  $10^{-5}$  e/Å<sup>3</sup> iso-surface of local density of states integrated from -1.0 eV to the Fermi level. All experiments proceeded in a UHV (Ultra-High Vacuum) chamber housing a variable temperature STM setup. The details for the experiments are discussed in [91].

#### 4.2.3 Results and Discussions

Figure 4-8(a) and (b) show the top and cross-sectional views of the minimal molybdenum-sulfur nanowire that we found to be stable: it consists of Mo-trimers stacked on top of each other at 60° rotation. Each trimer is decorated on the outside with 3 sulfur atoms for a total stoichiometry of  $\text{Mo}_6\text{S}_6$  (for a pair of  $\text{Mo}_3\text{S}_3$  subunits at 60° angle). Figure 4-8(c) shows a Cu(111) surface with its basis vectors ( $\bar{a}_1$  and  $\bar{a}_2$ ) indicated. Our DFT calculations result in an optimal Cu interatomic spacing of (denote D) of 2.564 Å, in excellent agreement with the experimental lattice parameter of bulk Cu [92]. The direction vertical in Figure 4-8(c) has a periodicity  $\sqrt{3}$  D, very close to the axial periodicity of  $\text{Mo}_6\text{S}_6$  nanowires (at a calculated

mismatch of  $\sim 2\%$ ), suggesting that  $\text{Mo}_6\text{S}_6$  nanowires may grow epitaxially along this direction on  $\text{Cu}(111)$ .

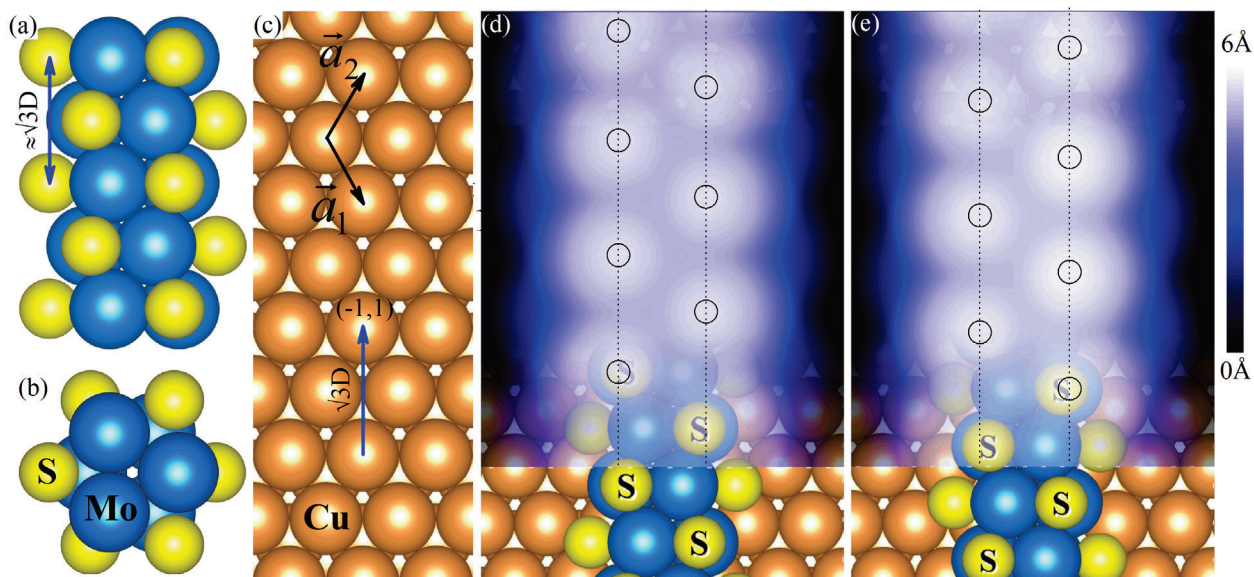


Figure 4-8. Atomic model of  $\text{Mo}_6\text{S}_6$  nanowires (a,b) and the  $\text{Cu}(111)$  surface (c). Panels (d) and (e) show models of two potential configurations of  $\text{Mo}_6\text{S}_6$  nanowires on  $\text{Cu}(111)$ , a symmetric one (d) and an asymmetric one (e). We superimpose simulated STM images, in which we mark the maxima with black circles. While in (d) both maxima have the same height, in (e) the ones on the right are more prominent than those on the left.

We modeled  $\text{Mo}_6\text{S}_6$  nanowires on a  $\begin{pmatrix} 6 & 6 \\ -1 & 1 \end{pmatrix}$   $\text{Cu}(111)$  super cell. The distance between the wires and their periodic images is  $6D$ , which is sufficiently large to suppress direct lateral interactions between them (*vide infra*). The results of structural relaxations indicate two potentially viable configurations: (Figure 4-8(d)) a symmetric one in which the “S legs” adsorb close to bridge sites and (Figure 4-8(e)) an asymmetric one in which half of the “S legs” adsorb close to hollow sites, while the other half adsorb close to bridge sites. Binding energies per  $\text{Mo}_6\text{S}_6$  unit in the two configurations are 2.61 and 2.59 eV, respectively, slightly favoring the symmetric configuration. We use absolute values of binding energies throughout this text.

We simulated the STM images expected from these two configurations as the  $10^{-5} \text{ e}/\text{\AA}^3$  iso-surface of local density of states integrated from -1.0 eV to the Fermi level: in each case, we find a double row of apparent protrusions in anti-phase; the protrusions are centered adjacent to the topmost S atoms (Figure 4-8(d) and (e)). In the symmetric configuration, the registries of the topmost S atoms are close to bridge sites of the Cu(111) surface and the apparent protrusions are very close to the hollow sites (Figure 4-8(d)). In the asymmetric configuration, half of the topmost S atoms are nearly in registry with the substrate bridge sites whereas the other half are closer to hollow sites and the apparent protrusions are close to bridge sites. Because of the difference in adsorption sites of the two “S legs” in the asymmetric configuration, we predict a small difference of the heights of the topmost S atoms ( $\sim 0.1 \text{\AA}$  difference) and, hence, of the protrusions in the STM image.

Figure 4-9 shows the experimental results obtained by our collaborators [91]. The nanowires were grown on a  $(\sqrt{7} \times \sqrt{7})R19^\circ$  sulfur-terminated Cu(111) surface which at the same time also produced  $\text{MoS}_2$  and  $\text{Mo}_2\text{S}_3$  patches [62]. The nanowires are aligned each with one of the three substrate atomic row directions. The nanowires show two rows of protrusion in antiphase along their body, as predicted from our calculations, and additional protrusions at their ends. Within the limits of the experimental observations, no difference in height between the protrusions on one or the other side of the nanowire can be made out, suggesting the symmetric adsorption configuration.



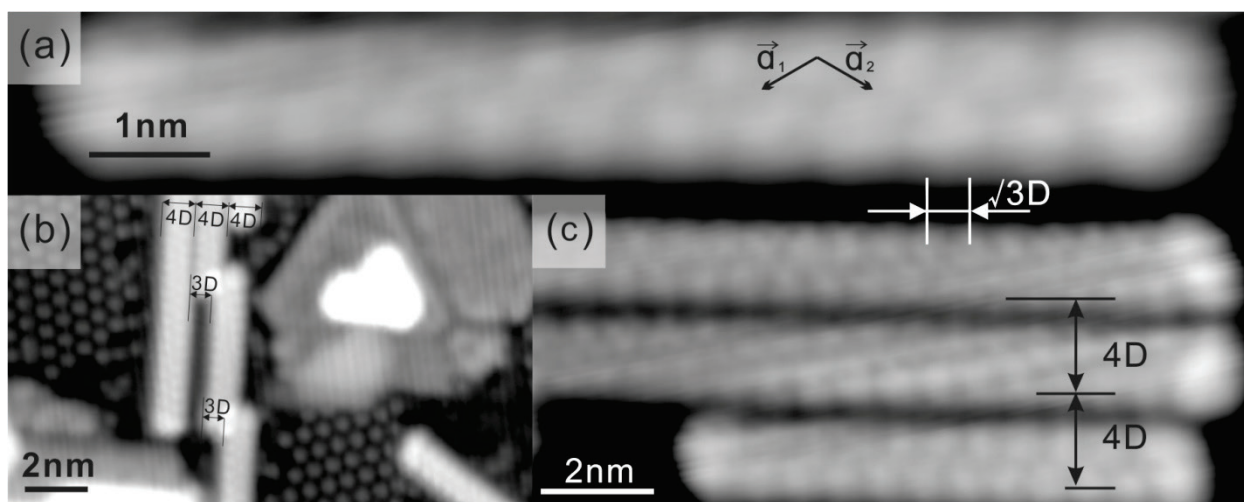


Figure 4-9. STM images (current: 0.13 nA, bias: -0.82 V) of a) isolated  $\text{Mo}_6\text{S}_6$  nanorod on Cu(111) in good agreement with the simulated STM image Figure 4-8(d); b) overview of our sample preparation showing the nanorods, the sulfur termination of Cu(111) as hexagonal pattern of apparent protrusions, and  $\text{MoS}_2$  islands with characteristic brim state (grey, smooth areas); c) cluster of aligned and equally spaced  $\text{Mo}_6\text{S}_6$  nanorods at  $4D$  separation. [Reprinted Figure with permission from “D. Le, D. Sun, W. Lu, M. Aminpour, C. Wang, Q. Ma, T. S. Rahman, and L. Bartels, *Surface Science*, 611, 1-4 (2013). Copyright (2013) by the American Physical Society.”]

Since the growth procedure leaves the Cu(111) surface covered by either sulfur or molybdenum sulfide ( $\text{MoS}_2$ ,  $\text{Mo}_2\text{S}_3$ , or  $\text{Mo}_6\text{S}_6$ ), registry information of the nanowires with regards to the bare substrate cannot be obtained. Moreover, the nature of the  $(\sqrt{7}\times\sqrt{7})R19^\circ$  sulfur termination is still under discussion [79]. Assuming the structure proposed by Foss *et al.* [93] or by Domange and Oudar [93], the apparent protrusions of the sulfur termination are in registry with the top sites of the underlying substrate. Under this assumption, the protrusions in the STM image are in registry either with the hollow or bridge sites of the substrate supporting both models (symmetry and asymmetry configurations) suggested by our DFT simulations. Given the very small separation between hollow and bridge sites, STM imagery was not able to distinguish them.



In the experiments, it is found that the nanowires are grown individually (Figure 4-9(a)) or in the form of a collinear array at regular spacing (Figure 4-9(c)). Nanowires of any other atomic-scale setup or wider cross section are not found. The presence of homogeneous populations (with regards to their cross section) of nanowires with a propensity for regular spacing is exciting. The latter gives rise to the question: what determines the separation between adjacent rows? In the absence of a substrate, the separation between  $\text{Mo}_6\text{S}_6$  nanowires is determined by inter-wire interactions consisting mainly of vdW interactions. Using theoretical modeling, the optimal distance can be determined straightforwardly by considering supercells that place adjacent nanowires at different separation. We thus performed DFT modeling of nanowires in vacuum and varied the spacing between them. Figure 4-10 shows the resulting interaction potential per  $\text{Mo}_6\text{S}_6$  repeat unit. For arrangement of adjacent wires both in-phase and anti-phase we find the presence of an optimal separation, i.e. a minimum in the interaction potential. The interaction energy at 0.27 eV per  $\text{Mo}_6\text{S}_6$  unit is higher for the in-phase than for the anti-phase arrangement (0.18 eV per  $\text{Mo}_6\text{S}_6$  unit), and the optimal distances is shorter (3.3D as compared to 3.5D, respectively). Notably, we find that when the wires get as close as 3D, their interaction starts to become very repulsive. This suggests that the wires found on HOPG in the work of Kibsgaard and coworkers [86] need to form inter-wire bonds to achieve their close packing.

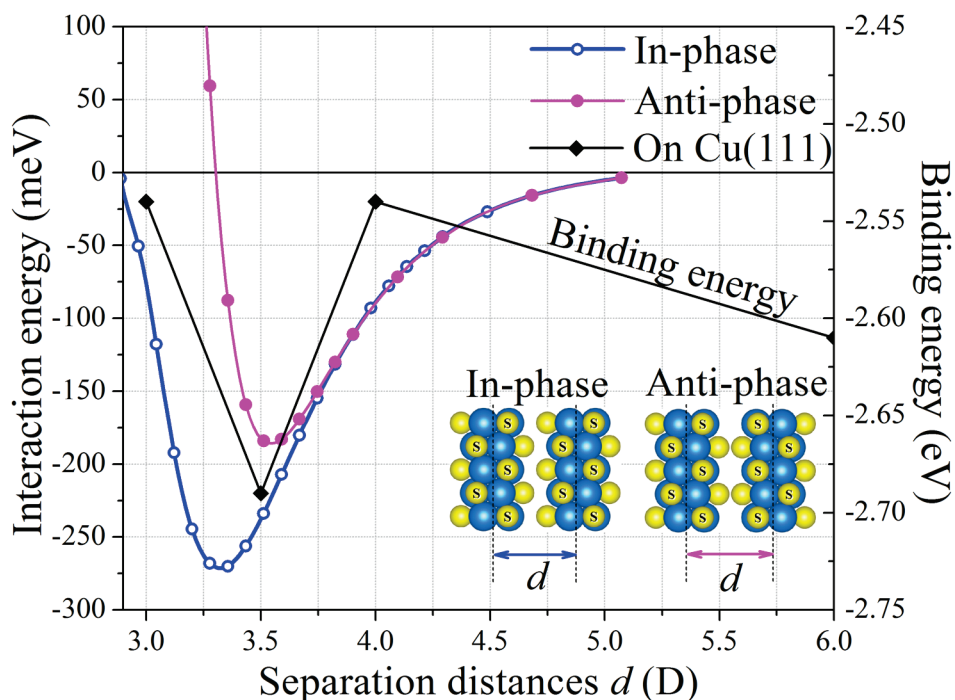


Figure 4-10. Interaction energy between two isolated  $\text{Mo}_6\text{S}_6$  nanowires per  $\text{Mo}_6\text{S}_6$  repeat unit (left ordinate) as functions of their separation measured in Cu-Cu bond length  $D$ . Binding energy of two  $\text{Mo}_6\text{S}_6$  nanowires to the Cu(111) substrate per  $\text{Mo}_6\text{S}_6$  repeat unit (right ordinate) as a function of their separation. The values are taken for the adsorption configuration (symmetric/asymmetric) that yields optimal binding energy at the indicated separations.

On a Cu(111) substrate, the inter-wire distances are limited by substrate registry and cannot be probed continuously in a meaningful manner. On the substrate, the direct vdW interaction of the wires is only one component of the inter-wire interaction: the presence of the  $\text{Mo}_6\text{S}_6$  nanowires also causes a significant perturbation of the substrate, which can cause substrate-induced preference for particular inter-wire distances. At the same time, the presence of the substrate can conceivably screen dispersion interactions. In order to understand whether  $\text{Mo}_6\text{S}_6$  nanowires have a substrate-controlled preferred separation, we modeled wires on Cu(111)

at three different separation,  $3D$ ,  $3.5D$  and  $4D$  using a  $\begin{pmatrix} 3 & 3 \\ -1 & 1 \end{pmatrix}$ ,  $\begin{pmatrix} 7 & 7 \\ -1 & 1 \end{pmatrix}$  and  $\begin{pmatrix} 4 & 4 \\ -1 & 1 \end{pmatrix}$  or

$\begin{pmatrix} 8 & 8 \\ -1 & 1 \end{pmatrix}$  Cu(111) super cell, respectively. We considered both nanowires with symmetric and

asymmetric adsorption configurations and arranged them in-phase and in anti-phase configurations, i.e. shifted by  $0.5\sqrt{3}D$  along the wire axis, except for the case of 3D separation, for which the antiphase wires clearly interpenetrate.

Similar substrate-mediated effects have been found for a great number of atomic and molecular adsorbates on Cu(111) and were ascribed largely to the Shockley surface state [94-99]. We note that its theoretical modeling typically requires very thick substrate slabs (8 and more layers) to effectively decouple the surface states on top and on the bottom of the slab [100]. The lateral size of the unit cell required to model nanowire interactions would render such calculations exceedingly time-consuming. Our use of 5 layer slabs limits the quantitative accuracy of our results, yet it reveals the presence of a preferred inter-wire separation on the substrate, in-line with our experimental findings: for a separation of 3.5D we find a binding energy per  $\text{Mo}_6\text{S}_6$  unit to the substrate of 2.69eV,  $\sim 80$  meV stronger than for isolated chains. Separation of the wires by 3D and 4D leads to binding energies of  $\sim 2.54$  eV, which is weaker than the binding of 3.5D separated wires.

Experimentally, the growth of  $\text{Mo}_6\text{S}_6$  nanowires was not sufficiently optimized to quantify statistically the interaction energy between adjacent wires. Such measurements have been carried out for interatomic and intermolecular separation distributions [95, 96, 98] and permitted mapping of an inter-wire interaction potential similar to Figure 4-10. In the experimental measurements, however, both the growth of isolated  $\text{Mo}_6\text{S}_6$  nanowire as shown in Figure 4-9(a) and a propensity for their growth in parallel arrays at 4D separation (Figure 4-9(c)) are observed. In contrast, if the nanowires start to grow so that their separation is smaller than 4D they terminate to avoid running in parallel (see, for instance, the  $\text{Mo}_6\text{S}_6$  nanowires at 3D on the

left of Figure 4-9(b)). In combination these findings attest to the presence of inter-wire interactions that favor a specific separation between adjacent nanowires even on a surface.

#### 4.2.4 Conclusions

The growth of molybdenum-sulfur nanowires on a Cu(111) surface is observed experimentally and we identified them as  $\text{Mo}_6\text{S}_6$  nanowires. We find that the substrate interactions are considerable, leading to the alignment of the nanowires with the substrate atomic rows. The nanowire growth favors a 4D separation on Cu(111), sufficiently far to separate them completely and slightly wider than expected from DFT simulation. In combination, our results suggest that Cu(111) may be a viable candidate for the aligned and regularly-spaced growth of  $\text{Mo}_6\text{S}_6$  nanowires.

## CHAPTER 5. ELECTRONIC STRUCTURE AND GROWTH OF Mg(0001) FILM

### MORPHOLOGIES

#### *5.1 Part I: Electronic Structure Features Controlling the Limit of and Reactivity in the Thin-Film Regime, Stacking Fault of Mg Adislands and Adatom Self-Diffusion*

##### 5.1.1 Introduction

The structural, electronic, and magnetic properties of low-dimensional structures generally strongly differ from those of the corresponding bulk materials. Ultrathin metal films have been a subject of intense research during the last few years [101-103] since they provide a laboratory for basic quantum-mechanical concepts, and because they find applications in the microelectronic industry, especially in magnetic data storage technology. Magnesium is of interest to many atomistic processes especially as a component in hydrogen storage materials [106].

Mg is considered a simple, free-electron-like material but nonetheless a reactive metal with various interesting properties owing to its particular location in the periodic table of elements. It has a closed subshell ground-state atomic configuration ( $[\text{Ne}]^{10} 3\text{S}^2$ ). Its chemical bonding is mainly through the two outer electrons. Since a Mg atom has a low excitation energy for electron transmission to states with 3p occupation, the two outer electrons in bulk (hcp) may also occupy 3p states ( $[\text{core}]^4 2\text{p}^6 3\text{s}^{2-x} 3\text{p}^x$ ). Since the 2p shell is closed and strongly bound, it barely participates in the bond and, at the same time, screens the ion's charge so that the  $3\text{s}^{2-x} 3\text{p}^x$  electrons are relatively loose bound [106].

Giant surface energy and work function oscillations have been predicted in the past as a function of the number of layers, as well as oxidation-rate, conductance, and H-binding [104-106].

For most of the metals the spacing tends to contract. Also the compact (0001) surfaces of most hcp metals exhibit a contraction of the interlayer spacing between the topmost layers, whereas for Be and Mg the opposite, i.e. a small expansion is observed [107, 108]. In accordance with the Smoluchowski smoothing effect [109], after the surface forms the charge density redistributes itself as the electrons lower their kinetic energy by moving into the regions between the ion cores, consequently creating a positively charged surface layer. Hence there will be an attractive electrostatic force between top layer ion cores to relax inward. In the "chemical picture", Fiebleman [110] proposed on the basis of Pauling's hypothesis [111] there is a correlation between bond order and bond length. In this picture surface will relax inward if the bond length of the dimer is smaller than that of the bulk, and outward if it is large. The first interlayer distance of Mg(0001) tends to expand instead of — a various groups have determined to be the case with other metals — to contract [106] and [112-114].

In this section, we undertake a thorough examination of the electronic structure of bulk and thin-film magnesium to investigate and revise predictions reported previously, regarding (1) the surface energy, oxidation rate and interlayer relaxation oscillations of the of Mg(0001) films as a function of thickness, (2) the well-known Friedel oscillations in Mg slabs (3) the weak binding of adatoms on Mg(0001) surface. We calculate undertake an thorough examination of electronic structure of bulk and thin-film Magnesium to investigate and revise predictions reported previously, such as (1) surface energy, oxidation rate of Mg film and the interlayer

relaxation oscillations of the of Mg(0001) films as a function of thickness, (2) the well-known Friedel oscillations in Mg slabs (3) the adatom weak binding. We calculate the energy barrier of the Mg adatom on Mg(0001) Terrace and consequently stacking fault of the magnesium layers. The energy barrier for the Mg adatom on Mg(0001) terrace and, through it, the stacking fault of the magnesium layers. To our knowledge, the stacking fault of magnesium layers has not been reported before. We show that the mechanism behind the stacking fault of the adatom and adislands on the magnesium surface can be explained by Friedel oscillations. Previous studies have shown that the Friedel oscillations are responsible for the expansion in first inter-planer distance of Mg(0001). We also reproduced longer-ranged Friedel oscillations. We show that the 3D Friedel charge-density oscillations of Mg(0001) are more complex than what has been depicted previously by 1D and 2D plots [106].

### 5.1.2 General Computational Details

We perform periodic super-cell density-functional-theory calculations of the total energy and the electronic structure of the systems of interest as implemented in the computational code QUANTUM ESPRESSO [115]. The interaction between ions and electrons is described by ultra-soft Vanderbilt pseudo-potentials with p-semicore states [26]. Namely, for atomic Mg, the valence electrons are as follows:  $[\text{core}]^4 2p^6 3s^{2-x} 3p^x$ . For the electron exchange-correlation functional, we have used the parameterization of Perdew and Wang 91 (PW91) [116, 117] based on the generalized gradient approximation (GGA). The electronic wave functions were expanded in a plane-wave basis set with a kinetic energy cut-off of 35 Ryd. The charge density Fourier expansion was truncated at 400 Ry. The positions of all atoms in the slab were optimized until the force on each atom and each direction was smaller than  $1.0 \times 10^{-4}$  Ryd Bohr<sup>-1</sup> [106]

We employed computational VASP code [59] for supporting calculations using a PBE [22] exchange-correlation functional based on the generalized gradient approximation (GGA) and the projected-augmented-wave-method (PAW) with  $p$  semi-core states ( $[\text{core}]4 2p^6 3s^{2-x} 3p^x$ ). We expanded the electronic wave functions in a plane-wave basis set with a kinetic energy cut-off of 265.6 eV. Minimization of the total energy of the slab as a function of atomic positions is achieved by reducing the Hellmann–Feynman forces [118] on the atoms below  $4 \times 10^{-3}$  eV/Å via the conjugated gradient algorithm [106].

The Mg(0001) surface was modeled by slabs of thickness from 2 to 30 layers with a  $1 \times 1$  in plane periodicity. For modeling Mg adatoms on Mg(0001), the number of layers for the supercell was fixed at 7 and the in-plane periodicity at  $3 \times 3$ . For integrations inside the Brillouin zone, we sampled it according to the Monkhorst–Pack scheme [76] with a uniform grid of  $k$ -points of dimensions  $16 \times 16 \times 8$ ,  $16 \times 16 \times 1$ , and  $5 \times 5 \times 1$  for the bulk, the  $1 \times 1$  surface, and the  $3 \times 3$  surface, respectively.

In order to simulate the adatom diffusion on (0001) terraces - away from steps, we have used a  $3 \times 3$  super-cell and 7-layer atomic layers. For simulating the diffusion barriers near step edges, we have used a super-cell containing a  $3 \times 8$ -slab of 7 atomic layers and a  $3 \times 4$  step. The integrations over the surface Brillouin zone were performed by using a  $5 \times 5 \times 1$  and  $2 \times 5 \times 1$  Monkhorst-Pack [76] mesh for the  $3 \times 3$  super-cell and the  $3 \times 8$  super-cell, respectively. In all calculations involving a surface, we separated the periodic images of the slab with a vacuum space of 20 Å to avoid interaction between them.

The diffusion barriers of the adatom have been determined by the dragging method: one obtains the total energy of the system at each point along the chosen diffusion path by fixing the



coordinate of the Mg adatom along that path and allowing its other coordinates and those of all other atoms in the system to relax.

The surface energy is calculated as one half of the total energy difference between the  $n$ -layer slab and the bulk with the same number of atoms. The factor  $1/2$  accounts for the two surfaces of the slab.

Charge densities differences are evaluated as  $\delta\rho = \rho[\text{Mg}_n/\text{Mg}(0001)] - \rho[\text{Mg}(0001)] - \rho[\text{Mg}_n]$ , where  $\rho[\text{Mg}_n/\text{Mg}(0001)]$  is the CHD of the entire system relaxed ( $n$ -mer plus the surface),  $\rho[\text{Mg}(0001)]$  is the CHD of the clean surface, and  $\rho[\text{Mg}_n]$  is the charge of the isolated  $n$ -mer,  $\text{Mg}_n$ . Nevertheless, the positions of the atoms used to compute  $\rho[\text{Mg}(0001)]$  and  $\rho[\text{Mg}_n]$  are extracted from those in the relaxed full systems and not from the actual relaxed coordinates of  $\text{Mg}(0001)$  and  $\text{Mg}_n$ .

### 5.1.3 Results and Discussion

#### 5.1.3.1 Bulk

The primitive unit cell of hcp crystals is a hexagonal supercell containing two atoms. Our corresponding calculations for bulk Mg yield lattice parameters ( $a = 3.213 \text{ \AA}$  and  $c/a = 1.607$ ) and cohesive energy values (1.45 eV) in very good agreement with the experimental values ( $a = 3.21 \text{ \AA}$  and  $c/a = 1.624$ ,  $E_{\text{coh}} = 1.46 \text{ eV}$ ) [119] and with the previous calculations, as shown in Table 5-1. Our preliminary calculations for bulk Mg using VASP code, render the lattice parameters to be  $a = 0.31980 \text{ nm}$  and  $c/a = 1.625$  in good agreement with the experiment and previous calculations [22-24].

Since the  $c/a$ -ratio of Mg is approximately constant for varying pressure [18], we have calculated its bulk modulus based on the equilibrium  $c/a$ -ratio. Our result, 35.48 GPa, is in excellent agreement with early measurements (35.4 GPa) [120, 121] but slightly underestimates the value according obtained in more recent measurements ( $36.8\pm 3$  GPa) [122]. In our preliminary calculations for bulk Mg using PBE exchange-correlation functional and the projected-augmented-wave-method similar values of lattice parameter were obtained. The lattice parameters is rendered to be  $a = 3.195 \text{ \AA}$  and  $c/a = 1.62 \text{ \AA}$  in good agreement with experiment, and with the present and previous calculations [106].

Table 5-1. Calculated (at 0 K) and measured lattice parameters ( $a$  and  $c/a$ ), cohesive energy, and bulk modulus of Mg [106].

Reference	Lattice parameters		Cohesive Energy (eV)	Bulk modulus (GPa)
	$a(\text{\AA})$	$c/a$		
This work, PW91	3.213	1.607	1.45	35.48
This work, PBE	3.198	1.625	1.50	
PW91 [105]	3.201	1.62	---	---
PW [123]	3.20	1.66	1.42	30.0
PW[124]	3.18	1.615	1.50	35.5
LDA[123]	3.16	1.59	1.76	39.0
LDA [113]	3.13	1.616	1.78	40.2
LDA[114]	5.88	1.62	---	---
LDA[125]	3.12	1.616	---	38.4
LDA[126]	3.18	1.623	---	37.7
Experiment[119]	3.21	1.624	1.51	35.4
Experiment[127]			---	$36.8\pm 3$

#### 5.1.3.1.1 Mg(0001): Structure, Energetics and Electronic Structure

In the following we will analyze how the properties of Mg(0001) films vary as a function of the film thickness and find convergent values characterizing such properties. Specifically, we look at (1) the thickness at which the interlayer distance among central layers recovers the bulk

value, (2) the formation energy of the film, (3) the surface energy, (4) the interlayer contraction/expansion of topmost layers, and (5) the surface electronic density of states. As we shall see, in this section it will be important to distinguish between the film thickness at which the properties of the surface (the topmost layer) are reliably obtained and the film thickness at which central layers recover the bulk properties: the *thin-film limit*. The two concepts are often equivalent but the long-range charge density Friedel oscillations inside the Mg films will prove that they are not necessarily the same.

#### 5.1.3.1.2 The Thin-film Limit, Formation Energy, Surface Energy, Interlayer Relaxation

First, we determined the thickness at which the central layers of the film recover the bulk properties, the thin-film limit. For example, we find that, in order that the interlayer relaxation at central layers falls below  $\pm 0.1\%$  (a value taken as a convergence parameter because it corresponds to the resolution of available LEED experiments [128]), the film must be at least 23 layers thick, despite the fact that  $\Delta d_{34}$  has been found to be vanishingly small in previous calculations [129, 130]. For the sake of brevity, we report here only the interlayer relaxation spectrum of the 23-layer film in Table 5-2. We compare these results are compared with those produced by calculations using a PBE exchange-correlation functional and the projected-augmented-wave-method [106].

We have then recalculated the properties that Li *et al.* reported [131] via first-principles calculations to explicitly test the striking thickness dependence found in their work. We have extracted well-converged values of (a) the formation energy per atom, (b) the surface energy,  $\sigma$ , and (c) the relaxation of the first interlayer spacing of Mg(0001),  $\Delta d_{12}$ . These quantities are

plotted in Figure 5-1(a)-(c) for  $N=2,\dots,30$ , together with the corresponding results of Li *et al.* [131] for comparison [106].

Table 5-2. Calculated changes (%) in the interlayer distances between the surface layers of Mg(0001) with respect to the bulk value (2.582 Å),  $\Delta d_{i,j+1}$ , for a 23-layer slab using both the ultra-soft PW91 within the Quantum espresso code (QE) and the PAW PBE pseudopotentials within the VASP code [106].

N	23-QE	23-VASP
$\Delta d_{12}$	2.17	1.76
$\Delta d_{23}$	1.12	0.74
$\Delta d_{34}$	0.08	-0.41
$\Delta d_{45}$	-0.03	-0.37
$\Delta d_{56}$	-0.07	-0.15
$\Delta d_{67}$	0.13	0.17
$\Delta d_{78}$	0.09	0.08
$\Delta d_{89}$	0.14	0.10
$\Delta d_{9,10}$	-0.00	0.04
$\Delta d_{10,11}$	0.05	0.02
$\Delta d_{11,12}$	-0.05	-0.21
$\Delta d_{12,13}$	-0.05	-0.21

Regarding the formation energy per atom Figure 5-1 (a)), which is also an indicator of the thin-film limit, in agreement with the results in [131], we find that it slowly and monotonically converges to the cohesive energy of bulk Mg,  $E_{\text{coh}} = 1.45$  eV/atom. For example, for a film of 17

layers the formation energy is 75 meV/atom lower than  $E_{\text{coh}}$ , while for a film of 23 layers it is only 15 meV/atom lower than  $E_{\text{coh}}$  [106].

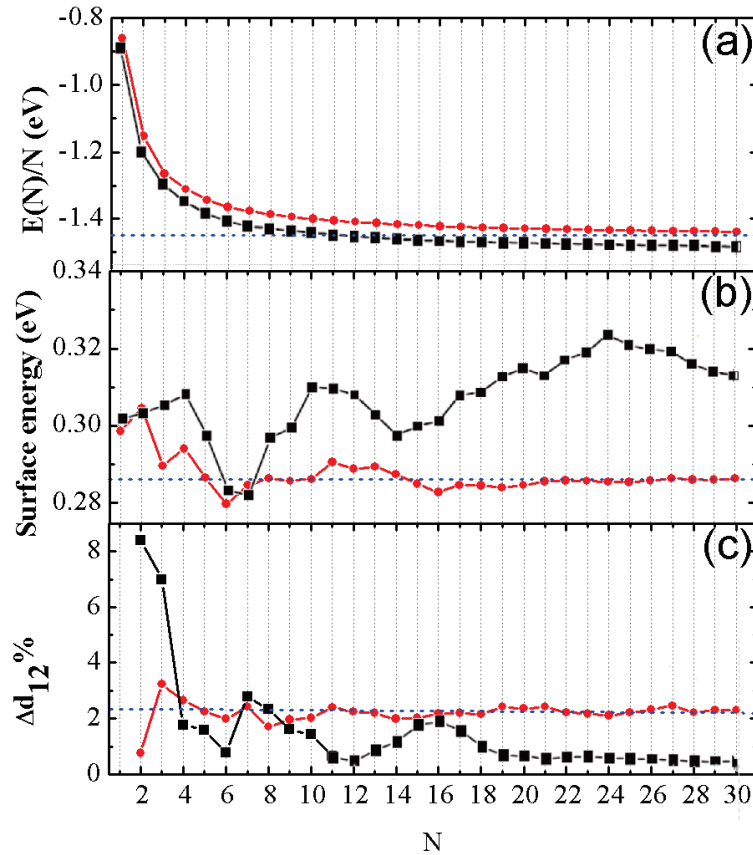


Figure 5-1. Calculated energetic and structural properties of Mg(0001) as a function of the number of layers forming the slab,  $N$ : (a) Formation energy per atom,  $E(N)/N$ ; the dashed line indicates the cohesive energy of bulk Mg, (b) surface energy and (c) the change (%) in the first interlayer distance with respect to the bulk value,  $\Delta d_{12}$ . In (b) and (c), the dashed line is a guide for the reader indicating the convergent value of surface energy  $\sigma$  and  $\Delta d_{12}$ , respectively. Grey (red) circles and black squares are data from Ref. [105] and this work, respectively. [Reprinted black squares in Figure with permission from “Li, X. G.; Zhang, P.; Chan, C. K., PHYSICA B; 390, 1-2; 225 (2007) . Copy right (2013) Elsevier”] [106]

Once we obtained the above indicator of the *thin-film limit* (around or more than 23 layers), we proceed to determine the thickness at which surface properties converge (the surface energy and the topmost interlayer relaxation). One might think that since a large number of

layers is needed to recover the bulk interlayer distance, the conclusions of Li *et al.* that the surface properties may need more than 30 layers to converge are further confirmed. As, we shall see, however, that this turns out not to be the case [106].

Figure 5-1(b) shows that the behavior of the surface energy  $\sigma$  as a function of thickness is indeed not monotonic – it may vary by as much as 7 meV/atom, but only for films of 3 -- 7 layers. However,  $\sigma$  is not at all periodically oscillatory. It actually converges to a value of 0.286 eV/atom, which is in excellent agreement with the experimental value, 0.28 eV/atom [132], within an accuracy of 2 meV/atom for films composed of only 18 layers (corresponding to films thicker than 4.1 nm). This result thus opposes that of Li *et al.*, who reported that the surface energy of thin films oscillates with a relatively long period of  $\Delta N \sim 8$  but actually does not but converge even at 30 layers (0.322 eV/atom). Specifically, in their calculations the surface energy has increments of more than 10 meV for films of less than 10 layers and almost steadily increases from 0.307 eV/atom to 0.334 eV/atom as the number of layers increases from 14 to 24 [131], a value 50% larger than the experimental one. Note, too, that while the formation energy, which is an indicator of the thin-film limit, varies by several meV beyond 24 layers, the corresponding variation of  $\sigma$  – a surface property -- is almost 10 times smaller; suggesting that the properties of the surface converge more rapidly than the properties of the bulk [106].

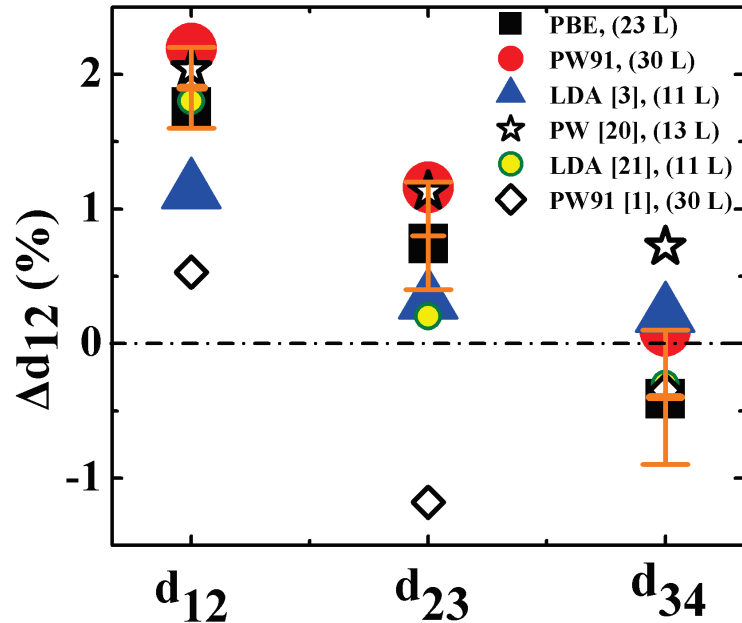


Figure 5-2. Calculated changes in the first ( $\Delta d_{12}$ ), second ( $\Delta d_{23}$ ), and third ( $\Delta d_{34}$ ) interlayer distances of Mg(0001) with respect to the bulk value. The (orange) bar represents the experimental value as measured by LEED [20]. The number inside the round parenthesis corresponds to the number of layers in the slab used in previous calculation and, in the case of the present PW91 calculation, the convergent value obtained from analyzing slabs formed by 2 to 30 layers. The numbers inside the squared parenthesis correspond to the references of previous works [106].

In addition, Figure 5-1(c) shows that the dependence of the outward interlayer relaxation  $\Delta d_{12}$  on the thickness of the film is not dramatic as suggested by the calculations of Li *et al.* [131]. Namely, although  $\Delta d_{12}$  varies from +3.23% to +1.70% when increasing the number of layers N from 3 to 8 layers, it is already reasonably well described by 11 layers, and totally converged at 17 layers. The converged value of  $\Delta d_{12}$  is 2.20%, which is in good agreement with the experimental value [128],  $+1.9 \pm 0.3\%$ . The results for the outward relaxation of Mg(0001) are thus again in contrast with those of Li *et al.*: They found a surprisingly large interlayer expansion of +7% for 3 layers and a converged value of  $\sim 0.7\%$ , which is an extremely small compared to the experimental value cited above. They found also that 20 layers are necessary to

converge this surface property because of a strong periodic oscillation of period  $\Delta N \sim 8$  for films of thickness ranging from 3 to 19 layers. Regarding the oscillations in  $\Delta d_{12}$  of period  $\Delta N \sim 8$ , our calculations barely indicate that  $\Delta d_{12}$  has local minima at 14-15, 23-24 layer and local maxima at 11, 19 and 27 that might be interpreted as the reported oscillations, however, not only are the deviations of these “extremes” negligible but also films of intermediate thickness fall out from any oscillatory pattern. Moreover, maxima of  $\Delta d_{12}$  in Li *et al.* calculations correspond to minima in our calculations and vice versa [106].

There are also experimental measurements of the relaxation of deeper layers. In Figure 5-2 we compare our converged values of the first, second and third interlayer relaxations ( $\Delta d_{12}$ ,  $\Delta d_{23}$  and  $\Delta d_{34}$ , respectively) with those attained from LEED measurements [108] and also with results obtained in previous calculations [128, 129, 131, 133].

Table 5-3. Changes in the first ( $\Delta d_{12}$ ), second ( $\Delta d_{23}$ ), and third ( $\Delta d_{34}$ ) interlayer distances of 23 layers of Mg(0001) with respect to the bulk value as rendered by our PAW-PBE-VASP calculations, our US-PW91-QE calculations, previous calculations and experiment [106].

	PBE-23L	PW91-23L	LDA-11L [134]	PW-13L [130]	LDA-11L [129]	PW 91-15L [131]	Experiment [128]
$d_{12}$	1.758	2.102	1.13	2.04	1.8	1.723	+1.9±0.3%
$d_{23}$	0.744	1.053	0.31	1.13	0.2	-0.93	+0.8±0.4%
$d_{34}$	-0.412	0.011	0.21	0.72	-0.3	-0.264	-0.4±0.5%



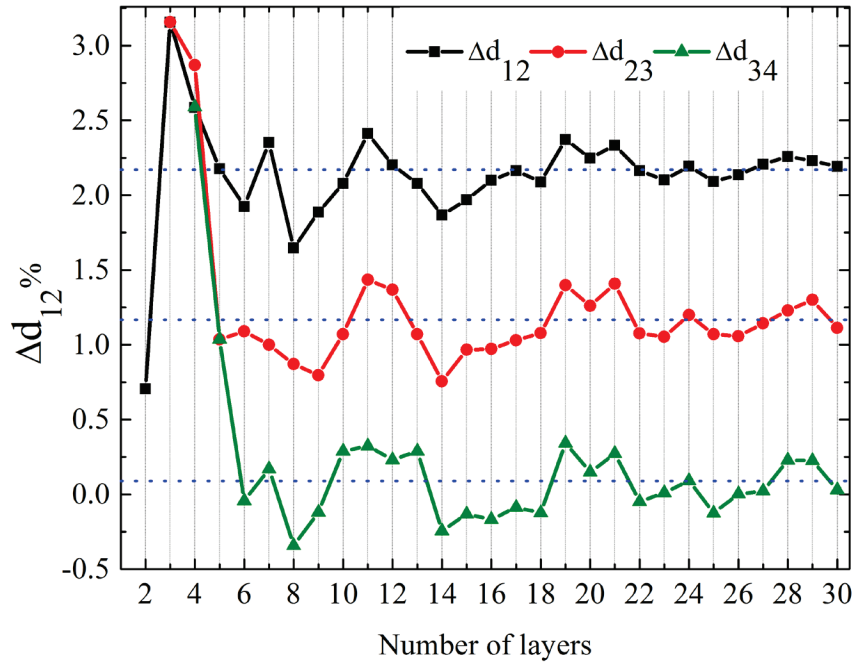


Figure 5-3. Calculated slab thickness dependence of the first, second and third interlayer relaxations,  $\Delta d_{12}$ ,  $\Delta d_{23}$  and  $\Delta d_{34}$  [106].

It is worth highlighting that the convergence of  $\Delta d_{23}$  and  $\Delta d_{34}$  is slower than that of  $\Delta d_{12}$  (see Figure 5-3). This result may seem surprising because previous calculations indicate that  $\Delta d_{34}$  approaches to zero, a feature ordinarily taken as indicative that the bulk properties have been recovered. The slow convergence of  $\Delta d_{23}$ ,  $\Delta d_{34}$ , etc. can be explained by the fact that Friedel oscillations are long-ranged and their wavelength is not perfectly commensurable with the interlayer distance. Therefore, varying the thickness of the film causes readjustments of the charge Friedel oscillations throughout the film which modulate atomic positions accordingly. Hence, we conclude that the slower convergence of subsurface interlayer distances speaks for the *thin-film limit* and thus confirms that properties associated with the *thin-film limit* are harder to converge than the properties exclusive to the surface [106].

In summary, our results indicate that although overcoming the *thin-film limit* requires more than 23 layers, the surface properties are well converged if the film is ~18 layers thick, contrary to the results of Li *et al.*, which have outputted that a film of 20 layers is needed to converge  $\Delta d_{12}$ , and films of more than 30 layers are needed to converge the surface energy. We do not know what caused the dramatic thickness dependence of the properties of Mg(0001) the DFT calculations by in Li *et al.* [131]. As of now, the discrepancies of our results with those Li *et al.* and, more importantly, the poor agreement of their results with available measurements may be provisionally ascribed to the fact that they used an ultrasoft pseudo-potential and without semicore p-electrons [106].

#### 5.1.3.1.3 The Electronic Density of States of Mg(0001) and Its Thickness Dependence in the Thin-Film Regime

We have already shown that the surface energy and the topmost interlayer distance are convergent for films of 18 layers or more. It remains to investigate the thickness dependence of the electronic structure of the surface atoms of Mg(0001), an issue that is important in understanding the initial stage of the oxidation rate of Mg thin films [135, 136], as we shall see.

The local density of states (LDOS) for the valence states of the Mg(0001) surface layer (as well as of bulk Mg) is nearly free-electron-like, as shown in Figure 5-4. Namely, the LDOS(E) of the surface atom in a 30-layer film increases roughly as  $\sqrt{E}$  up to the Fermi level, making Mg a very reactive metal [106].

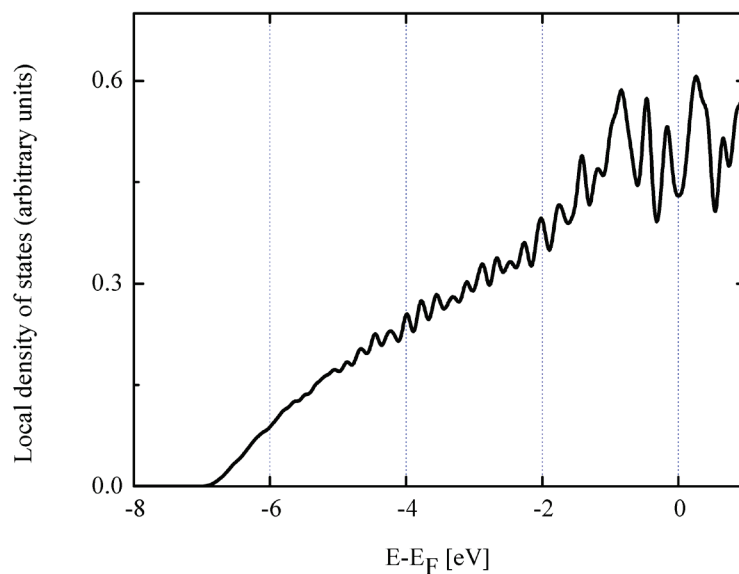


Figure 5-4. Normalized nearly free-electron like LDOS of the  $3s^{2-x} 3p^x$  valence electrons of Mg(0001) surfaceatoms for a 30-layer slab [106].

A closer look at the curve, however, shows that the potential of the Mg ions over that of the valence electrons, while weak, produces oscillations of significant amplitude in the LDOS(E) of the surface atom, particularly around the Fermi level ( $E_F$ ) -- the energy region that dominates chemical properties. In fact, we shall see that this region corresponds mainly to p-states rather than to s-states -- despite the fact that p-states comprise only a small fraction of the valence band. The LDOS(E) 1 eV below  $E_F$  is more wiggled but the variations have much smaller amplitude. This energy region could be involved in the hybridization with adsorbates bonded covalently; yet, the bonds with oxygen are essentially ionic [106].

The above description is for the surface layer of the thickest film (30 layers), for which both (1) the bulk Mg properties are recovered in the central layers and (2) the properties of the surface layer analyzed in the previous section are converged. So, let us now turn to analyzing the evolution of the surface LDOS as a function of film thickness. We find that the strongest

thickness-dependence occurs precisely close to the Fermi level. In Figure 5-5(a)-(d) we present the evolution of the LDOS of the surface layer of Mg(0001) as a function film thickness but only close to  $E_F$  for selected films ranging from 2 to 30 layers [106].

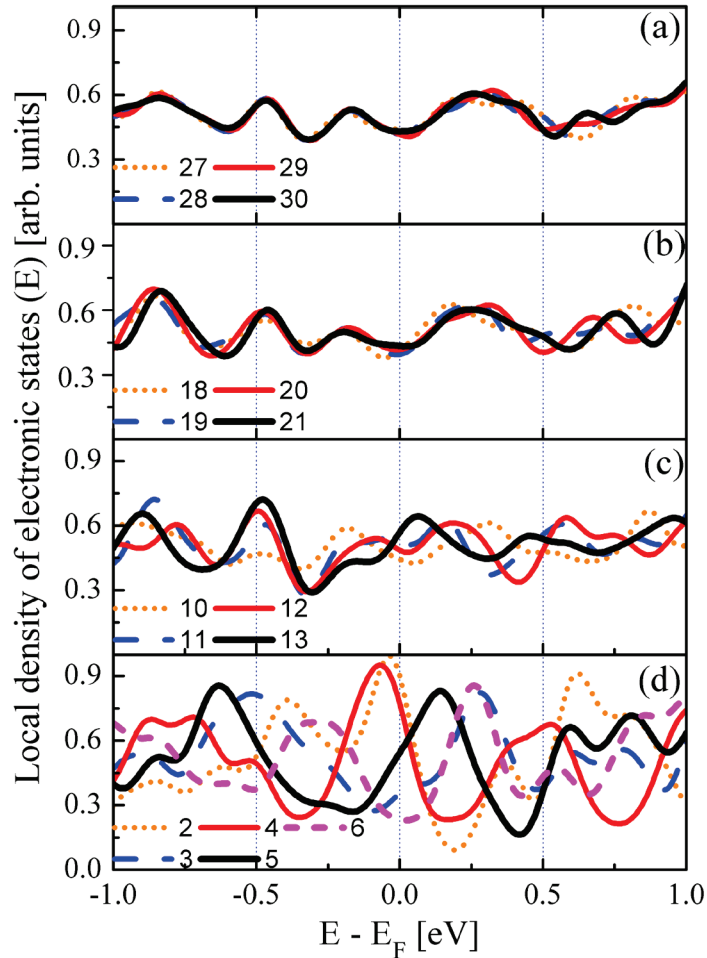


Figure 5-5. Calculated LDOS around the Fermi level for the surface atom of Mg(0001) as a function of the number of layers of the slab, which are indicated by the numbers labeling the curves. The LDOS is normalized and the scale in each inset is the same.

One can see from Figure 5-5(a) and (b) that films of 18 layers are thick enough to obtain a well converged electronic LDOS( $E$ ) – just as for other properties exclusive to the surface that we have discussed earlier. This result does not contradict to the current experimental evidence on

the thickness-dependence of the oxidation rate because the latter has been reported only for films of less than 16 layers [135]. Furthermore, our results do not oppose those of previous theoretical studies, since Hellman and Binggeli [136-138] have reported thickness dependence of the DOS for films of less than 17 layers only the calculations of Li *et al.* [131] have rendered oscillations in the reactivity of Mg(0001) for thicker films. In particular, they found variations in the binding energy of hydrogen (H) on Mg(0001). These are not of consequence but are rather unexpected for films thicker than 18 layers. For example, the binding energy of H decreases by up to 30 meV from N=25 to N=30. We have not reproduced their results because such calculations are beyond the scope of this work. However, the fact that the potential they used overestimates the dependence of surface properties on slab thickness calls for revising the binding energy of H as well [106].

#### 5.1.3.1.4 On the Oxidation Rate of Mg(0001) Thin Films

That the electronic structure around the Fermi level converges and is thus well described by 18 layers is only part of the problem we want to discuss here. The next question is whether the variations in the LDOS(E) for thinner layers correlate with those observed experimentally for the oxidation rate (Figure 5-6(a), data from [135]) [106].

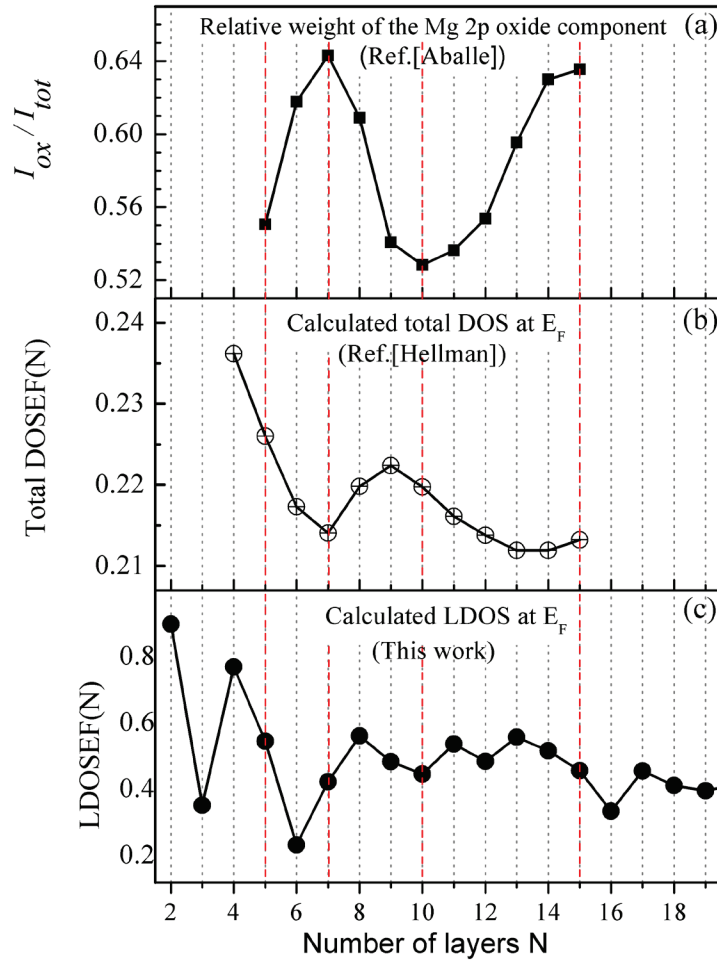


Figure 5-6. Comparison between experiment and electronic density of states calculations to explain the oxidation rate of Mg films (a) The relative weight of the intensity of the oxygen-induced peak in the Mg 2p spectrum (indicative of the oxidation rate) as a function of the number of layers,  $N$ , taken from [135]; (b) Calculated total  $DOS_{EF}(N)$  of a Mg(0001) slab (taken from [136]); (c) Calculated  $LDOS_{EF}(N)$  of the surface atoms of Mg(0001). The dashed line is a guide for the eye to compare the maxima/minima of the oxidation rate as a function of  $N$  with those of the calculation [106].

Since the specific correlation between the two properties has actually been debated during the last decade [135-138], it is worth reanalyzing it here. Hellman [136] calculated the *total*  $DOS(E)$  at  $E_F$  as a function of the film thickness,  $DOS_{EF}(N)$  (see Figure 5-6(b), data from [136]). Hellman *et al.* found that the thickness dependence of  $DOS_{EF}(N)$  – expected for thin films in general -- may be associated to that of the oxidation rate. Binggeli *et al.* [137, 138],

however, contested this correlation on the basis (1) that the actual variations in the total  $\text{DOS}_{\text{EF}}(N)$  are too small to account for the dramatic oscillations in the reactivity and (2) that the  $\text{DOS}_{\text{EF}}(N)$  necessarily increases monotonically with film thickness because it is normalized. Moreover, Hellman acknowledged that the position of each maxima and/or minima is shifted by two layers [136] (see Figure 5-6(b), data from [136]) from the dependence experiment report of oxidation rate on thickness since one expects that the larger the  $\text{DOS}_{\text{EF}}$  the larger the oxidation rate. They suggested, however, that it could be an effect from the interaction with the W substrate and Binggeli *et al.* subsequently demonstrated that such is the case: hybridization of the Mg states with those of the W substrate may slightly shift the position of the peaks at the Fermi level [137]. Such shift, however, is not a minor issue. The mismatch between the two curves is almost to the extent that maxima of the  $\text{DOS}_{\text{EF}}(N)$  correspond to minima of the oxidation-rate thickness dependence (see Figure 5-6). Still, another main drawback in explaining the thickness dependence via the total density of states is that the latter includes not only the topmost two layers -- which are the ones oxidized according to the  $\text{O}_2$  dose in experiment [135] -- but also all other layers that do not participate in this initial stage of oxidation. Naturally, the changes in the (normalized) total  $\text{DOS}_{\text{EF}}(N)$  as a function of the number of layers are negligible for the same reason [106].

As an initial step, we have also analyzed the (normalized) LDOS(E) but that of the surface atoms only. Figure 5-5(d), shows that there is indeed a dramatic thickness-dependence of the LDOS(E) for films thinner than 7 layers, just as one would expect from the observed oxidation rate. For example, one sees that the LDOS(E) of films of two and four layers have a conspicuous peak around the Fermi level that is not present at all in the converged surface LDOS(E) -- the converged surface has in fact a dip at  $E_{\text{F}}$  (see Figure 5-5(a)). In striking contrast,

the surface LDOS( $E$ ) for the film with 6 layers has a pronounced dip around  $E_F$ . In short, while the LDOS( $E=E_F$ ) of films with two and four layer is much higher than that of the converged value (Figure 5-5(a) and (b)), the LDOS( $E=E_F$ ) for the film with six layers is significantly lower. One expects that variations of the LDOS of such magnitude as a function of thickness must definitely affect the oxidation rate of Mg-thin films on W(110) [106, 135].

In order to characterize the reactivity of the Mg films we proceed as Hellman [136] did by plot the LDOS of surface atoms at  $E_F$  as a function of the number of layers,  $LDOS_{EF}(N)$ . We shall stress here that although, in general, a single number such as the LDOS at  $E_F$  does not characterize reactivity, in this particular case, this number is a good indicator because it tells us how the centroid of the LDOS peaks nearest to  $E_F$  shift as a function of thickness. For example, if  $LDOS_{EF}(N)$  is high that means that one of the maxima of the LDOS is very close to  $E_F$ , making more states available for oxygen. Conversely, if  $LDOS_{EF}(N)$  is low that means that  $E_F$  falls close to a dip of the DOS [106].

Therefore, in Figure 5-6(c), we plot the LDOS of surface atoms at  $E_F$  as a function of  $N$ ,  $LDOS_{EF}(N)$ . This inset shows that (1)  $LDOS_{EF}(N)$  varies quite significantly for  $N < 8$ , oscillates moderately for thicker films, but converges well at 18 layers, except for some oscillations in the range from  $N=18$  to 26 of negligible amplitude Figure 5-6(c)); (2)  $LDOS_{EF}(N)$  does not exhibit a monotonic staircase-like increase with film thickness (as expected by Binggeli for the normalized total DOS [138]); (3) the thickness dependence of the surface  $LDOS_{EF}(N)$  differs significantly from the total  $DOS_{EF}(N)$  (Figure 5-6(b), data taken from [136]); (4) although the data for the  $LDOS_{EF}(N)$  and the total  $DOS_{EF}(N)$  are both normalized, the relative changes of  $LDOS_{EF}(N)$  as a function of thickness are about one order of magnitude larger than the relative changes of total



$\text{DOS}_{\text{EF}}(\text{N})$ . The reason is that the former corresponds to one atom (at the surface) and the latter corresponds to as many atoms as the slab has (including buried layers that do not affect reactivity). Despite all the above, comparison between our  $\text{LDOS}_{\text{EF}}(\text{N})$  and the experimental thickness dependence of the oxidation rate (Figure 5-6(a) from [135]) does not indicate a clear correlation. In particular, our  $\text{LDOS}_{\text{EF}}(\text{N})$  does not display any sharp dip around  $\text{N}=10$  layers; thickness at which the oxidation rate is smallest. Furthermore, variations in the  $\text{LDOS}_{\text{EF}}(\text{N})$  for  $8 < \text{N} < 15$  are not large enough to explain the thickness dependence of the oxidation rate (Figure 5-6(c)). Neither do the peaks of the  $\text{LDOS}(\text{E})$  (Figure 5-5) shift monotonically as those observed in the valence band spectra for films of  $\text{N}=5-12$  [106, 135].

Binggeli *et al.* [137] have addressed the problem of the oxidation-rate thickness dependence in a different manner. They searched for a correlation between the oxidation rate and how much the electron density spreads beyond the surface over the vacuum ( $\lambda$ ) as well as how large the  $\Gamma$ -point DOS at  $E_{\text{F}}$  is. By analyzing their results, one sees that  $\lambda$  has a behavior exactly opposite to that of the oxidation rate (see Figure 5-8(c)). In other words, they found that large decaying lengths, corresponding to high  $\Gamma$ -point DOS at  $E_{\text{F}}$  [137], cause low oxidation rates. It is not clear, however, why films with charge density tails that extend the most into the vacuum and correspond to high  $\Gamma$ -point DOS at  $E_{\text{F}}$  would effectively hinder the oxidation of Mg(0001) and vice versa? In fact, one would expect exactly the opposite behavior. Moreover, in this work, the peak shift caused the substrate cannot account for the discrepancies since the influence of the W substrate was included [106, 137].

We have, therefore, reconsidered the electronic  $\text{DOS}(\text{E})$  from another perspective. A recent work has shown that in order to understand the reactivity of a surface via its electronic density of

states, it is necessary to identify and analyze the projections of the DOS(E) that predominantly participate in the bonding of the reactants. The reason is that the sum of all of them may hide essential features even if only the surface atoms are taken into consideration [139]. Such analysis may shed some light on the thickness dependence of the oxidation-rate if the LDOS(E) of the Mg films around  $E_F$  is the sum of directionally distinct parts and only some of them contribute to the bonding of a given adsorbate. In the case of Mg, although the valence electrons of isolated magnesium have s-character, 3s, in the extended systems, the 3p states can be partially occupied. In fact, we find that around the Fermi level, the electronic states have mostly p-character and, more unexpectedly, d-projections are not that negligible as one may think. Around the Fermi level, the contribution of 3d states of Mg is larger or comparable to that of s-states. In general, p- and d-states states, unlike s-states, have directional contributions ( $p_x, p_y, p_z, d_{xy}, d_{x^2-y^2}, d_{z^2}, d_{xz}, d_{yz}$ ). Because overlapping between states is also important in ionic bonds, these states may contribute less or more to the bonding of oxygen depending on the position it takes. For example, since O sits at hollow sites [136] and, in MgO, Mg atoms make planar bonds with O, then we postulate that in-plane states (oriented parallel to the surface:  $p_x, p_y, d_{xy}, d_{x^2-y^2}$ ) should be those mainly responsible for the bonding with oxygen. Furthermore, since the oxidation experiments estimate that only the first two layers are oxidized, we consider the second layer too. We have thus analyzed the sum of  $p_x, p_y, d_{xy}, d_{x^2-y^2}$ -states of the first- and second-layer atoms (the in-plane-projected LDOS integrated over the entire Brillouin zone and not only the  $\Gamma$ -point), expecting that variations in it should correlate with those in the oxidation rate. Indeed, Figure 5-5 shows that the position of the peaks around  $E_F$  of the in-plane-projected LDOS (PLDOS) shifts significantly as a function of film thickness in an orderly manner for  $N = 4 - 16$  [106].

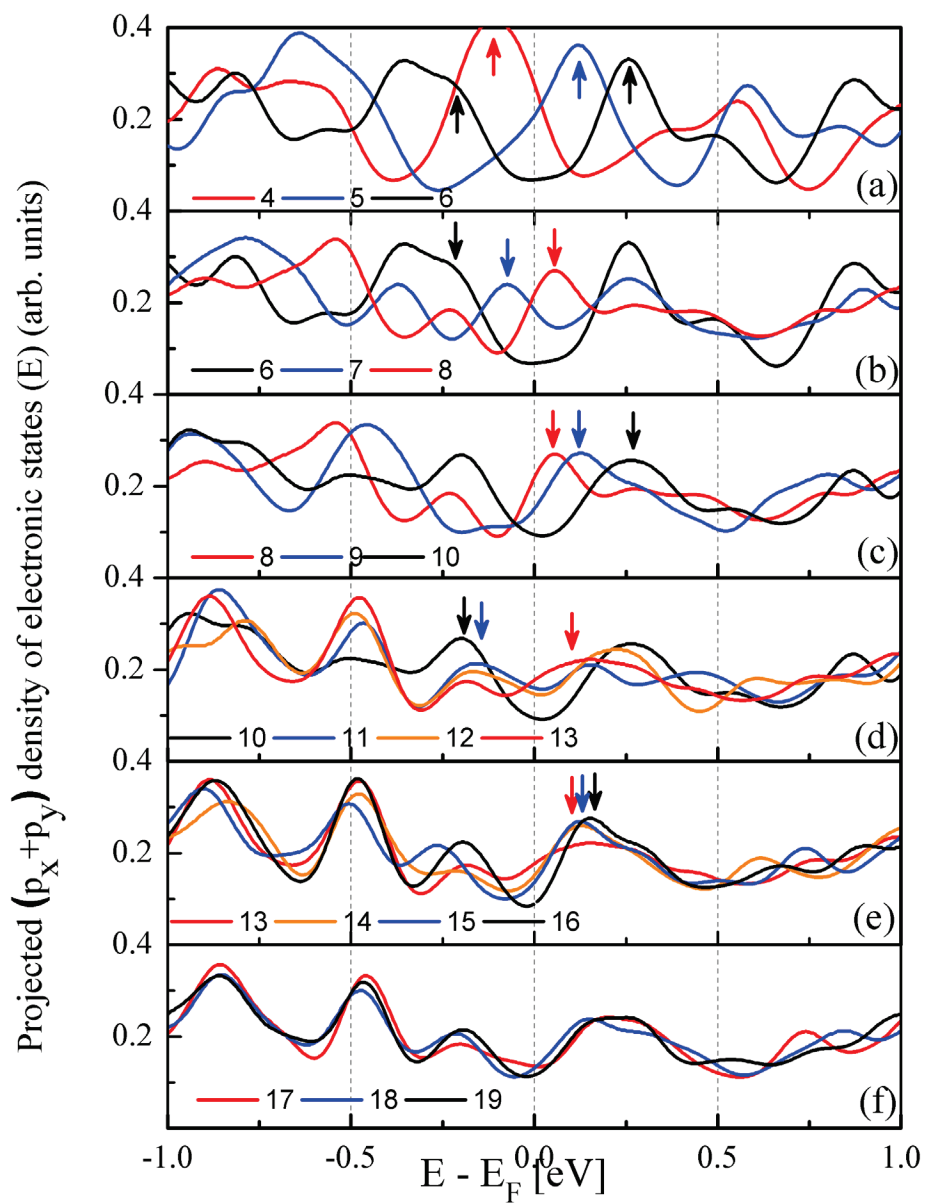


Figure 5-7. (Calculated in-plane ( $p_x+p_y+d_{xy}+d_{x^2-y^2}$ ) PLDOS of the first- and second-layer atoms of Mg(0001) for varying N (a) from 4 to 6; (b) from 6 to 8; (c) from 8 to 10; (d) from 10 to 13; (e) from 13 to 16; and (f) from 17 to 19. The PLDOS scale in each inset is the same. The arrows are a guide for the eye to identify the centroids of the PLDOS peaks around  $E_F$  and recognize how they shift as a function of number of layers [106].

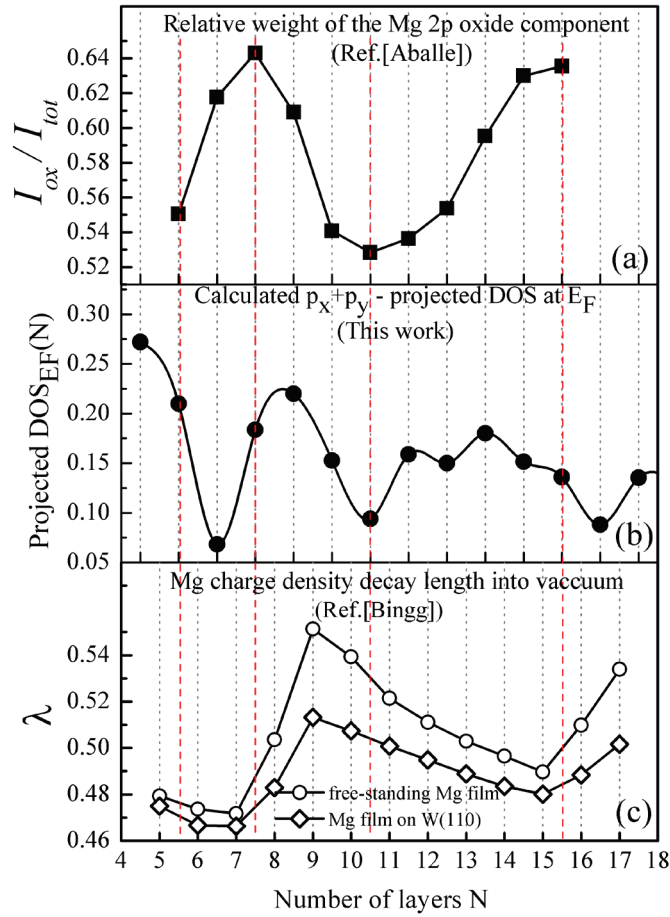


Figure 5-8. Comparison between experiment and theories to explain the oxidation rate of Mg films (a) The relative weight of the intensity of the oxygen-induced peak in the Mg 2p spectrum (indicative of the oxidation rate) as a function of the number of layers, N, taken from [135]; (b) Calculated in-plane ( $p_x+p_y+d_{xy}+d_{x^2-y^2}$ ) PLDOS $_{EF}(N)$  of the first- and second-layer atoms of Mg(0001); (c) Mg electronic charge density decay length into vacuum (calculated in analogy with the penetration depth of a wave-function into the classically forbidden region of the three dimensional finite square well) as a function of N, taken from [137]. The dashed line is a guide for the eye to compare the maxima/minima of the oxidation rate as a function of N with those of the calculation [106].

As a consequence, the in-plane-PLDOS(E) around  $E_F$  varies dramatic and oscillatory. Figure 5-8(b) shows more clearly that the in-plane-PLDOS at  $E_F$  as a function of the number of layers N, the in-plane-PLDOS $_{EF}(N)$ , has three conspicuous minima at N=6, 10, 16 and three maxima at N=4, 8, 13, to be compared with the observed oxidation rate that has two pronounced minima --- at N=5 and 10 --- and two maxima ---at N=7 and 15. The two steep minima of in-

plane-PLDOS<sub>EF</sub>(N) at 6 and 10 layers may be associated to those in the oxidation rate at 5 and 10 layers (Figure 5-8(b)). Also, our calculated in-plane-PLDOS<sub>EF</sub>(N) increases as N increases from 10 to 13, just as the oxidation rate does. The oxidation rate and the in-plane-PLDOS<sub>EF</sub>(N) only differ in that the former keeps increasing until the thickness reaches 15 layers, while the latter decreases from N=13 to 15. The in-plane-PLDOS<sub>EF</sub>(N) continues oscillating for N ranging from 17 to 26 layers but the amplitude is marginal, as seen from Figure 5-7(f). We thus conclude that the thickness dependence of the oxidation rate of Mg thin films (N<17) is directly related to the in-plane-PLDOS(E) of the first- and second-layer atoms around the Fermi level, as integrated over the entire Brillouin zone [106].

#### 5.1.3.1.5 New Insights into the Charge density Friedel Oscillations

In this subsection, we revisit the charge density Friedel oscillations occurring inside a Mg slab to discover how exactly they affect the charge distribution around the surface. As mentioned in the introduction, the charge density Friedel oscillations present inside a Mg slab have been corroborated more than one decade ago in [129, 134, 140]. Cho *et al.* [141] and later Staikov and Rahman [129] and Wachowicz and Kiejna [134] obtained the one-dimensional enhancement of the valence charge density (parallel to the surface) as a function of the position perpendicular to the surface, the z-axis, and localized the maxima and minima of the Friedel oscillations in Mg(0001) slabs. In order to do that, they all calculated the difference between the xy-average valence charge density profile of bulk Mg and that of a bulk-terminated slab. This result was then normalized it over the charge density profile of the bulk. Later on, Wachowicz and Kiejna [130] presented a more detailed view of the charge redistribution in Mg(0001) by using 2D cross sectional charge-density difference contours (see Figure 5-9) [106].

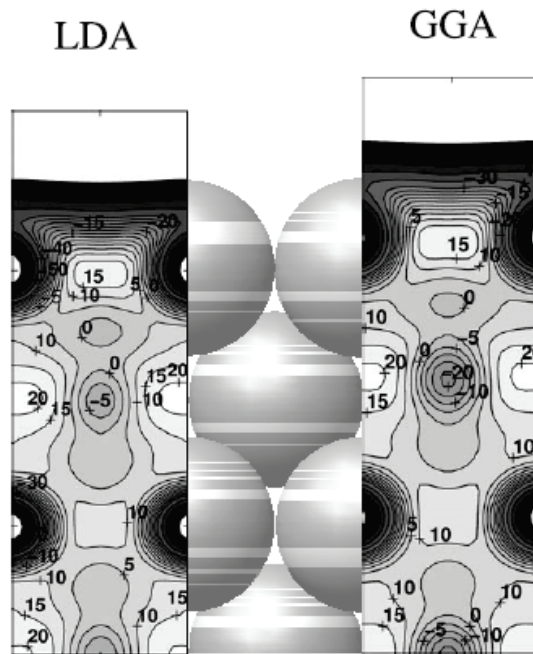


Figure 5-9. Fig. 4 from [130] 2D Electron-density-difference distributions near the relaxed Mg(0001) surface relative to the average electron density in the bulk expressed as a percentage of the latter and cut along the (10-10) plane. The atomic configuration commensurates with the optimized positions calculated in the LDA is also shown. Darker grey is used to indicate regions with smaller charge density while lighter shades represent regions with charge density above average. [Copyright included in Appendix A]

Although not mentioned in their work, the 2D plots of Wachowicz and Kiejna clearly show that the charge density Friedel oscillation peaks depicted in the 1D view [129] correspond to the interstitial space between the atoms at the surface. Yet, as we shall see in the following section, a three dimensional (3D) inspection of the Friedel oscillations is still lacking in order to locate exactly which region of the interstitial space is holding that “extra” charge and thus understand its effect on the binding of adatoms and their diffusion [106].

Before turning to new insights into Friedel oscillations through a 3D inspection, we must make some remarks about the current understanding of why the Friedel oscillations cause the interlayer expansion (5.3.2.1(a)). Based on these charge density profiles for Mg(1010) [141] and

Mg(0001) [129] and Be(0001) [130], it has been concluded that atoms at the first, second and third layers are effectively negatively charged. Hence, according to this interpretation, these ionic layers repel, causing the well-known interlayer expansion. However, some observations about this interpretation are in order. Namely, among atoms of the same species charge transfer is not possible as the atoms have the same electronic affinity and thus ionicity cannot be considered to describe their bonding. Moreover, were the atoms effectively negatively charged, we should find positively charged atoms somewhere else for the system to be neutral, just as in any ionic bonding. Say, if the first four Mg layers were effectively negatively charged, one would need other Mg layers positively charged (by the same magnitude). In reality, Fig. 4 (Cho *et al.*), Fig. 1 (Staikov *et al.*) and Fig.1 (Wachowicz *et al.*) of references [129, 134, 141] do not imply that the atoms are effectively charged; they only indicate that, since the first largest charge density peaks of the Friedel oscillations coincide with the position of the atomic layers, upon surface formation the bonding charge abandons the interlayer space and becomes more localized around the atomic layers [106].

Thus, from the one-dimensional average density, one could only say that the layer might be approaching to a free-standing monolayer condition. In summary, the layers are not effectively charged and all what the Friedel oscillations do is to reduce the interlayer charge. Naturally, this weakens the metallic bond and causes the first three layers to separate from each other. The latter will be further evidenced when we turn to the binding of a full Mg layer, whose binding energy per atom is only  $\sim 1.1$  eV [106].

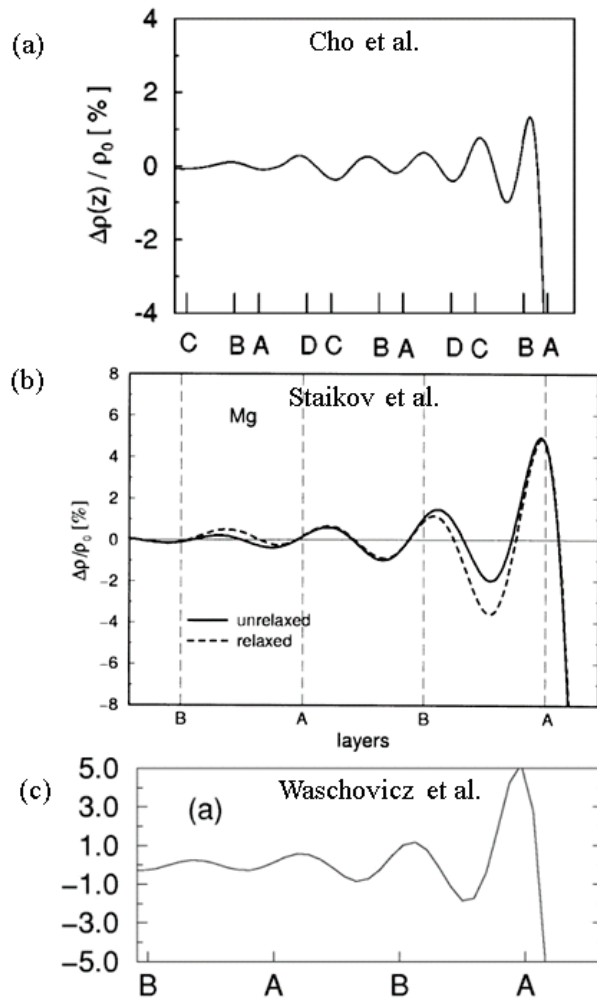


Figure 5-10. Change in the charge density profiles perpendicular to the surface for the bulk-truncated surfaces of Mg(0001). The electron densities are normalized by the average bulk value The figures are adopted from (a) Fig. 4 (Cho *et al.*), (b) Fig. 1 (Staikov *et al.*) and (c) Fig.1 (Wachowicz *et al.*) of references [129, 134, 141]. [Reprinted Figure with permission from “J. Cho, Ismail, Z. Zhang and E.W. Plummer, Phys. Rev. B 59, 1677–1680 (1999). Copy right (1999) by the American Physical Society ” and “Reprinted Figure with permission from “P. Staikov, Talat. S. Rahman, Phys. Rev. B 60, 15613–15616 (1999). Copy right (1999) by the American Physical Society.” and see Appendix A]

Once we have clarified that previous calculation have actually revealed that the Friedel oscillations reduce the interlayer bonding charge and send that charge around the layer, we turn to find where exactly that charge is localized.



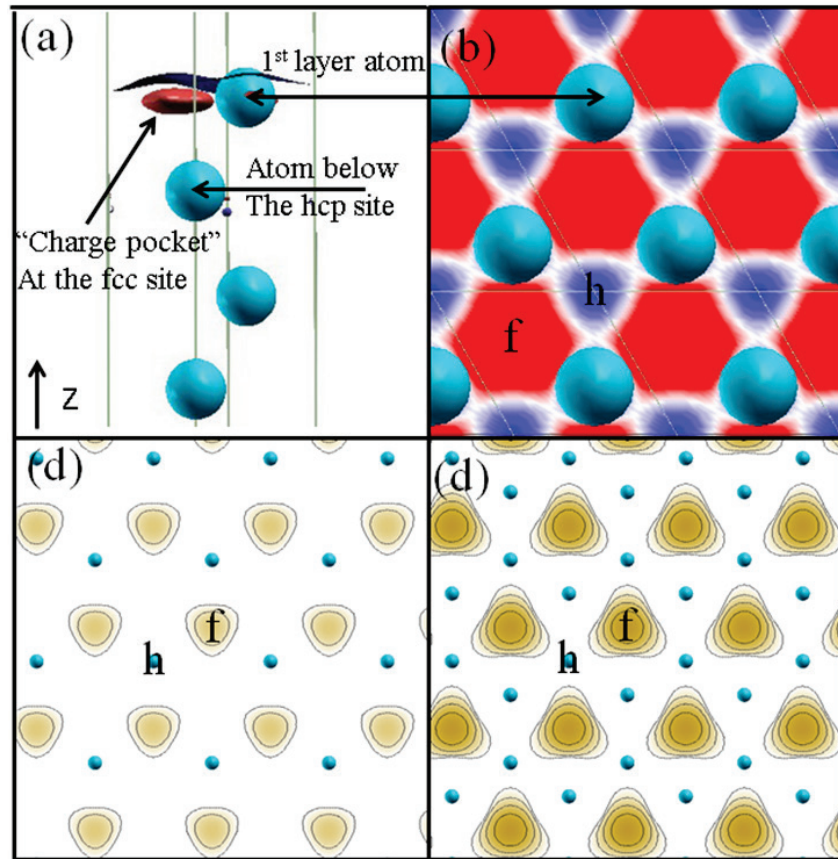


Figure 5-11. (higher insets) Difference between the charge density of bulk Mg and that of a non-relaxed bulk-terminated Mg(0001) surface (a) Isosurfaces. The z-axis is perpendicular to the surface. The blue balls represent the first four layers of the slab. The red color indicates the region of Mg(0001) that displays more charge density than the corresponding one in bulk Mg. (b) [0001] Cross section of the isosurface in (a). (Lower insets) [0001] Cross sectional planes of the total charge density around (c) the fully relaxed Mg(0001) and (d) bulk Mg. Darker (brown) regions in (c) and (d) indicate less charge. In (b)-(d), the plane is located at the height of the surface or bulk atoms under consideration in order to highlight the charge accumulation around the fcc hollow site of Mg(0001) [106].

To this end, we plot in Figure 5-11(a) the difference between the charge of bulk Mg minus that of a 18-layer slab -- as in previous calculation -- but this time in three dimensions. First of all, in agreement with [129, 134], we find that the displaced charge in Mg(0001) slabs is indeed located mainly around the position of the first layer and, as shown in [130], it is localized around the interstitial space between the atoms at the surface [106].

But more importantly, the present sight through 3D difference isosurfaces reveals in addition that the displaced charge lies at the fcc infinite-hollow site of Mg(0001) (red pocket). Figure 5-11(b) shows the [0001] cross section of the charge-density-difference isosurfaces in part(a). The latter two-dimensional view allows us to see that the charge excess extends up to the bridge, whereas the charge around at the hcp site is slightly reduced. We shall see that the latter features have implications on the Mg adatom binding energy and its diffusion. Yet, a word of caution has to be given before turning to these matters. Note that, in order to capture the Friedel oscillations, previous calculations and our Figure 5-11(a) and (b) display differences between the charge density of bulk Mg and that of a bulk-terminated slab. However, nothing guarantees that upon relaxing the forces on the atoms of a bulk-terminated slab the charge density enhancement remains as depicted in Figure 5-11(a) and (b). This uncertainty is particularly undesirable if we want to understand the effect on adatom binding and diffusion barriers. Therefore, in Figure 5-11(c) and (d) we contrast the [0001] cross section of the total charge density of a totally relaxed Mg slab at the surface layer (Figure 5-11(c)) and at a layer deep in the bulk (Figure 5-11(d)). Contrasting these two figures demonstrates that the charge density around the surface (totally relaxed) is enhanced around the fcc site with respect to the charge density of bulk layers even after force relaxation [106].

#### 5.1.3.2 Binding and Stacking Fault of an Mg Adatom and of Adislands on Mg(0001)

In this section, we shall see that the charge accumulation around the fcc site caused by the Friedel oscillations is of consequence for the binding and stacking of small Mg adatom islands on Mg(0001) [106].

#### 5.1.3.2.1 Adatom Binding Energy

First of all, we shall test the convergence of the binding energy. Table 2 displays the binding energy of a Mg adatom on Mg(0001) at the fcc and hcp sites for slabs of four thicknesses (N=3,5,7 and 9). As expected from the electronic DOS of the surface atoms, the binding energy of the adatom converges slowly. From N=5 to N=7, the binding energy drops by as much as 50 meV and from N=7 to N=9 increases by almost 30 meV. These variations are significant and measurable, but the fact that the surface properties analyzed in Section 2(a) and (b) for 9-layer slabs do not vary dramatically from the converged values, we can safely conclude that the convergent adatom binding energy is about 0.6 eV [106].

The binding of Mg adatoms on Mg(0001) has already been categorized as weak. Earlier effective medium calculations yielded that the adatom binding energy (0.85 eV [142]) is only about 57% Mg cohesive energy. Clearly, our calculations indicate that the binding is significantly weaker than that [106].

#### 5.1.3.2.2 Stacking Fault Preference for monomer on an fcc site

The same effective-medium calculations mentioned above reported that the binding energy of Mg adatoms on Mg(0001) is the same at the hcp site as that at the fcc site (site unspecificity). However, in this work we shall show that the the fcc site (fault site) is energetically more favorable for the adatom than the hcp site (See Table 5-4) [106].

Table 5-4. Slab thickness dependence of the adatom binding energy at the fcc and hcp sites,  $E_B(\text{fcc})$  and  $E_B(\text{hcp})$ , respectively, and of the stacking fault energy,  $\Delta E_B = E_B(\text{fcc}) - E_B(\text{hcp})$  [106].

N	$E_B(\text{fcc})$ (eV)	$E_B(\text{hcp})$ (eV)	$\Delta E_B$ (meV)
3	-0.727	-0.700	-27
5	-0.644	-0.627	-17
7	-0.597	-0.581	-16
9	-0.633	-0.618	-15

First, we notice that while convergence of the adatom binding energy down to few meV may require also up to 18 layers, the stacking fault energy is well described by 7-layer thick films. This is because the stacking fault energy involves energy differences and these are less sensitive than the energies themselves. Second, we notice that the stacking fault energy favors the fcc site by an unexpectedly large energy: 15 meV. This stacking fault energy is as large as that found for Ir/Ir(111) (16 meV [143]). Naturally, the origin of these apparently similar phenomena is completely different and it is worth to clarify it. Ir atoms are held together by particularly strong covalent bonds and thus the favored stacking fault in Ir(111) compensates the low-coordination of the adatom by sitting at the hollow site (hcp) that is directly above another Ir atom instead of sitting at the “correct” hollow site (fcc) in which the next Ir atom is one more layer away. In diametral contrast, Mg(0001) is a nearly free-electron metal in which the adatom prefers to sit at the fcc infinitely hollow site (no other atom is directly below) rather than at the site that is directly above another Mg atom! In other words, the stacking fault preference in Mg and Ir have opposite effect: Ir adatoms on Ir(111) prefer to be over coordinated while Mg adatom prefer to be low coordinated [106].

### 5.1.3.2.3 Stacking Fault Energy of Adislands

The preference for the fcc stacking fault is not exclusive to the monomer. We have calculated the binding energy per atom ( $E_B$ ) of several Mg adislands – from monomer to octamer – and of a full overlayer placed at both the fcc and the hcp sites. For the dimer and trimer, several configurations and orientations were tested. Table 5-5 shows the energetics of the adislands of at fcc and hcp sites (the data for the most stable dimer and trimer) [106].

Table 5-5. Binding energy,  $E_B$ , and stacking fault,  $\Delta E_B$ , per atom of Mg adislands on Mg(0001) – from a monomer to an octamer – and of a full overlayer placed at both the fcc and the hcp sites for a structure in which (a) the whole system is totally relaxed (b) only the Mg adisland atoms are allowed to relax but the Mg(0001) substrate is kept frozen [106].

N	Totally relaxed			Frozen substrate	
	$E_B(\text{fcc})$	$E_B(\text{hcp})$	$\Delta E_B$ (meV)	$E_B(\text{fcc})$ (eV)	$E_B(\text{hcp})$
Monomer	-0.60	-0.58	-15	-0.58	-0.57
Dimer	-0.75	-0.74	-4	-0.73	-0.75
Trimer	-0.75	-0.74	-10	-0.74	-0.73
Tetramer	-0.78	-0.78	1	-0.77	-0.77
Hexamer	-0.92	-0.92	4		
Heptamer	-0.93	-0.95	11		
Octamer	-1.02	-1.03	12		
Full	-1.09	-1.11	15		

Our calculations exhibit that the preference for the fcc stacking fault persists at least up to the trimer. Furthermore, it shows that the behavior of these small adislands is not qualitatively dependent on whether the position of substrate atoms is kept frozen or not [106].

We cannot rule out that bigger islands also display a preference for the stacking fault because in our calculation, as the adislands grow larger (tetramer, hexamer, heptamer and octamer), they necessarily interact with each other and favor again hcp [106].

In fact, a full layer prefers the hcp site over the fcc stacking fault by 15 meV per atom (See Table 5-5). So what our calculations actually suggest that as the islands get closer to each other the preferred site is again the hcp one. In our particular supercell setup, the turning point between fcc and hcp preferred binding corresponds to a coverage between one-third and one-half monolayer [106].

#### 5.1.3.2.4 Structural Characterization of the $Mg_n$ Adislands on Mg(0001)

We now turn to investigate the origin of the preference of the fcc stacking fault. In pursuing this aim, we shall examine the adislands that display this preference (from monomer to trimer) and the turning-point adisland to the hcp preference, the tetramer. As a preliminary step we analyze the bond-length of the Mg adatom/adislands adsorbed on Mg(0001) when the whole system is allowed to relax and when the substrate is kept frozen. The structural characterization is presented in Table 5-6 and Table 5-7, respectively [106].

However, upon analyzing the data, we find that neither, the distances among the adisland atoms, the height of the adisland with respect to its substrate nearest neighbors (NN) or the distances among the adisland NNs provide a hint about the mechanism behind the stacking fault preference or establish a consistent bond-order trend. For example, the data for the monomer could in principle indicate a slight tendency of the adatom to stay farther from its substrate neighbors (weaker bond) when sitting at the hcp site than when sitting at the fcc site. However, the opposite trend is displayed by the trimer whether the substrate is relaxed or not. The structure

of the dimer on Mg(0001) does not provide much insight either. The dimer in the totally relaxed system (Table 5-6) actually reflects that the hcp-hcp configuration is not stable: the dimer spontaneously slides toward the bridge, almost reaching the fcc sites. As a result, it displays two relatively short bonds and two bonds that are significantly longer than the lattice parameter,  $a$ . One could think that such instability of the hcp site could “cause” to the stacking fault preference. However, it is the reverse. The stacking fault preference causes the instability of the hcp site: Allowing both the dimer and the substrate to relax toward the bridge-like configuration minimizes the fcc stacking fault preference, whereas if the substrate is frozen, the hcp configuration of the dimer is stabilized but the hcp site becomes even less favorable than the fcc site. Furthermore, the bonds related to the tetramer are so spread out that it is not possible to draw any conclusion. Clearly, no argument can be built upon the bond lengths [106].

Table 5-6. Structural characterization of the Mg adislands -- dimer, trimer and tetramer – on the Mg(0001) surface. These values correspond to the case in which all atoms are allowed to relax. The distance among atoms forming the adislands are denoted by  $d_{IA}$ ;  $Z_{AS}$  stands for the height (vertical distance) of the atoms forming the adisland with respect to their non-equivalent substrate neighbors,  $d_{NN-S}$  stands for distance between the atoms forming the island and their substrate non-equivalent nearest neighbors [106].

adisland	$d_{IA}$	$Z_{AS}$	$d_{NN-S}$
Monomer-fcc		2.47	3.12
Monomer-hcp		2.48	3.12
Dimer-fcc	2.97	2.46, 2.64, 2.34	3.08, 3.09, 3.24
Dimer-hcp	2.96	2.46, 2.65, 2.36	3.04, 3.06, 3.42, 3.72
Trimer-fcc	3.06	2.43, 2.51, 2.51	3.10, 3.10, 3.13
Trimer-hcp	3.06	2.50, 2.50, 2.40	3.10, 3.10, 3.10
Tetramer-fcc	3.07, 3.08, 3.09	2.54, 2.42, 2.62	3.08, 3.14, 3.20
	3.10, 3.11, 3.11	2.60, 2.38, 2.38	3.10, 3.11, 3.11
Tetramer-hcp	3.09, 3.09, 3.13	2.44, 2.55, 2.36	3.09, 3.13, 3.19
	3.09, 3.09	2.60, 2.36, 2.36	3.08, 3.10, 3.10
	3.07, 3.07	2.40, 2.47, 2.47	3.06, 3.10, 3.10

Table 5-7. Structural characterization of the Mg adislands -- dimer, trimer and tetramer -- on the Mg(0001) surface. These values correspond to the case in which only the atoms of the adisland are allowed to relax while the atoms of the substrate are kept frozen. The distance among atoms forming the adislands are denoted by  $d_{IA}$ ;  $Z_{AS}$  stands for the height (vertical distance) of the atoms forming the adisland with respect to their non-equivalent substrate neighbors,  $d_{NN-S}$  stands for distance between the atoms forming the island and their non-equivalent substrate nearest neighbors [106].

adisland	$d_{IA}$	$Z_{AS}$	$d_{NN-S}$
Monomer-fcc		2.53	3.13
Monomer-hcp		2.53	3.14
Dimer-fcc	3.01	2.53,2.53,2.53	3.08,3.18,3.16
Dimer-hcp	3.02	2.52,2.52,2.52	3.06,3.16,3.17
Trimer-fcc	3.06	2.50,2.50,2.50	3.09,3.09,3.16
Trimer-hcp	3.07	2.49,2.49,2.49	3.08,3.08,3.15
Tetramer-fcc	3.08,3.08	2.49,2.49,2.49	3.13,3.14,3.20
	3.14, 3.14	2.49, 2.49, 2.49	3.05, 3.14, 3.14
	3.08, 3.08	2.50, 2.50, 2.50	3.10, 3.10,3.15
Tetramer-hcp	3.09,3.09,3.13	2.53,2.53,2.53	3.09,3.11,3.12
	3.13,3.13	2.48, 2.48,2.48	3.03, 3.13, 3.13
	3.09, 3.09	2.48, 2.48,2.48	3.08, 3.08, 3.13

#### 5.1.3.2.5 Friedel Oscillations and Stacking Fault with Adislands

Let us now turn to a charge density analysis. We know by the Hohenberg-Kohn theorems that if small Mg adislands prefer the fcc site over the hcp site, that must necessarily be reflected in the charge density distribution. In this subsection, we thus scrutinize the charge density (CHD) distribution to locate the features responsible for such preference. In fact, that the enhanced charge density around the first layer -- derived from the Friedel oscillations -- lies precisely at the fcc site may suggest that the “extra” CHD pocket (Figure 5-11(a)) contributes to bind the adatom. Still, such explanation begs the question: why would those factors promoting the stacking fault stop operating as the adisland reaches the size of a tetramer or as the adislands approach each other? We shall see that although the “extra” CHD pocket does causes the



stacking fault preference, its role is not as simple as that of strengthening the adatom bonds. In fact, Figure 5-11 shows that for both the totally relaxed and the bulk-terminated Mg(0001), the fcc site render less charge density than the hcp site despite the “extra” CHD pocket. Still, Fig.10 also indicates that both the totally relaxed and the bulk-terminated Mg(0001) display qualitatively the same landscape to the adatom and we shall use that qualitative similitude in the following [106].

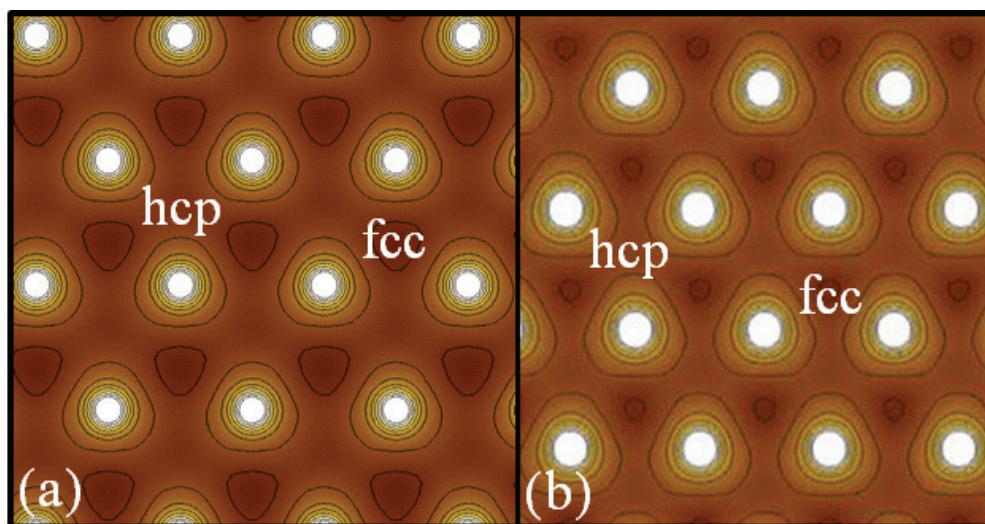


Figure 5-12. [0001] Cross section of the total charge density of (a) non-relaxed bulk-terminated Mg(0001) and (b) fully relaxed Mg(0001). Darker (brown) regions indicate less charge. The plane is located at  $\sim 1.2 \text{ \AA}$  above the position of the surface atoms [106].

The goal of understanding the CHD distribution responsible for the preference of small islands to sit at fcc sites rather than at hcp sites is not an easy task. Actually, it would not be reasonable trying to trace the answer via CHD differences (as those shown for the clean surface in Figure 5-11(a) and (b)). The reason is that we are after CHD variation causing a stacking-fault energy of only few meV, energy values that are likely to be smaller than those caused by the inherent errors in the CHD differences analysis. Namely, in order to obtain a CHD difference, it

is necessary to evaluate  $\delta\rho = \rho[\text{Mg}_n/\text{Mg}(0001)] - \rho[\text{Mg}(0001)] - \rho[\text{Mg}_n]$ , where  $\rho[\text{Mg}_n/\text{Mg}(0001)]$  is the CHD of the entire system relaxed (n-mer plus the surface),  $\rho[\text{Mg}(0001)]$  is the CHD of the clean surface and  $\rho[\text{Mg}_n]$  is the charge of the isolated n-mer,  $\text{Mg}_n$ . Yet, the positions of the atoms used to compute  $\rho[\text{Mg}(0001)]$  and  $\rho[\text{Mg}_n]$  are extracted from those in the relaxed full systems and not the actual relaxed coordinates of  $\text{Mg}(0001)$  and  $\text{Mg}_n$ . Therefore, one can expect that the errors introduced by the unphysical CHD of the non-relaxed  $\text{Mg}(0001)$  and the non-relaxed  $\text{Mg}_n$  are much larger than the stacking fault energies we are trying to trace. In fact, such analysis does not provide rationale for the stacking fault [106].

The only option is to investigate the total CHD of the composite system,  $\rho[\text{Mg}_n/\text{Mg}(0001)]$ . The approach of visualizing the total valence charge involved in the bonds is not free of challenges. On the one hand, three dimensional plots do not reveal a CHD profile within a charge interval but isosurfaces for a fixed charge density value. On the other hand, turning to analyze two-dimensional cross-sectional CHD profiles (e.g. planes parallel to the surface) is not straightforward because comparisons ought to be made between the monomer at fcc and the monomer at hcp, between the monomer cases and the dimer cases and so on, but in each of these cases the height of the adisland (A) with respect of the surface atoms (S),  $Z_{AS}$ , varies significantly, as shown in Table 4, and a fair comparison could be compromised [106].

Nevertheless, since both the totally relaxed and the bulk-terminated  $\text{Mg}(0001)$  display qualitatively the same landscape to the adatom and the stacking fault energy trend is also qualitatively the same, we can grasp the essentials of the charge density distribution responsible for the stacking fault preference in small adislands by first considering the frozen bulk-terminated  $\text{Mg}(0001)$ . We have thus relaxed only the n-mers ( $n=1,\dots,4$ ) at the fcc and hcp sites on

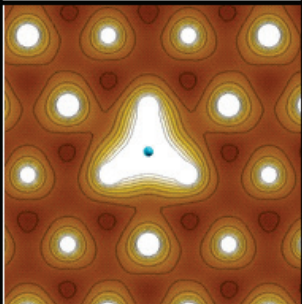
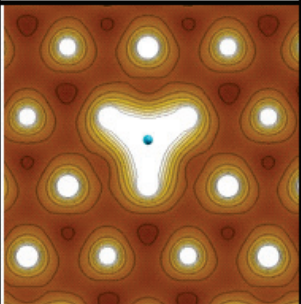
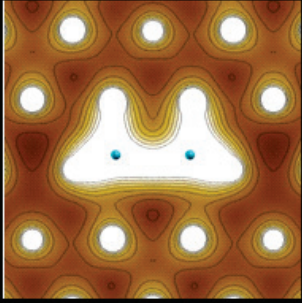
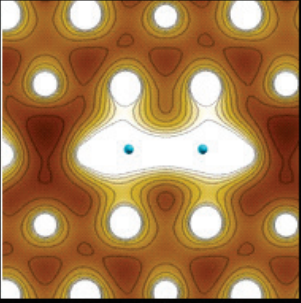
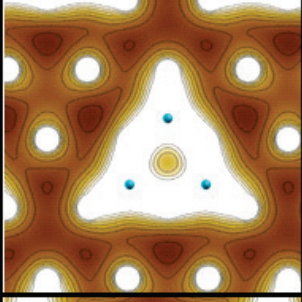
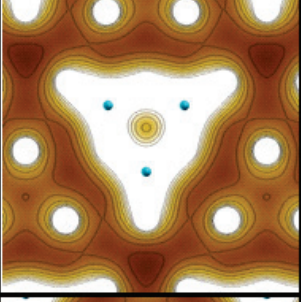
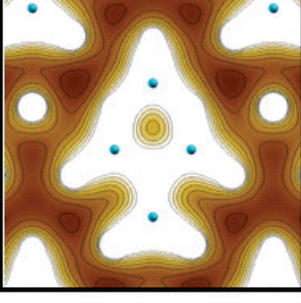
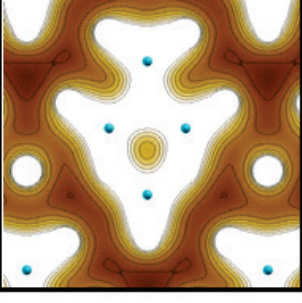
a bulk-terminated Mg(0001). Since in this case, the adislands heights do not vary as much as for the totally relaxed system (See  $Z_{AS}$  in Table 5-6 and Table 5-7), this allows us to make a meaningful comparison: We compare two-dimensional CHD profiles of all the adislands for planes at exactly the same height with respect to the substrate. The two-dimensional CHD profiles of  $\rho[\text{Mg}_n/\text{Mg}(0001)]$  described above are displayed in Table 6. The height of the CHD plane (1.2 Å above the surface) lies between the adatom/adisland and the surface atoms. It was easily chosen because the charge profiles at other heights for a given n-mer are very similar at fcc and hcp site except around the plane shown in Table 5-8 [106].

Most importantly, the two-dimensional profiles of  $\rho[\text{Mg}_n/\text{Mg}(0001)]$  in Table 6 reveal that when the monomer sits on the fcc site, the bonds among its NN substrate atoms are strengthened, rather than those between the monomer and its substrate NN atoms. Table 6 also demonstrates that while the same effect is displayed by the fcc dimer, it does not occur for the hcp monomer or the hcp dimer. In the case of the trimer, the CHD profiles at hcp and fcc are more complex and less distinct. However, by analyzing each of its bonds to neighboring atoms in the substrate, one see they are furnished with more CHD that when the trimer sits at hcp sites. For the tetramer, when the adislands start to strongly interact, only subtle features might indicate a more energetically favorable configuration at the fcc site. Not surprisingly, the stacking fault energy becomes very small [106].

Table 5-8. Two-dimensional plots of the total charge density of the n-mers ( $n=1, \dots, 4$ ) at the fcc and hcp sites of a bulk-like Mg(0001) substrate. The plots correspond to a plane parallel to the substrate at  $\sim 1.2 \text{ \AA}$  above it (see Sec.3d). The scale is such that dark regions denote less charge. The left-most column displays the stacking-fault energy per atom,  $\Delta E_B$ . [106]

	fcc	hcp	$\Delta E_B$ (meV)
Monomer			-14
Dimer			-10
Trimer			-12
Tetramer			-2

Table 5-9. Two-dimensional plots of the total charge density of the totally relaxed n-mers ( $n=1,\dots,4$ ) at the fcc and hcp sites of Mg(0001). The plots correspond to a plane parallel to the substrate at  $\sim 1.2$  Å above it (see Sec.3d). The scale is such that dark regions denote less charge. The left-most column displays the stacking-fault energy per atom,  $\Delta E_B$ . (\*) Note that, strictly speaking, the dimer does not sit at hcp sites but rather at the bridge [106].

	fcc	hcp	$\Delta E_B$ (meV)
Monomer			-15
Dimer			-4*
Trimer			-10
Tetramer			1



The insight provided by  $\rho[\text{Mg}_n/\text{Mg}(0001)]$  when the substrate is kept frozen can now be used to make a step forward. Once we have identified the feature of the charge density redistribution that could account for the preference of the fcc stacking fault, we can proceed to trace the same features in the two-dimensional profiles of  $\rho[\text{Mg}_n/\text{Mg}(0001)]$  when the entire system is allowed to relax. To our surprise, the similar features appear for the totally relaxed system and at practically the same distance from the substrate atoms ( $\sim 1.2 \text{ \AA}$ ) [106].

Specifically, having the monomer at fcc site also induces a charge density enrichment in the bonds between its NNs and other neighboring atoms that does not appear when the monomer sits at the hcp site. In the case of the dimer, one sees that the dimer at the fcc site also induces a charge density enrichment in the bonds between its NNs and other neighboring atoms, yet, the same happens when the dimer is at the bridge (rather than hcp) position and at a larger extent. So, the fact that it is unstable at the hcp site ruins any possible comparison. Nevertheless, the features in the charge density when the dimer sits at the hcp, although not adding to the supporting evidence, are not enough to rule out our argument because the strong enrichment of the bonds between its NNs and other neighboring atoms occurs also at the expense of or accompanied by a bond breakage its bonds with two neighbors (See Table 5-7 and Table 5-8). Overall, the energy associated to the fcc stacking fault preference is reduced significantly to 4 meV per atom. The trimer at fcc, in contrast, is favored by as much as 10 meV per atom and induces a charge density enrichment in the bonds between its NNs and other neighboring atoms that does not appear when the monomer sits at the hcp site. As we turn to the tetramer, one sees that the bonds between its NNs and other neighboring atoms are furnished by extra charge

density at both sites. However, at the hcp site, which becomes more favorable, the charge enrichment is slightly larger [106].

Based on the above analysis, we propose that the role of the charge-density pocket and is that of strengthening the substrate bonds and that is the reason for which the fcc site is preferred over the hcp. In other words, the extra charge density pocket at the fcc site tends to be distributed among the surface atoms enhancing their mutual binding and possibly reducing the electronic kinetic energy. A similar behavior happens for the hcp adislands but only when they approach each other. The plots in Tables 6 and 7 also provide a rationale for the decline in the preference for the fcc stacking fault as the adisland grow larger and/or coalesce. For example, by comparing the CHD profile between the clean surface (Figure 5-12(b)) and monomer (at fcc in Table 5-8), one sees that the charge density at neighboring fcc sites from the monomer is reduced. That indicates that the enhanced bonding among substrate atoms does not withdraw charge exclusively from the site where the monomer sits but also does it from neighboring fcc sites. The same trend we find by comparing the effect on neighboring fcc sites of the monomer environment and those of the dimer: Again, the neighboring fcc sites of the dimer become more depleted, and so on. For the trimer and tetramer at fcc, one clearly sees that neighboring fcc sites are significantly more charge-depleted than in the clean surface [106].

Up to now, we have shown the features of the charge density distribution responsible for the preference of small islands to sit at fcc sites rather than at hcp sites. However, this is only indirect evidence that the stacking fault is caused by the Friedel oscillations. We thus find necessary and opportune to strengthen our argument by testing another material. We shall thus consider Be(0001), another hcp sp- and nearly-free-electron metal that is also strongly influenced

by Friedel oscillations [130]. The question is three-folded: (1) whether the maxima of the FO are also around the first layer; (2) whether they also induce a charge accumulation precisely at the fcc site and (3) whether Be monomer at least does also prefer the fcc stacking fault. The Ref. [130] answer the first question: Be(0001) also display the maxima of the Friedel oscillations at the first layer. Notice that the maxima of the Friedel oscillations appear to be less conspicuous than those of Mg(0001) (See Fig.? of [130]). The reason is that they divide the charge density differences by the charge density of the bulk in order to present a normalized value. However, in that way it is not highlighted that since Be holds much smaller bonds than those of Mg, therefore, the charge density around Be atoms is in general much larger than that in Mg. As a result, Fig.? of [130] does not anticipate that the Friedel oscillation maxima are, in absolute value, more larger than those of Mg. In Figure 5-13, we compare the Friedel oscillations in Mg(0001) and Be(0001) by three dimensional charge-density difference [106].

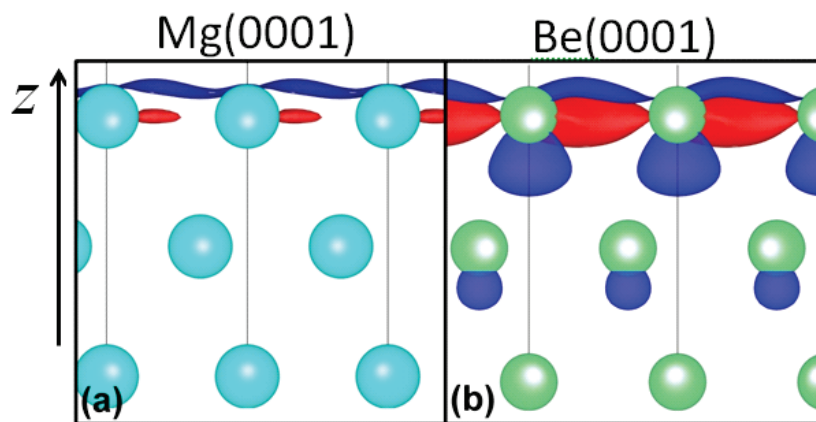


Figure 5-13. Three dimensional charge-density difference isosurfaces showing the Friedel oscillations in (a) Mg(0001) and (b) Be(0001). The charge density isovalue is the same for both surfaces. The difference is taken between the charge density of bulk Mg and that of a non-relaxed bulk-terminated Mg(0001) surface. The z-axis is perpendicular to the surface. The light blue and green balls represent the three layers of the slab. The red surfaces indicate the regions in the surface displaying more charge density than the corresponding one in bulk [106].



Clearly, the charge density enhancement at the fcc for Be(0001) is dramatically larger than that found for Mg(0001). Most importantly, the Be monomer on Be(0001) indeed prefers the fcc stacking fault site than the hcp site. And, further evidencing that the stacking fault preference is driven by the charge-density pocket, the latter, which is so big for Be(0001), causes a strikingly large stacking fault energy of 44 meV favoring the fcc site. To our knowledge this is the first time, the stacking fault of Be on Be0001 is reported as well as the mechanism responsible for it [106].

In summary, we have shown that the fcc stacking fault preference of the Mg adatom on Mg(0001) --- and of the Be adatom on Be(0001) --- is a result of the extra charge density at the fcc site derived from their Friedel oscillations [106].

### 5.1.3.3 Self-Diffusion of Mg Adatom on Terraces

Finally, we shall turn to the diffusion barrier of the Mg adatom on Mg(0001). Table 5-10 shows that just as in the case of the stacking fault energy, the diffusion barriers from fcc to hcp and from hcp to fcc are also well described by 7-layer thick films [106].

Table 5-10. Slab thickness dependence of the adatom diffusion energy barrier from fcc to hcp,  $\Delta E_D(\text{fcc} \rightarrow \text{hcp})$ , and from hcp to fcc,  $\Delta E_D(\text{hcp} \rightarrow \text{fcc})$  [106].

N	$\Delta E_D(\text{fcc} \rightarrow \text{hcp})$ (meV)	$\Delta E_D(\text{hcp} \rightarrow \text{fcc})$ (meV)
3	23	6
5	23	6
7	25	9
9	25	9

Again, the reason is that energy differences cancel out the errors in the minuend and subtrahend derived from the fact that these quantities are not converged. The energy barriers (25

and 9 meV) are very small compared to those of any transition metal. The order of magnitude of the barrier is in very good agreement with effective-medium calculations [142], which yielded the two energy barriers to be  $\sim 20$  meV [106].

Something that calls our attention, however, is that our barrier is quite asymmetric, in contrast to what effective-medium calculations [142] indicate. Thus, our calculations predict that at sufficiently low temperatures (few Kelvin) the adatom should very rarely be found at the hcp site. The barriers are equal according to effective-medium calculations because they did not render neither the fcc stacking fault preference nor a preference for the hcp site (site unspecificity), indicating that they do not grasp the Friedel oscillations. Then, the site unspecificity can be understood from the CHD profiles in Figure 5-11(b). Specifically, if not for the Friedel oscillations, the binding energy of the fcc site would be higher than that of the hcp site and the latter would be lower than it actually is (since the hcp site is slightly depleted from charge with respect to the bulk). So, we can expect that if somehow we could artificially freeze the charge density to the bulk value, the fcc  $\rightarrow$  hcp and the hcp  $\rightarrow$  fcc energy barriers would be more symmetric. In this sense, concerning the position of the two local minima, while the Friedel oscillations tend to lower the hcp  $\rightarrow$  fcc energy barrier, they increase the fcc  $\rightarrow$  hcp one [106].

The fact that the barriers are so low is of course related to the fact that Mg bonds are rather weak compared to most metals. We shall see, however, that the Friedel oscillations also tune the barrier. They do not act only to modulate the binding energy of the two local minima (hcp and fcc), as described above, but also those along the diffusion path. Namely, although the extra charge-density pocket caused by the Friedel oscillations is strongly localized at the fcc site, Figure 5-11(b) and comparison of Figure 5-11(c) and (d) clearly show that the charge

enhancement at the surface extends well up to the bridge. Since furnishing charge at the bridge smoothens the potential energy surface for the adatom by increasing the binding energy around the transition state, we conclude that the Friedel oscillations actually further lower the energy barrier. In summary, we have shown that the Friedel oscillations in Mg(0001) lower the adatom self-diffusion barriers and make the barrier asymmetric. The Friedel oscillations thus promote adatom diffusion with very short transit time at hcp sites [106].

#### 5.1.4 Conclusions

We perform first-principles calculations of the properties of Mg(0001) surface to undertake a thorough examination and correlate diverse features of Mg(0001) reported previously, such as (1) the giant oscillations of the surface energy and the interlayer relaxation of Mg(0001) films as a function of thickness, (2) the thickness-dependent oscillations in the early-stage oxidation rate of Mg films, (3) the well-known Friedel oscillations in Mg slabs, (4) the adatom weak binding and (5) the adatom site unspecificity. We find that, although overcoming the thin-film limit requires up to 25 layers, properties exclusive to the surface layer are well converged for 18-layer thick films (~4.1 nm). Regarding the thickness-dependent oxidation rate for Mg films of less than 16 layers, we discuss previous explanations and provide evidence that it is in fact related to the in-plane-projected density of states of the first- and second-layer atoms around the Fermi level. With respect to the charge density profile of Mg(0001), we clarify that Friedel oscillations in Mg(0001) are not inducing interlayer electrostatic repulsion but rather a withdrawal of bonding charge that simply weakens the interlayer bonding. Three dimensional charge density difference plots demonstrate that the Friedel oscillations have maxima spatially more localized than one-dimensional average density or two-dimensional cross sectional plots

could possibly inform: The charge-density enhancement at the surface layer of Mg(0001) is strongly localized at the fcc hollow site of Mg(0001). The charge accumulation at this site makes the stacking fault of Mg monomers energetically favorable by an unexpectedly large energy ( $\sim 15$  meV), a feature that escaped previous effective-medium calculations. To strengthen this argument, we analyzed the adatom stacking fault for Be(0001) -- a surface also largely influenced by Friedel oscillations and discovered a striking stronger effect. The trend of favoring the stacking fault persists for Mg adislands of at least 3 atoms. We also find that the binding energy of the Mg adatom ( $\sim 0.6$  eV) is significantly weaker than the value reported by previous calculations. Finally, the charge accumulation at the fcc, which spreads to the bridge, and charge depletion at hcp account for the remarkably small diffusion barriers for the monomer (9 and 25 meV) [106].

## 5.2 *Part II: Mg film Morphologies: A multi-scale Study of Mg(0001) Growth*

### 5.2.1 Introduction

One of the challenges in recent studies of materials at the nanoscale is the development of an understanding of microscopic processes that control thin film growth. This is a necessary task if we are to build materials of choice by design. A realistic study of film morphologies demands continuous integration of information obtained at the microscopic level into formulations which predict and characterize behavior of systems at the macroscopic scale. Phenomena at the atomic level extend themselves over nanometers with characteristic time scales of femto or picoseconds, while thin films for industrial applications are of mesoscopic or macroscopic dimensions and typically take milli-seconds or more to grow and evolve morphologically [144].

In the multi-scale modeling of thin films, fundamental studies are being carried out at the atomistic level using as accurate a technique as feasible. In combination with techniques like kinetic Monte Carlo (KMC) these microscopic models are also expected to facilitate simulation of thin-film growth at realistic length and time scales. These microscopic studies are critical because of the experimentally demonstrated impact that structural and vibrational properties at the atomic level have on the eventual properties (including quality) of thin films. For example, whether a film grows layer-by-layer, or through the formation of 3D islands, depends on the details of the motion of adatoms on the potential energy surface provided by the substrate. Three types of growth modes are often discussed in the literature. The Frank-van der Merwe or layer-by-layer growth, and the Volmer-Weber or 3D island growth, appear to be accompanied by the more complex Stranski-Krastanov mode, which incorporates a competition between the other two types exists [144].

The simple explanation of the first two types was provided by Schwoebel and Ehrlich who proposed that the existence (or lack thereof) of an additional activation energy barrier as an atom tries to descend a step edge, could be deciding factor for a 3D or layer-by-layer evolution of the film under growth conditions. This is the so-called “Schwoebel/Ehrlich” barrier whose determination from theory and experiments has led to substantial clarity in understanding thin film growth. The existence of the Stranski-Krastanov mode, however, implies that thin film growth patterns may be far more complex in general, and may require consideration of the role of quantities like surface strain and local perturbations [144].

Experimentally, nearly perfect Mg(0001) films can be grown on Si(111) substrate by low-temperature deposition and annealing [145] and on W(110) substrate [146-148]. . In addition

QSE have been observed for the growth of Mg on Si(111) although in this case the large lattice mismatch between Si and Mg (20%) needs to be accommodated thus excluding the possibility of building films layer by layer. Owing to its sharp interface, with high reflectivity in the energy region of the Mg s-p band, the Mg/W(110) system has proven an excellent test system for studying the influence of confinement on the electronic structure [149-151] and on such metal properties as surface reactivity [152, 153]. With this goal in mind we focus on way the growth of Mg films on W(110) affects their morphology. Within this context, it is necessary to determine the energetics of the various diffusion mechanisms for adatoms, on terraces and step edges, in order to determine whether growth proceeds three-dimensionally or layer by layer.

### 5.2.2 Results and Discussion

We have studied the initial stages of Mg/W(110) epitaxy, starting from the initial adatom adsorption and growth of films. The results of Scanning Tunneling Microscopy (STM) experiments are done by our experimentalist collaborators [154] and the results of the experiments were analyzed by combination of DFT and using Kinetic Monte Carlo simulations (KMC) undertaken by our theorist collaborators [154]. As input for the KMC simulations we employed DFT to calculate activation energy barriers for a number of relevant processes for adatom diffusion via hopping on terraces and near step edges of Mg(0001). KMC Simulations are used to obtain measures the values of critical terrace widths corresponding to switching of the growth mode from step flow to terrace nucleation.

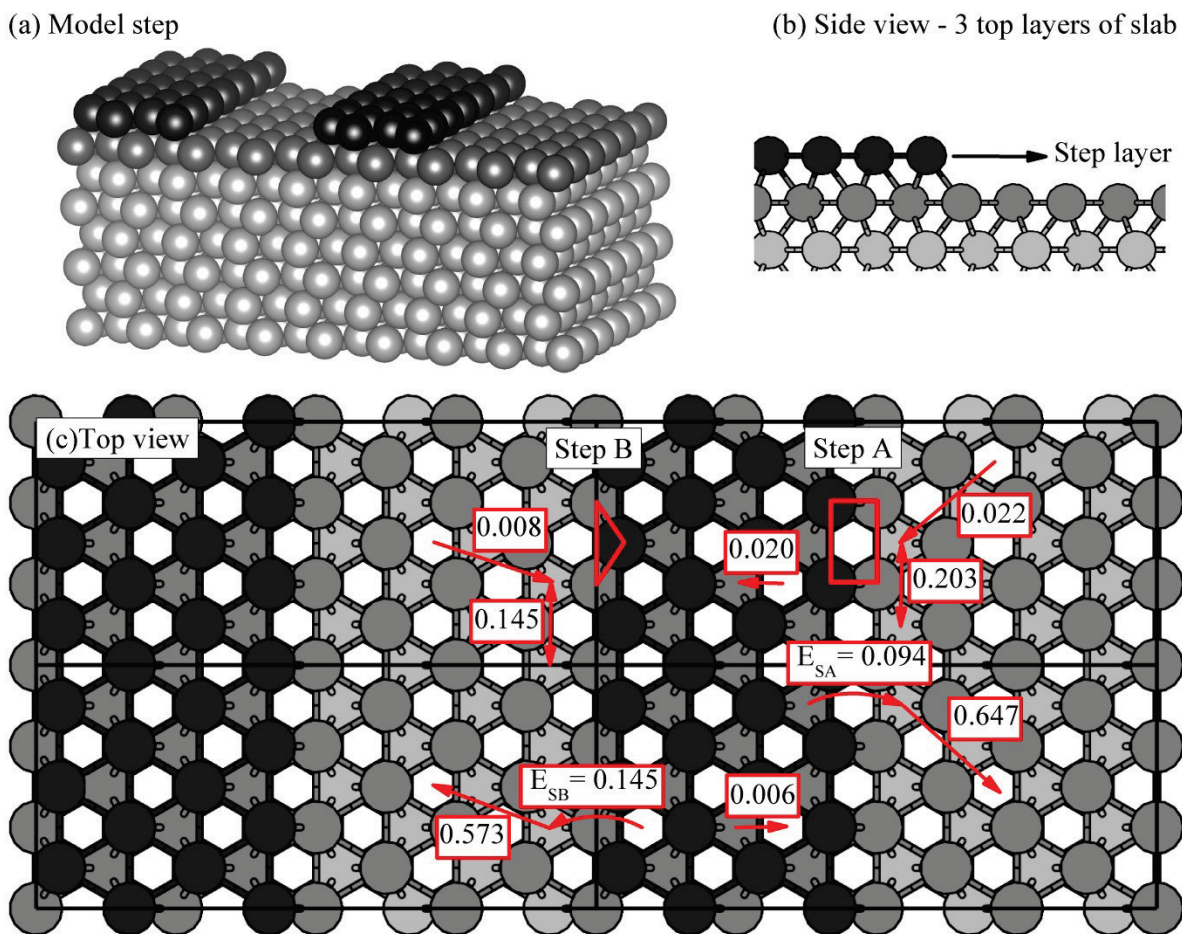


Figure 5-14. (a) Model system with thickness of 7 atomic layers as substrate and one atomic layer as step (b) Side view of 3 top layers of the model system. The darkest gray is the (3x4) step layer. The gray color get lighter as it goes toward the inner layers. (c) Top view of the model system The white and the light gray triangles represent the fcc and hcp sites of the Mg(0001) step Model. The arrows point to the actual sites where it initializes (fcc) and ends up (hcp). The number corresponding to each arrow shows the energy barrier of the  $i$  diffusion path illustrated by arrows. The Ehrlich-Schwoebel barrier energy of steps A and B are depicted as  $E_{SA}$  and  $E_{SB}$  correspondingly.

We find that the energy barrier for adatom diffusion on the “semi-infinite” Mg(0001) terraces(at a 0.1 ML coverage and away from the steps) is 0.032 eV, with atom hopping from fcc to hcp site, and even smaller 0.009 eV, from hcp to fcc. This value is in agreement with the one obtained from effective-medium theory [28], although the latter method does not show the propensity for forming stacking faults that shows up in DFT calculations. The energy barriers

for the stepped Mg(0001) surface are displayed in . The adatom terrace diffusion barriers (0.020 eV and 0.006 eV from fcc to hcp and from hcp to fcc sites, respectively) on the stress free 1-nm step are similar to the ones for the “semi-infinite” terrace.

The Mg steps are strongly attractive for Mg adatoms on the lower terrace (and repulsive for adatoms on the higher side). While the detachment barrier from step A is 0.647 eV, the attachment barrier is only 0.022 eV and its next local minimum position not one but three sites away from the step (i.e., ~0.5nm away from the attachment site). Similarly, the barrier for detachment from and attachment to step B are 0.573 eV and 0.008 eV, respectively. The  $\Delta E_s$  barriers for an adatom to descend from the step terrace to the lower one are 0.094 eV (at step A) and 0.145 eV (at step B). Since the  $\Delta E_s$  barriers are relatively large they indicate a 3D growth for annealing temperatures below 200 K; In contrast, the strong attraction of the steps suggests instability towards mound formation [29].

### 5.2.3 Conclusions

One interesting conclusion from the current study is that regions on the W(110) of different morphology can be prepared (large flat 100nm terraces where growth is layer by layer and only two layers are exposed vs step bunched regions of regular step arrays with average terrace width 10nm). Using the calculated and simulated results we conclude that the diffusion barrier is substantially higher on the bunched regions than that on flat regions. This is a very promising result for the hydrogen adsorption studies since it shows that the fraction of atoms with low coordination is considerably larger in such reasons because many small islands can nucleate on films in the step bunched regions, thus offering potential sites with higher probability for H<sub>2</sub> sticking The details of KMC and experimental results can be found in reference [154].



## CHAPTER 6. ANISOTROPY IN SURFACE DIFFUSION DUE TO PROXIMITY TO MISFIT DISLOCATION

Engineering of ordered self-assembled nano-patterns plays an increasingly important role in design and development of functional nanometer-scale materials and devices, as an alternative to conventional costly and time-consuming top-down approaches or to artificially drawing nanostructures by atomic manipulation with a scanning tunneling microscopy tip or through electron-beam lithography. There are many ways to induce self-assembly processes through inhomogeneities introduced on the surface at atomic scale. Examples are reconstruction (e.g. Ni, Co, Mo and Ru [155-157] growth on herringbone reconstructed Au(111)), atomic steps [158] and implanted ions [159]. But the main challenge in exploiting self-assembly processes lies in controlling the size, symmetry and spatial ordering of nano-islands. Introduction of a dislocation network as a template is one of the promising methods for steering growth of adislands toward predetermined nucleation sites.

In general, growth of a thin-film on a dissimilar substrate results in lattice-mismatch strain that at a certain critical point is relieved through the formation of network of dislocations [160]. Each dislocation line in the film generates a long-range inhomogeneous strain field, which alters adatoms's potential energy surface, resulting in anisotropy in atomic transportation on the thin film and consequently formation of patterned nano-structures. The possibility of producing such ordered arrays in this fashion has already been observed experimentally. Heteroepitaxial systems are good candidate for generating these well-ordered arrays, since the size and symmetry of their dislocation networks can be tuned by adjusting the misfit between the thin film and the substrate, whether by changing the species that make up the thin-film/substrate system, by

varying the temperature, or by altering the adlayer coverage (i.e., varying the thickness of the film).

The trigonal network of dislocations in metal-on-metal heteroepitaxial films has been exploited as a template for growing well-ordered arrays of triangular nanostructures [161]. This phenomenon has been explained as the result of strong repulsion of adatoms from the dislocation line. Similar effects had previously been demonstrated in Ge/SixGe1-x/Si(100) family of systems [162]. Furthermore, dislocations in Ag/Ru(0001) and Cu/Ru(0001) as templates for two-dimensional sulfur nano-cluster arrays have been studied through scanning tunneling microscopy [155]. Also, the Ag/Pt(111) dislocation network has been used for templating the growth of molecular nano structure assemblies on account of its laterally strongly inhomogeneous adsorption properties [163].

Up to now, studies of dislocation-steered self-assembly of nanostructures have been mostly confined to systems under compressive strain. There have been several theoretical studies of adatom diffusion on systems strained by negative misfit [164, 165], but to our knowledge, none has taken up the effect on adatom transport dislocation induced by such strain. And in tensile strain the sole experimental observation of self-assembled structures (quantum dots) in a heteroepitaxial metallic system (PbSe/PbTe) likewise did not reach the critical point that results in dislocation [166]. This relative disinterest in tensile-strained systems, initially under examination were of semiconductors, of interest for electro-optical applications, and the reduction in band gap that accompanies the increase in lattice parameter of semiconductor for this films is unsuitable for such applications.

In this context, we have undertaken two complementary studies. The first study deals with the diffusion of a Cu adatom on Cu/Ni(111) whereas we investigate a Ni adatom on Ni/Cu(111) in the second study.

### *6.1 Part I: Cu/Ni(111)*

#### 6.1.1 Introduction

Modern microelectronic technology depends on the ability to control the growth of thin films. Because a key factor in thin-film growth is surface diffusion [167], a great deal of effort has been devoted to devising realistic models of this process. Many studies have focused on the effects of surface strain on diffusivity, a few on inhomogeneous [168, 169] but most on homogenous stress fields [170-173], and all considering only surfaces free of dislocations. Any realistic material, however, is found to be characterized by certain density of dislocations and related defects when serving as a substrate for film growth. In heteroepitaxial growth, for example, the first few deposited layers grow pseudomorphically (following the substrate geometry) until the strain due to the lattice mismatch is relieved at a certain critical thickness, leading to the formation of misfit dislocations [174, 175]. In several works [176-178] the formation of such misfit dislocations for heteroepitaxial Lennard-Jones systems was documented using molecular static calculations of system energetics and activation energy barriers coupled with either off-lattice kinetic Monte Carlo simulations [176, 177, 179] or application of spherical repulsive potentials [13] to activate the nucleation process. More recently, Trushin *et al.* [180] applied semiempirical interaction potentials arrived at by the embedded atom method (EAM) [181] to generate misfit dislocation in heteroepitaxial growth of Pd/Cu(100) and Cu/Pd(100). As expected, the presence of misfit dislocations was found to have consequences for growth patterns

through the transformation of the potential energy surface for the diffusion of the deposited atoms and their clusters [168, 178]. To our knowledge, a systematic study that documents the effect of inhomogeneous strain in modifying the diffusion dynamics of adatoms, via hopping, on heteroepitaxial systems with well-defined misfit dislocations, has not yet been carried out. In such a system, the lattice mismatch generates stress that is eventually released through a defect, — a misfit dislocation network. We opted to study, as a first prototype system, Cu layers on Ni(111). Our first task was to create a misfit dislocation in this system for several thicknesses of the Cu film. We then study the effects of isolated defects upon the diffusion of a Cu adatom on the Cu layers on Ni(111).

### 6.1.2 Construction of the Cu/Ni(111) Model Sample

Our system consists of several layers (3-7) of Cu placed on top of a Ni(111) substrate. The misfit dislocations are created with the core located at the interface between the Cu film and the Ni substrate, using repulsive biased potential (RBP) method [182]. To the original potential energy surface, we add an exponentially decaying spherically symmetric potential sufficiently localized around the initial harmonic basin to ensure that final state energy depends not upon an artificial repulsive bias but solely upon the true potential of the system. The main idea here is to modify the local energy surface to make the initial epitaxial state unstable. The procedure of sample construction consists of four stages as described in Figure 6-1.

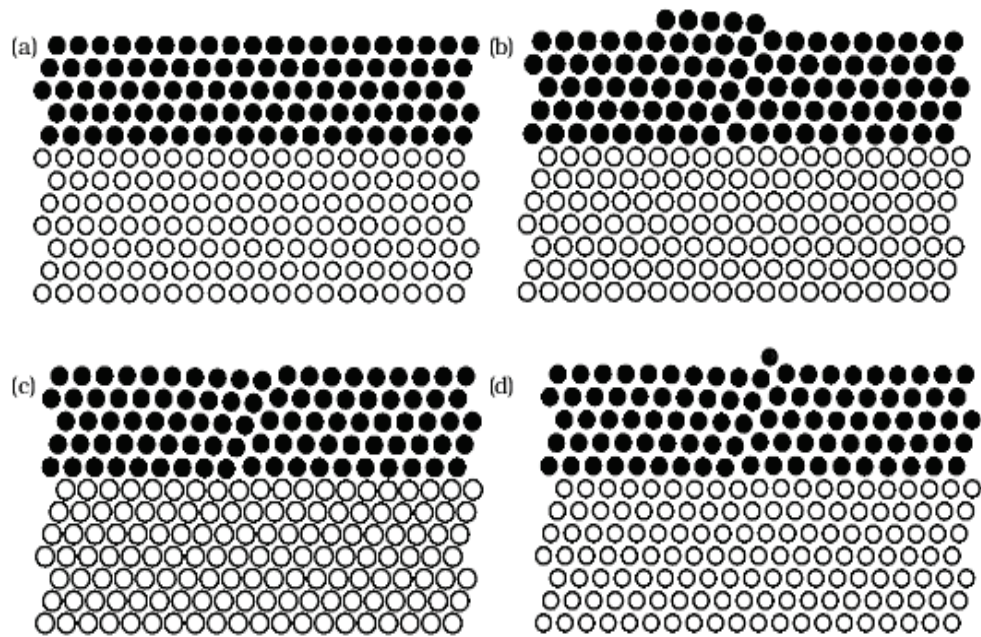


Figure 6-1. Summary (2D) of the procedure for preparing of a sample illustrated here with a 5-layer film to study the diffusion: (a) Relaxation of the sample using standard MD cooling energy minimization; (b) Formation of an extended Cu island, resulting from application of RBP, followed by a second phase of MD cooling; (c) Removal of the island; (d) Addition of a single Cu adatom atop the film. (In this study, we vary the position of this adatom with respect to the defect).

### 6.1.3 Computational Details

To study the effect of misfit dislocations on adatom diffusion in close proximity to the dislocation core in heteroepitaxial systems, we apply molecular dynamics and molecular static methods using many-body interaction potentials. We find that presence of the defect under the surface strongly affects the adatom's trajectory, creating anisotropy in atomic diffusion, even for the case of 7-layer of Cu film. We also calculate the potential surface energy available to the adatom and compare the energy barriers for adatom diffusion in the core region and on the defect free sample.

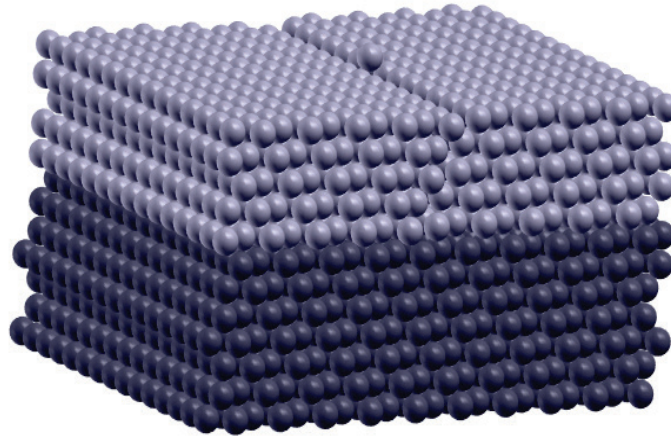


Figure 6-2. A Cu adatom on the dislocated surface of a 5-layer Cu film on a Ni(111) substrate.

#### 6.1.4 Mapping the Potential Energy Surface of Cu Adatom on Ni(111)

To see how the presence of the defect under the substrate surface modifies the potential energy experienced by the adatom at different locations on the film, we compared the energy maps of the potential energy surface of our sample with and without dislocation.

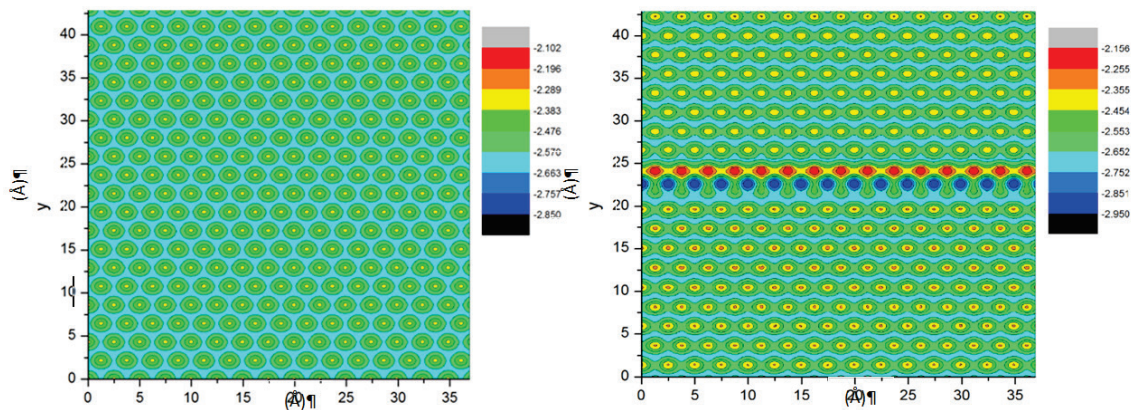


Figure 6-3. Potential Energy Surface for (a) the defect-free surface and (b) for the dislocated surface.

Clearly, the presence of the defect beneath the film surface alters the binding-energy map of the adatoms to the surface in two striking respects. The isotropy of the surface vanishes in

favor of an axis of asymmetry along the dislocation line, and trap zones (very deep minima) emerge along the dislocation line, any of which can immobilize any adatom that strays into its vicinity during a random walk across the surface.

### 6.1.5 MD Simulations of Adatom Diffusion on the Cu Film on Ni(111)

Another way to probe the effect of the defect on surface diffusion is direct MD simulation of adatom motion on the surface. Diffusion at one or more rows away from the dislocation border is anisotropic, and symmetrical on both sides of the dislocation, in contrast to the isotropic trajectory that emerges on a defect-free surface. If we place the adatom directly on the dislocation line, it almost always exhibits a severely confined (spot-bound) trajectory. Although escapes do occur, they are extremely rare; usually when an adatom wanders from its initial position, it shortly returns, and continues to hover around it.

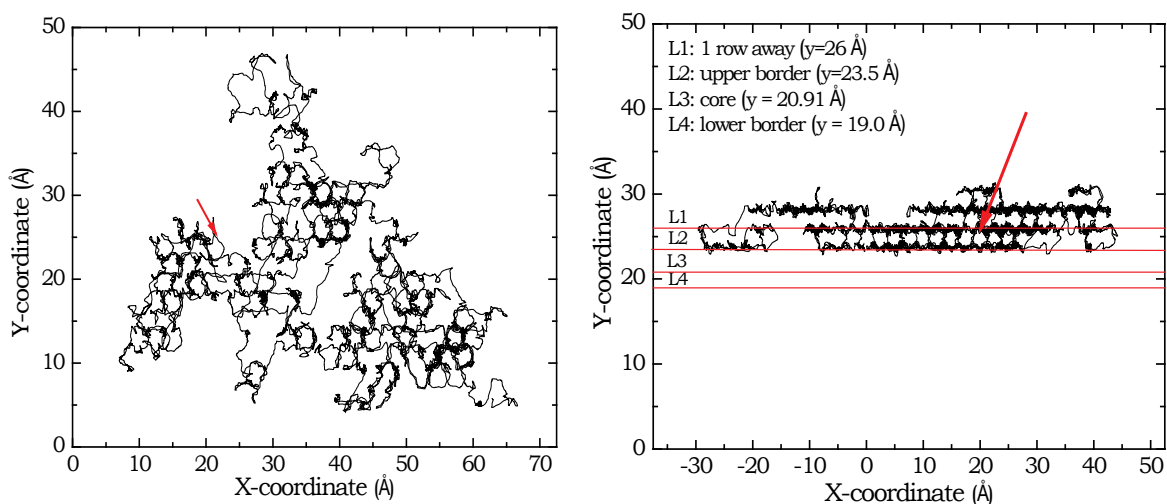


Figure 6-4. (a) A typical isotropic trajectory of the adatom on a defect-free surface. The arrow shows the starting point of the simulation. (b) A typical anisotropic trajectory of the adatom on a defective surface when its initial position is one row distant from the dislocation line, which runs parallel to the edge of the slab 26 Å from it. The arrow shows the starting point of the simulation.

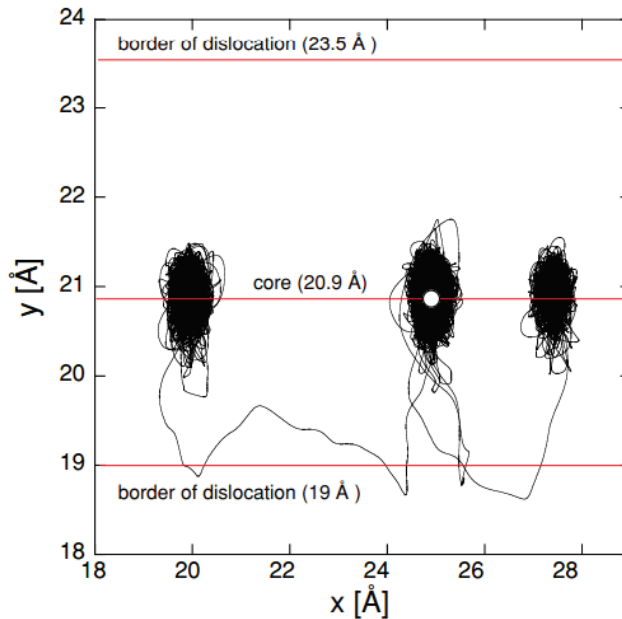


Figure 6-5. Trajectory from MD simulations of attachment and detachment of adatom along the dislocation line (starting point is 21 Å away from the edge of the slab). The white dot is the starting point of the simulation.

#### 6.1.6 Energy Barriers for Adatom Diffusion

To further pin down the effect of the submerged defect on surface diffusion we calculated – using the Nudged Elastic Method [20] – the energy barriers for the adatom to diffuse along all possible paths both on the defect-free substrate and on the defective one. The barrier to go in either direction within the dislocation core is 0.42 eV ( $a \rightarrow c$  &  $a \rightarrow b$ ), which is considerably higher than the barriers for diffusion from any locations outside the dislocation core. We thus expect that the atom will only very rarely move along the dislocation line. Instead it will stay for some time in the trap zone. The barriers for moving out of the trap zone towards the dislocation border are strikingly different for movement towards the higher and lower planes. While the barrier for diffusion towards the higher border ( $a \rightarrow d$ : 0.5 eV) is even slightly greater than that for movement along the dislocation line, that for movement towards the lower border ( $a \rightarrow e$ : 0.23



eV) is approximately 1/2 as great. On the other hand, the barrier for return from the lower border directly to the original location in the core is negligible ( $e \rightarrow a$ : 0 eV). Hence we would expect to see from time to time - as we did in our MD simulations – a detachment towards the lower plane followed by either a return to the original zone of entrapment or a fall into a neighboring entrapment zone. Our calculations thus show that energy barriers are affected by the dislocation depending the adatoms' distance from the dislocation core. To make this clear in spatial and quantitative terms, we present the diagram in Figure 6-6. The entrapment zones at the dislocation core, the asymmetry between the lower and upper borders along the core, and the symmetry of anisotropic behavior at one or more rows beyond the core will determine the morphology of the thin-film growth. In future, the results concerning tensile dislocation and its effect on the subsequent growth of the film will be compared with those concerning the compressive case.

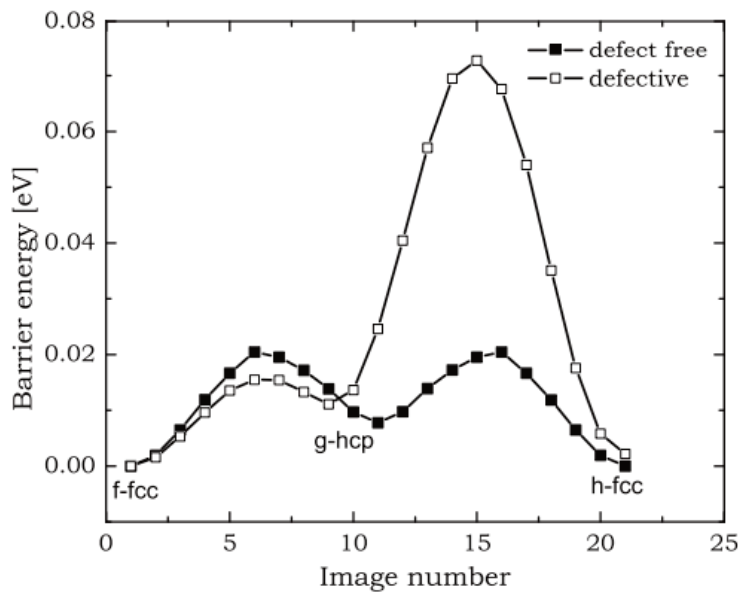


Figure 6-6. Locations of the adatom on the dislocated surface



regions farther away from it. In either case, the growth pattern on surfaces such as the ones considered here will be reflective of a dislocation network. We note that such surface nanostructuring induced by a dislocation network has already been observed experimentally [183, 184]. We hope that our work will motivate more experimental research in the area. Of course, additional diffusion processes have to be considered if one aims at the study of multilayer growth on dislocation networks.

## 6.2 *Part II: Ni/Cu(111)*

### 6.2.1 Introduction

In order to achieve precise control of ordered self-assembled nanoparticles through manipulation of inhomogeneous field, we need a better understanding of how the presence of dislocations – tensile as well as compressive affect the transport of adatoms on hetero epitaxial metallic systems. Previously [185] and in the preceding section (Section 6.1), we reported the effect of dislocation in compressively strained system on diffusion of an adatom. In this section, we address diffusion of adatom on a system of the same prototype and materials but one that is under tensile strain.

The remainder of this section is organized as follows: Sections 6.2.2 and 6.2.3 discuss computational details and the construction of model system, respectively. Section 6.2.4 reports and analyses the results of our MD simulation of the Ni adatom diffusion on the Ni/Cu(111) and Cu adatom on Cu/Ni(111) surfaces. Calculated energy barriers for adatom diffusion are summarized in Section 6.2.4 and our conclusions are presented in Section 6.2.5.

## 6.2.2 Computational Details

Our simulations were performed with LAMMPS (Large-scale Atomic/Molecular Massively Parallel Simulator), a parallel MD code [186], at 300 K, using the canonical ensemble. We used the Verlet algorithm with the Nose-Hoover thermostat to solve classical equations of motion for atoms interacting through interatomic potentials given by the embedded atom method (EAM) [181, 187]. To prevent the motion of the system as a whole, we fixed the two bottom layers of the substrate. To compute minimum energy configurations we chose the Conjugate Gradient (CG) method [188]. To monitor the overall trajectory of the adatom diffusing from a given initial position, we ran each simulation for 10 ns, recording configurations every 10 time steps. To calculate all activation energy barriers we used the nudged elastic band (NEB) method [189], modeling the path in configuration space by 20 discrete images and minimization until forces on the images converged to better than  $10^{-6}$  eV/Å.

## 6.2.3 Construction of the Model Systems

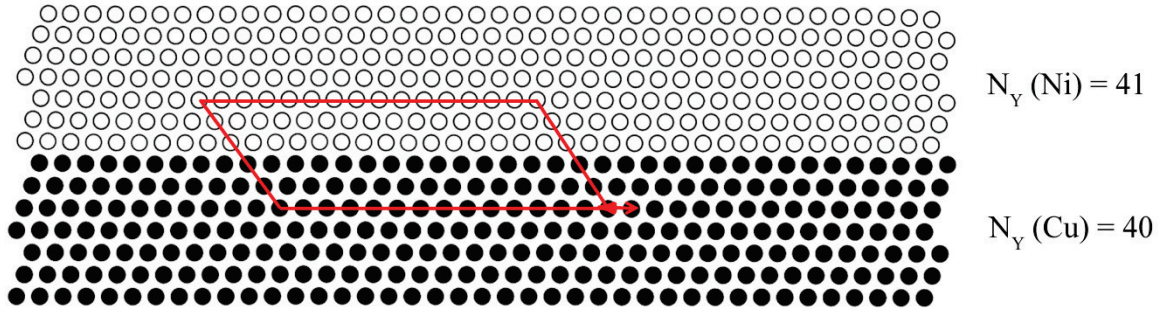
Diffusion of a Cu adatom on a Cu/Ni(111) slab has been described before [185] – and in the preceding section (Section 6.1). In that study we prepared the sample was prepared by the Repulsive Biased Potential (RBP) method [178]. Here we reiterate those simulations, but on a sample prepared, for the sake of strict comparison, by the bicrystal method [190] we have adopted for preparing the Ni on Ni/Cu(111) slab, prompted by well-established general facts about heteroepitaxial growth.

Nucleation of a dislocation is the mechanism by which the strain governed by lattice mismatch is relieved. Two distinct sources of strain, and hence two kinds of dislocation, are possible, depending on the nature of the misfit between film and substrate. When the lattice

parameter of the film is smaller than that of the substrate (negative misfit), the result is tensile strain. When tensile strain is relieved through relaxation, more atoms can eventually be accommodated within a given length of film than in the substrate, therefore the atoms in the film get closer to one another. That is, while the misfit parameter in a compressively strained system is positive, the strain tensor (the magnitude of deformation upon relief of the strain) is negative while in a tensilely strained system the misfit parameter is negative, and the strain tensor is positive.

Accordingly we set about constructing the Ni/Cu(111) and Cu/Ni(111) slabs in the following way (see Figure 6-8). Both parts of both slabs were made of fcc crystal layers in which the Ni lattice constant = 3.53 Å and the Cu lattice constant = 3.62 Å. To construct both samples, we first set the dimensions of the film and substrate. We settled upon 7 layers of film on 7 layers of substrate because in both the energy barrier for diffusion of an adatom converges at 7 layer (NZ =7); that is, the barrier increases for each layer added (starting with a single layer) until it remains constant). We keep the number of atoms at X direction the same for films and substrates of both samples (NX = 10). The only direction that we alter to get dislocation to occur is the Y direction of the film. In each sample we construct the substrate by setting NY = 40 and fixing two layers. For dislocation in a tensilely strained system, we set NY = 41 and for dislocation in a compressively strained system, we set NY = 39. Joining the film and substrate crystals along their x-y faces produces a mismatching bi-crystal, relaxation of which introduces a misfit dislocation – a decrease in interatomic distances between Ni atoms in the tensile case, increase the interatomic distances between the Cu atoms in the compressive case. The closed lines in Figure 6-8(a) and Figure 6-8(b) are Burgers circuits around the dislocations.

(a) Dislocation via relief of tensile strain ( $f = -2.49\%$ )



(b) Dislocation via relief of compressive strain ( $f = 2.6\%$ )

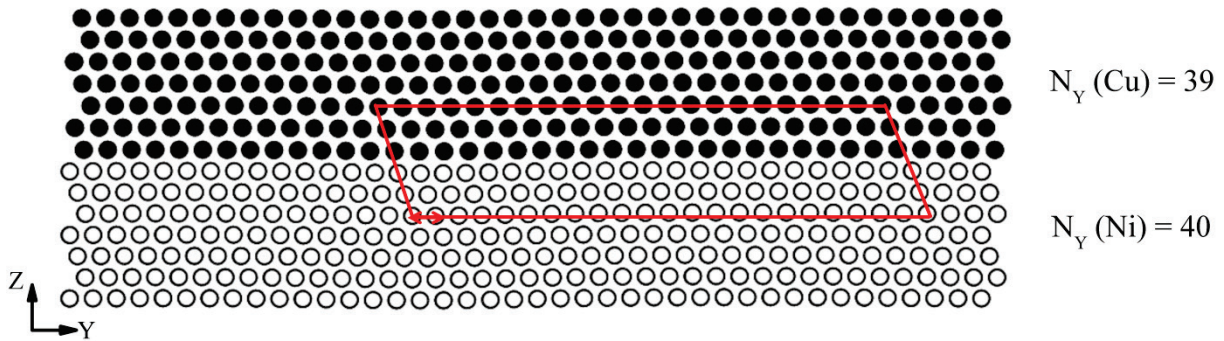


Figure 6-8. Schematic cross-section of slab containing a dislocation: (a) in a tensilely strained system (b) in a compressively strained system. The numbers of atoms in the Z and X directions is the same for both samples, as are the numbers of atoms in the Y direction of the two substrates:  $N_Z = 7$ ;  $N_X = 10$ ;  $N_Y(\text{Cu-substrate}) = 40 = N_Y(\text{Ni-substrate})$ . But in the tensilely strained system (a), the number of atoms in the Y dimension of the (Ni) film is one more (41) than in the substrate, while in the compressively strained system the number of atoms in the Y direction of the (Cu) film is one less (39). The closed line in Fig 2a and Fig.2b are the Burgers circuits around the dislocation misfits ( $f = [(a_{film} - a_{substrate})/a_{film}] \times 100$ ) – negative when the dislocation results from tensile strain, positive when it results from compressive strain. Note that the X direction is in to the sheet.

#### 6.2.4 MD Simulation of Adatom Diffusion in the Presence of Tensile and Compressive Dislocations

To see how the presence and nature of the defect under the substrate surface affects surface diffusion, we used direct MD simulation of adatom motion on the surface. We compare a typical trajectory of adatom motion on ideal surfaces with that on a dislocated surface for both compressive and tensile cases. Since we find the same anisotropy all the way to the slab edge, we

infer that the strain field due to isolated edge dislocation extends far beyond the dislocation core. In Figure 6-9 we confront the effects of both kinds of dislocations. Figure 6-9(b) and Figure 6-9(d), show a typical anisotropic trajectory in the presence of dislocation in a tensilely and in a compressively strained system, respectively, while a typical random trajectory of adatom on corresponding non-defective surfaces is shown in Figure 6-9(a) and Figure 6-9(c). There is a difference between the effect of tensile (Figure 6-9(b)) and effect of compressive (Figure 6-9(d)) dislocation on the trajectory of an adatom.

For dislocation in a tensilely strained system, adatom diffusion is preferentially faster toward to the dislocation (perpendicular to it) but for compressive dislocation the adatom avoids diffusing toward the dislocation line (along it). In both Figure 6-9(b) and Figure 6-9(d), the approximate borders of the dislocation area have been indicated by red lines, while the starting point of the simulation is marked by dashed green lines. We repeated the calculations many times: in all of them dislocation in a tensilely strained system functions as an attractor, while in a compressively strained system dislocation works to repel diffusion. The results here, with our Cu/Ni sample here prepared with new method, confirm the results we obtained [13] with the sample built by RBP. Energy Barriers for Adatom Diffusion Processes

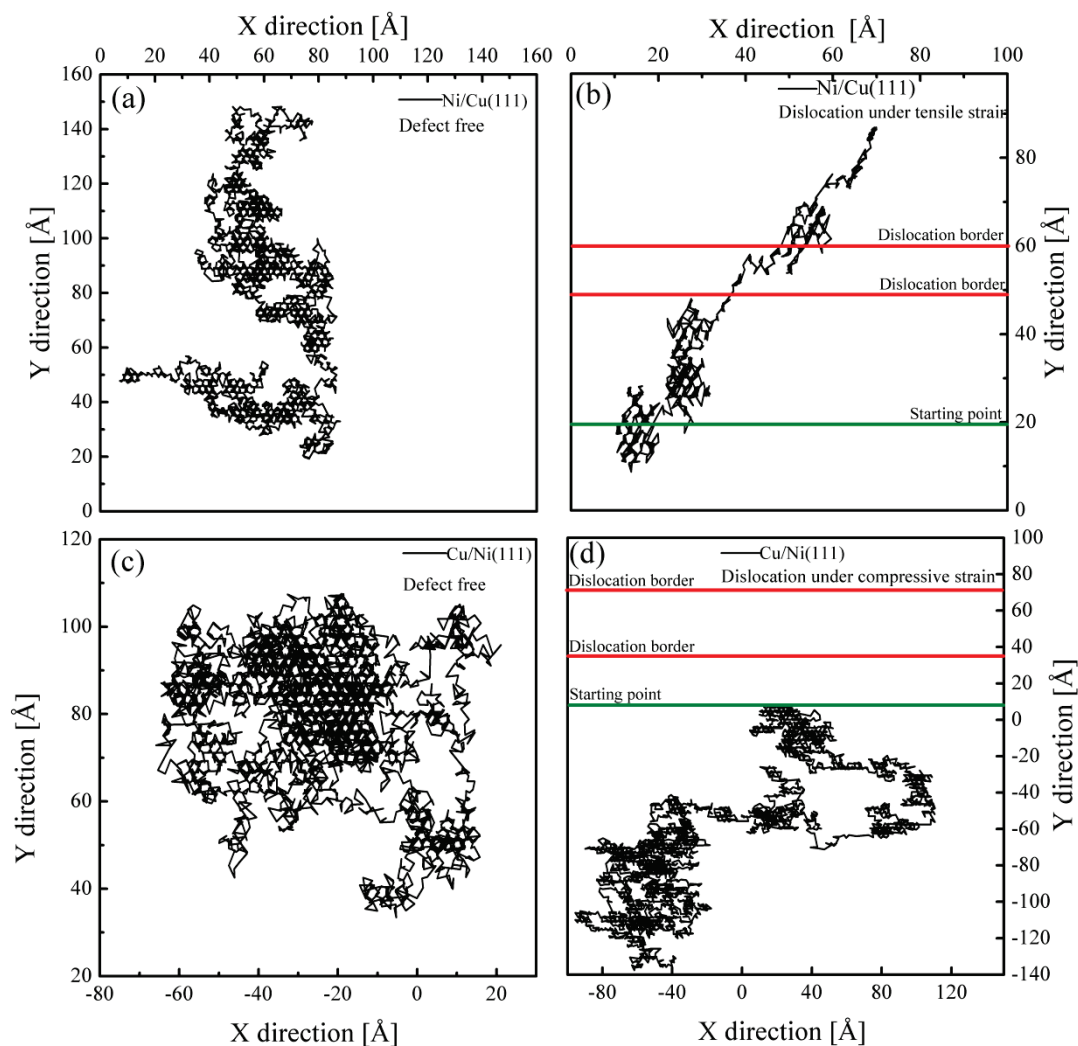


Figure 6-9. (a), (c) Typical isotropic trajectories of an adatom on defect-free surfaces (b), (d) Typical anisotropic trajectories of an adatom on dislocated surfaces generated by different types of strain.

To further pin down the effect of the submerged defect on surface diffusion, we calculated the energy barriers for the adatom to diffuse via hopping along possible paths both on the defect-free substrate and on the defective ones. In Figure 6-10(a) and Figure 6-10(b) we graph the energy profile along transition path for an adatom's diffusion from one fcc to another fcc site by way of an hcp site on both the defect-free surfaces and on each of the defective surfaces. On all the surfaces the path consists of two steps: the first from the initial fcc site to an



hcp site, and the second from there to the other fcc site. On the defective surface (see Figure 6-10(d)), for an adatom away from the border of the dislocation, the first step (fcc→hcp) is “parallel” to the dislocation line (actually at an acute angle to it), while the second (hcp→fcc) is perpendicular to that border. Figure 6-10(a) and Figure 6-10(b) dramatize how the saddle points of the energy barriers for diffusion steps on the defect-free surface are symmetrical, while those for the equivalent steps on the defective surface are highly asymmetrical: On the defect-free surface, the energy barriers for the two steps (fcc→hcp and hcp→fcc) are 0.04 and 0.06 eV for Ni on Ni/Cu(111) and 0.01 and 0.02 eV for Cu on Cu/Ni(111) surface, respectively. In the compressively dislocated surface the barrier for the step perpendicular to the dislocation border (hcp→fcc: 0.06 eV) is three times higher (fcc→hcp: 0.02 eV) than that for the step parallel to it, while on a surface dislocated by tensile strain the barrier for the step parallel to the dislocation border (fcc→hcp: 0.08 eV) is 4 times higher (hcp→fcc: 0.02 eV) than that for the step perpendicular to it. The difference explains the contrast between anisotropic diffusion trajectories typical on the defective surfaces and the isotropic trajectories typical on the defect-free surfaces. As it is shown in Figure 6-10(c) and Figure 6-10(e), in the tensile case, the adatom has a low barrier for diffusion perpendicular to the dislocation, while in compressive case, the adatom has a tendency to diffuse parallel to the dislocation because of the lower barrier in that direction. In other words, in a compressively strained system, introducing dislocations leads to partial strain relief and increase of activation energy for surface diffusion towards the dislocation line. The effect manifests itself as an effective repulsion from dislocation.

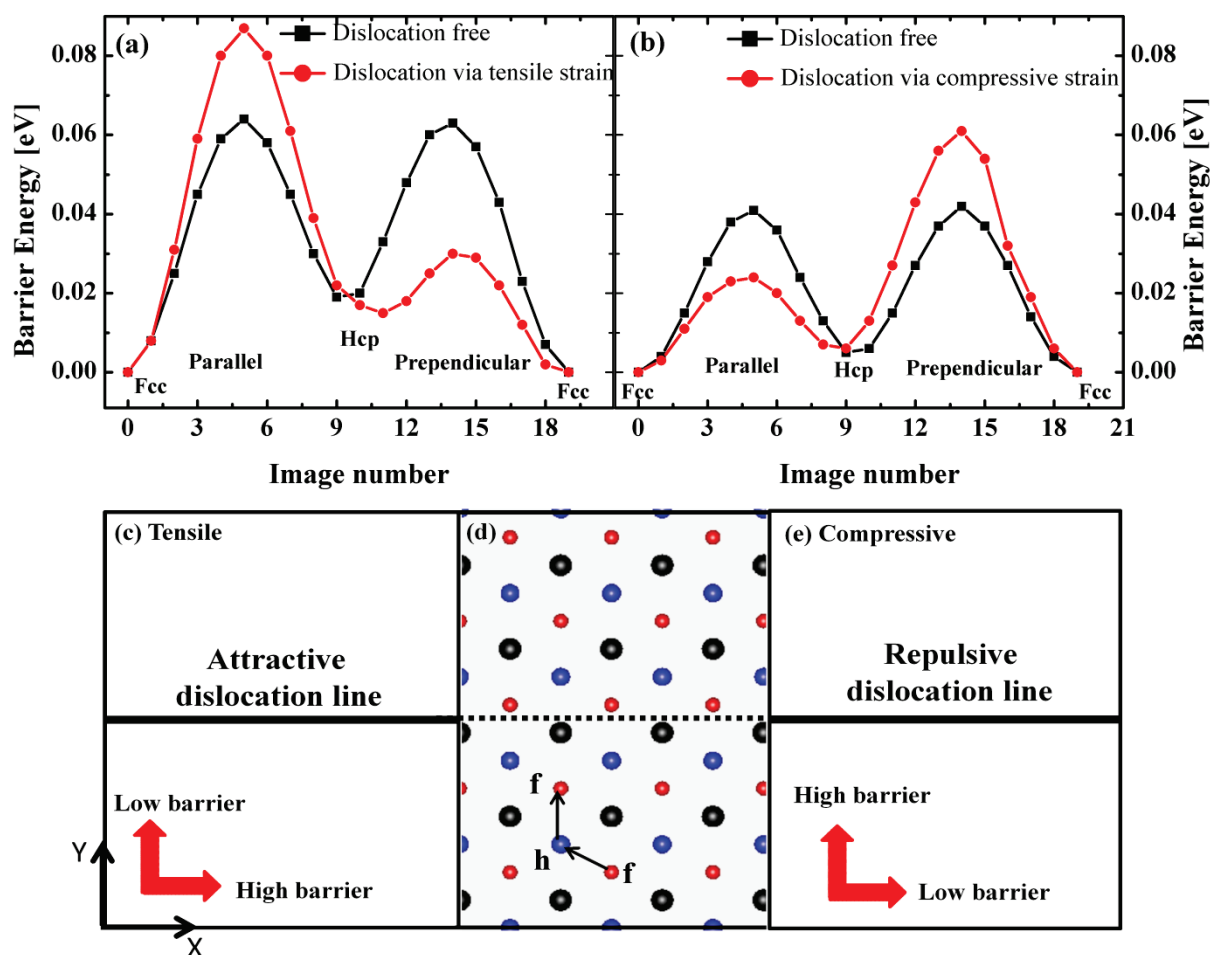


Figure 6-10. Energy barriers for diffusion of (a) Ni on non-defective and (tensilely generated) defective Ni/Cu(111) and of (b) Cu on non-defective and compressively generated defective Cu/Ni(111) – in each case from an fcc to an fcc site by way of an hcp site, as schematized in (d). The contrast between the relative strengths of barriers to diffusion along paths parallel and perpendicular to the dislocation line is schematized in the juxtaposition of (d) and (f), for tensilely and compressively generated dislocations, respectively.

## 6.2.5 Conclusions

We compared the diffusion of the Ni adatom on Ni/Cu(111) on a surface dislocated by tensile strain with diffusion of Cu adatom on Cu/Ni(111) surface dislocated by compressive strain and with diffusion of adatoms on the corresponding defect-free surfaces. Our simulations

show that presence of a defect under a substrate surface effectively changes the energy barriers for adatom diffusion and consequently the kinetics of thin-film growth.

We predict that in general one will observe a clear correlation between the sign of misfit dislocations and the positions of the mounds grown on the surface: Negative misfit has an attractive effect on deposited adatoms (mounds prefer to form directly above the tensile dislocation), while positive misfit has a repulsive effect on the adatom diffusion (mounds grow away from the dislocations). This effect of change in energy barrier due to the presence of defect has a very simple interpretation. An atomic lattice with large interatomic distances is characterized by deep minima at binding sites and consequently high energy barriers for surface diffusion, while a dense lattice has shallow minima and low energy barriers. Thus any change in interatomic distances should lead to change in energy barriers. It is known that introducing a defect in misfit-strained systems causes different effects depending on the misfit sign. Compressive strain relief results in increase in interlayer distance, while relief of tensile strain reduces these. Since this effect is based on the geometry of lattice packing, it should prove universal – that is independent of any particular choice of interatomic potential. Of course additional diffusion processes have to be considered if one aims at the study of multilayer growth on dislocation networks. Meanwhile, we await experimental verification of these predictions.

## CHAPTER 7. CONCLUSIONS

In summary, we studied the electronic structure of four different model structures involving different possibilities of interfaces of single layer MoS<sub>2</sub> with Au contact. The features of the electrostatic potentials and the charge redistributions at the interface between the metal and the MoS<sub>2</sub> are different between the four interfaces and one of the samples shows the most current passing through the MoS<sub>2</sub>. Schottky barriers calculated between interface of MoS<sub>2</sub> and Au contact shows both p-type and n-type MoS<sub>2</sub>-Au contact.

We find a novel MoS<sub>x</sub> surface structure on copper whose ability to interact and activate adsorbates far exceeds that of MoS<sub>2</sub> while proving to be of similar thermal stability and also recoverable post adsorption via annealing. We propose two models. Both of the model structures (Mo<sub>2</sub>S<sub>3</sub> and Mo<sub>2</sub>S<sub>5</sub>) are dynamically stable, at least at Gamma, and therefore the calculated dynamical stability cannot discern or favor one structure or the other. Mo<sub>2</sub>S<sub>3</sub> has several high-frequency features while Mo<sub>2</sub>S<sub>5</sub> has very-clearly distinguishable, well separated frequencies. Two features in Mo<sub>2</sub>S<sub>3</sub> structure could very well lend themselves to being distinguished through Raman spectroscopy, enabling researchers to understand which the real structure is. Some catalyst compositions of MoS<sub>x</sub> for the formation of products from syngas contain copper<sup>1</sup>; thus, our finding of a high affinity MoS<sub>x</sub> composition specifically on copper may point toward an alternative origin of the actual working of such catalysts, if further corroborated by studies at high pressure.

Our experimentalist collaborators observe the growth of molybdenum-sulfur nanowires on a Cu(111) surface. We identify them as Mo<sub>6</sub>S<sub>6</sub> nanowires. We find that the substrate interactions are considerable, leading to the alignment of the nanowires with the substrate atomic

rows. The nanowire growth favors a 4D separation on Cu(111), sufficiently far to separate them completely and slightly wider than expected from DFT simulation. In combination, our results suggest that Cu(111) may be a viable candidate for the aligned and regularly-spaced growth of  $\text{Mo}_6\text{S}_6$  nanowires.

We have performed DFT first-principles calculations to reanalyze the surface relaxation and electronic structure of Mg(0001), in order to determine the binding site and energy of  $\text{Mg}_n$  islets ( $n=1-4$ ) on Mg(0001), to understand the low-diffusion barrier of the Mg monomer, and to perform a full analysis of the dimer diffusion on this surface. We have not found strong variations of the first-layer expansion and surface energy as a function of film thickness, as reported previously [105]. We found, instead, that these properties as well as the DOS at the Fermi level are well converged for films thicker than 24 nm (18 layers). We found, however, that distinct electronic properties of Mg(0001) films could be observed for some very narrow film thicknesses. For example, one could obtain dramatic changes in the DOS at the Fermi level (and thus in reactivity) for films ranging from tetralayer to hexalayer. Charge-density plots show that the long-known charge-density enhancement at the surface of Mg(0001), as a result of Friedel oscillations, happens to be strongly localized in the fcc hollow site of Mg(0001). Our analysis indicates that the charge accumulation at this “infinite” hollow site causes an energetically favorable and unexpectedly large stacking fault for the Mg monomer (15 meV), which eluded previous effective-medium calculations [191]. This trend decreases but persists all the way up to the tetramer. Our calculations also suggest that this FO-driven charge accumulation may also be responsible for the relatively small diffusion barriers for the monomer (fcc  $\rightarrow$  hcp: 25 meV and hcp  $\rightarrow$  fcc : 9 meV).

We compared the diffusion of the Ni adatom on Ni/Cu(111) on a surface dislocated by tensile strain and diffusion of Cu adatom on Cu/Ni(111) surface dislocated by compressive strain with each other and with diffusion of adatoms on the corresponding defect-free surfaces. Our simulations showed that presence of a defect under a substrate surface effectively changes the energy barriers for adatom diffusion and consequently the kinetics of thin-film growth. We predict that in general one will observe a clear correlation between the sign of misfit dislocations and the positions of the mounds grown on the surface: Negative misfit has an attractive effect on deposited adatoms (mounds prefer to form directly above the tensile dislocation), while positive misfit has a repulsive effect on the adatom diffusion (mounds grow away from the dislocations). This effect of change in energy barriers due to the presence of defect has a very simple interpretation. An atomic lattice with large interatomic distances is characterized by deep minima at binding sites and consequently high energy barriers for surface diffusion, while a dense lattice has shallow minima and low energy barriers. Thus any change in interatomic distances should lead to change in energy barriers. It is known that introducing a defect in misfit strained systems causes different effects depending on the misfit sign. Compressive strain relief results in increase in interlayer distance, while relief of tensile strain reduces these. Since this effect is based on the geometry of lattice packing, it should prove universal – that is, independent of any particular choice of interatomic potential. Of course additional diffusion processes have to be considered if one aims at the study of multilayer growth on dislocation networks. Meanwhile, we await experimental verification of these predictions.

## LIST OF REFERENCES

1. Lundstrom, M., P. Cummings, and M. Alam, *Investigative Tools: Theory, Modeling, and Simulation,* in *Nanotechnology Research Directions for Societal Needs in 2020.* Springer Netherlands, 2011.
2. Ercolessi, F., *A molecular dynamics primer* 1997.
3. Novoselov, K.S., A.K. Geim, S.V. Morozov, D. Jiang, Y. Zhang, S.V. Dubonos, I.V. Grigorieva, and A.A. Firsov, *Electric Field Effect in Atomically Thin Carbon Films.* Science, 2004. **306**(5696): p. 666-669.
4. Berger, C., Z.M. Song, T.B. Li, X.B. Li, A.Y. Ogbazghi, R. Feng, Z.T. Dai, A.N. Marchenkov, E.H. Conrad, P.N. First, and W.A. de Heer, *Ultrathin epitaxial graphite: 2D electron gas properties and a route toward graphene-based nanoelectronics.* Journal of Physical Chemistry B, 2004. **108**(52): p. 19912-19916.
5. Bolotin, K.I., K.J. Sikes, Z. Jiang, M. Klima, G. Fudenberg, J. Hone, P. Kim, and H.L. Stormer, *Ultrahigh electron mobility in suspended graphene.* Solid State Communications, 2008. **146**(9-10): p. 351-355.
6. Zhang, Y., T.T. Tang, C. Girit, Z. Hao, M.C. Martin, A. Zettl, M.F. Crommie, Y.R. Shen, and F. Wang, *Direct observation of a widely tunable bandgap in bilayer graphene.* Nature, 2009. **459**(7248): p. 820-3.
7. Xia, F., D.B. Farmer, Y.M. Lin, and P. Avouris, *Graphene field-effect transistors with high on/off current ratio and large transport band gap at room temperature.* Nano Lett, 2010. **10**(2): p. 715-8.
8. Han, M.Y., B. Ozyilmaz, Y. Zhang, and P. Kim, *Energy band-gap engineering of graphene nanoribbons.* Phys Rev Lett, 2007. **98**(20): p. 206805.
9. Li, X., X. Wang, L. Zhang, S. Lee, and H. Dai, *Chemically derived, ultrasmooth graphene nanoribbon semiconductors.* Science, 2008. **319**(5867): p. 1229-32.
10. Jiao, L., L. Zhang, X. Wang, G. Diankov, and H. Dai, *Narrow graphene nanoribbons from carbon nanotubes.* Nature, 2009. **458**(7240): p. 877-80.
11. Mak, K.F., C. Lee, J. Hone, J. Shan, and T.F. Heinz, *Atomically thin MoS(2): a new direct-gap semiconductor.* Phys Rev Lett, 2010. **105**(13): p. 136805.
12. Kam, K.K., and B.A. Parkinson, *DETAILED PHOTOCURRENT SPECTROSCOPY OF THE SEMICONDUCTING GROUP-VI TRANSITION-METAL DICHALCOGENIDES.* Journal of Physical Chemistry, 1982. **86**(4): p. 463-467.
13. Radisavljevic, B., A. Radenovic, J. Brivio, V. Giacometti, and A. Kis, *Single-layer MoS2 transistors.* Nature Nanotechnology, 2011. **6**(3): p. 147-150.
14. Sholl, D.S., and J.A. Steckel, *Density Functional Theory: A Practical Introduction.* 2009: Wiley.
15. Thomas, L.H., *The calculation of atomic fields.* Mathematical Proceedings of the Cambridge Philosophical Society, 1927. **23**(05): p. 542-548.

16. Fermi, E., *Eine statistische Methode zur Bestimmung einiger Eigenschaften des Atoms und ihre Anwendung auf die Theorie des periodischen Systems der Elemente*. Zeitschrift für Physik, 1928. **48**(1-2): p. 73-79.
17. Cuevas, J.C., *Molecular Electronics: An Introduction to Theory and Experiment* June 23, 2010 ed. 2000: World Scientific Publishibg Co. Pte. Ltd. .
18. Kohn, W., and L.J. Sham, *Self-Consistent Equations Including Exchange and Correlation Effects*. Physical Review, 1965. **140**(4A): p. A1133-A1138.
19. Perdew, J.P., and W. Yue, *Accurate and simple density functional for the electronic exchange energy: Generalized gradient approximation*. Physical Review B, 1986. **33**(12): p. 8800-8802.
20. Lee, C., W. Yang, and R.G. Parr, *Development of the Colle-Salvetti correlation-energy formula into a functional of the electron density*. Physical Review B, 1988. **37**(2): p. 785-789.
21. Perdew, J.P., J.A. Chevary, S.H. Vosko, K.A. Jackson, M.R. Pederson, D.J. Singh, and C. Fiolhais, *Atoms, molecules, solids, and surfaces: Applications of the generalized gradient approximation for exchange and correlation*. Physical Review B, 1992. **46**(11): p. 6671-6687.
22. Perdew, J.P., K. Burke, and M. Ernzerhof, *Generalized gradient approximation made simple*. Physical Review Letters, 1996. **77**(18): p. 3865-3868.
23. Born, M., and R. Oppenheimer, *Zur Quantentheorie der Molekeln*. Annalen der Physik, 1927. **389**(20): p. 457-484.
24. Hohenberg, P., and W. Kohn, *Inhomogeneous Electron Gas*. Physical Review, 1964. **136**(3B): p. B864-B871.
25. Hamann, D.R., M. Schlüter, and C. Chiang, *Norm-Conserving Pseudopotentials*. Physical Review Letters, 1979. **43**(20): p. 1494-1497.
26. Vanderbilt, D., *Soft self-consistent pseudopotentials in a generalized eigenvalue formalism*. Physical Review B, 1990. **41**(11): p. 7892-7895.
27. Blöchl, P.E., *Projector augmented-wave method*. Physical Review B, 1994. **50**(24): p. 17953-17979.
28. Kresse, G., and D. Joubert, *From ultrasoft pseudopotentials to the projector augmented-wave method*. Physical Review B, 1999. **59**(3): p. 1758-1775.
29. Ashcroft, N.W., and D. Mermin. Solid State Physics. 1976, Philadelphia: Saunders College.
30. Marques, M.A.L., A. Castro, G.F. Bertsch, and A. Rubio, *octopus: a first-principles tool for excited electron-ion dynamics*. Computer Physics Communications, 2003. **151**(1): p. 60-78.
31. Gonze, X., J.M. Beuken, R. Caracas, F. Detraux, M. Fuchs, G.M. Rignanese, L. Sindic, M. Verstraete, G. Zerah, F. Jollet, M. Torrent, A. Roy, M. Mikami, P. Ghosez, J.Y. Raty,



- and D.C. Allan, *First-principles computation of material properties: the ABINIT software project*. Computational Materials Science, 2002. **25**(3): p. 478-492.
32. Arfken, G.B., and H.J. Weber, *Mathematical Methods for Physicists*. 5 ed. 2001, San Diego: Harcourt Academic Press.
  33. Rath, J., and A.J. Freeman, *Generalized magnetic susceptibilities in metals: Application of the analytic tetrahedron linear energy method to Sc*. Physical Review B, 1975. **11**(6): p. 2109-2117.
  34. Monkhorst, H.J., and J.D. Pack, *Special points for Brillouin-zone integrations*. Physical Review B, 1976. **13**(12): p. 5188-5192.
  35. Allen, M.P., and D.J. Tildesley, *Computer Simulation of Liquids*. 1988, USA: Oxford University Press.
  36. Alder, B.J., and T.E. Wainwright, *Phase Transition for a Hard Sphere System*. The Journal of Chemical Physics, 1957. **27**(5): p. 1208-1209.
  37. Mills, G., H. Jonsson, and G.K. Schenter, *Reversible Work Transition-State Theory - Application to Dissociative Adsorption of Hydrogen*. Surface Science, 1995. **324**(2-3): p. 305-337.
  38. Rocha, A.R., *Theoretical and computational aspects of electronic transport at the nanoscale*, 2007, School of Physics Trinity College Dublin: Dublin.
  39. Datta, S., *Electronic Transport in Mesoscopic Systems*. 1995, Cambridge, UK: Cambridge University Press.
  40. Caroli, C., R. Combescot, P. Nozieres, and D. Saint-James, *A direct calculation of the tunnelling current: IV. Electron-phonon interaction effects*. Journal of Physics C: Solid State Physics, 1972. **5**(1): p. 21.
  41. Emberly, E.G., and G. Kirczenow, *Theoretical study of electrical conduction through a molecule connected to metallic nanocontacts*. Physical Review B, 1998. **58**(16): p. 10911-10920.
  42. Rego, L.G.C., A.R. Rocha, V. Rodrigues, and D. Ugarte, *Role of structural evolution in the quantum conductance behavior of gold nanowires during stretching*. Physical Review B, 2003. **67**(4): p. 045412.
  43. Landauer, R., *Electrical resistance of disordered one-dimensional lattices*. Philosophical Magazine, 1970. **21**(172): p. 863-867.
  44. Economou, E.N., and C.M. Soukoulis, *Static Conductance and Scaling Theory of Localization in One Dimension*. Physical Review Letters, 1981. **46**(9): p. 618-621.
  45. Fisher, D.S., and P.A. Lee, *Relation between conductivity and transmission matrix*. Physical Review B, 1981. **23**(12): p. 6851-6854.
  46. Büttiker, M., Y. Imry, R. Landauer, and S. Pinhas, *Generalized many-channel conductance formula with application to small rings*. Physical Review B, 1985. **31**(10): p. 6207-6215.

47. Landauer, R., *Spatial variation of currents and fields due to localized scatterers in metallic conduction*. IBM J. Res. Dev., 1988. **32**(3): p. 306-316.
48. Buttiker, M., *Symmetry of electrical conduction*. IBM J. Res. Dev., 1988. **32**(3): p. 317-334.
49. A.R. Rocha, V.M.G.-S., S.W. Bailey, C.J. Lambert, J. Ferrer, S. Sanvito, *SMEAGOL (Spin and Molecular Electronics in an Atomically-Generated Orbital Landscape, [www.smeagol.tcd.ie](http://www.smeagol.tcd.ie))*.
50. Rocha, A.R., V.M. Garcia-Suarez, S.W. Bailey, C.J. Lambert, J. Ferrer, and S. Sanvito, *Towards molecular spintronics*. Nature Materials, 2005. **4**(4): p. 335-339.
51. Sánchez-Portal, D., P. Ordejón, E. Artacho, and J.M. Soler, *Density-functional method for very large systems with LCAO basis sets*. International Journal of Quantum Chemistry, 1997. **65**(5): p. 453-461.
52. H. Haug, A.P.J., *Quantum Kinetics in Transport and Optics of Semiconductors*. 1996, Berlin, Heidelberg: Springer.
53. Jauho, A.P., N.S. Wingreen, and Y. Meir, *Time-Dependent Transport in Interacting and Noninteracting Resonant-Tunneling Systems*. Physical Review B, 1994. **50**(8): p. 5528-5544.
54. Buttiker, M., Y. Imry, R. Landauer, and S. Pinhas, *Generalized Many-Channel Conductance Formula with Application to Small Rings*. Physical Review B, 1985. **31**(10): p. 6207-6215.
55. Bollinger, M.V., K.W. Jacobsen, and J.K. Nørskov, *Atomic and electronic structure of MoS<sub>2</sub> nanoparticles*. Physical Review B, 2003. **67**(8): p. 085410.
56. Botello-Méndez, A.R., F. López-Urías, M. Terrones, and H. Terrones, *Metallic and ferromagnetic edges in molybdenum disulfide nanoribbons*. Nanotechnology, 2009. **20**(32): p. 325703.
57. Li, Y., Z. Zhou, S. Zhang, and Z. Chen, *MoS<sub>2</sub> Nanoribbons: High Stability and Unusual Electronic and Magnetic Properties*. Journal of the American Chemical Society, 2008. **130**(49): p. 16739-16744.
58. Le, D., and T.S. Rahman, *Joined edges in MoS<sub>2</sub>: metallic and half-metallic wires*. Journal of Physics: Condensed Matter, 2013. **25**(31): p. 312201.
59. Kresse, G., and J. Hafner, *Abinitio Molecular-Dynamics for Liquid-Metals*. Physical Review B, 1993. **47**(1): p. 558-561.
60. Dandrea, R.G., and C.B. Duke. *Calculation of the Schottky barrier height at the Al/GaAs(001) heterojunction: Effect of interfacial atomic relaxations*. 1993. Chicago, Illinois (USA): AVS.
61. Le, D., D.Z. Sun, W.H. Lu, L. Bartels, and T.S. Rahman, *Single layer MoS<sub>2</sub> on the Cu(111) surface: First-principles electronic structure calculations*. Physical Review B, 2012. **85**(7).

62. D. Sun, W. Lu, D. Le, Q. Ma, M. Aminpour, M. Alcántara Ortigoza, S. Bobek, J. Mann, J. Wyrick, T. S. Rahman, and L. Bartels, *A Novel MoS<sub>x</sub> Structure with High Affinity for Adsorbate Interaction*. *Angewandte Chemie International Edition*, 2012. **51**: p. 10284–10288.
63. Domange, J.L., and J. Oudar, *Structure and Formative Conditions of Sulfur Layer Adsorption on Copper*. *Surface Science*, 1968. **11**(1): p. 124-&.
64. Prince, N.P., D.L. Seymour, M.J. Ashwin, C.F. McConville, D.P. Woodruff, and R.G. Jones, *A SEXAFS and X-ray standing wave study of the Cu(111)(sqrt 7 X sqrt 7)R19-S surface: Adsorbate-substrate and adsorbate-adsorbate registry*. *SURFACE SCIENCE*, 1990. **230**(1-3): p. 13-26.
65. Ruan, L., I. Stensgaard, F. Besenbacher, and E. Laegsgaard, *A Scanning Tunneling Microscopy Study of the Interaction of S with the Cu(111) Surface*. *Ultramicroscopy*, 1992. **42**: p. 498-504.
66. Motai, K., T. Hashizume, H. Lu, D. Jeon, T. Sakurai, and H.W. Pickering, *STM of the Cu(111)1x1 Surface and Its Exposure to Chlorine and Sulfur*. *Applied Surface Science*, 1993. **67**(1-4): p. 246-251.
67. Campbell, C.T., and B.E. Koel, *H<sub>2</sub>S/Cu(111) - a Model Study of Sulfur Poisoning of Water-Gas Shift Catalysts*. *Surface Science*, 1987. **183**(1-2): p. 100-112.
68. Foss, M., R. Feidenhans'l, M. Nielsen, E. Findeisen, T. Buslaps, R.L. Johnson, and F. Besenbacher, *Sulfur induced Cu<sub>4</sub> tetramers on Cu(111)*. *SURFACE SCIENCE*, 1997. **388**(1缺?): p. 5-14.
69. Saidy, M., and K.A.R. Mitchell, *Tensor LEED analysis for the Cu(111)-(sqrt 7x sqrt 7)R19.1-S surface structure*. *SURFACE SCIENCE*, 1999. **441**(2-3): p. 425-435.
70. Blochl, P.E., C.J. Forst, and J. Schimpl, *Projector augmented wave method: ab initio molecular dynamics with full wave functions*. *Bulletin of Materials Science*, 2003. **26**(1): p. 33-41.
71. Blöchl, P.E., *Projector augmented-wave method*. *PHYSICAL REVIEW B*, 1994. **50**(24): p. 17953.
72. Mortensen, J.J., L.B. Hansen, and K.W. Jacobsen, *Real-space grid implementation of the projector augmented wave method*. *PHYSICAL REVIEW B*, 2005. **71**(3): p. 035109.
73. M. Dion, H.R., E. Schröder, D.C. Langreth, B.I. Lundqvist, *Phys. Rev. Lett.* , 2004. **92**: p. 246401.
74. Klimes, J., D.R. Bowler, and A. Michaelides, *Chemical accuracy for the van der Waals density functional*. *Journal of Physics-Condensed Matter*, 2010. **22**(2): p. 022201.
75. Roman-Perez, G., and J.M. Soler, *Efficient Implementation of a van der Waals Density Functional: Application to Double-Wall Carbon Nanotubes*. *Physical Review Letters*, 2009. **103**(9): p. 096102
76. H. Monkhorst , J.P., *Special points for Brillonin-zone integrations\**. *Phys. Rev. B*, 1976. **13**: p. 5188.

77. K. Parlinski, Z.Q.L.a.Y.K., Phys. Rev. Lett., 1997. **78**: p. 4063-4066.
78. Atsushi Togo, F.O., and Isao Tanaka, *First-principles calculations of the ferroelastic transition between rutile-type and CaCl<sub>2</sub>-type SiO<sub>2</sub> at high pressures*. Phys. Rev. B. **78**.
79. Alfonso, D.R., *Computational Studies of Experimentally Observed Structures of Sulfur on Metal Surfaces*. Journal of Physical Chemistry C, 2011. **115**(34): p. 17077-17091.
80. Visic, B., R. Dominko, M. Gunde, N. Hauptman, S. Skapin, and M. Remskar, *Optical properties of exfoliated MoS<sub>2</sub> coaxial nanotubes - analogues of graphene*. Nanoscale Research Letters, 2011. **6**(1): p. 593.
81. Albiter, M.A., R. Huirache-Acuña, F. Paraguay-Delgado, J.L. Rico, and G. Alonso-Nuñez, *Synthesis of MoS<sub>2</sub> nanorods and their catalytic test in the HDS of dibenzothiophene*. Nanotechnology, 2006. **17**(14): p. 3473.
82. Zong, X., Y. Na, F. Wen, G. Ma, J. Yang, D. Wang, Y. Ma, M. Wang, L. Sun, and C. Li, *Visible light driven H<sub>2</sub> production in molecular systems employing colloidal MoS<sub>2</sub> nanoparticles as catalyst*. Chemical Communications, 2009(30): p. 4536-4538.
83. Wiesel, I., H. Arbel, A. Albu-Yaron, R. Popovitz-Biro, J. Gordon, D. Feuermann, and R. Tenne, *Synthesis of WS<sub>2</sub> and MoS<sub>2</sub> fullerene-like nanoparticles from solid precursors*. Nano Research, 2009. **2**(5): p. 416-424.
84. V. Turkowski, A. Kabir, N. Nayyar, and T.S. Rahman, *Magnetic properties of small iron clusters: application of Dynamical Mean Field Theory*. to be published.
85. Popov, I., S. Gemming, S. Okano, N. Ranjan, and G. Seifert, *Electromechanical Switch Based on Mo<sub>6</sub>S<sub>6</sub> Nanowires*. Nano Letters, 2008. **8**(12): p. 4093-4097.
86. Kibsgaard, J., A. Tuxen, M. Levisen, E. Laegsgaard, S. Gemming, G. Seifert, J.V. Lauritsen, and F. Besenbacher, *Atomic-Scale Structure of Mo<sub>6</sub>S<sub>6</sub> Nanowires*. Nano Letters, 2008. **8**(11): p. 3928-3931.
87. DiMasi, E., V.M. Patel, M. Sivakumar, M.J. Olszta, Y.P. Yang, and L.B. Gower, *Polymer-controlled growth rate of an amorphous mineral film nucleated at a fatty acid monolayer*. Langmuir, 2002. **18**(23): p. 8902-8909.
88. Dion, M., H. Rydberg, E. Schröder, D.C. Langreth, and B.I. Lundqvist, *Van der Waals density functional for general geometries*. Physical Review Letters, 2004. **92**(24): p. 246401.
89. Thonhauser, T., V.R. Cooper, S. Li, A. Puzder, P. Hyldgaard, and D.C. Langreth, *Van der Waals density functional: Self-consistent potential and the nature of the van der Waals bond*. Physical Review B, 2007. **76**(12).
90. Klimes, J., D.R. Bowler, and A. Michaelides, *Van der Waals density functionals applied to solids*. Physical Review B, 2011. **83**(19).
91. Le, D., D. Sun, W. Lu, M. Aminpour, C. Wang, Q. Ma, T.S. Rahman, and L. Bartels, *Growth of aligned Mo<sub>6</sub>S<sub>6</sub> nanowires on Cu(111)*. Surface Science, 2013. **611**(0): p. 1-4.
92. Kittel, C., *Introduction to solid state physics*. 7th ed. 1996, New York: Wiley. xi, 673 p.

93. Domange, J.L., and J. Oudar, *Structure et conditions de formation de la couche d'adsorption du soufre sur le cuivre*. SURFACE SCIENCE, 1968. **11**(1): p. 124-142.
94. Binnig, G., H. Rohrer, C. Gerber, and E. Weibel, *7x7 Reconstruction on Si(111) Resolved in Real Space*. PHYSICAL REVIEW LETTERS, 1983. **50**(2): p. 120.
95. Repp, J., F. Moresco, G. Meyer, K. Rieder, P. Hyldgaard, and M. Persson, *Substrate mediated long-range oscillatory interaction between adatoms: Cu/Cu(111)*. Physical Review Letters, 2000. **85**(14): p. 2981-2984.
96. Knorr, N., H. Brune, M. Epple, A. Hirstein, M. Schneider, and K. Kern, *Long-range adsorbate interactions mediated by a two-dimensional electron gas*. Physical Review B, 2002. **65**(11): p. -.
97. Wang, Y.F., X. Ge, C. Manzano, J. Korger, R. Berndt, W.A. Hofer, H. Tang, and J. Cerda, *Supramolecular Patterns Controlled by Electron Interference and Direct Intermolecular Interactions*. Journal of the American Chemical Society, 2009. **131**(30): p. 10400-+.
98. Mitsui, T., M.K. Rose, E. Fomin, D.F. Ogletree, and M. Salmeron, *Diffusion and pair interactions of CO molecules on Pd(111)*. Physical Review Letters, 2005. **94**(3): p. 036101.
99. Wong, K.L., B.V. Rao, G. Pawin, E. Ulin-Avila, and L. Bartels, *Coverage and nearest-neighbor dependence of adsorbate diffusion*. Journal of Chemical Physics, 2005. **123**(20): p. 201102.
100. Lyubinetsky, I., D.B. Dougherty, T.L. Einstein, and E.D. Williams, *Dynamics of step fluctuations on a chemically heterogeneous surface of Al/Si(111)-(root 3x root 3)*. Physical Review B, 2002. **66**(8): p. 085327.
101. Chiang, T.C., *Photoemission studies of quantum well states in thin films*. Surface Science Reports, 2000. **39**(7-8): p. 181-235.
102. De'Bell, K., A.B. MacIsaac, and J.P. Whitehead, *Dipolar effects in magnetic thin films and quasi-two-dimensional systems*. Reviews of Modern Physics, 2000. **72**(1): p. 225-257.
103. Himpsel, F.J., *Magnetic quantum wells*. Journal of Physics: Condensed Matter, 1999. **11**(48): p. 9483.
104. N. Binggeli, M.A., *Quantum-size effects in ultrathin Mg films*. Phys. Rev. B, 2008. **78**: p. 035438.
105. Xiang-Gui Li, P.Z., C.K. Chan, *First-principles calculation of Mg(0 0 0 1) thin films: Quantum size effect and adsorption of atomic hydrogen*. PhysicaB, 2007. **390**: p. 225-230.
106. Aminpour, M., M.A. Ortigoza, and T.S. Rahman, *Electronic Structure Features Controlling The Limit Of Aand Reactivity Iin Tthe Thin-Film Regime, Stacking Fault Oof Mg Adislands Aand Adatom Self-Diffusion*. To be Submitted, 2013.

107. H.L. Davis, J.B.H., K.B. Ray, E.W. Plummer, Phys., *Anomalous interplanar expansion at the (0001) surface of Be*. Phys. Rev. Lett, 1992. **68**: p. 2632.
108. P.T. Sprunger, K.P., H.L. Davis, E.W. Plummer, Surf. Sci., 1993. **297**: p. L48.
109. Smoluchowski, R., Phys.Rev., 1941. **60**: p. 661.
110. P.J. Feibelman, R.S., *Physics of the Be(0001) surface core-level spectrum*. Phys. Rev. B, 1994. **50**(17): p. 480.
111. Pauling, L., *The nature of the chemical bond*, ed. r. ed. 19860, Ithaca, NY: Cornell University Press.
112. A. Kiejna, K.F.W., *Metal Surface Electron Physics*. Pergamon Press, Oxford, UK.
113. Kiejna, E.W.a.A., *Bulk and surface properties of hexagonal-close-packed Be and Mg*. J. Phys.: Condens. Matter, 2001. **13**: p. 10767–10776.
114. Rahman, P.S.a.T.S., *Multilayer relaxations and stresses on Mg surfaces*. PHYSICAL REVIEW B, 1999. **60**: p. 15 613-15617.
115. 7. QUANTUM-ESPRESSO is a community project for high-quality quantum-simulation software, b.o.d.-f.t.S.h.w.q.-e.o.a.h.w.p.
116. Wang, J.P.P.a.Y., *Accurate and simple analytic representation of the electron-gas correlation energy*. Phys. Rev. B, 1992. **45**: p. 13244.
117. Paolo Giannozzi, S.B., Nicola Bonini, Matteo Calandra, Roberto Car, Carlo Cavazzoni, Davide Ceresoli, Guido L Chiarotti, Matteo Cococcioni, Ismaila Dabo, Andrea Dal , Stefano de Gironcoli, Stefano Fabris, Guido Fratesi, Ralph Gebauer, Gerstmann, Christos Gougoussis , Anton Kokalj , Michele Lazzeri , 5, L.M.-S. , 1, N.M. , 4, , F. Mauri, 5, R.M. , 16, S.P. , 3, , A. Pasquarello, 17, L.P. , 1, C.S. , 1, , S. Scandolo, 1, G.S. , 1, A.P.S. , 5, , A. Smogunov, 13, P.U. , 1, and, R.M. Wentzcovitch, and 13244, *QUANTUM ESPRESSO: a modular and open-source software project for quantum simulations of materials*. J. Phys.: Condens. Matter 2009. **21**: p. 395502.
118. Hellmann, L., Franz Deuticke, 1973. **285**.
119. V.M. Amonenko, V.Y.I., G.F. Tikhinskij, V.A. Finkel, 1962. **14**: p. 47.
120. Kittel, C., *Introduction to Solid State Physics*. Wiley, John & Sons, Incorporated.
121. Gschneldner K A, J., Solid State Phys., 1964. **16**: p. 275-426.
122. Errandonea, D., Y. Meng, D. Hausermann, and T. Uchida, *Study of the phase transformations and equation of state of magnesium by synchrotron x-ray diffraction*. Journal of Physics-Condensed Matter, 2003. **15**(8): p. 1277-1289.
123. Fuchs, M., M. Bockstedte, E. Pehlke, and M. Scheffler, *Pseudopotential study of binding properties of solids within generalized gradient approximations: The role of core-valence exchange correlation*. Physical Review B, 1998. **57**(4): p. 2134-2145.
124. E. Wachowicz, A.K., *Multilayer relaxations at the (0001) surface of Be and Mg*. Solid State Communications, 2000. **116**: p. 17-20.

125. Wright A F, F.P.J.a.A.S.R., Surf.Sci., 1994. **302**: p. 215.
126. Ismail, P. Hofmann, E.W. Plummer, C. Bungaro, and W. Kress, *Surface lattice dynamics of Mg(0001)*. PHYSICAL REVIEW B, 2000. **62**(24): p. 17012-17019.
127. Errandonea, D., Y. Meng, D. Häusermann, and T. Uchida, *Study of the phase transformations and equation of state of magnesium by synchrotron x-ray diffraction*. Journal of Physics: Condensed Matter, 2003. **15**(8): p. 1277.
128. Sprunger, P.T., K. Pohl, H.L. Davis, and E.W. Plummer, *Multilayer relaxation of the Mg(0001) surface*. Surface Science, 1993. **297**(1): p. L48-L54.
129. Staikov, P., and T.S. Rahman, *Multilayer relaxations and stresses on Mg surfaces*. Physical Review B, 1999. **60**(23): p. 15613-15616.
130. Wachowicz, E., and A. Kiejna, *Bulk and surface properties of hexagonal-close-packed Be and Mg*. Journal of Physics-Condensed Matter, 2001. **13**(48): p. 10767-10776.
131. Li, X.G., P. Zhang, and C.K. Chan, *First-principles calculation of Mg(0001) thin films: Quantum size effect and adsorption of atomic hydrogen*. Physica B-Condensed Matter, 2007. **390**(1-2): p. 225-230.
132. Hayden, B.E., E. Schweizer, R. Kötz, and A.M. Bradshaw, *The early stages of oxidation of magnesium single crystal surfaces*. Surface Science, 1981. **111**(1): p. 26-38.
133. Wu, G., J. Zhang, Y. Wu, Q. Li, K. Chou, and X. Bao, *Adsorption and dissociation of hydrogen on MgO surface: A first-principles study*. Journal of Alloys and Compounds, 2009. **480**(2): p. 788-793.
134. Wachowicz, E., and A. Kiejna, *Multilayer relaxations at the (0001) surface of Be and Mg*. Solid State Communications, 2000. **116**(1): p. 17-20.
135. Aballe, L., C. Rogero, and K. Horn, *Quantum size effects in ultrathin epitaxial Mg films on Si(111)*. Physical Review B, 2002. **65**(12): p. 125319.
136. Hellman, A., *Nonadiabaticity in the initial oxidation of Mg(0001): First-principles density-functional calculations*. Physical Review B, 2005. **72**(20): p. 201403.
137. Binggeli, N., and M. Altarelli, *Quantum-size effects in ultrathin Mg films*. Physical Review B, 2008. **78**(3): p. 035438.
138. Binggeli, N., and M. Altarelli, *Surface Reactivity and Quantum-Size Effects on the Electronic Density Decay Length of Ultrathin Metal Films*. Physical Review Letters, 2006. **96**(3): p. 036805.
139. Stolbov, S., and S. Zuluaga, *Factors Controlling the Reactivity of Catalytically Active Monolayers on Metal Substrates*. The Journal of Physical Chemistry Letters, 2013. **4**(9): p. 1537-1540.
140. Chou, M.Y., P.K. Lam, and M.L. Cohen, *Ab initio study of structural and electronic properties of beryllium*. PHYSICAL REVIEW B, 1983. **28**(8): p. 4179-4185.
141. Cho, J.-H., Ismail, Z. Zhang, and E.W. Plummer, *Oscillatory lattice relaxation at metal surfaces*. Physical Review B, 1999. **59**(3): p. 1677-1680.

142. Tian, Z.J., U. Yxklinten, B.I. Lundqvist, and K.W. Jacobsen, *Calculated chemisorption properties of magnesium*. Surface Science, 1991. **258**(1–3): p. 427-438.
143. Brune, H., *Metals on metals*, in *Adsorbed Layers on Surfaces. Part 1: Adsorption on Surfaces and Surface Diffusion of Adsorbates*, A.P. Bonzel, Editor. 2001, Springer Berlin Heidelberg. p. 217-243.
144. Rahman, T.S., C. Gosh, O. Trushin, A. Kara, and A. Karim. *Atomistic studies of thin film growth*. 2004.
145. L. Aballe, C.R., and K. Horn, *Quantum size effects in ultrathin epitaxial Mg films on Si(111)*. PHYSICAL REVIEW B, 2002. **65**: p. 125319- 125327.
146. F. Schiller, M.H., V.D. Servedio, C. Laubschat, *Electronic structure of Mg: From monolayers to bulk*. Phys. Rev. B, 2004. **70**: p. 125106.
147. C. Koitzsch, C.B., F. Clerc, L. Despont, M. G. Garnier, and P. Aebi *Photoemission of a Quantum Cavity with a Nonmagnetic Spin Separator*. PHYSICAL REVIEW LETTERS, 2005. **95**: p. 126401-126405.
148. F. Schiller, R.K., E.V. Chulkov, and J. E. Ortega, *Surface State Scattering at a Buried Interface*. PHYSICAL REVIEW LETTERS, 2005. **95**: p. 126402-126406.
149. Koitzsch, C., C. Battaglia, F. Clerc, L. Despont, M.G. Garnier, and P. Aebi, *Photoemission of a Quantum Cavity with a Nonmagnetic Spin Separator*. Physical Review Letters, 2005. **95**(12): p. 126401.
150. Schiller, F., M. Heber, V.D.P. Servedio, and C. Laubschat, *Electronic structure of Mg: From monolayers to bulk*. Physical Review B, 2004. **70**(12): p. 125106.
151. Schiller, F., R. Keyling, E.V. Chulkov, and J.E. Ortega, *Surface State Scattering at a Buried Interface*. Physical Review Letters, 2005. **95**(12): p. 126402.
152. Aballe, L., A. Barinov, A. Locatelli, S. Heun, and M. Kiskinova, *Tuning Surface Reactivity via Electron Quantum Confinement*. Physical Review Letters, 2004. **93**(19): p. 196103.
153. Kuntová, Z., M.C. Tringides, S.M. Binz, M. Hupalo, and Z. Chvoj, *Controlling nucleation rates in nanostructures with electron confinement*. Surface Science, 2010. **604**(5–6): p. 519-522.
154. Chromcová, Z., M. Hupalo, M.C. Tringides, M. Aminpour, M.A. Ortigoza, T.S. Rahman, and Z. Chvoj, *Controllable Mg film morphologies: DFT, kinetic Monte Carlo simulations and experiments on Mg films on stepped W(110) surfaces*. submitted to Surf. Sci., 2013.
155. Diaconescu, B., G. Nenchev, J. Jones, and K. Pohl, *Self-organized nanotemplating on misfit dislocation networks investigated by scanning tunneling microscopy*. Microscopy Research and Technique, 2007. **70**(6): p. 547-553.
156. Chambliss, D.D., R.J. Wilson, and S. Chiang, *Nucleation of ordered Ni island arrays on Au(111) by surface-lattice dislocations*. Physical Review Letters, 1991. **66**(13): p. 1721-1724.



157. Meyer, J.A., I.D. Baikie, E. Kopatzki, and R.J. Behm, *Preferential island nucleation at the elbows of the Au(111) herringbone reconstruction through place exchange*. Surface Science, 1996. **365**(1): p. L647-L651.
158. Himpsel, F.J., A. Kirakosian, J.N. Crain, J.L. Lin, and D.Y. Petrovykh, *Self-assembly of one-dimensional nanostructures at silicon surfaces*. Solid State Communications, 2001. **117**(3): p. 149-157.
159. Omi, H., D.J. Bottomley, Y. Homma, and T. Ogino, *Wafer-scale strain engineering on silicon for fabrication of ultimately controlled nanostructures*. Physical Review B, 2003. **67**(11): p. 115302.
160. Günther, C., J. Vrijmoeth, R.Q. Hwang, and R.J. Behm, *Strain Relaxation in Hexagonally Close-Packed Metal-Metal Interfaces*. Physical Review Letters, 1995. **74**(5): p. 754-757.
161. Brune, H., M. Giovannini, K. Bromann, and K. Kern, *Self-organized growth of nanostructure arrays on strain-relief patterns*. Nature, 1998. **394**(6692): p. 451-453.
162. Kim, H., C. Shin, and J. Chang, *Formation of Ge self-assembled quantum dots on a SixGe1-x buffer layer*. Applied Surface Science, 2005. **252**(5): p. 1476-1480.
163. Ait-Mansour, K., M. Treier, P. Ruffieux, M. Bieri, R. Jaafar, P. Groning, R. Fasel, and O. Groning, *Template-Directed Molecular Nanostructures on the Ag/Pt(111) Dislocation Network*. Journal of Physical Chemistry C, 2009. **113**(19): p. 8407-8411.
164. Larsson, M.I., R.F. Sabiryanov, K. Cho, and B.M. Clemens, *Surface strain effects on adatom kinetics and self-assembly*. Surface Science, 2003. **536**(1-3): p. L389-L395.
165. Y.X. Wang, Z.Y.P., Z.J. Li, Q. Wei, L.K. Zang and Z.X. Zhang, *Effect of tensile strain on adatom diffusion on Cu(111) surface*. SURFACE SCIENCE, 2003. **545**: p. 137-142.
166. Pinczolits, M., G. Springholz, and G. Bauer, *Direct formation of self-assembled quantum dots under tensile strain by heteroepitaxy of PbSe on PbTe (111)*. Applied Physics Letters, 1998. **73**(2): p. 250-252.
167. Ala-Nissila, T., R. Ferrando, and S.C. Ying, *Collective and single particle diffusion on surfaces*. Advances in Physics, 2002. **51**(3): p. 949-1078.
168. Schroeder, M., and D.E. Wolf, *Diffusion on strained surfaces*. Surface Science, 1997. **375**(1): p. 129-140.
169. Goyhenex, C., K. Farah, and A. Taobane, *Lattice mismatch effect in atomic migration along steps during heteroepitaxial metal growth*. Surface Science, 2007. **601**(23): p. L132-L135.
170. Brune, H., K. Bromann, H. Röder, K. Kern, J. Jacobsen, P. Stoltze, K. Jacobsen, and J. No/rskov, *Effect of strain on surface diffusion and nucleation*. Physical Review B, 1995. **52**(20): p. R14380-R14383.
171. Ratsch, C., and M. Scheffler, *Density-functional theory calculations of hopping rates of surface diffusion*. Physical Review B, 1998. **58**(19): p. 13163-13166.

172. Xiao, W., P.A. Greaney, and D.C. Chrzan, *Adatom Transport on Strained Cu(001): Surface Crowdions*. Physical Review Letters, 2003. **90**(15): p. 156102.
173. Xiao, W., P.A. Greaney, and D.C. Chrzan, *Pt adatom diffusion on strained Pt(001)*. Physical Review B, 2004. **70**(3): p. 033402.
174. Bean, J.C., *Strained-Layer Epitaxy of Germanium-Silicon Alloys*. Science, 1985. **230**(4722): p. 127-131.
175. Matthews, J.W., and A.E. Blakeslee, *Defects in epitaxial multilayers: I. Misfit dislocations*. Journal of Crystal Growth, 1974. **27**(0): p. 118-125.
176. Much, F., and M. Biehl, *Simulation of wetting-layer and island formation in heteroepitaxial growth*. EPL (Europhysics Letters), 2003. **63**(1): p. 14.
177. Volkmann, T., F. Much, M. Biehl, and M. Kotrla, *Interplay of strain relaxation and chemically induced diffusion barriers: Nanostructure formation in 2D alloys*. Surface Science, 2005. **586**(1-3): p. 157-173.
178. Trushin, O., E. Granato, S.C. Ying, P. Salo, and T. Ala-Nissila, *Minimum energy paths for dislocation nucleation in strained epitaxial layers*. Physical Review B, 2002. **65**(24): p. 241408.
179. Walther, M., M. Biehl, and W. Kinzel, *Formation and consequences of misfit dislocations in heteroepitaxial growth*. physica status solidi (c), 2007. **4**(9): p. 3210-3220.
180. Trushin, O., J. Jalkanen, E. Granato, S.C. Ying, and T. Ala-Nissila, *Atomistic studies of strain relaxation in heteroepitaxial systems*. Journal of Physics: Condensed Matter, 2009. **21**(8): p. 084211.
181. Foiles, S.M., M.I. Baskes, and M.S. Daw, *Embedded-Atom-Method Functions for the Fcc Metals Cu, Ag, Au, Ni, Pd, Pt, and Their Alloys*. Physical Review B, 1986. **33**(12): p. 7983-7991.
182. Semancik, S., R.E. Cavicchi, K.G. Kreider, J.S. Suehle, and P. Chaparala, *Selected-area deposition of multiple active films for conductometric microsensor arrays*. Sensors and Actuators B: Chemical, 1996. **34**(1-3): p. 209-212.
183. Aït-Mansour, K., M. Treier, P. Ruffieux, M. Bieri, R. Jaafar, P. Gröning, R. Fasel, and O. Gröning, *Template-Directed Molecular Nanostructures on the Ag/Pt(111) Dislocation Network*. The Journal of Physical Chemistry C, 2009. **113**(19): p. 8407-8411.
184. Brune, H., M. Giovannini, K. Bromann, and K. Kern, *Self-organized growth of nanostructure arrays on strain-relief patterns*. Nature, 1998. **394**(6692).
185. Aminpour, M., O. Trushin, and T.S. Rahman, *Effect of misfit dislocation on surface diffusion*. Physical Review B, 2011. **84**(3): p. 035455.
186. Plimpton, S., *Fast Parallel Algorithms for Short-Range Molecular Dynamics*. J Comp Phys, 1995. **117**: p. 1-19.
187. G. Bonny, R.C.P., N. Catsin, L. Malerba *Ternary Fe-Cu-Ni many-body potential to model reactor pressure vessel steels: First validation by simulated thermal annealing*. Philosophical Magazine & Philosophical Magazine Letter, 2009. **89**(34-36): p. 3531.

188. Press, W.H., S.A. Teukolsky, W.T. Vetterling, and B.P. Flannery, *Numerical Recipes: The Art of Scientific Computing*. Cambridge University Press, 1989.
189. H. Jonsson, G.M., and K. W. Jacobsen *Classical and Quantum Dynamics in Condensed Phase Simulations edited by B. J. Berne et al.* World Scientific, Singapore, 1998.
190. Bulatov, V., and W. Cai, *Computer Simulations of Dislocations, Chapter 4*, 2006, Oxford University Press.
191. Z.J.Tian, U.Y., B.I. Lundqvist, *Calculated chemisorption properties of magnesium Surf. Sci.*, 1991. **258**: p. 427-438.

## **APPENDIX A: COPYRIGHTS AND PERMISSIONS**



November 14, 2013

Dr. Maral Aminpour  
Graduate Research Assistant  
Department of Physics  
University of Central Florida

**Ref # 25010**

Thank you for your permission request dated Nov. 12, 2013. We are pleased to grant you a non-exclusive, non-transferable permission, English rights, limited to **print and electronic format**, provided you meet the criteria outlined below. Permission is for a one-time use and does not include permission for future editions, updates, databases, translations, or any other matters. Permission must be sought for each additional use. This permission does not include the right to modify APS material.

Please print the required copyright credit line on the first page that the material appears: “Reprinted (abstract/excerpt/figure) with permission from [FULL REFERENCE CITATION] as follows: authors names, journal title, volume number, page number and year of publication. Copyright (YEAR) by the American Physical Society.

The following language must appear somewhere on the website: “Readers may view, browse, and/or download material for temporary copying purposes only, provided these uses are for noncommercial personal purposes. Except as provided by law, this material may not be further reproduced, distributed, transmitted, modified, adapted, performed, displayed, published, or sold in whole or part, without prior written permission from the American Physical Society.”

Provide a hyperlink from the reprinted APS material (the hyperlink may be embedded in the copyright credit line). APS’s link manager technology makes it convenient and easy to provide links to individual articles in APS journals. For information, see: <http://link.aps.org/>.

You must also obtain permission from at least one of the authors for each separate work, if you haven’t done so already. The author’s name and address can be found on the first page of the published Article.

Use of the APS material must not imply any endorsement by the American Physical Society.

Permission is granted for use of the following APS material only:

- Fig. 4, Phys. Rev. B 59, 1677–1680 (1999)
- Fig. 2, Phys. Rev. B 85, 075429 (2012)
- Fig. 3, Phys. Rev. B 72, 201403(R) (2005)
- Fig. 1, Phys. Rev. B 60, 15613–15616 (1999)

Permission is limited to the single title specified of the publication as follows:

A thesis entitled THEORETICAL STUDIES OF NANOSTRUCTURE FORMATION AND TRANSPORT ON SURFACES to be published by University of Central Florida.

If you have any questions, please refer to the Copyright FAQ at: <http://publish.aps.org/copyrightFAQ.html> or send an email to [assocpub@aps.org](mailto:assocpub@aps.org).

Sincerely,

Jamie L. Casey  
Circulation and Fulfillment Assistant

## ELSEVIER LICENSE TERMS AND CONDITIONS

Nov 14, 2013

This is a License Agreement between Maral Aminpour ("You") and Elsevier ("Elsevier") provided by Copyright Clearance Center ("CCC"). The license consists of your order details, the terms and conditions provided by Elsevier, and the payment terms and conditions.

**All payments must be made in full to CCC. For payment instructions, please see information listed at the bottom of this form.**

Supplier	Elsevier Limited The Boulevard, Langford Lane Kidlington, Oxford, OX5 1GB, UK
Registered Company Number	1982084
Customer name	Maral Aminpour
Customer address	University of Central Florida ORLANDO, FL 32816
License number	3266381028256
License date	Nov 12, 2013
Licensed content publisher	Elsevier
Licensed content publication	Physica B: Condensed Matter
Licensed content title	First-principles calculation of Mg(0001) thin films: Quantum size effect and adsorption of atomic hydrogen
Licensed content author	Xiang-Gui Li, Ping Zhang, C.K. Chan
Licensed content date	1 March 2007
Licensed content volume number	390
Licensed content issue number	1-2
Number of pages	6
Start Page	225
End Page	230
Type of Use	reuse in a thesis/dissertation
Intended publisher of new work	other
Portion	figures/tables/illustrations
Number of figures/tables/illustrations	4
Format	both print and electronic
Are you the author of this Elsevier article?	No
Will you be translating?	No
Title of your thesis/dissertation	THEORETICAL STUDIES OF NANOSTRUCTURE FORMATION AND TRANSPORT ON SURFACES



Expected completion date	Nov 2013
Estimated size (number of pages)	180
Elsevier VAT number	GB 494 6272 12
Permissions price	0.00 USD
VAT/Local Sales Tax	0.00 USD / 0.00 GBP
<b>Total</b>	<b>0.00 USD</b>
<a href="#">Terms and Conditions</a>	

#### INTRODUCTION

1. The publisher for this copyrighted material is Elsevier. By clicking "accept" in connection with completing this licensing transaction, you agree that the following terms and conditions apply to this transaction (along with the Billing and Payment terms and conditions established by Copyright Clearance Center, Inc. ("CCC"), at the time that you opened your Rightslink account and that are available at any time at <http://myaccount.copyright.com>).

#### GENERAL TERMS

2. Elsevier hereby grants you permission to reproduce the aforementioned material subject to the terms and conditions indicated.
3. Acknowledgement: If any part of the material to be used (for example, figures) has appeared in our publication with credit or acknowledgement to another source, permission must also be sought from that source. If such permission is not obtained then that material may not be included in your publication/copies. Suitable acknowledgement to the source must be made, either as a footnote or in a reference list at the end of your publication, as follows:  
"Reprinted from Publication title, Vol /edition number, Author(s), Title of article /title of chapter, Pages No., Copyright (Year), with permission from Elsevier [OR APPLICABLE SOCIETY COPYRIGHT OWNER]." Also Lancet special credit -  
"Reprinted from The Lancet, Vol. number, Author(s), Title of article, Pages No., Copyright (Year), with permission from Elsevier."
4. Reproduction of this material is confined to the purpose and/or media for which permission is hereby given.
5. Altering/Modifying Material: Not Permitted. However figures and illustrations may be altered/adapted minimally to serve your work. Any other abbreviations, additions, deletions and/or any other alterations shall be made only with prior written authorization of Elsevier Ltd. (Please contact Elsevier at [permissions@elsevier.com](mailto:permissions@elsevier.com))
6. If the permission fee for the requested use of our material is waived in this instance, please be advised that your future requests for Elsevier materials may attract a fee.
7. Reservation of Rights: Publisher reserves all rights not specifically granted in the combination of (i) the license details provided by you and accepted in the course of this licensing transaction, (ii) these terms and conditions and (iii) CCC's Billing and Payment terms and conditions.
8. License Contingent Upon Payment: While you may exercise the rights licensed immediately upon issuance of the license at the end of the licensing process for the transaction, provided that you have disclosed complete and accurate details of your proposed use, no license is finally effective unless and until full payment is received from you (either by publisher or by CCC) as provided in CCC's Billing and Payment terms and conditions. If full payment is not received on a timely basis, then any license preliminarily granted shall be deemed automatically revoked and shall be void as if never granted. Further, in the event that you breach any of these terms and conditions or any of CCC's Billing and Payment terms and conditions, the license is automatically revoked and shall be void as if never granted. Use of materials as described in a revoked license, as well as any use of the materials beyond the scope of an unrevoked license, may constitute copyright infringement and publisher reserves the right to take any and all action to protect its copyright in the materials.
9. Warranties: Publisher makes no representations or warranties with respect to the licensed material.
10. Indemnity: You hereby indemnify and agree to hold harmless publisher and CCC, and their respective officers, directors, employees and agents, from and against any and all claims arising out of your use of the licensed material other than as specifically authorized pursuant to this license.
11. No Transfer of License: This license is personal to you and may not be sublicensed, assigned, or transferred by you to any other person without publisher's written permission.
12. No Amendment Except in Writing: This license may not be amended except in a writing signed by both parties (or, in the case of publisher, by CCC on publisher's behalf).
13. Objection to Contrary Terms: Publisher hereby objects to any terms contained in any purchase order, acknowledgment, check endorsement or other writing prepared by you, which terms are inconsistent with these terms and conditions or CCC's Billing and Payment terms and conditions. These terms and conditions, together with CCC's Billing and Payment terms and conditions (which are incorporated herein), comprise the entire agreement between you

and publisher (and CCC) concerning this licensing transaction. In the event of any conflict between your obligations established by these terms and conditions and those established by CCC's Billing and Payment terms and conditions, these terms and conditions shall control.

14. **Revocation:** Elsevier or Copyright Clearance Center may deny the permissions described in this License at their sole discretion, for any reason or no reason, with a full refund payable to you. Notice of such denial will be made using the contact information provided by you. Failure to receive such notice will not alter or invalidate the denial. In no event will Elsevier or Copyright Clearance Center be responsible or liable for any costs, expenses or damage incurred by you as a result of a denial of your permission request, other than a refund of the amount(s) paid by you to Elsevier and/or Copyright Clearance Center for denied permissions.

#### LIMITED LICENSE

The following terms and conditions apply only to specific license types:

15. **Translation:** This permission is granted for non-exclusive world **English** rights only unless your license was granted for translation rights. If you licensed translation rights you may only translate this content into the languages you requested. A professional translator must perform all translations and reproduce the content word for word preserving the integrity of the article. If this license is to re-use 1 or 2 figures then permission is granted for non-exclusive world rights in all languages.

16. **Website:** The following terms and conditions apply to electronic reserve and author websites:

**Electronic reserve:** If licensed material is to be posted to website, the web site is to be password-protected and made available only to bona fide students registered on a relevant course if:

This license was made in connection with a course,

This permission is granted for 1 year only. You may obtain a license for future website posting,

All content posted to the web site must maintain the copyright information line on the bottom of each image,

A hyper-text must be included to the Homepage of the journal from which you are licensing at

<http://www.sciencedirect.com/science/journal/xxxx> or the Elsevier homepage for books at <http://www.elsevier.com>, and

Central Storage: This license does not include permission for a scanned version of the material to be stored in a central repository such as that provided by Heron/XanEdu.

17. **Author website** for journals with the following additional clauses:

All content posted to the web site must maintain the copyright information line on the bottom of each image, and the

permission granted is limited to the personal version of your paper. You are not allowed to download and post the

published electronic version of your article (whether PDF or HTML, proof or final version), nor may you scan the printed

edition to create an electronic version. A hyper-text must be included to the Homepage of the journal from which you are

licensing at <http://www.sciencedirect.com/science/journal/xxxx>. As part of our normal production process, you will receive an e-mail notice when your article appears on Elsevier's online service ScienceDirect ([www.sciencedirect.com](http://www.sciencedirect.com)).

That e-mail will include the article's Digital Object Identifier (DOI). This number provides the electronic link to the published

article and should be included in the posting of your personal version. We ask that you wait until you receive this e-mail

and have the DOI to do any posting.

Central Storage: This license does not include permission for a scanned version of the material to be stored in a central

repository such as that provided by Heron/XanEdu.

18. **Author website** for books with the following additional clauses:

Authors are permitted to place a brief summary of their work online only.

A hyper-text must be included to the Elsevier homepage at <http://www.elsevier.com>. All content posted to the web site

must maintain the copyright information line on the bottom of each image. You are not allowed to download and post the

published electronic version of your chapter, nor may you scan the printed edition to create an electronic version.

Central Storage: This license does not include permission for a scanned version of the material to be stored in a central

repository such as that provided by Heron/XanEdu.

19. **Website** (regular and for author): A hyper-text must be included to the Homepage of the journal from which you are

licensing at <http://www.sciencedirect.com/science/journal/xxxx> or for books to the Elsevier homepage at

<http://www.elsevier.com>

20. **Thesis/Dissertation:** If your license is for use in a thesis/dissertation your thesis may be submitted to your institution

in either print or electronic form. Should your thesis be published commercially, please reapply for permission. These

requirements include permission for the Library and Archives of Canada to supply single copies, on demand, of the

complete thesis and include permission for UMI to supply single copies, on demand, of the complete thesis. Should your

thesis be published commercially, please reapply for permission.

21. **Other Conditions:**

v1.6



11/14/13

RightsLink Printable License

If you would like to pay for this license now, please remit this license along with your payment made payable to "COPYRIGHT CLEARANCE CENTER" otherwise you will be invoiced within 48 hours of the license date. Payment should be in the form of a check or money order referencing your account number and this invoice number RLNK501156998. Once you receive your invoice for this order, you may pay your invoice by credit card. Please follow instructions provided at that time.

**Make Payment To:**  
Copyright Clearance Center  
Dept 001  
P.O. Box 843006  
Boston, MA 02284-3006

For suggestions or comments regarding this order, contact RightsLink Customer Support:  
[customercare@copyright.com](mailto:customercare@copyright.com) or +1-877-622-5543 (toll free in the US) or +1-978-646-2777.

Gratis licenses (referencing \$0 in the Total field) are free. Please retain this printable license for your reference. No payment is required.

---

## NATURE PUBLISHING GROUP LICENSE TERMS AND CONDITIONS

Nov 14, 2013

This is a License Agreement between Maral Aminpour ("You") and Nature Publishing Group ("Nature Publishing Group") provided by Copyright Clearance Center ("CCC"). The license consists of your order details, the terms and conditions provided by Nature Publishing Group, and the payment terms and conditions.

**All payments must be made in full to CCC. For payment instructions, please see information listed at the bottom of this form.**

License Number	3266390111406
License date	Nov 12, 2013
Licensed content publisher	Nature Publishing Group
Licensed content publication	Nature Nanotechnology
Licensed content title	Single-layer MoS2 transistors
Licensed content author	B. Radisavljevic, A. Radenovic, J. Brivio, V. Giacometti, A. Kis
Licensed content date	Jan 30, 2011
Volume number	6
Issue number	3
Type of Use	reuse in a dissertation / thesis
Requestor type	non-commercial (non-profit)
Format	print and electronic
Portion	figures/tables/illustrations
Number of figures/tables/illustrations	2
High-res required	no
Figures	Figure 1a and Figure 2c
Author of this NPG article	no
Your reference number	None
Title of your thesis / dissertation	THEORETICAL STUDIES OF NANOSTRUCTURE FORMATION AND TRANSPORT ON SURFACES
Expected completion date	Nov 2013
Estimated size (number of pages)	180
<b>Total</b>	<b>0.00 USD</b>
Terms and Conditions	

### Terms and Conditions for Permissions

Nature Publishing Group hereby grants you a non-exclusive license to reproduce this material for this purpose, and for no other use, subject to the conditions below:

1. NPG warrants that it has, to the best of its knowledge, the rights to license reuse of this material. However, you should ensure that the material you are requesting is original to Nature Publishing Group and does not carry the copyright of another entity (as credited in the published version). If the credit line on any part of the material you have requested indicates that it was reprinted or adapted by NPG with permission from another source, then you should also seek permission from that source to reuse the material.

2. Permission granted free of charge for material in print is also usually granted for any electronic version of that work, provided that the material is incidental to the work as a whole and that the electronic version is essentially equivalent to, or substitutes for, the print version. Where print permission has been granted for a fee, separate permission must be obtained for any additional, electronic re-use (unless, as in the case of a full paper, this has already been accounted for during your initial request in the calculation of a print run). NB: In all cases, web-based use of full-text articles must be authorized separately through the 'Use on a Web Site' option when requesting permission.
3. Permission granted for a first edition does not apply to second and subsequent editions and for editions in other languages (except for signatories to the STM Permissions Guidelines, or where the first edition permission was granted for free).
4. Nature Publishing Group's permission must be acknowledged next to the figure, table or abstract in print. In electronic form, this acknowledgement must be visible at the same time as the figure/table/abstract, and must be hyperlinked to the journal's homepage.
5. The credit line should read:  
Reprinted by permission from Macmillan Publishers Ltd: [JOURNAL NAME] (reference citation), copyright (year of publication)  
For AOP papers, the credit line should read:  
Reprinted by permission from Macmillan Publishers Ltd: [JOURNAL NAME], advance online publication, day month year (doi: 10.1038/sj.[JOURNAL ACRONYM].XXXXX)

**Note: For republication from the *British Journal of Cancer*, the following credit lines apply.**

Reprinted by permission from Macmillan Publishers Ltd on behalf of Cancer Research UK: [JOURNAL NAME] (reference citation), copyright (year of publication)  
For AOP papers, the credit line should read:  
Reprinted by permission from Macmillan Publishers Ltd on behalf of Cancer Research UK: [JOURNAL NAME], advance online publication, day month year (doi: 10.1038/sj.[JOURNAL ACRONYM].XXXXX)

6. Adaptations of single figures do not require NPG approval. However, the adaptation should be credited as follows:

Adapted by permission from Macmillan Publishers Ltd: [JOURNAL NAME] (reference citation), copyright (year of publication)

**Note: For adaptation from the *British Journal of Cancer*, the following credit line applies.**

Adapted by permission from Macmillan Publishers Ltd on behalf of Cancer Research UK: [JOURNAL NAME] (reference citation), copyright (year of publication)

7. Translations of 401 words up to a whole article require NPG approval. Please visit <http://www.macmillanmedicalcommunications.com> for more information. Translations of up to a 400 words do not require NPG approval. The translation should be credited as follows:

Translated by permission from Macmillan Publishers Ltd: [JOURNAL NAME] (reference citation), copyright (year of publication).

**Note: For translation from the *British Journal of Cancer*, the following credit line applies.**

Translated by permission from Macmillan Publishers Ltd on behalf of Cancer Research UK: [JOURNAL NAME] (reference citation), copyright (year of publication)

We are certain that all parties will benefit from this agreement and wish you the best in the use of this material. Thank you.

Special Terms:

v1.1

**If you would like to pay for this license now, please remit this license along with your payment made payable to**

<https://s100.copyright.com/MyAccount/web/sp/view/printablelicenseform/yourorders.jsp?ref=ecdac938-20a7-4c5f-8454-edf6c5285ec2&email=>

2/3

11/14/13

RightsLink Printable License

**"COPYRIGHT CLEARANCE CENTER" otherwise you will be invoiced within 48 hours of the license date. Payment should be in the form of a check or money order referencing your account number and this invoice number RLNK501157007. Once you receive your invoice for this order, you may pay your invoice by credit card. Please follow instructions provided at that time.**

**Make Payment To:  
Copyright Clearance Center  
Dept 001  
P.O. Box 843006  
Boston, MA 02284-3006**

**For suggestions or comments regarding this order, contact RightsLink Customer Support:  
[customercare@copyright.com](mailto:customercare@copyright.com) or +1-877-622-5543 (toll free in the US) or +1-978-646-2777.**

**Gratis licenses (referencing \$0 in the Total field) are free. Please retain this printable license for your reference. No payment is required.**

---





## ELSEVIER LICENSE TERMS AND CONDITIONS

Nov 14, 2013

This is a License Agreement between Maral Aminpour ("You") and Elsevier ("Elsevier") provided by Copyright Clearance Center ("CCC"). The license consists of your order details, the terms and conditions provided by Elsevier, and the payment terms and conditions.

**All payments must be made in full to CCC. For payment instructions, please see information listed at the bottom of this form.**

Supplier	Elsevier Limited The Boulevard, Langford Lane Kidlington, Oxford, OX5 1GB, UK
Registered Company Number	1982084
Customer name	Maral Aminpour
Customer address	University of Central Florida ORLANDO, FL 32816
License number	3266371189679
License date	Nov 12, 2013
Licensed content publisher	Elsevier
Licensed content publication	Surface Science
Licensed content title	Growth of aligned MoS <sub>2</sub> nanowires on Cu(111)
Licensed content author	Duy Le, Dezheng Sun, Wenhao Lu, Maral Aminpour, Chen Wang, Quan Ma, Talat S. Rahman, Ludwig Bartels
Licensed content date	May 2013
Licensed content volume number	611
Licensed content issue number	None
Number of pages	4
Start Page	1
End Page	4
Type of Use	reuse in a thesis/dissertation
Portion	full article
Format	both print and electronic
Are you the author of this Elsevier article?	Yes
Will you be translating?	No
Title of your thesis/dissertation	THEORETICAL STUDIES OF NANOSTRUCTURE FORMATION AND TRANSPORT ON SURFACES
Expected completion date	Nov 2013
Estimated size (number of pages)	180

Elsevier VAT number	GB 494 6272 12
Permissions price	0.00 USD
VAT/Local Sales Tax	0.00 USD / 0.00 GBP
<b>Total</b>	<b>0.00 USD</b>
<a href="#">Terms and Conditions</a>	

#### INTRODUCTION

1. The publisher for this copyrighted material is Elsevier. By clicking "accept" in connection with completing this licensing transaction, you agree that the following terms and conditions apply to this transaction (along with the Billing and Payment terms and conditions established by Copyright Clearance Center, Inc. ("CCC"), at the time that you opened your Rightslink account and that are available at any time at <http://myaccount.copyright.com>).

#### GENERAL TERMS

- Elsevier hereby grants you permission to reproduce the aforementioned material subject to the terms and conditions indicated.
- Acknowledgement:** If any part of the material to be used (for example, figures) has appeared in our publication with credit or acknowledgement to another source, permission must also be sought from that source. If such permission is not obtained then that material may not be included in your publication/copies. Suitable acknowledgement to the source must be made, either as a footnote or in a reference list at the end of your publication, as follows:  
"Reprinted from Publication title, Vol /edition number, Author(s), Title of article / title of chapter, Pages No., Copyright (Year), with permission from Elsevier [OR APPLICABLE SOCIETY COPYRIGHT OWNER]." Also Lancet special credit - "Reprinted from The Lancet, Vol. number, Author(s), Title of article, Pages No., Copyright (Year), with permission from Elsevier."
- Reproduction of this material is confined to the purpose and/or media for which permission is hereby given.**
- Altering/Modifying Material:** Not Permitted. However figures and illustrations may be altered/adapted minimally to serve your work. Any other abbreviations, additions, deletions and/or any other alterations shall be made only with prior written authorization of Elsevier Ltd. (Please contact Elsevier at [permissions@elsevier.com](mailto:permissions@elsevier.com))
- If the permission fee for the requested use of our material is waived in this instance, please be advised that your future requests for Elsevier materials may attract a fee.
- Reservation of Rights:** Publisher reserves all rights not specifically granted in the combination of (i) the license details provided by you and accepted in the course of this licensing transaction, (ii) these terms and conditions and (iii) CCC's Billing and Payment terms and conditions.
- License Contingent Upon Payment:** While you may exercise the rights licensed immediately upon issuance of the license at the end of the licensing process for the transaction, provided that you have disclosed complete and accurate details of your proposed use, no license is finally effective unless and until full payment is received from you (either by publisher or by CCC) as provided in CCC's Billing and Payment terms and conditions. If full payment is not received on a timely basis, then any license preliminarily granted shall be deemed automatically revoked and shall be void as if never granted. Further, in the event that you breach any of these terms and conditions or any of CCC's Billing and Payment terms and conditions, the license is automatically revoked and shall be void as if never granted. Use of materials as described in a revoked license, as well as any use of the materials beyond the scope of an unrevoked license, may constitute copyright infringement and publisher reserves the right to take any and all action to protect its copyright in the materials.
- Warranties:** Publisher makes no representations or warranties with respect to the licensed material.
- Indemnity:** You hereby indemnify and agree to hold harmless publisher and CCC, and their respective officers, directors, employees and agents, from and against any and all claims arising out of your use of the licensed material other than as specifically authorized pursuant to this license.
- No Transfer of License:** This license is personal to you and may not be sublicensed, assigned, or transferred by you to any other person without publisher's written permission.
- No Amendment Except in Writing:** This license may not be amended except in a writing signed by both parties (or, in the case of publisher, by CCC on publisher's behalf).
- Objection to Contrary Terms:** Publisher hereby objects to any terms contained in any purchase order, acknowledgment, check endorsement or other writing prepared by you, which terms are inconsistent with these terms and conditions or CCC's Billing and Payment terms and conditions. These terms and conditions, together with CCC's Billing and Payment terms and conditions (which are incorporated herein), comprise the entire agreement between you and publisher (and CCC) concerning this licensing transaction. In the event of any conflict between your obligations established by these terms and conditions and those established by CCC's Billing and Payment terms and conditions, these terms and conditions shall control.



14. Revocation: Elsevier or Copyright Clearance Center may deny the permissions described in this License at their sole discretion, for any reason or no reason, with a full refund payable to you. Notice of such denial will be made using the contact information provided by you. Failure to receive such notice will not alter or invalidate the denial. In no event will Elsevier or Copyright Clearance Center be responsible or liable for any costs, expenses or damage incurred by you as a result of a denial of your permission request, other than a refund of the amount(s) paid by you to Elsevier and/or Copyright Clearance Center for denied permissions.

#### LIMITED LICENSE

The following terms and conditions apply only to specific license types:

15. **Translation:** This permission is granted for non-exclusive world **English** rights only unless your license was granted for translation rights. If you licensed translation rights you may only translate this content into the languages you requested. A professional translator must perform all translations and reproduce the content word for word preserving the integrity of the article. If this license is to re-use 1 or 2 figures then permission is granted for non-exclusive world rights in all languages.

16. **Website:** The following terms and conditions apply to electronic reserve and author websites:

**Electronic reserve:** If licensed material is to be posted to website, the web site is to be password-protected and made available only to bona fide students registered on a relevant course if:

This license was made in connection with a course,

This permission is granted for 1 year only. You may obtain a license for future website posting,

All content posted to the web site must maintain the copyright information line on the bottom of each image,

A hyper-text must be included to the Homepage of the journal from which you are licensing at

<http://www.sciencedirect.com/science/journal/xxxx> or the Elsevier homepage for books at <http://www.elsevier.com>, and Central Storage: This license does not include permission for a scanned version of the material to be stored in a central repository such as that provided by Heron/XanEdu.

17. **Author website** for journals with the following additional clauses:

All content posted to the web site must maintain the copyright information line on the bottom of each image, and the permission granted is limited to the personal version of your paper. You are not allowed to download and post the published electronic version of your article (whether PDF or HTML, proof or final version), nor may you scan the printed edition to create an electronic version. A hyper-text must be included to the Homepage of the journal from which you are licensing at <http://www.sciencedirect.com/science/journal/xxxx>. As part of our normal production process, you will receive an e-mail notice when your article appears on Elsevier's online service ScienceDirect ([www.sciencedirect.com](http://www.sciencedirect.com)). That e-mail will include the article's Digital Object Identifier (DOI). This number provides the electronic link to the published article and should be included in the posting of your personal version. We ask that you wait until you receive this e-mail and have the DOI to do any posting.

Central Storage: This license does not include permission for a scanned version of the material to be stored in a central repository such as that provided by Heron/XanEdu.

18. **Author website** for books with the following additional clauses:

Authors are permitted to place a brief summary of their work online only.

A hyper-text must be included to the Elsevier homepage at <http://www.elsevier.com>. All content posted to the web site must maintain the copyright information line on the bottom of each image. You are not allowed to download and post the published electronic version of your chapter, nor may you scan the printed edition to create an electronic version.

Central Storage: This license does not include permission for a scanned version of the material to be stored in a central repository such as that provided by Heron/XanEdu.

19. **Website** (regular and for author): A hyper-text must be included to the Homepage of the journal from which you are licensing at <http://www.sciencedirect.com/science/journal/xxxx> or for books to the Elsevier homepage at <http://www.elsevier.com>

20. **Thesis/Dissertation:** If your license is for use in a thesis/dissertation your thesis may be submitted to your institution in either print or electronic form. Should your thesis be published commercially, please reapply for permission. These requirements include permission for the Library and Archives of Canada to supply single copies, on demand, of the complete thesis and include permission for UMI to supply single copies, on demand, of the complete thesis. Should your thesis be published commercially, please reapply for permission.

21. **Other Conditions:**

v1.6

**If you would like to pay for this license now, please remit this license along with your payment made payable to "COPYRIGHT CLEARANCE CENTER" otherwise you will be invoiced within 48 hours of the license date. Payment should be in the form of a check or money order referencing your account number and this invoice number RLNK501156980.**



11/14/13

RightsLink Printable License

Once you receive your invoice for this order, you may pay your invoice by credit card. Please follow instructions provided at that time.

**Make Payment To:**  
Copyright Clearance Center  
Dept 001  
P.O. Box 843006  
Boston, MA 02284-3006

For suggestions or comments regarding this order, contact RightsLink Customer Support:  
[customercare@copyright.com](mailto:customercare@copyright.com) or +1-877-622-5543 (toll free in the US) or +1-978-646-2777.

Gratis licenses (referencing \$0 in the Total field) are free. Please retain this printable license for your reference. No payment is required.

---

---

## Maral Aminpour

---

**From:** Ludwig Bartels <ludwig.bartels@ucr.edu>  
**Sent:** Thursday, November 14, 2013 12:46 PM  
**To:** Maral Aminpour  
**Subject:** Re: copyright permission

Sure, no need to ask...

On 11/14/2013 9:36 AM, Maral Aminpour wrote:

Dear Dr. Bartels,

Attached you can find the copyright permission that I got from

1. Elsevier to include Figure.2 (experimental result) of "Growth of aligned MoS<sub>2</sub> nanowires on Cu(111)" paper.
2. Angewandte Chemie to include Figure.1a of "An MoS<sub>x</sub> Structure with High Affinity for Adsorbate Interaction"

I also would like to ask permission from you to include the mentioned STM figures to my dissertation thesis with the title of "THEORETICAL STUDIES OF NANOSTRUCTURE FORMATION AND TRANSPORT ON SURFACES".

I would appreciate if you could let me know about your decision.

Thank you very much  
Best regards,  
Maral

---

Maral Aminpour, PhD Candidate  
Graduate Research Assistant  
Department of Physics  
University of Central Florida

--

Ludwig Bartels  
Professor of Chemistry  
Member of the Departments/Programs of  
Electrical Eng., Materials Science and Eng., Mechanical Eng. & Physics  
Graduate Advisor of Materials Science and Eng.  
University of California at Riverside  
Ph: 951 827 2041, email: [Ludwig.Bartels@ucr.edu](mailto:Ludwig.Bartels@ucr.edu)

## Maral Aminpour

---

**From:** Duy Le <Duy.Le@ucf.edu>  
**Sent:** Thursday, November 14, 2013 12:27 PM  
**To:** Maral Aminpour  
**Subject:** RE: copyright permission

Yes. It is my honor to have the Figure used in your PhD Thesis.  
Good luck!

-----  
Duy Le  
Postdoctoral Associate  
Department of Physics  
University of Central Florida.  
Website: <http://www.physics.ucf.edu/~dle>

---

**From:** Maral Aminpour [<mailto:maral@knights.ucf.edu>]  
**Sent:** Thursday, November 14, 2013 12:21 PM  
**To:** Duy Le  
**Subject:** copyright permission

Dear Dr. Le,

As attached you can find the copyright permission that I got from Physical Review B Journal to include "Fig. 2, Phys. Rev. B 85, 075429 (2012)."

I also would like to ask permission from you to include the mentioned figure to my dissertation thesis with the title of "THEORETICAL STUDIES OF NANOSTRUCTURE FORMATION AND TRANSPORT ON SURFACES".

I appreciate if you could let me know about your decision.

Thank you very much  
Best regards,  
Maral

---

Maral Aminpour, PhD Candidate  
Graduate Research Assistant  
Department of Physics  
University of Central Florida

## Maral Aminpour

---

**From:** Adam Kiejna <kiejna@ifd.uni.wroc.pl>  
**Sent:** Thursday, November 14, 2013 4:17 PM  
**To:** Maral Aminpour  
**Subject:** Re: copyright permission

Dear Maral,

It is good to hear from you and to learn that you are finishing your PhD dissertation. I am glad to grant you a permission to include the figure mentioned by you in your thesis. Of course, as usual, you should give a full reference to the source.

I think more important than my consent is a consent you should get from the Institute of Physics, UK, who is a copyright owner of that publication, because I have transferred my copyrights to IOP on publication of our work in J. Phys. Condens. Matter. Please check it and write to them.

With best regards,  
Adam

-----  
Prof. Dr. Adam Kiejna  
University of Wroclaw  
Institute of Experimental Physics  
Plac M. Borna 9  
50-204 Wroclaw  
Poland

email: [kiejna@ifd.uni.wroc.pl](mailto:kiejna@ifd.uni.wroc.pl)  
phone: +48 71 3759264  
fax: +48 71 3287365  
-----

On 2013-11-14 18:48, Maral Aminpour wrote:

> Dear Dr. Kiejna,  
> I ALSO WOULD LIKE TO ASK PERMISSION FROM YOU TO INCLUDE FIGURE.4 OF  
> "BULK AND SURFACE PROPERTIES OF HEXAGONAL-CLOSE-PACKED BE AND MG"  
> PAPER TO MY DISSERTATION THESIS WITH THE TITLE OF " THEORETICAL  
> STUDIES OF NANOSTRUCTURE FORMATION AND TRANSPORT ON SURFACES".  
> I would appreciate if you could let me know about your decision.  
> Thank you very much  
> Best regards,  
> Maral  
>  
> \_\_\_\_\_  
> Maral Aminpour, PhD Candidate  
> Graduate Research Assistant  
> Department of Physics  
> University of Central Florida

## **APPENDIX B: LIST OF PUBLICATIONS**

1. **M. Aminpour**, O. Trushin and T. S. Rahman, "Effect of misfit dislocation on surface diffusion," Phys. Rev. B 84, 035455 (2011).
2. **M. Aminpour**, O. Trushin, and T. S. Rahman, "Anisotropy in surface diffusion due to proximity to misfit dislocation," (Submitted to J. Phys.: Condens. Matter-first revisions received)
3. **M. Aminpour**, M. Alcántara-Ortigoza, and T. S. Rahman, "Ab-initio study of size effects on Mg thin films and Mg self-diffusion on wide vs. narrow (0001) terraces, " (paper finalized, to be submitted very soon)
4. **M. Aminpour**, D. Le, M. Alcántara-Ortigoza, and T. S. Rahman, "First-principle investigation of the stability and vibrational spectrum of MoS<sub>x</sub> nanostructures grown on Cu(111)," (in preparation, 90% complete)
5. Z. Chromcová, M. Hupalo, M. C. Tringides, **M. Aminpour**, M. Alcántara-Ortigoza, T. S. Rahman, and Z. Chvoj, "Controllable Mg film morphologies: DFT, kinetic Monte Carlo simulations and experiments on Mg films on stepped W(110) surfaces," (submitted to Surface Science-second revisions received)
6. D. Le, D. Sun, W. Lu, **M. Aminpour**, C. Wang, Q. Ma, T. S. Rahman, and L. Bartels, "Growth of aligned Mo<sub>6</sub>S<sub>6</sub> nanowires on Cu(111)," Surface Science, 611, 1 (2013)
7. D. Sun, W. Lu, D. Le, Q. Ma, **M. Aminpour**, M. Alcántara-Ortigoza, S. Bobek, J. Mann, J. Wyrick, T. S. Rahman, and L. Bartels, "An MoS<sub>x</sub> structure with high affinity for adsorbate interaction," Angew. Chem. Int. Ed. 51, 10284 (2012).
8. D. Le, **M. Aminpour**, A. Kiejna, and T. S. Rahman, "The role of van der Waals interaction in the tilted binding of amine molecules to the Au(111) surface," J. Phys.: Condens. Matter 24, 222001 (2012). (IOPSELECT)

9. M. Alcántara-Ortigoza, **M. Aminpour**, and T. S. Rahman, “Vibrational spectrum and stability of the long-debated models for the  $(\sqrt{7}\times\sqrt{7})R19$  Phase of S/Cu(111),” (in preparation)
10. D. T. Restrepo, K. E. Giesler, R. A. Penabe, **M. Aminpour**, D. Le, T. S. Rahman, and R. G. Blair. “Heterogeneous metal-free hydrogenation over defect hexagonal Boron nitride,” (Science, second revisions received)